

JAERI-M

88-177

U.S./JAERI COLLABORATIVE PROGRAM ON
FUSION NEUTRONICS
PHASE I FUSION INTEGRAL EXPERIMENTS
VOLUME II : ANALYSIS

September 1988

Masayuki NAKAGAWA
Takamasa MORI
Kazuaki KOSAKO
Yujiro IKEDA
Tomoo NAKAMURA

Mahmoud Z. YOUSSEF
Chen-Yu GUNG
Mohamed A. ABDOU
Robert T. SANTORO
Rufard. G. ALSMILLER
John M. BARNES
Tony A. GABRIEL

JAERI-Mレポートは、日本原子力研究所が不定期に公刊している研究報告書です。

入手の間合わせは、日本原子力研究所技術情報部情報資料課（〒319-11茨城県那珂郡東海村）あて、お申しこしてください。なお、このほかに財団法人原子力弘済会資料センター（〒319-11茨城県那珂郡東海村日本原子力研究所内）で複写による実費頒布をおこなっております。

JAERI-M reports are issued irregularly.

Inquiries about availability of the reports should be addressed to Information Division, Department of Technical Information, Japan Atomic Energy Research Institute, Tokai-mura, Naka-gun, Ibaraki-ken 319-11, Japan.

© Japan Atomic Energy Research Institute, 1988

編集兼発行	日本原子力研究所
印刷	日立高速印刷株式会社

U.S./JAERI Collaborative Program on
Fusion Neutronics
Phase I Fusion Integral Experiments
Volume II: Analysis

JAERI

Masayuki Nakagawa
Takamasa MORI
Kazuaki KOSAKO
Yujiro IKEDA
Tomoo NAKAMURA

U.S.

Mahmoud Z. YOUSSEF(UCLA)
Chen-Yu GUNG(UCLA)
Mohamed A. ABDOU(UCLA)
Robert T. SANTORO(ORNL)
Rufard. G. ALSMILLER(ORNL)
John M. BARNES(ORNL)
Tony A. GABRIEL(ORNL)

Edited by M. NAKAGAWA(JAERI) and M. Z. YOUSSEF(UCLA)

Department of Reactor Engineering
Tokai Research Establishment
Japan Atomic Energy Research Institute
Tokai-mura, Naka-gun, Ibaraki-ken

(Received August 25, 1988)

The U.S./JAERI Collaborative Program on Fusion Neutronics is in progress using the FNS facility at JAERI. Phase I experiments of the program have been completed and independently analyzed. The predictions of key neutronics parameters were compared to measurements to derive information on the accuracy involved in the calculations of these parameters. First, measurements were performed to characterize the neutron field by the foil activations method and spectrum measurements using both TOF technique as well as NE213 and proton recoil counters. The measurements inside the Li_2O assembly included tritium production rate

(TPR), foil activation and neutron spectrum measurements above 1 MeV. Analyses for these measured parameters were performed by using two-dimensional discrete ordinates codes, DOT3.5(JAERI) and DOT4.3(U.S.) and Monte Carlo codes, MORSE-DD(JAERI) and MCNP(U.S.). The nuclear data used by JAERI were based on JENDL3/PR1 and PR2 while the U.S. calculations were based on ENDF/B-V and data evaluated at LANL for ^7Li and Be.

The configurations considered for the test assembly were: (a) a reference Li_2O assembly, (b) first wall preceded the Li_2O assembly with and without a coolant channel simulated by polyethylene, and (c) beryllium zone in front of the assembly as well as sandwiched between a front Li_2O zone and the main assembly. In this document, results of the analysis for these experiments are reported as Volume II. Details of the experiments and the experimental techniques applied are reported separately as Volume I.

Keywords: Fusion Neutronics, Tritium Production Rate, Neutron Spectrum, Foil Activation Measurements, Nuclear Data, Discrete Ordinates Codes, Monte Carlo Technique, Cross-Section Sensitivity/Uncertainty Analysis

日米協力核融合ニュートロニクス計画

フェイズ 1 核融合積分実験

第 2 巻：解 析

日本原子力研究所東海研究所原子炉工学部

(原 研) (米 国)

中川 正幸	Mahmoud Z. YOUSSEF(UCLA)
森 貴正	Chen-Yu GUNG(UCLA)
小迫 和明	Mohamed A. ABDOL(UCLA)
池田裕二郎	Robert T. SANTORO(ORNL)
中村 知夫	Rufard G. ALSMILLER(ORNL)
	John M. BARNES(ORNL)
	Tony A. GABRIEL(ORNL)

編集 中川 正幸(原研)・M.Z.YOUSSEF(UCLA)

(1988年8月25日受理)

核融合ニュートロニクスに関する日米協力計画が、原研のFNSを用いて進められている。そのフェイズ1実験が終了し、各々の側で独立に解析が行われた。主要な中性子特性パラメータの予測値を、これらのパラメータの予測精度を明らかにするため実験と比較した。まず測定では箔放射化法並びにNE213計数管を用いたTOF法及び反踏陽子計数管を用いたスペクトル測定により中性子場の特性が明らかにされた。酸化リチウム体系中では、トリチウム生成率、箔放射化率、1 MeV 以上の中性子スペクトルが測定された。これらの諸パラメータの解析は、二次元SnコードDOT3.5(原研)及びDOT4.3(米国)並びにモンテカルロコードMORSE-DD(原研)及びMCNP(米国)を用いて行われた。原研が用いた核データはJENDL3/PR1とPR2であり、一方米国はENDF/B-V及び⁷LiとBeについてはLANLの評価値を用いた。

試験体系として選ばれた配置は、1) 基準酸化リチウム体系、2) 基準体系前面に第一壁を設けた系及びさらに冷却管を模擬するためポリエチレン層も入れた体系、3) 基準体系の前面にベリリウム層を設けた系及び更にこのベリリウム層の前に酸化リチウムを設けたサンドイッチ体系である。本報告書では、これらの実験の解析結果が第2巻として記述されている。実験及び用いた実験技術の詳細については第一巻で別に述べられている。

TABLE OF CONTENTS

	Page
I. <u>Introduction</u>	1
I.1 Scope.....	1
I.2 Brief Description of the Experiments and Measured Parameters.....	1
II. <u>Analytical Methods, Nuclear Data and Calculation Models</u>	6
II.1 JAERI Analysis.....	6
II.1.1 Nuclear Data.....	6
II.1.2 Transport Codes.....	6
II.1.3 Calculational Models.....	9
A. Two-Dimensional Models Used by DOT3.5.....	9
B. Three-Dimensional Model Used by MORSE-DD.....	12
II.2 U.S. Analysis.....	20
II.2.1 Nuclear Data.....	20
II.2.2 Transport Codes.....	22
II.2.3 Calculational Models.....	24
A. Two-Dimensional Model Used by DOT4.3.....	24
B. Three-Dimensional Model Used by MCNP.....	27
III. <u>Neutron Source Characterization</u>	32
III.1 Analysis with Monte Carlo Codes.....	32
III.1.1 Neutron Source Generation.....	32
III.1.2 Neutron Source Spectrum at the Entrance to Experimental Cavity.....	38
III.1.3 Source Characterization by Integral Quantities (Flux Mapping).....	63
IV. <u>Tritium Production Rates</u>	81
IV.1 The Reference Li ₂ O Experiment.....	81
IV.1.1 Tritium Production Rate from ⁶ Li (T ₆).....	81
IV.1.2 Tritium Production Rate from ⁷ Li (T ₇).....	91
IV.2 First Wall Experiments.....	98
IV.2.1 2-D Analysis.....	98
IV.2.2 Monte Carlo Analysis.....	108
IV.3 The Beryllium Neutron-Multiplier Experiments.....	135
V. <u>Reaction Rates of Activation Foils</u>	164
V.1 Reference System.....	164
V.2 Beryllium-Sandwiched System.....	179
V.3 Possible Causes for the Observed Trends in the C/E Curves of Various Activation Reaction Rates.....	184
VI. <u>In-System Spectra</u>	191
VI.1 Reference System.....	191
VI.2 Beryllium-Sandwiched System.....	191
VII. <u>Cross-Section Sensitivity and Uncertainty Analysis</u>	211
VII.1 Introduction.....	211
VII.2 Definitions and Theoretical Background.....	214
VII.3 Experiments Considered and Calculational Models.....	216
VII.4 Calculational Procedures.....	221
VII.5 Tritium Production Rate Profiles.....	225
VII.6 Sensitivity Analysis Results.....	225

	Page
VII.6.1 Sensitivity Profiles of T_6	229
VII.6.1.1 Variation in Σ_t of ^6Li	229
VII.6.1.2 Variation in Σ_t of ^7Li	235
VII.6.1.3 Variation in Σ_t of Oxygen.....	241
VII.6.1.4 Variation in Σ_t of Iron.....	245
VII.6.1.5 Variation in Σ_t of Other Materials.....	245
VII.6.2 Sensitivity Profiles of T_7	248
VII.7 Uncertainty Analysis Results.....	252
VII.7.1 Uncertainty in T_6	252
VII.7.2 Uncertainties in T_7	257
VII.8 Summary and Conclusions.....	259
VIII. <u>Summary and Concluding Remarks</u>	261
Source Characterization.....	261
Tritium Production Rate.....	262
Activation Foil Measurements.....	263
In-System Spectrum Measurement.....	264
<u>References</u>	266

目 次

I. 序 論	1
I.1 範 囲	1
I.2 実験及び測定されたパラメータの主要項目	1
II. 解析法, 核データ及び計算モデル	6
II.1 原研の解析	6
II.1.1 核データ	6
II.1.2 輸送コード	6
II.1.3 計算モデル	9
A. DOT 3.5 で用いた二次元モデル	9
B. MORSE-DD で用いた三次元モデル	12
II.2 米国の解析	20
II.2.1 核データ	20
II.2.2 輸送コード	22
II.2.3 計算モデル	24
A. DOT 4.3 で用いた二次元モデル	24
B. MCNP で用いた三次元モデル	27
III. 中性子源特性	32
III.1 モンテカルロ法による解析	32
III.1.1 中性子発生	32
III.1.2 実験孔入口における中性子源スペクトル	38
III.1.3 積分量(中性子束)による線源特性表示	63
IV. トリチウム生成率	81
IV.1 基準酸化リチウム体系	81
IV.1.1 ${}^6\text{Li}$ によるトリチウム生成率 (T_6)	81
IV.1.2 ${}^7\text{Li}$ によるトリチウム生成率 (T_7)	91
IV.2 第一壁体系	98
IV.2.1 二次元解析	98
IV.2.2 モンテカルロ法による解析	108
IV.3 ベリリウム中性子増倍体系	135
V. 放射化箔の反応率	164
V.1 基準体系	164
V.2 ベリリウムサンドイッチ体系	179
V.3 各種放射化反応率の C/E 値曲線に見られる傾向の原因検討	184
VI. 系内スペクトル	191

VI.1	基準体系	191
VI.2	ベリリウムサンドイッチ体系	191
VII.	断面積の感度と不確かさの解析	211
VII.1	序	211
VII.2	定義と理論的背景	214
VII.3	対象とした実験と計算モデル	216
VII.4	計算手法	221
VII.5	トリチウム生成率分布	225
VII.6	感度解析の結果	225
VII.6.1	T_6 の感度傾向	229
VII.6.1.1	${}^6\text{Li}$ の Σ_t における変化	229
VII.6.1.2	${}^7\text{Li}$ の Σ_t における変化	235
VII.6.1.3	酸素の Σ_t における変化	241
VII.6.1.4	鉄の Σ_t における変化	245
VII.6.1.5	他の物質の Σ_t における変化	245
VII.6.2	T_7 の感度傾向	248
VII.7	不確かさの解析結果	252
VII.7.1	T_6 における不確かさ	252
VII.7.2	T_7 における不確かさ	257
VII.8	まとめと結論	259
VIII.	まとめと結果の検討	261
	中性子源特性	261
	トリチウム生成率	262
	放射化箔測定	263
	系内中性子スペクトル測定	264
	参考文献	266

List of Tables

Table	Page
II.1 Comparison of Nuclear Cross-Section Library Sets.....	8
II.2 Regions of Track Length Estimators Used in Test Channel Dimension: 4.82 x 4.82 x ΔZ cm ³	15
II.3 Number of Neutron Histories Used in JAERI's Monte Carlo Calculations.....	19
II.4 53-Neutron Energy Group Structure and Tritium Breeding Cross-Sections Used in the Monte Carlo Analysis of the First Wall Experiments.....	21
II.5 Detector Locations and Monte Carlo Estimator Cell Dimensions ^(a) Used in the Monte Carlo Calculations of the First Wall Experiments.....	31
III.1 Energy and Angular Distribution of the Emitted (D,T) Neutron.....	35
III.2 Source Neutron from Target Assembly (Source/4 π).....	39
III.3 Comparison of Source Neutron Spectrum with Measurements.....	48
III.4 Horizontal Distribution of Various Reaction Rates (U.S. Calculations).....	75
III.5 Vertical Distribution of Various Reaction Rates (U.S. Calculations).....	80
IV.1 Ratio of the Calculated Tritium Production Rate from ⁷ Li to the Values in the Reference Li ₂ O Assembly ^(a)	101
IV.2 Ratio of Calculated Tritium Production Rate From ⁶ Li, T ₆ , to the Reference Experiment.....	102
IV.3 Calculated to Measured Values for Tritium Production Rate from ⁶ Li In the First Wall Experiment along the Central Axis ^(a)	106
IV.4 Ratios of the Calculated T ₆ by U.S. to the Calculated T ₆ by JAERI in the First Wall Experiments ^(a)	109
IV.5 Experimental Configurations Used in the Monte Carlo Analysis for the First Wall Experiments.....	113
V.1 Cross-Sections for ⁷ Li at 10 MeV.....	186
VII.1 The Atomic Densities of Materials Considered in the Analysis (Atoms/cm ³ 10 ⁻²⁴).....	220
VII.2 Locations of the Point Detectors, P _i , and Zone Detectors, Z _i , in the Benchmark and the Reference Systems ^(a)	224
VII.3 Integrated Relative Sensitivity Coefficients of T ₆ , at the Middle Point of the Li ₂ O Assembly.....	246
VII.4 Integrated Relative Sensitivity Coefficients of T ₇ , at the Middle Point of the Li ₂ O Assembly.....	253

List of Figures

<u>Figure</u>		<u>Page</u>
I.1	Geometrical arrangement of Phase I experiments.....	2
I.2	Geometrical arrangement for the first wall experiments.....	4
I.3	Geometrical arrangement for the beryllium experiments.....	5
II.1	Calculation flow of the group cross-section libraries used by JAERI.....	7
II.2	Calculational model of Phase I experiments with first walls used by DOT3.5 (JAERI).....	10
II.3	Calculational model of Phase I experiment with beryllium zone as used by DOT3.5 (JAERI)...	11
II.4	Horizontal view of experimental configuration.....	13
II.5	Calculational model of the center and off-center channels in the Li ₂ O block.....	14
II.6	Second step in the calculational model used by MORSE-DD.....	16
II.7	Effect of concrete wall thickness surrounding Li ₂ O on T ₆ along the axis of the central drawer.....	18
II.8	The 2-D (R-Z) calculational model for the reference and first wall experiments used by DOT4.3 (U.S.).....	25
II.9	The 2-D (R-Z) calculational model for the beryllium experiments (U.S.).....	26
II.10	Anisotropic point source and isotropic plane source used in the MCNP calculational model....	28
II.11	The biasing scheme used by the U.S. (ORNL) in the Monte Carlo analysis of the reference and first wall experiments.....	30
III.1	Cross-sectional view of the rotating neutron target (RNT) (calculational model).....	33
III.2	Angular distribution of neutrons emitted from RNT. The distribution curves are normalized to unity at $\theta = 80$ degrees. (JAERI).....	36
III.3	Angular distribution of neutrons emitted from RNT (U.S.).....	37
III.4	Angular distribution of neutrons emitted from RNT (absolute value).....	40
III.5	Layout of the time-of-flight spectrum measurements.....	41
III.6	Comparison of neutron spectrum for RNT between calculations and measurements by the TOF method, no collimator, L=17.445 m.....	43
III.7	Comparison of neutron spectrum for RNT between calculations and measurements by the TOF method, no collimator, L=11.445 m.....	45
III.8	Comparison of neutron spectra for RNT between calculations and measurements by the TOF method, with collimator, L=17.445 m.....	46
III.9	Comparison of incident neutron current into the entrance of the experimental hole.....	49
III.10	Measured and calculated neutron spectra on the entrance of experimental hole with and without shadow shield.....	50
III.11	Measured and calculated neutron spectrum on the entrance of the experimental hole (MCNP calculation, U.S.).....	52

III.12	Measured and calculated spectrum on the entrance of the experimental hole with a small-bar between RNT and the experimental hole (MCNP calculation, U.S.).....	53
III.13	Measured and calculated spectrum on the entrance of the experimental hole with a heavy shield between RNT and the experimental hole (MCNP calculation, U.S.).....	54
III.14	Comparison of neutron spectra in front of the Li ₂ O assembly and with shadow cone out (JAERI).....	55
III.15	Comparison of neutron spectra in front of the Li ₂ O assembly contributed from room returned neutrons (shadow cone in place, JAERI).....	56
III.16	Comparison of neutron spectra in front of experimental hole without the Li ₂ O assembly (assembly out, shadow cone out, JAERI).....	57
III.17	Comparison of neutron spectra in front of the Li ₂ O assembly and with the shadow cone out (U.S.).....	59
III.18	Comparison of neutron spectra in front of the Li ₂ O assembly contributed from room returned neutrons (shadow cone in place, U.S.).....	60
III.19	Comparison of neutron spectra in front of the experimental hole without the Li ₂ O assembly (assembly out, shadow cone out, U.S.).....	61
III.20	Comparison of neutron spectra in front of the experimental hole without the Li ₂ O assembly (assembly out, shadow cone out, U.S.).....	62
III.21	Horizontal distributions of NE213 detector response.....	64
III.22	Horizontal distribution of the ¹⁹⁷ Au(n,2n) ¹⁹⁶ Au reaction rate on the front surface of the Li ₂ O assembly.....	66
III.23	C/E values of the ¹⁹⁷ Au(n,2n) ¹⁹⁶ Au reaction rates on the front surface in the horizontal direction.....	67
III.24	Horizontal distribution of the ⁵⁸ Ni(n,2n) ⁵⁷ Ni reaction rate on the front surface of the Li ₂ O assembly.....	68
III.25	C/E values of the ⁵⁸ Ni(n,2n) ⁵⁷ Ni reaction rate on the front surface in the horizontal direction.....	69
III.26	Horizontal distribution of the ²⁷ Al(n,α) ²⁴ Na reaction rate on the front surface of the Li ₂ O assembly.....	70
III.27	C/E values of the ²⁷ Al(n,α) ²⁴ Na reaction rate on the front surface in the horizontal direction.....	71
III.28	Horizontal distribution of the ¹⁹⁷ Au(n,γ) ¹⁹⁸ Au reaction rate on the front surface of the Li ₂ O assembly.....	72
III.29	C/E values of the ¹⁹⁷ Au(n,γ) ¹⁹⁸ Au reaction rate on the front surface in the horizontal direction.....	73
III.30	Vertical distribution of the ⁵⁸ Ni(n,2n) ⁵⁷ Ni reaction rate on the front surface of the Li ₂ O assembly.....	76
III.31	C/E values of the ⁵⁸ Ni(n,2n) ⁵⁷ Ni reaction rate on the front surface in the vertical direction.....	77
III.32	Vertical distribution of the ²⁷ Al(n,α) ²⁴ Na reaction rate on the front surface of the Li ₂ O assembly.....	78
III.33	C/E values of the ²⁷ Al(n,α) ²⁴ Na reaction rate on the front surface in the vertical direction.....	79

IV.1	Distribution of tritium production rate by ^6Li in the reference system.....	82
IV.2	C/E values for T_6 in the reference system calculation: DOT3.5 with JACKAS.....	84
IV.3	Comparison of C/E values for T_6 in the reference system. Measured values were obtained by a Li-glass detector.....	85
IV.4	Comparison of C/E values for T_6 in the reference system. Measured values were obtained by Li_2O pellets.....	86
IV.5	Comparison of C/E values for T_6 in the reference system. Measured values were obtained by Li-metal detectors.....	88
IV.6	Components contributing to T_6 in the reference system. Measured values were obtained by Li-glass detectors and calculations were performed by MORSE-DD.....	89
IV.7	Components contributing to T_6 in the reference system. Measured values were obtained by Li-glass detectors and calculations were performed by DOT3/5/JACKAS.....	90
IV.8	Tritium production rate by ^7Li in the reference system.....	92
IV.9	Comparison of C/E values for T_7 in the reference system based on calculations performed by DOT3.5 with JACKAS library.....	93
IV.10	Comparison of C/E values for T_7 in the reference system. Experimental values were obtained by Li-metal detectors.....	94
IV.11	Comparison of cross-sections for $^7\text{Li}(n,n'\alpha)t$ reaction.....	95
IV.12	The C/E values for T_7 in the reference system using the NE213 indirect method.....	96
IV.13	The C/E values for T_7 in the reference system using Li metal detectors.....	97
IV.14	Effect of first wall on tritium production from ^7Li , T_7 (U.S. calculation: DOT4.3/MATXS6)...	99
IV.15	Effect of first wall on tritium production from ^6Li , T_6 (U.S. calculation: DOT4.3/MATXS6)...	100
IV.16	Effect of first wall on tritium production from ^6Li , T_6	103
IV.17	The C/E values for tritium production rate from ^6Li , T_6 in the first wall experiment without a polyethylene layer (2-D model).....	104
IV.18	The C/E values for tritium production rate from ^6Li , T_6 in the first wall experiments with a polyethylene layer (2-D model).....	105
IV.19	The C/E values for T_6 in the first wall experiments, based on the calculated values by DOT3.5/JACKAS (JAERI).....	107
IV.20	Ratio of the calculated T_6 by U.S. to calculated T_6 by JAERI in the first wall experiments (2-D model).....	110
IV.21	C/E values for T_7 in the first wall experiments (without a coolant channel).....	111
IV.22	C/E values for T_7 in the first wall experiments (with a coolant channel).....	112
IV.23	Profile of TPR from ^6Li in the reference system (U.S.: ORNL calculations).....	114
IV.24	Profile of TPR from ^6Li in 0.5 cm SS first wall system (U.S.: ORNL calculations).....	115
IV.25	Profile of TPR from ^6Li in 1.5 cm SS first wall system (U.S.: ORNL calculations).....	116
IV.26	Profile of TPR from ^6Li in 0.5 cm SS + 0.5 cm PE first wall system (U.S.: ORNL calculations).....	117
IV.27	Profile of TPR from ^6Li in 1.5 cm SS + 0.5 cm PE first wall system (U.S.: ORNL calculations).....	118

IV.28	C/E values for T_6 in the reference system (U.S.: ORNL calculations).....	120
IV.29	C/E values for T_6 in 0.5 cm SS first wall system (U.S.: ORNL calculations).....	121
IV.30	C/E values for T_6 in 1.5 cm SS first wall system (U.S.: ORNL calculations).....	122
IV.31	C/E values for T_6 in 0.5 cm SS + 0.5 cm PE first wall system (U.S.: ORNL calculations)....	123
IV.32	C/E values for T_6 in 1.5 cm SS + 0.5 cm PE first wall system (U.S.: ORNL calculations)....	124
IV.33	Profile of TPR from ^7Li in the reference system (U.S.: ORNL calculations).....	125
IV.34	Profile of TPR from ^7Li in 0.5 cm SS first wall system (U.S.: ORNL calculations).....	126
IV.35	Profile of TPR from ^7Li in 1.5 cm SS first wall system (U.S.: ORNL calculations).....	127
IV.36	Profile of TPR from ^7Li in 0.5 cm SS + 0.5 cm PE first wall system (U.S.: ORNL calculations).....	128
IV.37	Profile of TPR from ^7Li in 1.5 cm SS + 0.5 cm PE first wall system (U.S.: ORNL calculations).....	129
IV.38	C/E values for T_7 in the reference system (U.S.: ORNL calculations).....	130
IV.39	C/E values for T_7 in 0.5 cm SS first wall system (U.S.: ORNL calculations).....	131
IV.40	C/E values for T_7 in 1.5 cm SS first wall system (U.S.: ORNL calculations).....	132
IV.41	C/E values for T_7 in 0.5 cm SS + 0.5 cm PE first wall system (U.S.: ORNL calculations)....	133
IV.42	C/E values for T_7 in 1.5 cm SS + 0.5 cm PE first wall system (U.S.: ORNL calculations)....	134
IV.43	Neutron multiplication effect of Be on T_6 measured by Li-glass detectors.....	136
IV.44	Neutron multiplication effect of Be on T_6 as calculated by DOT3.5 with JACKAS library.....	137
IV.45	Neutron multiplication effect of Be on T_6 as calculated by the Monte Carlo method.....	138
IV.46	Comparison of Be neutron multiplication effect on T_6 , between measurements and calculations (JAERI).....	139
IV.47	C/E values for tritium production rate from ^6Li , T_6 , in the beryllium experiments (2-D model, U.S. calculations).....	141
IV.48	C/E values for tritium production rate from ^6Li , T_6 , in the beryllium experiments (2-D model, JAERI calculations).....	142
IV.49	Comparison of C/E values for T_6 between experiments with and without Be multiplier (calculation: MORSE-DD with DDL/J3P1, experiment: Li-glass).....	143
IV.50	C/E values for tritium production rate from ^6Li , T_6 , in the Be-sandwiched system, obtained by various codes and libraries.....	145
IV.51	C/E values for T_6 in the Be-sandwiched system based on the calculated values by DOT3.6 with JACKAS library.....	146
IV.52	Comparison of self-shielding factors for $^6\text{Li}(n,\alpha)$ reaction in the Be-sandwiched system.....	147
IV.53	Comparison of C/E values for T_6 in the reference and the Be-sandwiched systems based on the experimental values obtained by the Li_2O -pellet detectors.....	149
IV.54	Comparison of C/E values for T_6 in the reference and the Be-sandwiched systems based on the experimental values obtained by the Li-metal detectors.....	150
IV.55	C/E of TPR by ^6Li in the Be-sandwiched system (Li-metal).....	151

IV.56	C/E values for tritium production rate from ${}^6\text{Li}, T_6$ in the Be-sandwiched system based on DOT calculations and li-metal Li_2O pellet measurements.....	152
IV.57	Neutron multiplication effect of Be on T_7 measured by the NE213 indirect method (DOT3.5/JACKAS calculations).....	153
IV.58	Neutron multiplication effect of Be on T_7 calculated by MORSE-DD with DDL/J3P1.....	154
IV.59	Comparison of C/E values for T_7 based on experimental values obtained by the NE213 indirect method.....	156
IV.60	Comparison of C/E values for T_7 between experiments with and without Be multiplier (experiment: NE213 detector, calculation: DOT3.5 with JACKAS).....	157
IV.61	C/E values for tritium production from ${}^7\text{Li}, T_7$ in the beryllium experiments (experiments: NE213 detectors, calculation: DOT54.3/MATXS6).....	158
IV.62	C/E values for tritium production rate from ${}^7\text{Li}, T_7$, in the beryllium-sandwiched system using two measuring techniques.....	159
IV.63	Comparison of C/E values for T_7 in Be-sandwiched system based on experimental values by the NE213 indirect method.....	160
IV.64	Comparison of C/E values for T_N in Be-sandwiched system between experiments with Li_2O and Li metal detectors based on the calculation performed by DOT3.5 with the JACKAS library (JAERI).....	161
IV.65	Tritium production rate from natural lithium in the beryllium sandwiched system.....	163
V.1	Cross-sections for activation foils used in reaction rates measurements.....	165
V.2	C/E values for ${}^{58}\text{Ni}$ (n,2n) reaction rate in the reference system.....	166
V.3	C/E values for ${}^{197}\text{Au}$ (n,2n) reaction rate in the reference system.....	168
V.4	C/E values for ${}^{27}\text{Al}$ (n, α) reaction rate in the reference system.....	169
V.5	C/E values for ${}^{58}\text{Ni}$ (n,p) reaction rate in the reference system.....	171
V.6	C/E values for ${}^{197}\text{Au}$ (n, γ) reaction rate in the reference system.....	173
V.7	C/E values for ${}^{58}\text{Ni}$ (n,2n) ${}^{57}\text{Ni}$ reaction rate in the reference system(JAERI).....	174
V.8	C/E values for ${}^{197}\text{Au}$ (n,2n) ${}^{196}\text{Au}$ reaction rate in the reference system(JAERI).....	175
V.9	C/E values for ${}^{27}\text{Al}$ (n, α) ${}^{24}\text{Na}$ reaction rate in the reference system(JAERI).....	176
V.10	C/E values for ${}^{58}\text{Ni}$ (n,p) ${}^{58}\text{Co}$ reaction rate in the reference system(JAERI).....	177
V.11	C/E values for ${}^{197}\text{Au}$ (n, γ) ${}^{198}\text{Au}$ reaction rate in the reference system(JAERI).....	178
V.12	C/E values for ${}^{27}\text{Al}$ (n, α) ${}^{24}\text{Na}$ reaction rate in the Be-sandwiched system.....	180
V.13	C/E values for ${}^{90}\text{Zr}$ (n,2n) ${}^{89}\text{Zr}$ reaction rate in the Be-sandwiched system.....	181
V.14	C/E values for ${}^{115}\text{In}$ (n,n') ${}^{115\text{m}}\text{In}$ reaction rate in the Be-sandwiched system.....	182
V.15	C/E values for ${}^{197}\text{Au}$ (n, γ) ${}^{198}\text{Au}$ reaction rate in the Be-sandwiched system.....	183
V.16	Comparison of total cross-sections for ${}^7\text{Li}$	187
V.17	Comparison of elastic scattering cross-sections for ${}^7\text{Li}$	188
VI.1	Neutron spectrum at z=0 cm in the reference system.....	193
VI.2	Neutron spectrum at z=2.5 cm in the reference system.....	194

VI.3	Neutron spectrum at z=10 cm in the reference system.....	195
VI.4	Neutron spectrum at z=20 cm in the reference system.....	196
VI.5	Neutron spectrum at z=30 cm in the reference system.....	197
VI.6	Neutron spectrum at z=40 cm in the reference system.....	198
VI.7	Integrated flux above 10 MeV in the reference system.....	199
VI.8	Integrated flux from 1 MeV to 10 MeV in the reference system.....	200
VI.9	Neutron spectrum at z=-10 cm in the Be-sandwiched system.....	201
VI.10	Neutron spectrum at z=-5 cm in the Be-sandwiched system.....	202
VI.11	Neutron spectrum at z=0 cm in the Be-sandwiched system.....	203
VI.12	Neutron spectrum at z=2.5 cm in the Be-sandwiched system.....	204
VI.13	Neutron spectrum at z=-5 cm in the Be-sandwiched system.....	205
VI.14	Neutron spectrum at z=10 cm in the Be-sandwiched system.....	206
VI.15	Neutron spectrum at z=20 cm in the Be-sandwiched system.....	207
VI.16	Neutron spectrum at z=40 cm in the Be-sandwiched system.....	208
VI.17	Integrated flux above 10 MeV in the Be-sandwiched system.....	209
VI.18	Integrated flux from 1 MeV to 10 MeV in the Be-sandwiched system.....	210
VII.1	Calculated-to-experimental values of tritium production rate from ${}^6\text{Li}, T_6$ in in the reference experiment (experimental values are corrected for self-shielding effect)	212
VII.2	Calculated-to-experimental values of tritium production rate from ${}^7\text{Li}, T_7$ in in the reference experiment	213
VII.3(a)	The R-Z two-dimensional geometrical model for the benchmark system. The detector locations P_i and Z_i are shown.....	218
VII.3(b)	The R-Z two-dimensional geometrical model for the reference system. The detector locations P_i and Z_i are shown.....	219
VII.4	Outlines of the FORSS sensitivity and uncertainty procedures. Computer codes used are shown.....	223
VII.5	Profiles for the TPR from ${}^6\text{Li}$ and ${}^7\text{Li}$ along the central axis of the Li_2O assembly.....	226
VII.6	The incident D-T neutron spectrum in the benchmark system.....	227
VII.7	The incident D-T neutron spectrum in the reference system.....	228
VII.8	The sensitivity profiles $P(T_6, P_i, \Sigma_t)B$ [$i = 1-3$] due to a 1% increase in Σ_t of ${}^6\text{Li}$ in the benchmark system. Point detectors P_1, P_2 and P_3 at $Z = 5, 30$ and 55 cm are considered.....	230
VII.9	The integrated relative sensitivity coefficients for T_6 in the benchmark and reference systems due to variations in the Σ_t of various elements. Point detectors are considered.....	232
VII.10	The integrated relative sensitivity coefficients for T_6 in the benchmark system due to variations in various partial cross-sections of ${}^6\text{Li}$. Point detectors are considered.....	233
VII.11	The sensitivity profiles $P(T_6, P_i, \Sigma_t)R$ [$i = 1,3,4,5$] due to a 1% increase in Σ_t of ${}^6\text{Li}$ in the reference system. Point detectors P_1, P_3, P_4 , and P_5 at $Z = 0.5, 5, 30$ and 55 cm are considered.....	234

VII.12	The sensitivity profiles $P(T_6, P_i, \Sigma_t)B$ [$i = 1-3$] due to a 1% increase in Σ_t of ^7Li in the benchmark system. Point detectors P_1, P_2 and P_3 at $Z = 5, 30$ and 55 cm are considered.....	236
VII.13	The sensitivity profiles $P(T_6, P_i, \Sigma_t)R$ [$i = 1,3,4,5$] due to a 1% increase in Σ_t of ^7Li in the reference system. Point detectors P_1, P_3, P_4 , and P_5 at $Z = 0.5, 5, 30$ and 55 cm are considered.....	238
VII.14	The sensitivity profile $P(T_6, P_5, \Sigma_t)R$ due to a 1% increase in Σ_t of ^7Li in the benchmark system. Point detector P_5 is considered.....	239
VII.15	The sensitivity profile $P(T_6, P_5, \Sigma_t)R$ due to a 1% increase in Σ_t of ^7Li in the benchmark system. Point detector P_3 is considered.....	240
VII.16	The sensitivity profiles $P(T_6, P_i, \Sigma_t)B$ [$i = 1-3$] due to a 1% increase in Σ_t of ^{16}O in the benchmark system. Point detectors P_1, P_2 , and P_3 at $Z = 0.5, 5, 30$ and 55 cm are considered.....	242
VII.17	The integrated relative sensitivity coefficients for T_6 in the benchmark system due to variations in various partial cross-sections of oxygen. Point detectors are considered.....	243
VII.18	The sensitivity profiles $P(T_6, P_i, \Sigma_t)R$ [$i = 1,3,4,5$] due to a 1% increase in Σ_t of oxygen in the reference system. Point detectors P_1, P_3, P_4 , and P_5 at $Z = 0.5, 5, 30$ and 55 cm are considered.....	244
VII.19	The sensitivity profile $P(T_6, P_3, \Sigma_t)R$ due to a 1% increase in Σ_t of oxygen in the reference system. Zone detector P_3 is considered.....	247
VII.20	The sensitivity profile $P(T_7, P_2, \Sigma_t)R$ due to a 1% increase in Σ_t of oxygen in the benchmark system. Point detector P_2 is considered.....	249
VII.21	The integrated relative sensitivity coefficients for T_7 in the benchmark and reference systems due to variations in the Σ_t of various elements. Point detectors are considered.....	250
VII.22	The integrated relative sensitivity coefficients for T_7 in the benchmark system due to variations in various partial cross-sections of oxygen. Point detectors are considered.....	251
VII.23	The relative standard deviation in T_6 in the benchmark and reference systems due to uncertainties in the cross-sections of various materials. Point detectors are considered.....	254
VII.24	The total uncertainty in T_6 and T_7 in the benchmark and reference systems. Point detectors are considered.....	256
VII.25	The relative standard deviation in T_7 in the benchmark and reference systems due to uncertainties in the cross-sections of various materials. Point detectors are considered.....	258

I. INTRODUCTION

I.1 Scope

Phase I integral experiments of the JAERI/U.S. Collaborative Program on Fusion Blanket Neutronics, which were carried out at the Fusion Neutronics Source (FNS) facility at JAERI, ranged from D-T neutron source characterization experiments, tritium production rate (TPR) measurements in a reference Li_2O assembly, first wall experiments with and without simulated coolant materials and beryllium neutron multiplier experiments in various configurations. The U.S. and Japan have independently analyzed these experiments using their own data bases and codes. Analytical predictions obtained by both countries were compared to measured values. Results of this intercomparison are presented in this volume.

The experiments aimed at verifying the potential of Li_2O for tritium breeding in a simulated fusion blanket. In this respect, analytical predictions for tritium production rates (TPR) in a simulated test module of single and multi-zone configurations were compared to the experimental values measured by various techniques. This intercomparison will provide the data base needed for evaluating the overall uncertainty (both analytical and experimental) associated with the tritium breeding rate (TBR) and for selecting breeder materials and configurations in primary candidates for fusion blankets and be useful in resolving the discrepancies found between experimental and analytical results. The basic breeder material used is Li_2O at the present phase. The objectives, planning, and progress in Phase I experiments of this collaborative program and details of the measuring items and associated techniques can be found in Volume I of this report and in References (1) and (2), respectively.

Since both the U.S. and JAERI have independently carried out the analyses for these experiments using their own codes and data bases, four calculational benchmarks were selected prior to analyzing the experiments, intercomparison between the analytical results was made based on the same transport codes and nuclear data bases used in the present analysis. This joint effort aimed at identifying the discrepancies in results when different methodologies are implemented in transport codes and when different data evaluations are used in the analyses. Findings from this separate study can be found in Ref. (3). In this volume, analytical predictions for the tritium production rate and other neutronics parameters are compared to the measured values and discussions are pursued on the reasoning for the discrepancies found in this intercomparison.

I.2 Brief Description of the Experiments and Measured Parameters

The test assembly is a cylinder of diameter $D = 60$ cm and length $L = 61$ cm constructed from Li_2O blocks of different sizes, the smallest of which is 5.08 cm \times 5.08 cm \times 5.08 cm. The test assembly is loaded in the experimental cavity connecting target room #2 (4.96 m \times 4.96 m and 4.5 m height), where the experiments are performed, and the large target room #1. The physical center of the rotating target (neutron source generator) is at a distance of ~ 2.48 m from the side walls and at 2.7 m and 1.8 m from the ceiling and the floor level, respectively (see Fig. I.1).

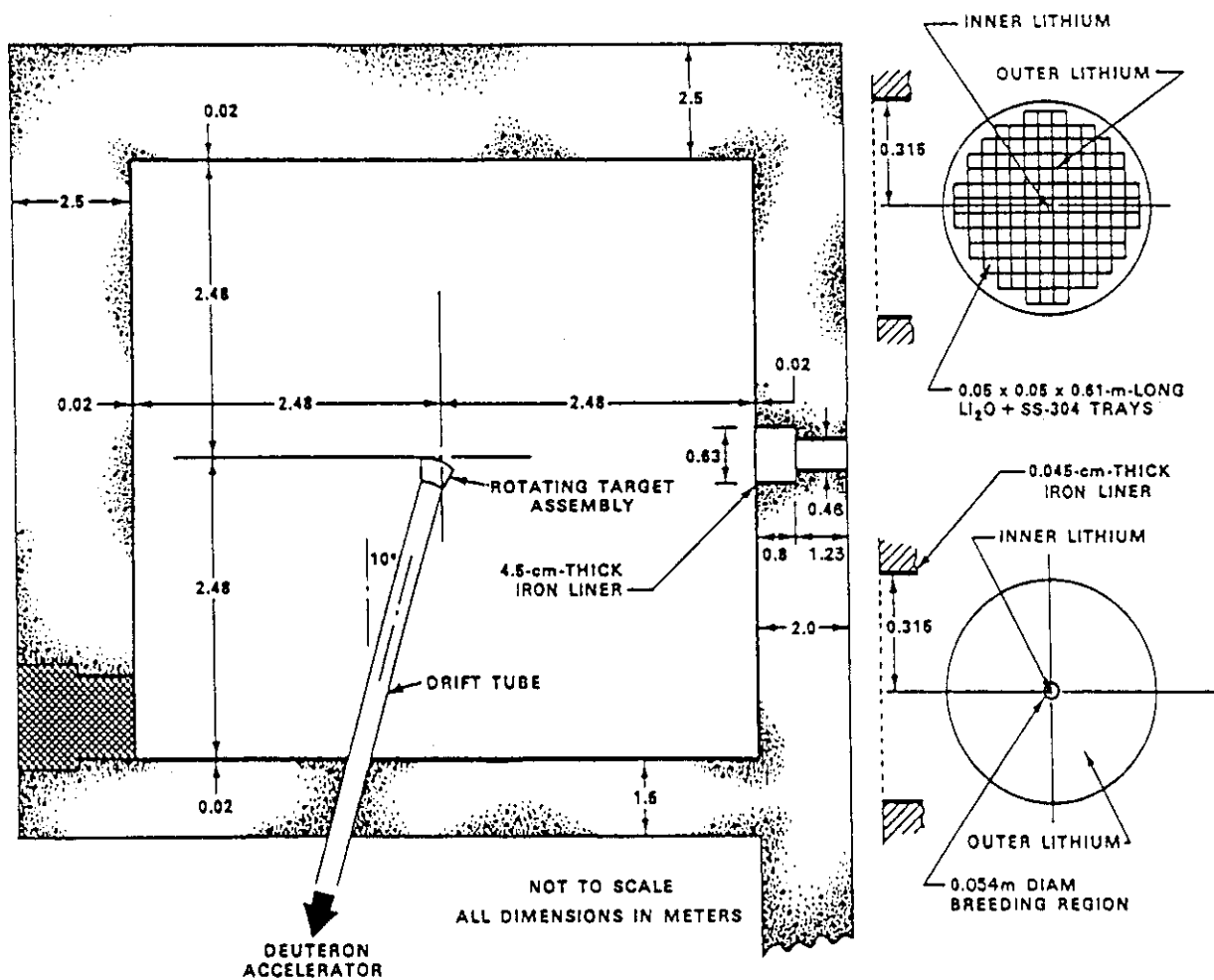


Figure I.1 Geometrical Arrangement of Phase I experiments

In the reference experiment, measurements for the tritium production rate (TPR) from ${}^6\text{Li}$ (T_6) and ${}^7\text{Li}$ (T_7) were performed at various locations along the central axis of the assembly using Li glass detector, Li-metal pellets, and Li_2O -pellets. The T_7 was also measured by unfolding the measured spectrum by an NE213 detector with the response ${}^7\text{Li}(n,n'\alpha)$ cross-section. The in-system spectrum measurements were performed using small spherical NE213 detectors. Several activation rates were also measured using foils. The reaction rates measured in the reference experiment are ${}^{27}\text{Al}(n,\alpha)$, ${}^{58}\text{Ni}(n,2n)$, ${}^{58}\text{Ni}(n,p)$, ${}^{197}\text{Au}(n,2n)$ and ${}^{197}\text{Au}(n,\gamma)$ along the 10 cm off-central axis. These reactions were used as spectral indices referring to the neutron flux level throughout the assembly and thus to support the TPR measurements.

The second series of experiments was devoted to studying the impact of a first wall and coolant inclusion on tritium production profiles along the central axis of the test module (Fig. I.2). In this series, a 0.5 cm-thick stainless steel layer (316SS) was placed in front of the Li_2O assembly and tritium production measurements were performed. A 0.5 cm-thick polyethylene (PE) plate was then placed between the first wall and the Li_2O assembly and measurements were carried out. The PE layer in this case simulates a water coolant channel in a fusion blanket. Similar experiments were performed using a 1.5-cm-thick SS layer instead, as shown in Fig. I.2. The T_6 and T_7 measurements were carried out with the Li-glass detectors and the NE213 indirect methods, respectively.

In the third series, beryllium was deployed as a neutron multiplier. Three configurations were assembled, namely: 5 cm-thick Be, 10 cm-thick Be, and 5 cm-thick Li_2O + 5 cm-thick Be layers were placed in front of the Li_2O assembly, separately (see Fig. I.3). In the latter case, beryllium is sandwiched between the front Li_2O layer and the Li_2O test assembly. This series of experiments has been performed to examine the change in tritium production profiles in comparison to the reference experiment resulting from including the Be multiplier. As in the reference experiment, T_6 and T_7 were measured by Li-glass, Li-metal, and Li_2O -pellet methods and NE213 indirect method was also used to obtain the T_7 values. The off-central activation reaction rates were measured in the Be-sandwiched systems for Al, Ni, In, Au, Zr, Zn, and Ti foils.

The experiments mentioned above proceeded from a simple one-zone configuration of Li_2O to multiple-zone configurations that included basic characteristics of a fusion blanket, e.g., first wall, simulated coolant channel, and a neutron multiplier. The present experimental systems are influenced from the room-return component of neutrons because of the feature of an open geometry, i.e., the area of the front surface of the Li_2O assembly is much smaller than the area of the room walls. Therefore, TPR from ${}^6\text{Li}$ rapidly varies within the front few-centimeters region inside the test module. The neutron current incident on the front surface differs from the one found in a fusion environment. Accordingly, in Phase II of the program (in progress) the experimental system specifications (geometrical arrangement, material selection, etc.) are chosen to give a closer simulation by using a closed geometry.

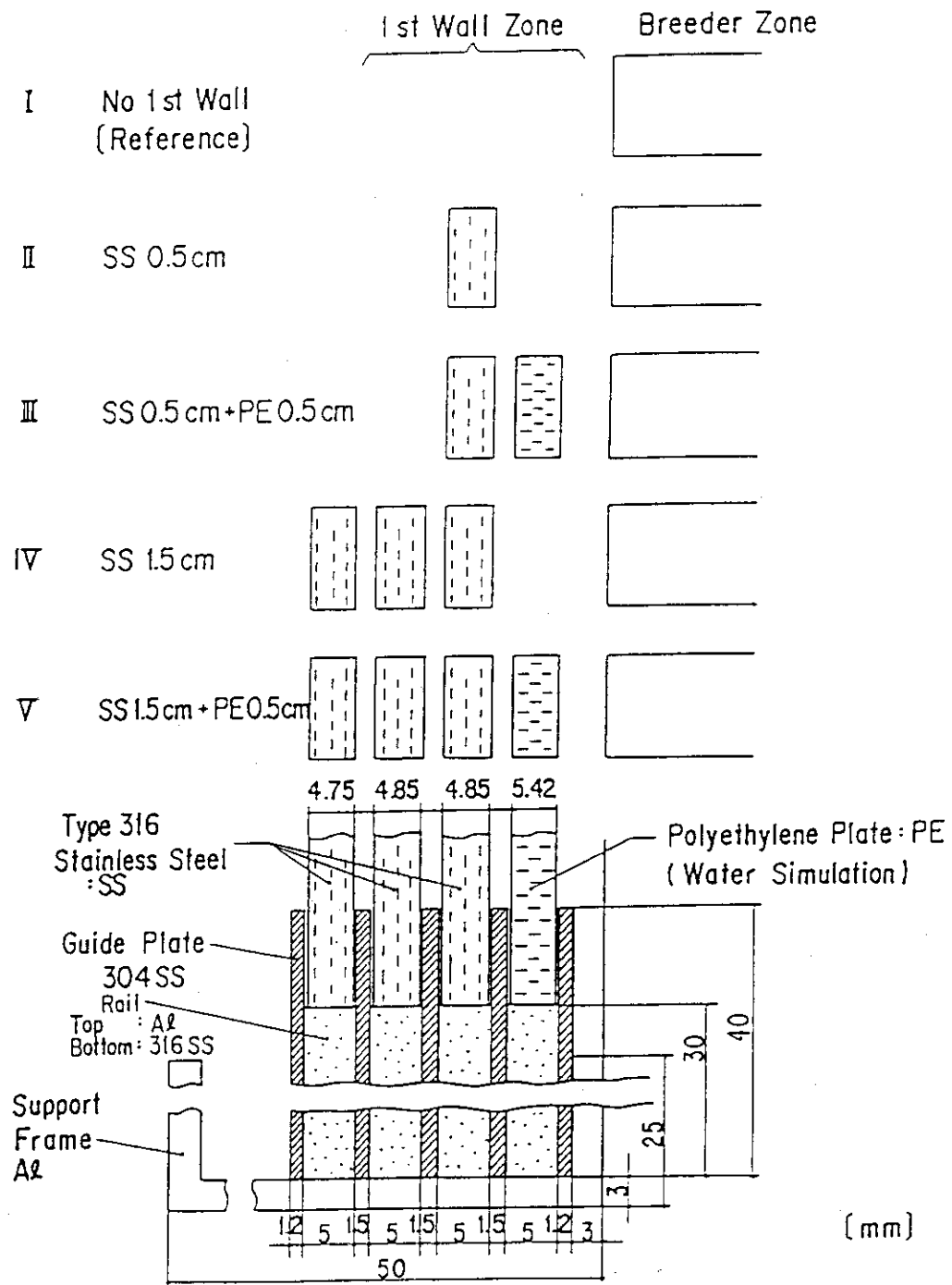


Figure I.2 Geometrical arrangement for the first wall experiments

Assemblies for the Experiments on Neutron Multiplier Effect

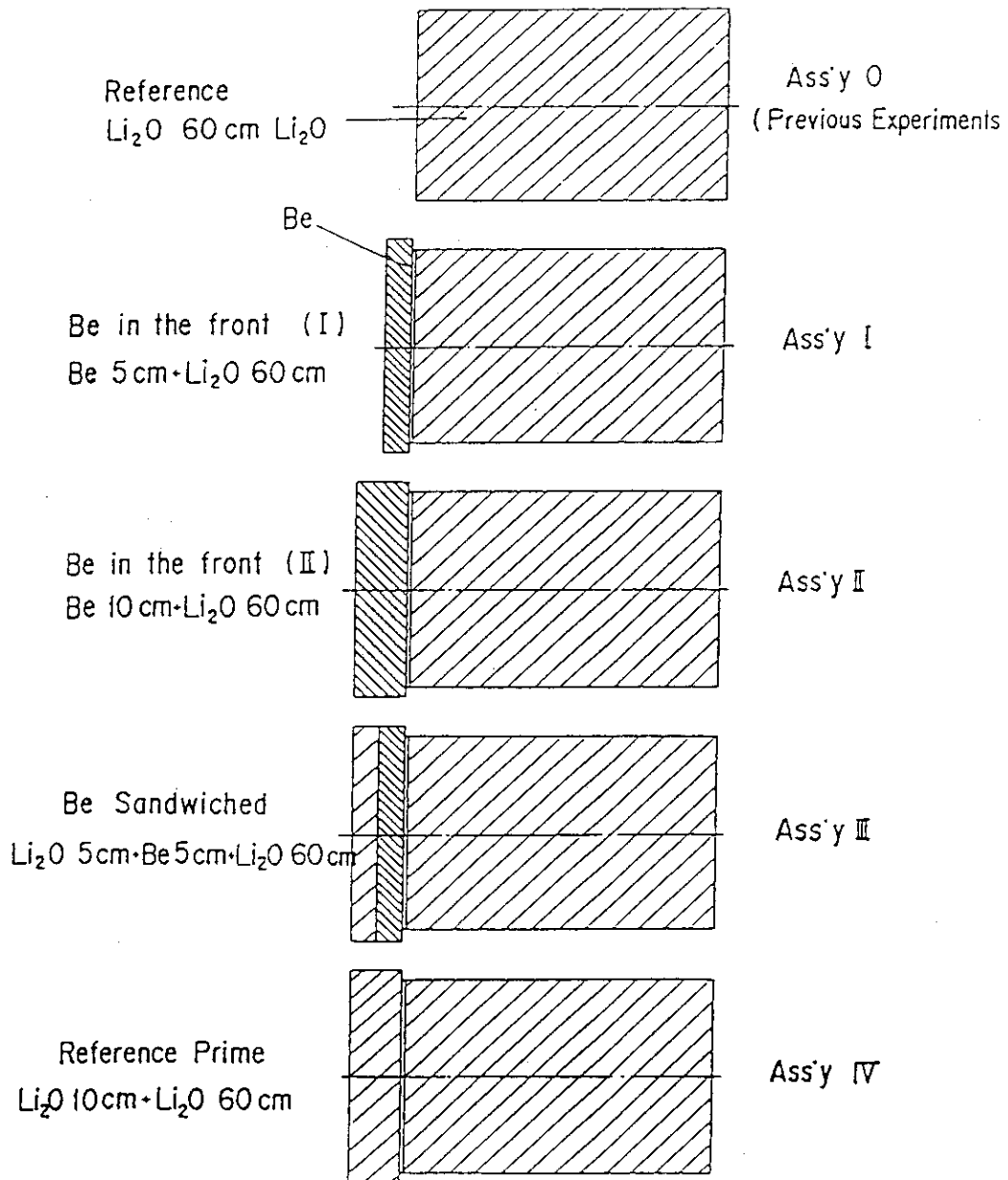


Figure I.3 Geometrical arrangement for the beryllium experiments

II. Analytical Methods, Nuclear Data and Calculation Models

II.1 JAERI Analysis

II.1.1 Nuclear Data

The evaluated nuclear data files adopted by JAERI in the experimental analysis include ENDF/B-IV,⁽⁴⁾ JENDL3-PR1⁽⁵⁾ and JENDL3-PR2.⁽⁶⁾ The latter two files have been evaluated at JAERI's Nuclear Data Center mainly to be used for fusion applications. The JENDL3-PR2 file includes a revised version of the ^6Li and ^7Li data in the JENDL3-PR1 file. The two files include cross-sections of beryllium, lithium-6, lithium-7, carbon, oxygen, iron, chromium, and nickel. The standard version of JENDL3 will be published in 1988. These nuclear data files have been processed into group cross-section sets with a 125-group structure. Since two different types of transport codes have been used in the analysis, generating the corresponding group constants was necessary. One cross-section library is used for calculations using the discrete ordinates code which is based on the conventional Legendre expansion method. Other libraries used in the Monte Carlo method are based on the double-differential cross-section (DDX) form. The calculation flow of these libraries is illustrated in Fig. II.1. The main features of these libraries (JACKAS, DDL/B4, and DDL/J3P1) are compared in Table II.1. Note that in the JACKAS library, data for H, ^{23}Na , ^{27}Al , Si, and Ca are based on JENDL2 while JENDL3-PR1 data were used for Cr, Fe, Be, ^{16}O , and Ni. In the library, the data for ^6Li , ^7Li and ^{12}C are extracted from JENDL3-PR2. Note also that the DDL/B4 library is based entirely on ENDF/B-IV data. The details of processing codes are described in Ref. (7) for PGG-BII and Ref. (8) for PROF-DD.

Besides these sets, all group activation cross-sections have been produced from ENDF/B-IV. These are nearly the same as those in the ENDF/B-V dosimetry file.

II.1.2 Transport Codes

The analysis has been performed using the discrete ordinates code, DOT3.5,⁽⁹⁾ and the Monte Carlo code MORSE-DD.⁽¹⁰⁾ The former, of course, needs to geometrically approximate an experimental system in two dimensions, but the latter can simulate it as detailed as possible in three dimensions. The original DOT3.5 was developed at ORNL and the MORSE-DD code was modified from MORSE⁽¹¹⁾ in order to accurately treat the anisotropy in the elastic and inelastic scattering processes by using the double-differential form cross-section data library.

As is well known, a conventional low-order Legendre expansion method causes a negative flux, ray effect and mispredicts flux in a highly anisotropic energy region. The MORSE-DD code, however, can overcome such difficulties and give correct predictions.⁽¹²⁾ To determine the neutron flight direction after

Nuclear Data File

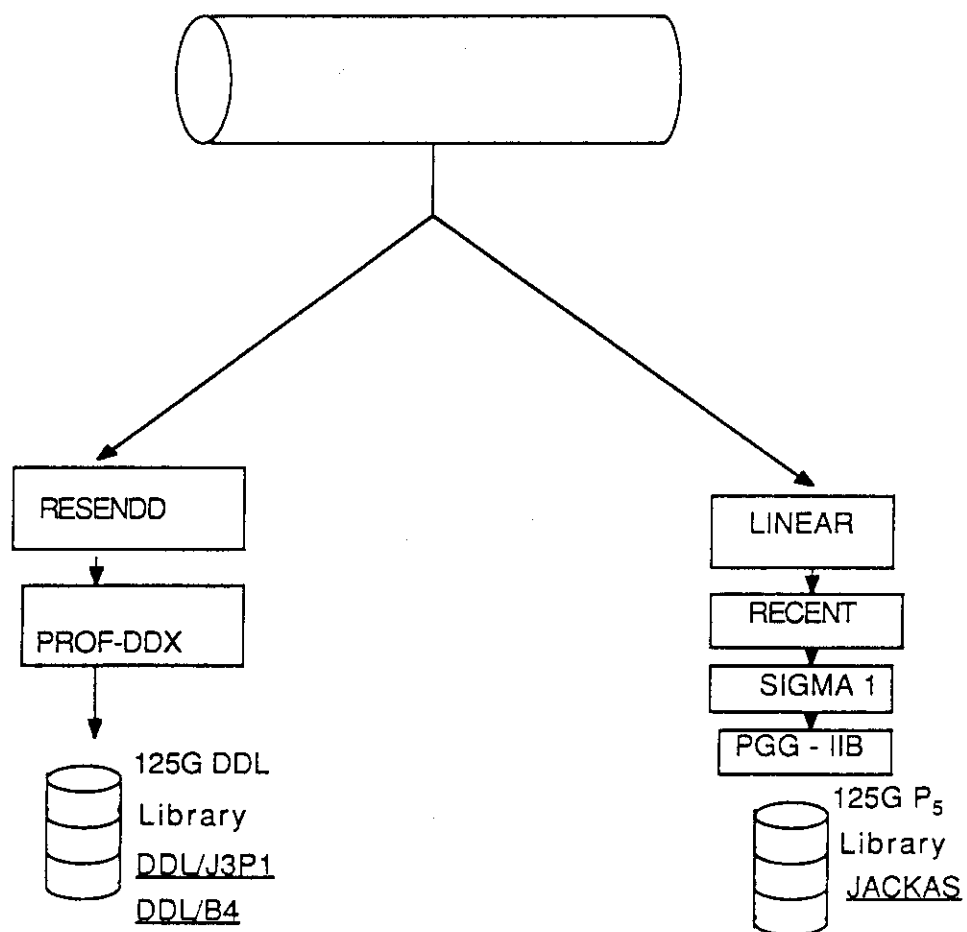


Fig. II.1 Calculation flow of the group cross-section libraries used by JAERI

Table II.1 Comparison of Nuclear Cross-Section Library Sets

SET	JACKAS	DDL/J3P1	DDL/B4
Nuclear Data	JENDL3-PR2+ JENDL3-PR1+JENDL2	JENDL3-PR1+ENDF/B-IV	ENDF/B-IV
Weighting Function	E flat + Maxwellian	1/E + arbitrary thermal G	Same as DDL/J3P1
Anisotropic Scattering	P ₅	DDX type with 20 angular meshes	Same as DDL/J3P1
Temperature	300°K	300°K	Same as DDL/J3P1

a collision event, MORSE-DD can select a scattering direction μ continuously based on the kinematics of the reaction, where the scattering probability is given for twenty intervals with an equal width, $\Delta\mu$, in the range $-1 < \mu < 1$. On the other hand, the original MORSE code will sample a value among limited discrete angles. A detailed description of the MORSE-DD code is given in Ref. (10).

In the DOT3.5 calculations, the first collision source was first calculated by the GRTUNCL code and used as an input to the DOT3.5 code. The quadrature set used was S_{10} .

II.1.3 Computational Models

A. Two-Dimensional Models Used by DOT3.5

In the DOT calculations, the whole room including a concrete wall and a Li_2O test zone were approximated in a cylindrical model, where each zone volume was conserved. The neutron source was approximated as a point placed at the symmetric center. The calculation models are shown in Figs. II.2 and II.3 which describe those for the first wall and the beryllium systems, respectively. The reference system corresponds to the model shown in Fig. II.2 with the first wall regions removed. It is difficult to accurately calculate the measured quantities without a proper selection of spatial mesh spacing which may noticeably increase the computation time. The mesh size effect was compared between the results obtained by JAERI and the U.S., and it was found that this effect is important. A finer mesh size is required at the front region and at the boundaries between different material zones.

The models shown in Figs. II.2 and II.3 are symmetric with respect to the Z direction, so that imaginary Li_2O zone appears at the opposite side from the symmetric center. However, its effect on the actual test zone would be negligible because the solid angle subtended by the test zone as seen from the neutron source is very small compared with that of the room walls.

The Li_2O test assembly was approximated by cylindrical zones where the central channel (drawer) and the surrounding Li_2O zones have different densities, as seen in Figs. II.2 and II.3. Moreover, the simulated first walls and coolant (polyethylene plate) with the same center line were modified as cylindrical plates with an effective radius of 40 cm. The actual air regions between these plates were not taken into account in the model except for those in front of the Li_2O system and between regions III and IV, as shown in Figure II.2. In the beryllium systems, two beryllium regions of thickness 10.16 cm and of an effective radius of 38.98 cm, were modelled as cylinders, as shown in Fig. II.3. The zones shown in the figure are in contact with each other and also with the Li_2O system.

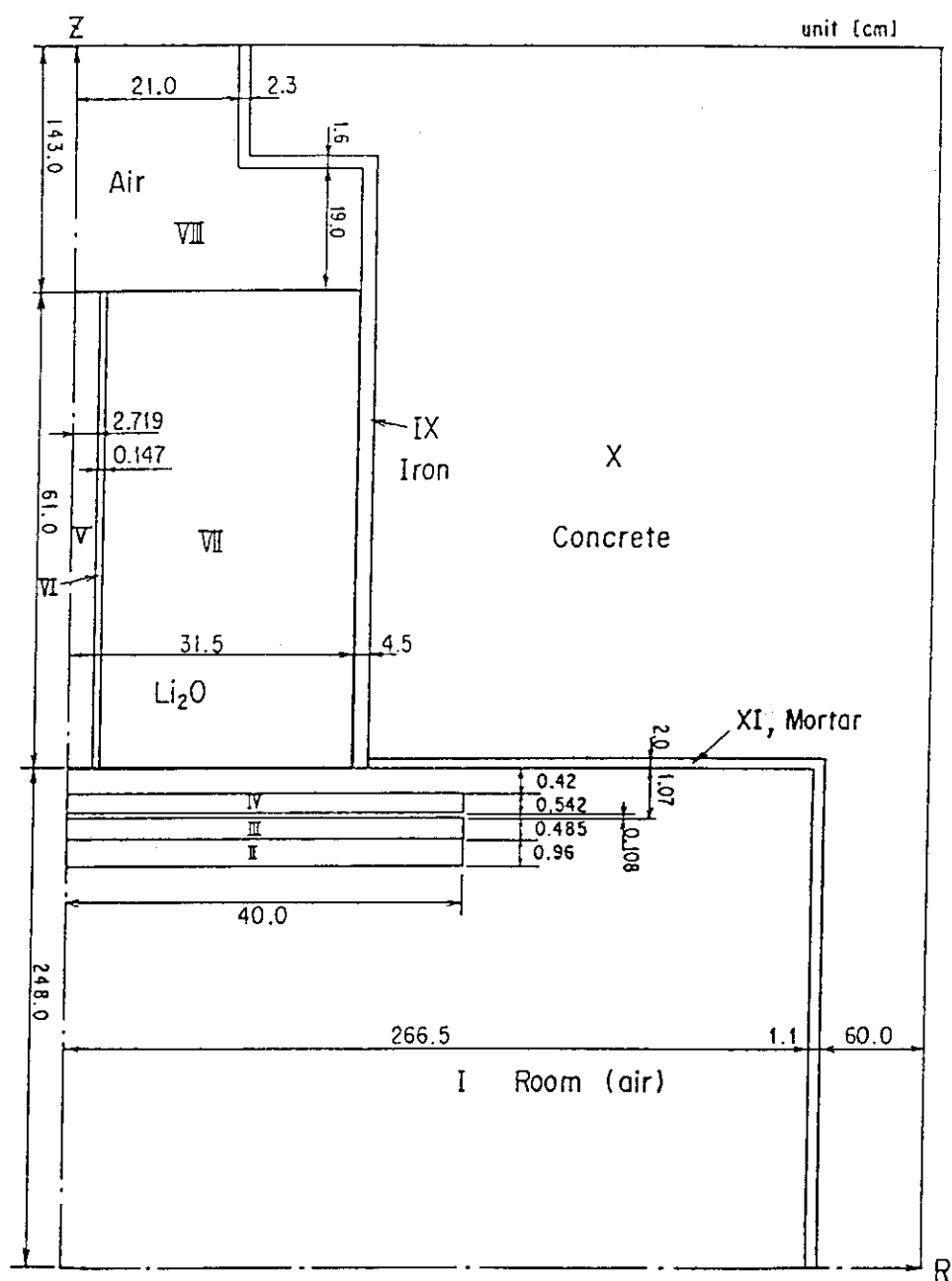


Figure II.2 Calculational model of Phase I experiments with first walls used by DOT3.5 (JAERI)

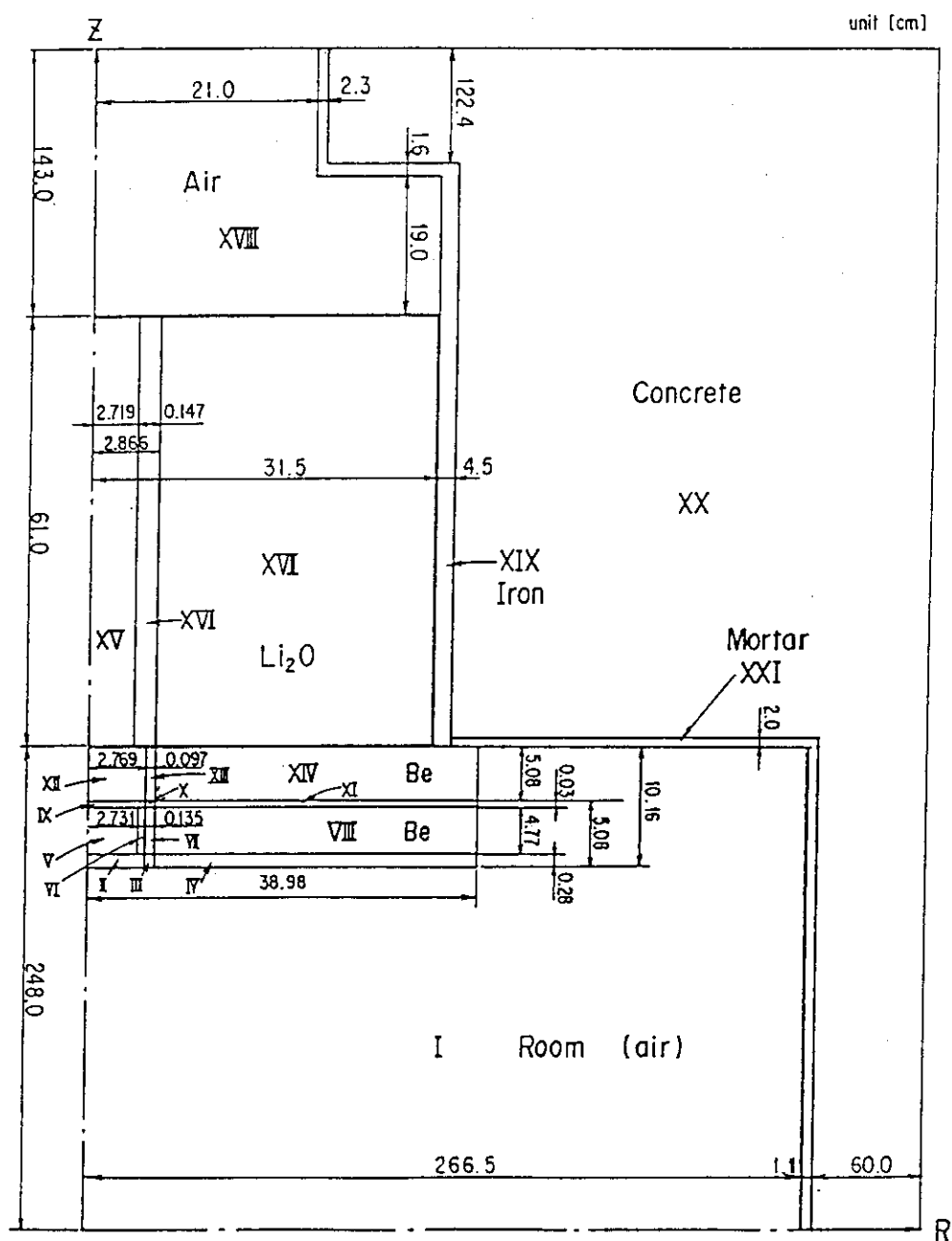


Figure II.3 Calculational model of Phase I experiment with beryllium zone as used by DOT3.5 (JAERI)

B. Three-Dimensional Model Used by MORSE-DD

The FNS target room #2, the Li_2O test module, and the penetration hole where the test module is placed, are modelled as accurately as possible in the three-dimensional model shown in Fig. II.4. In the figure, the detail structure of the rotating neutron target (RNT) is not explicitly shown and will be described in the next section. The thickness of the concrete wall considered in the model is smaller than the actual one. A 60 cm-thick wall was considered in the analysis in order to take account of the room-returned component of the source neutrons. A mortar zone with thickness of 2 cm is considered in the model, as shown in Fig. II.4. The broken line shows the region boundary used in the Russian roulette of Monte Carlo runs. The height of the room is 450 cm and the target is placed at 180 cm above the floor level. The test zone of the Li_2O assembly was approximated by a cylinder so as to preserve the total volume of the Li_2O region. The iron region between the wall of the circular penetration hole and the non-circular Li_2O region was approximated by annular geometry.

As described in Volume I, each Li_2O block used to construct the Li_2O test assembly is canned with stainless steel, and all the blocks are homogeneously mixed in the model except for the measuring channels positioned at the center and off-center of the Li_2O assembly (central drawer and off-central drawer zones). These test channels are independently treated from the smeared Li_2O surrounding region, as shown in Fig. II.5. The characteristics of these channels are that the smallest Li_2O blocks ($5.08 \times 5.08 \times 5.08$ cm) are used in their construction. Blocks in the outer Li_2O region have larger sizes. The Li_2O zone, the stainless steel, and the void of the measuring channels were homogenized into two regions of Li_2O and stainless steel along the z-direction. As an estimator, a track length was used in the Monte Carlo calculations. The dimensions of the estimated regions for the Be-sandwiched system are shown in Table II.2.

The analysis proceeded in two steps in order to save computation time. At first, only the reflected neutron component from the concrete wall was calculated and the neutron current over the entrance of the experimental hole was determined. This component was confirmed to be spatially flat and isotropic in angle, and had a quite similar neutron spectrum over the entrance surface. Then, the direct neutron source distribution (in space, angle and energy) from the RNT was calculated (see next section) and bunched into nine vertical intervals on the surface of the wall which covers a square area of $2 \text{ m} \times 2 \text{ m}$, as shown in Figure II.6(b). This component includes uncollided neutrons and neutrons which collided only with the structural materials of the RNT. These calculational procedures represent the first step in the calculational method used.

In the second calculational step, only the test zone and its surrounding iron and concrete regions (with a cylindrical shape having a 1 m radius) were considered in the model, as illustrated in Fig. II.6. To examine the effect of the concrete wall thickness shown in Fig. II.6 on tritium production rate by ${}^6\text{Li}(\text{T}_6)$ at the central axis, some calculations with different thicknesses for the concrete wall were carried

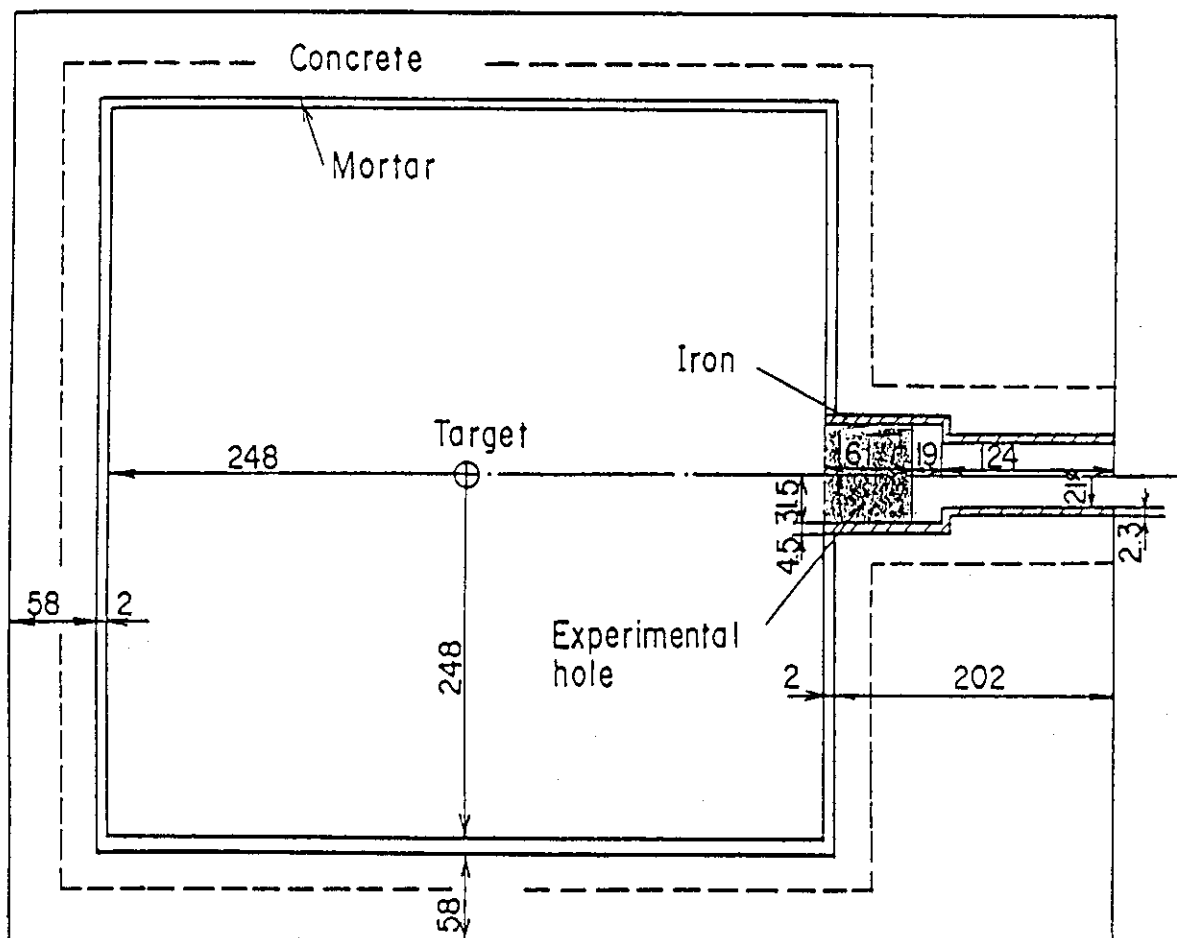


Figure II.4 Horizontal view of experimental configuration

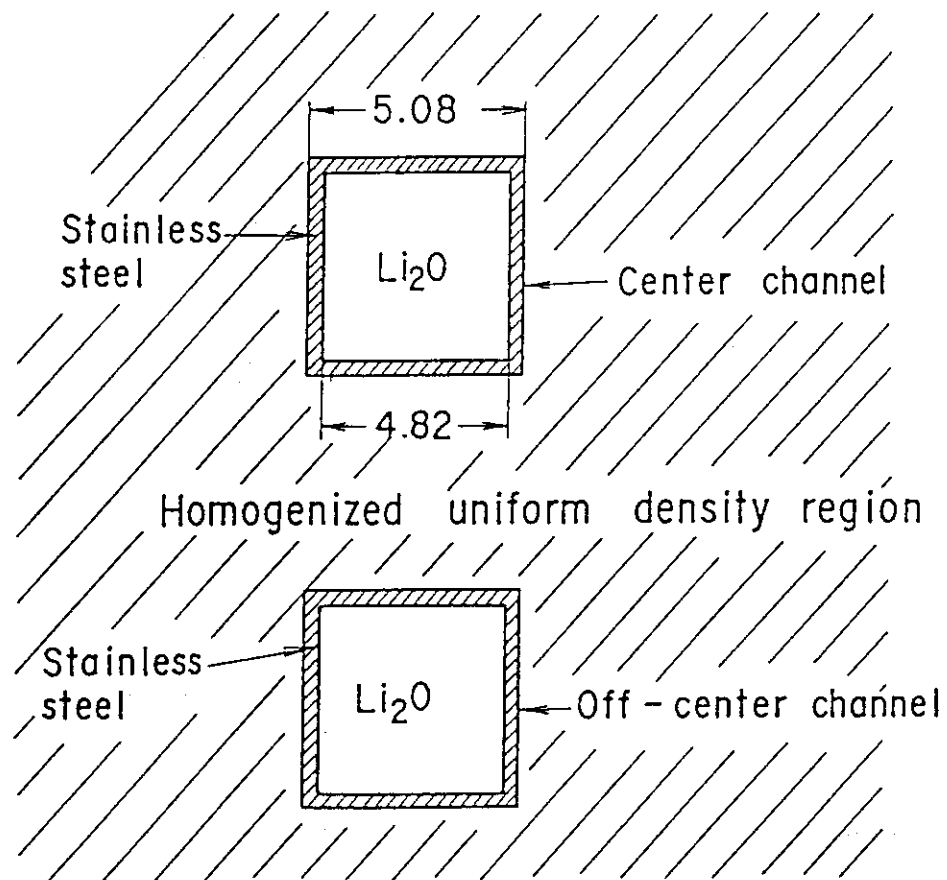


Figure II.5 Calculation model of the center and off-center channels in Li_2O block

Table II.2 Regions of Track Length Estimators Used in Test Channel
 Dimension: $4.82 \times 4.82 \times \Delta Z \text{ cm}^3$

Region Number	Position (cm)	$\Delta Z(\text{cm})$
1	237.6 - 237.8	0.2 ⁺
2	237.8 - 239.8	2.0 ⁺
3	239.8 - 240.8	1.0 ⁺
4	240.8 - 242.8	2.0 ⁺
5	242.8 - 244.8	2.0 ⁺
6	244.8 - 245.8	1.0 ⁺
7	245.8 - 247.8	2.0 ⁺
8	247.8 - 248.0	0.2
9 - 25	248.0 - 282.0	2.0
26 - 34	282.0 - 309.0	3.0

⁺Be sandwiched system

The same region boundaries are adopted for the off center channel

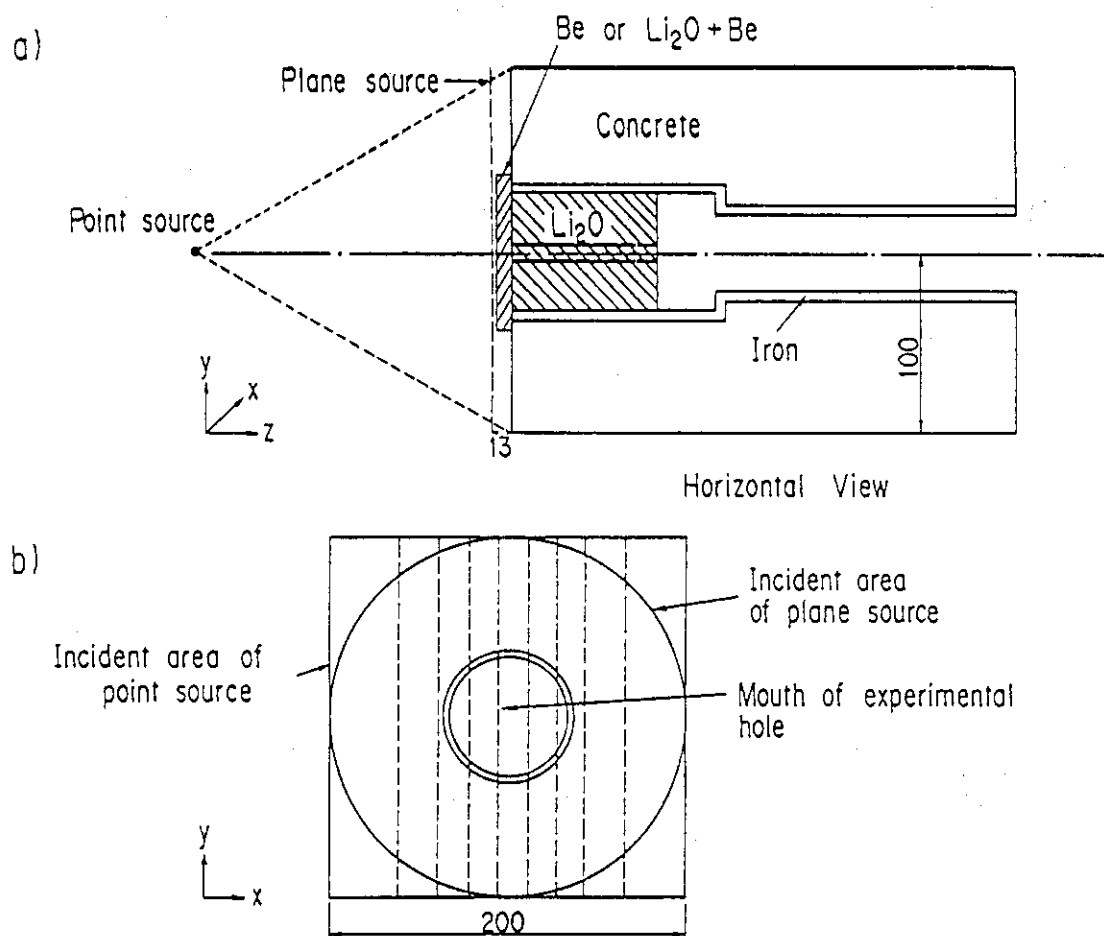


Figure II.6 Second step in the calculational model used by MORSE-DD

out. Figure II.7 shows the ratio of T_6 obtained in two systems, i.e., 60 cm and 100 cm-thick walls, as compared to a 300 cm-thick wall. In these two cases, no account was taken for the whole room. The T_6 profile that results from including the room-return component is also shown in the figure. If we consider a 100 cm-thick concrete wall, the results obtained are almost the same as those for the 300 cm-thick case except for a few cm range from the wall, but such a quantity is too small compared with the room return component shown in Fig. II.7. Therefore the model adopted in JAERI's calculations was considered satisfactory in view of the concrete wall thickness surrounding the Li_2O system. The number of neutron histories for each run is summarized in Table II.3.

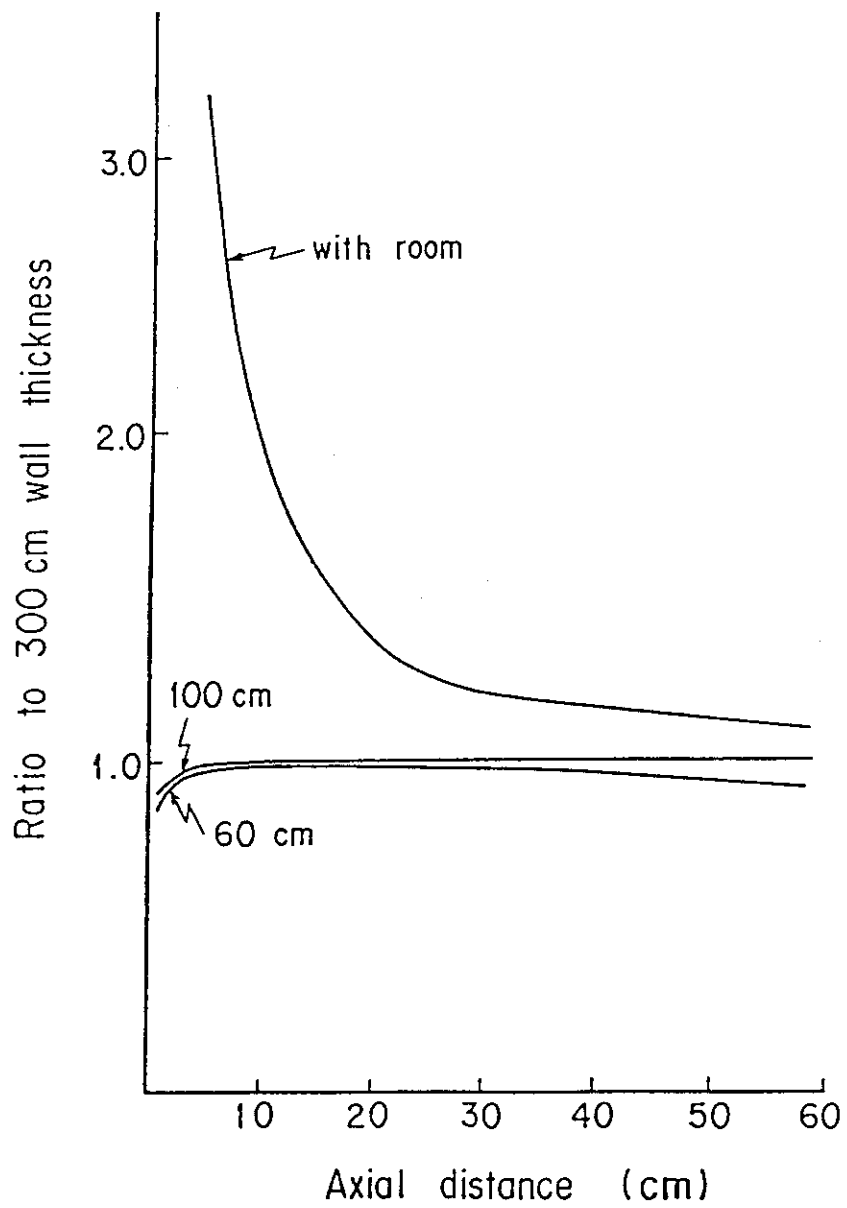


Figure II.7 Effect of concrete wall thickness surrounding Li_2O on T_6 along the axis of the central drawer

Table II.3 Number of Neutron Histories used in JAERI's Monte Carlo Calculations

	History (cpu time* (h))		
	125 group		64 group (> 1 MeV)
	Direct	Room Reflected	Direct
Reference	900000 (2)	2000000 (2)	5000000 (3)
Be 5 cm	700000 (2)	700000 (1)	-----
Be sandwiched	1500000 (3)	1100000 (1)	2720000 (3)
Ref	900000 (2)	700000 (1)	-----

* by FACOM M380 computer

II.2 U.S. Analysis

II.2.1 Nuclear Data

For the Monte Carlo analysis, the default Recommended Monte Carlo Cross-Section Library, RMCCS, of the MCNP code (see below),⁽¹³⁾ which includes data for 77 materials and isotopes, was used. This library is based on pointwise cross-section data generated by using the ACER routine of the NJOY⁽¹⁴⁾ processing code. For most materials, the data in this library are based on the ENDF/B-V data file. With general energy grids, the length of the cross-section tables in the RMCCS library is usually shorter than that in the ENDF/B-V file. If the resonance absorption is not important, the results obtained from the RMCCS library and from the direct ENDF/B-V file are similar. Besides the default library, the MCNP code also utilizes other libraries based on ENDF/B-IV, LANL SUB, ENDL, etc. In the present U.S. results, the RMCCS library based on ENDF/B-V data was used in the analysis of the source characterization, the reference, and beryllium experiments. ENDF/B-V cross-sections were also taken from the RMCCS, ENDF5P3 and ENDF5V3 data files in the MCNP calculations for the first wall experiments.

Monte Carlo calculations were also carried out for the first wall experiments using the MORSE code. In these calculations, a 53 neutron energy group based on the VITAMIN-E data library (ENDF/B-V) was used.⁽¹⁵⁾ The VITAMIN-E library was created as a general purpose cross-section data set for fusion neutronics and other radiation analysis problems. The original fine group library was collapsed using the ANISN code⁽¹⁶⁾ using forward emitted (0-40-deg) neutron angular flux as the weighting function. The angular dependence of the cross-sections for all nuclei was approximated by using P3 Legendre expansion scattering coefficients. The energy boundaries of the collapsed data library are given in Table II.4. Also given in the table are cross-sections for the tritium production from neutron reactions with ^6Li and ^7Li nuclei.

As for the library used in the deterministic calculations, the MATXS6 library⁽¹⁷⁾ was utilized. This library has an 80-group energy structure and is based on ENDF/B-V data. This library is also generated by using the NJOY processing code with P5 Legendre coefficients and a fusion peak + $1/E$ + Maxwellian weighting function. The U.S. calculations were based on the latest evaluations for beryllium⁽¹⁸⁾ and ^7Li ⁽¹⁹⁾ ENDF/B-V, version 2 carried out at LANL. Comparison was also made to results based on the previous evaluations (ENDF/B-V, version 1). The neutron group structure of the libraries used by the U.S. and JAERI can be found in Ref. (3)

Table II.4 53-Neutron Energy Group Structure and Tritium Breeding Cross-Sections Used in the Monte Carlo Analysis of the First Wall Experiments

Neutron	Upper Energy ev	${}^6\text{Li}$ Breeding b	${}^7\text{Li}$ Breeding b	Neutron	Upper Energy ev	${}^6\text{Li}$ Breeding b	${}^7\text{Li}$ Breeding b
1	17.33+06(a)	0.0193	0.2468	28	6.081+05	0.3386	
2	15.58+06	0.0239	0.2869	29	4.978+05	0.4881	
3	14.92+06	0.0246	0.2929	30	3.688+05	0.9891	
4	14.55+06	0.0253	0.2095	31	2.985+05	1.5127	
5	14.19+06	0.0260	0.3039	32	2.972+05	2.4440	
6	13.84+06	0.0266	0.3091	33	1.832+05	0.9060	
7	13.50+06	0.0273	0.3149	34	1.111+05	0.6553	
8	12.84+06	0.0294	0.3542	35	6.737+04	0.7194	
9	12.21+06	0.0323	0.3419	36	4.087+04	0.8693	
10	11.05+06	0.0359	0.3542	37	2.479+04	0.9860	
11	10.00+06	0.0402	0.3636	38	2.359+04	1.1017	
12	9.048+06	0.0454	0.3707	39	1.503+04	1.2824	
13	8.187+06	0.0506	0.3751	40	4.119+03	1.7608	
14	7.408+06	0.0598	0.3714	41	5.531+03	2.2521	
15	6.065+06	0.0752	0.2525	42	3.354+03	2.8847	
16	4.966+06	0.0956	0.0753	43	2.035+03	3.7109	
17	4.066+06	0.1122	0.0158	44	1.234+03	4.7769	
18	3.679+06	0.1436	0.0010	45	7.485+01	6.1240	
19	2.725+06	0.1925		46	4.540+02	7.8654	
20	2.365+06	0.2025		47	2.754+02	10.102	
21	2.307+06	0.2051		48	1.670+02	12.978	
22	2.231+06	0.2102		49	1.013+02	16.660	
23	1.651+06	0.2141		50	6.144+01	21.404	
24	2.353+06	0.2265		51	4.726+01	31.860	
25	8.629+05	0.2484		52	1.067+01	76.377	
26	8.208+05	0.2584		53	4.139-01	526.5	
27	7.527+05	0.2842			1.000-05		

II.2.2 Transport Codes

Among the many Monte Carlo codes available at the U.S. (e.g., MORSE⁽¹¹⁾, TARTNP⁽²⁰⁾, VIM⁽²¹⁾, etc.), the MCNP and MORSE codes were chosen for the present analysis. MCNP is a general purpose, continuous energy, generalized geometry, time-dependent, coupled neutron-photon Monte Carlo transport code. MCNP treats an arbitrary, three-dimensional configuration of materials in geometric cells bounded by first- and second-degree surfaces and some special fourth-degree surfaces. Pointwise cross-section data are used (RMCCS library). A unique advantage of using pointwise data is to eliminate approximations in data due to group averaging. For neutrons, all reactions in a particular cross-section evaluation are accounted for. For photons (not applied in the present study), the code takes into account incoherent and coherent scattering, the possibility of fluorescent emission following photoelectric absorption, and absorptions in pair production with local emission of annihilation radiation.

MCNP embodies numerous types of variance reduction methods. Some of them are: (1) importance sampling, (2) weight cutoff with Russian roulette, (3) time and energy cutoff, (4) implicit capture or analog capture (5) exponential transformation, (6) forced collisions, (7) energy splitting and Russian roulette, (8) correlated sampling, (9) source biasing, (10) point detectors, (11) DXTRAN, and (12) weight windows. Readers are referred to Ref. (13) for more information on these techniques.

MORSE is a multipurpose neutron and photon transport Monte Carlo code. Through the use of multigroup cross-sections, the solution of neutron, photon, or coupled neutron-photon problems may be obtained in either the forward or adjoint mode. Time dependence for both shielding and criticality problems is provided. General three-dimensional geometry may be used with an albedo option available at any material surface. The geometry module implemented in MORSE consists of the combinatorial geometry package. It is based on the MAGI combinatorial geometry⁽²²⁾ but the format was changed to fit the MORSE format. Standard multi-group cross-sections such as those used in discrete-ordinates codes may be used as input; either ANISN-DOT^(16,9) or DTF-IV⁽²³⁾ cross-section formats are acceptable. Anisotropic scattering is treated for each group-to-group transfer by utilizing a generalized Gaussian quadrature technique (PL expansion method).

MORSE provides versatile types of variance reduction techniques including energy-space-dependent splitting and Russian roulette and exponential transformation. Source energy biasing is an option, as well as energy biasing at each collision. In fission problems, the fission weights may be renormalized as a function of an estimate of criticality k so that the number of histories per generation remains approximately constant. In the present study, Russian roulette and particle splitting were used to reduce the variance in the estimated results.

The two-dimensional code used by the U.S. is DOT 4.3.⁽²⁴⁾ This code determines the flux or fluence of particles throughout a one- or two-dimensional geometry system due to sources either generated as a result of particle interaction with the medium or incident upon the system from extraneous sources.

Basically, the Boltzmann transport equation is solved using either the method of discrete ordinates or the diffusion theory approximation. In the discrete ordinates method, balance equations are solved for the flow of particles moving in a set of discrete directions in each cell of space mesh and in each group of multigroup energy structure. Iterations are performed until a prescribed criterion for convergence is met. There is a variety of options that allows sources to be specified at internal or external boundaries, distributed by the space and energy, or determined from an input flux file. In a similar fashion, the code has a variety of output source information that can be coupled to other problems. The "first collision source" data which is an analytical first-flight scattering source can be accommodated, and the final flux is the sum of the collided and uncollided fluxes. In this case, the GRTUNCL code (modified to be compatible with DOT 4.3) can be used to generate the first collision source needed for cases where a localized external source is used. This is the approach used in the present analysis to treat the D-T point source from the rotating neutron target, RNT.

The code can also generate a single output file containing both distributed flux moments and boundary directional fluxes, so that this file, plus the original input data, provide an "exact" restart. This allows a few groups of a large problem to be solved in each computer run without loss of efficiency.

A special feature of the DOT 4.3 code is "variable meshing." This allows the number of first-dimension (i) mesh interval to vary with the second dimension (j) index. The directional quadrature set can be chosen from an arbitrary number of input sets, and the choice can vary with spatial position and energy group. This feature can reduce the computational time considerably by concentrating the calculation in areas needing attention, such as streaming gaps. Unsymmetric direction sets can also be used in cases where streaming is directed either upward or downward. In the present analysis, the variable mesh feature was not used. The S_8 symmetrical direction set was used throughout the geometry.

II.2.3 Computational Models

A. Two-Dimensional Model Used by DOT 4.3

The 2-D model used by the U.S. in the discrete ordinates calculations performed by DOT 4.3 is shown in Fig. II.8 for the first wall experiments. The model used for the reference experiment is identical except that regions I, II, and III are filled with air. These regions correspond to regions II, III, and IV in Fig. II.2, respectively, and the R-Z dimensions of the several zones considered are identical to those shown in Fig. II.2. In assigning the dimensions shown in the cylindrical models shown in Figs. II.2 and II.8, the volume of the room and the inner and outer Li_2O zones were preserved, as discussed in subsection II.1.3(A). Besides the dimensions of the zone boundaries, the number of spatial meshes used in the model in the R and Z directions are also shown in Fig. II.8. As was stated earlier, fine meshes are required at the front zones and at zone boundaries to accurately predict neutron transport in those zones.

The 2-D model in R-Z geometry used for the 10 cm-thick beryllium experiment is shown in Fig. II.9. The four layers of beryllium consist of blocks each of size 1.932" x 1.932" x 0.995". The total thickness is thus 4 x 0.995". The beryllium blocks in the central drawer have an effective radius of 2.769 cm, while the Li_2O blocks in the central drawer (zone VIII) have an effective radius of 2.719 cm. Zones VI and IX are the outer stainless steel canning of the central drawer. Note from Fig. II.9 that zones I, II, III, IV, V, and VII contain the beryllium blocks. Zone VIII is the inner Li_2O zone of the central drawer that has atomic densities different from those of the outer Li_2O zone (zone X) due to the reasons discussed in subsection II.1.3(B). The model used for the 5 cm-thick beryllium experiment is identical to the one shown in Fig. II.9 except that the front Be zone consists of two layers of thickness $2 \times 0.995" = 5.0546$ cm. As in Fig. II.8., the number of spatial meshes used in the model in the R and Z directions is also shown in Fig. II.9, in addition to zone dimension.

In the Be-sandwiched experiment, the model used and the dimensions considered in the 2-D geometrical configuration are identical to those shown in Fig. II.3 except that zones VIII and V are made of the Li_2O blocks.

In determining the specification of the external D-T neutron source in the 2-D calculations performed by both JAERI and the U.S. for all the experiments that have been carried out, the following procedures were used. First, one should notice that the D+ beam line makes an angle of 10 to the room wall and the test module is placed at an angle of 80 with respect to the beam line. The angle and energy distributions of the generated neutrons for the reaction of the D+ beam at the beam spot on the Ti-T layer of the RNT were used along with the geometrical details of the structure of the rotating target (without the room details) to calculate by the Monte Carlo method [MCNP (U.S.), MORSE-DD (JAERI)] the incident neutron spectrum in the 80 direction where the Li_2O assembly is placed in the penetration hole. This incident neutron spectrum was considered as an isotropic neutron source located at $r = z = 0$ in the 2-D models used by both JAERI and the U.S.

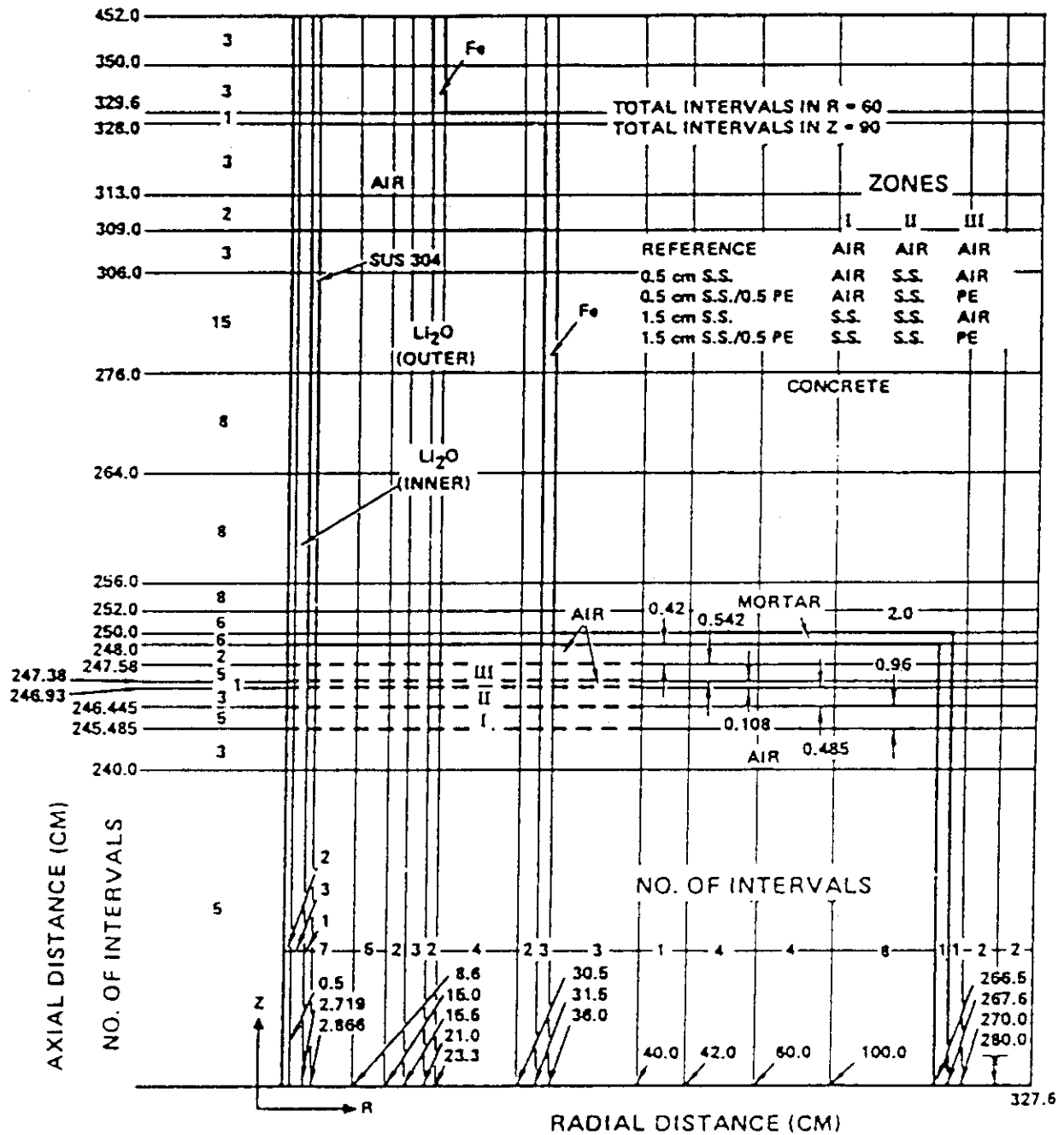


Figure II.8 The 2-D (R-Z) calculational model for the reference and first wall experiments used by DOT4.3 (U. S.)

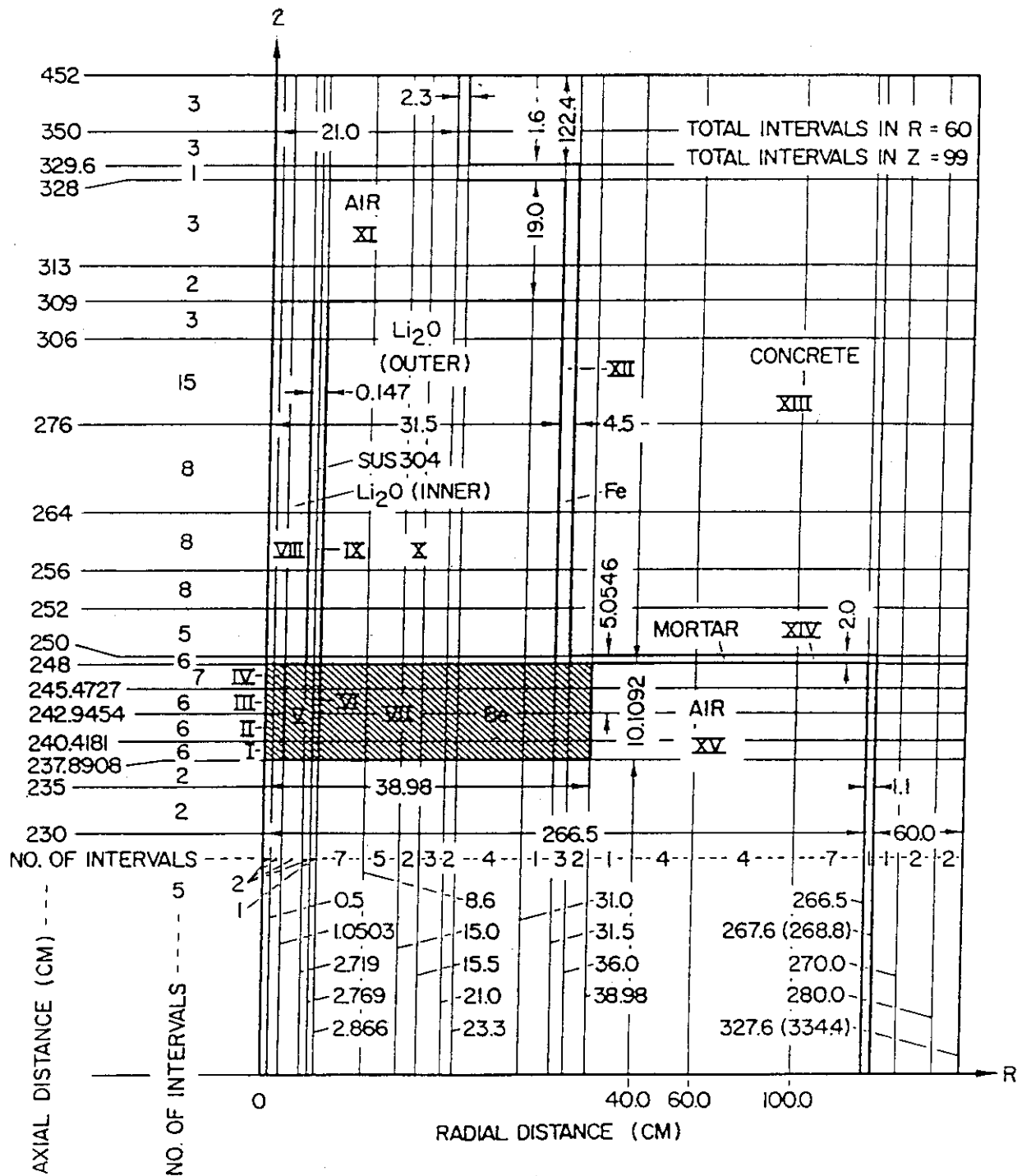


Figure II.9 The 2-D (R-Z) calculational model for the beryllium experiments (U.S.)

B. Three-Dimensional Model Used by MCNP

In calculating the reaction rates inside the test assembly by the MCNP code, the statistics obtained were very poor (if the whole room and test assembly were including in a single run) since the volume of the test assembly and its front surface is very small in comparison to the room walls and room size. To obtain better statistics, the in-system reaction rates (e.g., T_6 , T_7 , $^{27}\text{Al}(n,\alpha)$, etc.) were calculated based on the Monte Carlo calculational model shown in Fig. II.10. In this model, the neutron source at the entrance of the experimental port was separated into two components, an anisotropic point source (direct component) located at a distance 2.48 m from the front surface of the Li_2O assembly, and an isotropic plane source (indirect component) located at a distance of 13 cm from the front surface. The direct component includes the uncollided neutrons and neutrons collided with the target assembly and scattered into the experimental port. The indirect component includes those neutrons collided by the room walls and scattered in that direction.

The angular distribution of direct source component was estimated at 13 points (9 in JAERI's calculation; see Fig. II.6) covering an angle $\theta' = -22$ to 22 where θ' is measured from the center line of the experimental port or $\theta = 58$ to 102 in the θ direction with respect to the D+ beam line ($\theta = 0$). This source treatment model was the same as that used by JAERI, as was discussed in subsection II.1.3(B). Note from Fig. II.10 that the room-returned component was calculated separately and was shown to be almost isotropic over the entrance to the experimental hole. As in JAERI's model, this component was presented by a plane source of dimension 2m x 2m located as shown in Figs. II.6 and II.10. After determining both the direct and the indirect components of the incident neutrons, only the experimental hole, the Li_2O test assembly and the surrounding concrete (of a thickness ~64 cm) were modeled in the subsequent MCNP calculations to arrive at estimates to the in-system reaction rates and spectra.

The above calculational model was used in the analysis of the reference and the beryllium experiments. Another calculational model for the Monte Carlo analysis was adopted by the U.S. (ORNL) for the reference and the first-wall experiments using the MORSE and MCNP codes. The room walls, the Li_2O assembly, and the rotating target were modeled in detail using the combinatorial geometry subroutines unique to each code system. All of the components were represented in sufficient detail to assure that the neutron transport was accurately treated in the calculations. The inner and outer Li_2O regions were modeled as co-axial cylinders, as was discussed earlier. The inner Li_2O region was represented as a 0.127-m-radius cylinder surrounded by a 0.07-m-thick SS-304 liner. The Li_2O and SS-304 can were homogenized in each region in the appropriate Li_2O to steel ratios.

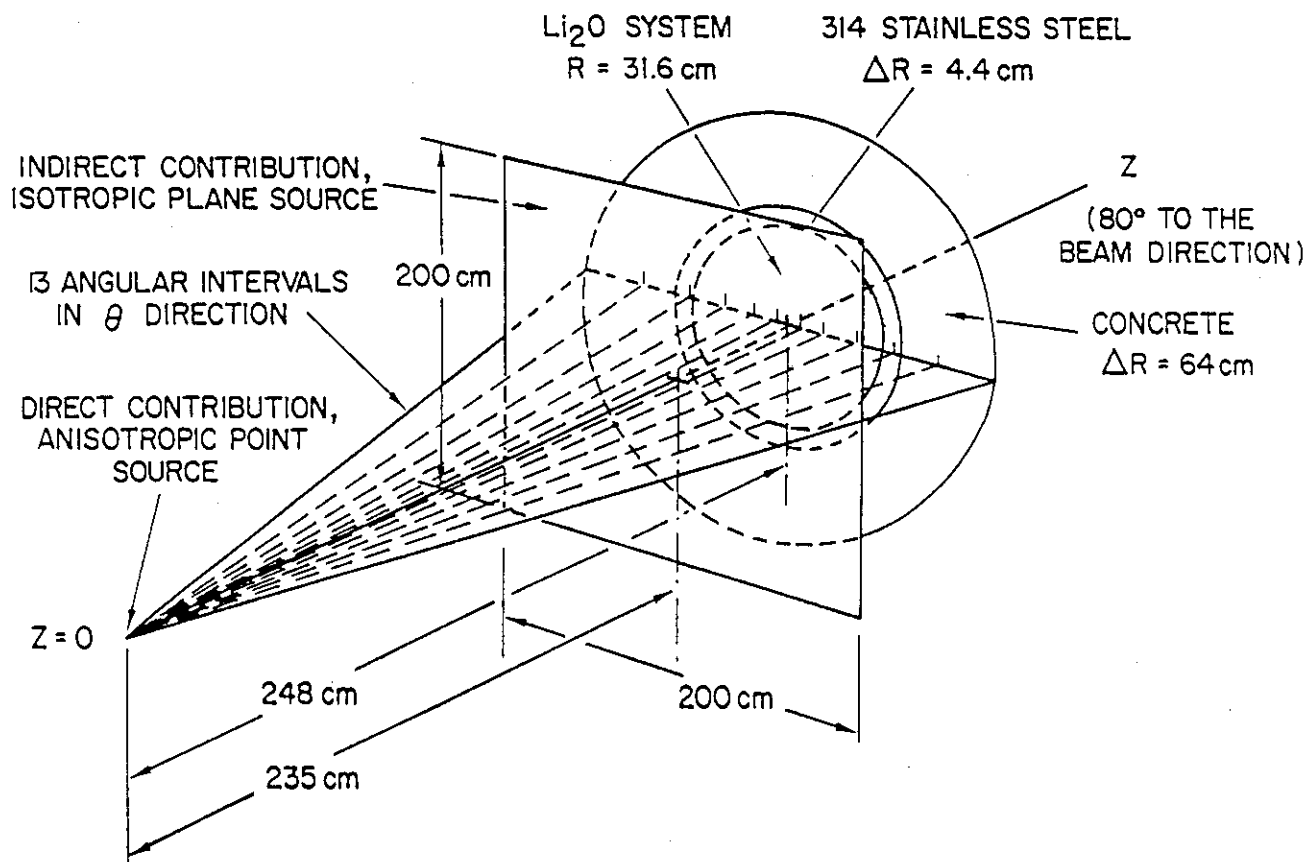


Figure II.10 Anisotropic point source and isotropic plane source used in the MCNP calculational model

Neutrons produced in the D-T reactions in the titanium-tritide target are distributed in energy and angle with respect to the incident deuteron beam. The probability that a deuteron of energy E_d reacts while traveling a distance dx in a target containing N_t tritium atoms per cm^3 is

$$P = N_t \int_0^{E_d} \sigma/(dE/dx) \quad (\text{II.1})$$

where σ is the microscopic cross-section for the $T(D,n)^4\text{He}$ reaction and dE/dx is the stopping power for deuterons in titanium-tritide. When the reaction cross-section is a differential angular cross-section, then P is the probability for emission per unit solid angle. In the U.S. (ORNL) analysis, Eq. (II.1) was solved using the procedures outlined in Ref. (25) to obtain the neutron source data in multigroup energy format for use in the MORSE calculation. The procedure in Ref. (25) was modified to obtain the energy-angle data in continuous energy format for use with MCNP.

Since the solid angle subtended by the front face of the Li_2O assembly is small (5×10^{-2} sr), biased neutron source sampling was used wherein 50% of the neutrons were directed into a "cone" having polar and azimuthal angles of 10° with respect to the direction from the point on the target where the D-T reactions occur to the center of the face of the Li_2O assembly. All other source neutrons were taken to be uniformly emitted everywhere else. The neutron source biasing scheme is shown schematically in Fig. II.11. The neutron emission into the polar angular interval was determined using the calculated energy-angle distribution discussed above. Neutron emission into the azimuthal angles was taken to be uniform.

The tritium production as a function of depth in the Li_2O assembly was calculated using collision density estimator in MORSE and track length estimator in MCNP. The collision density estimator used in the MORSE calculation is given by

$$T = (\sigma_i/\sigma_T) \cdot \text{neutron weight, } i = 6, 7 \quad (\text{II.2})$$

where i is the cross-section for the tritium production from neutron reactions with ^6Li ($i=6$) or ^7Li ($i=7$) and T is the neutron transport cross-section in Li_2O . The ratio of these probabilities is multiplied by the weight of the neutron prior to initiation of the reaction. The spatial distribution of the tritium production was obtained by dividing the inner Li_2O region into 12 axial intervals. The interval dimensions selected to bracket the locations of the detectors used in the measurements and the locations of the detectors are summarized in Table II.5.

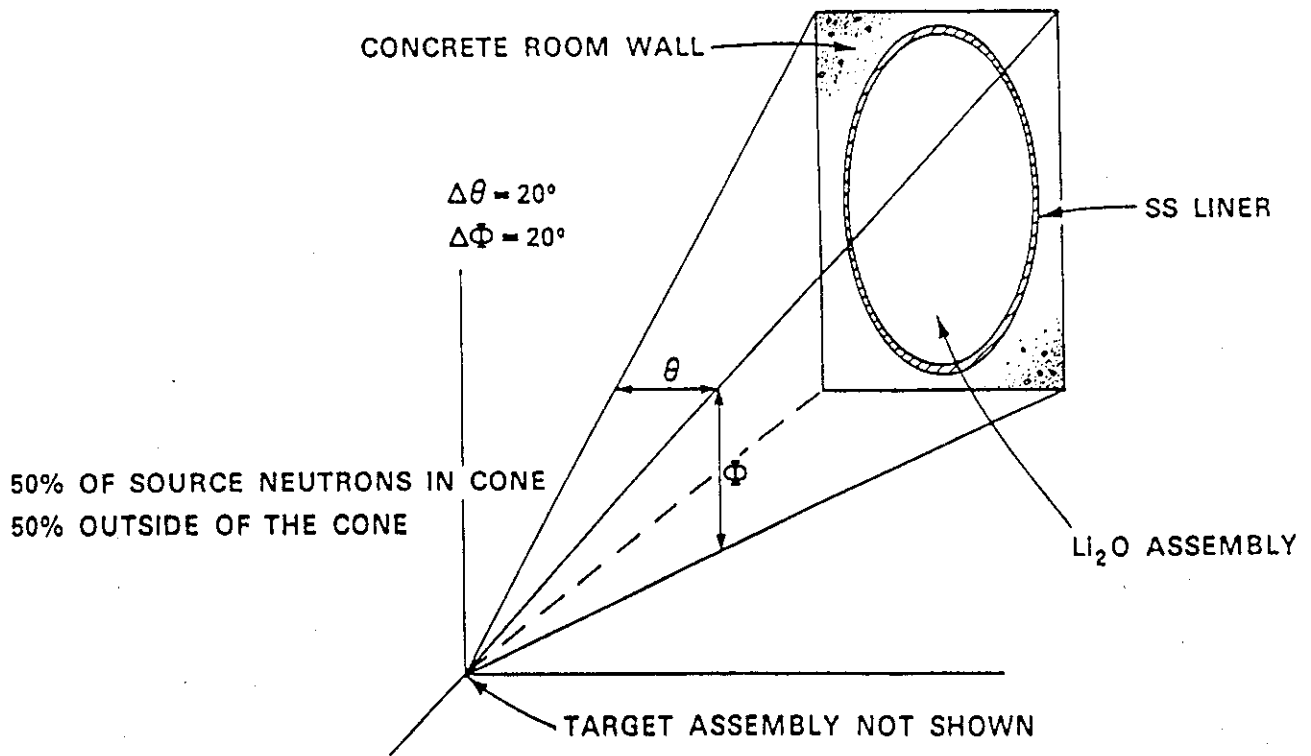


Figure II.11 The biasing scheme used by the U.S. (ORNL) in the Monte Carlo analysis of the reference and first wall experiments

Table II.5 Detector Locations and Monte Carlo Estimator Cell Dimensions^(a) Used in the
Monte Carlo Calculations of the First Wall Experiments

Detector No.	⁶ Li Detectors	⁷ Li Detectors	Estimator Interval Thickness	Estimator ^(b) Volume
	(cm)	(cm)	(cm)	(cm ³)
1	0.25		0.0	1558.62
2	1.26	1.60	0.50	4728.20
3	2.53		2.06	3179.58
4	3.81	3.88	3.04	4800.55
5	5.06		4.58	4426.48
6	7.61		6.00	6234.48
7	10.12	11.47	8.00	12468.96
8	15.20		12.00	18703.44
9	20.24	21.59	18.00	21820.68
10	30.30	31.71	25.00	31172.45
11	40.45	41.85	35.00	31172.45
12	55.72		45.00	49439.43
		60.86		

(a) Measured from the front face of the Li₂O assembly

(b) Scoring radius = 31.5 cm

III. NEUTRON SOURCE CHARACTERIZATION

III.1 Analysis with Monte Carlo Codes

III.1.1 Neutron Source Generation

The neutron source used in the experiments was generated based on the $^3\text{T}(d,n)^4\text{He}$ reaction. Accelerated D^+ beams bombard the tritiated titanium target coated on the copper plate of the rotated neutron target (RNT), as illustrated in Fig. III.1. The target is cooled with water. This figure shows the calculation model used in the present analysis. The actual RNT has a more complex structure. Bombarding deuterons are slowed down to zero energy in the titanium coating. During this process, neutron-generation reactions are possible at various energies. Accordingly, the energy of the emitted neutrons depends on that of deuteron, though such dependence is small since emitted neutron energy is about 14 MeV compared with about 300 KeV of the deuteron. Nevertheless, such energy dependence was taken into account in the MORSE-DD calculations based on Ref. (26) in which the reaction probability table is given, corresponding to the energy of deuteron.

The angular distribution of the emitted neutrons is almost isotropic in the center-of-mass (CM) system but anisotropic effect was considered using the following experimental formulae given by Benveniste, et al.⁽²⁷⁾

$$\frac{\sigma_c(\theta)}{\sigma_c(0)} = 0.998 + 0.213 \cos\theta_n - 0.0190 \cos^2\theta_n. \quad (\text{III.1})$$

The above equation was given for a deuteron incident energy $E = 350$ KeV, but we applied it in our case for $E = 310$ KeV.

From the relation between the CM angle, θ_c , and the Lab. angle, ϕ_n , we can determine the emission angle, ϕ_n ,

$$\cos\phi_n = \frac{1 + \gamma\cos\theta_c}{\sqrt{1 + 2\gamma\cos\theta_c + \gamma^2}} \quad (\text{III.2})$$

where

$$\frac{1}{\gamma^2} = \frac{m_\alpha(m_1+m_2)}{m_n m_1} \left(\frac{m_2}{m_1+m_2} + \frac{Q}{E_1} \right)$$

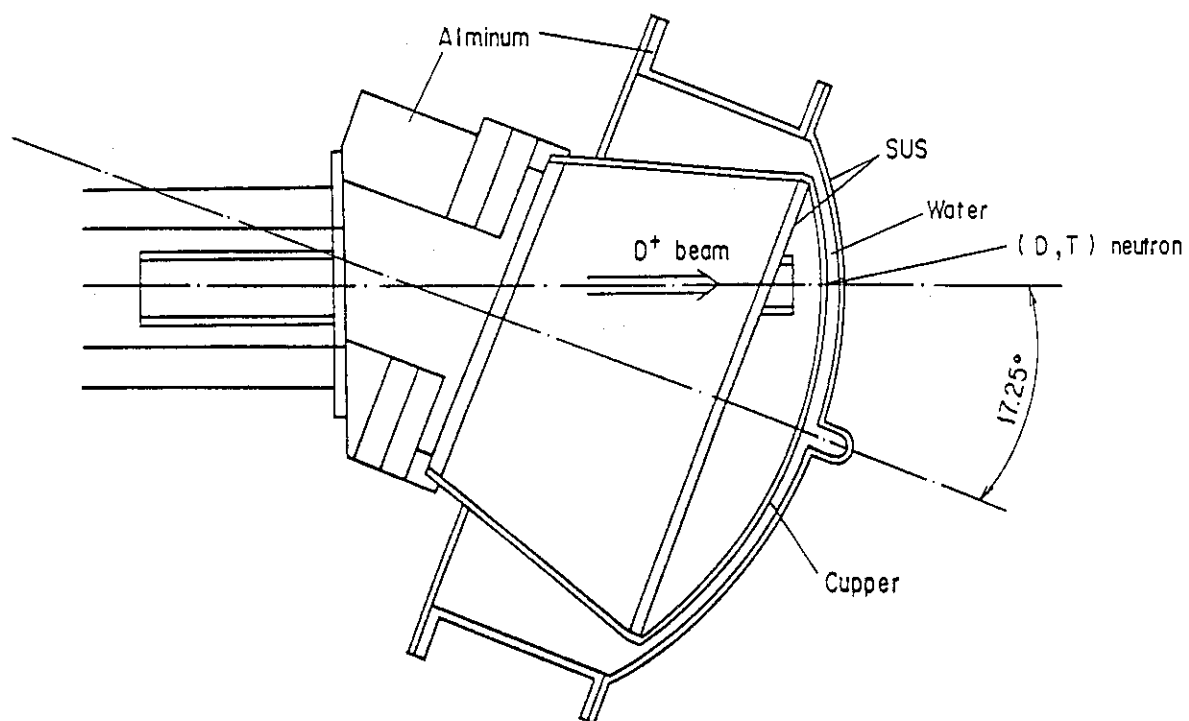


Figure III.1 Cross-sectional view of the rotating neutron target (RNT) (calculational model)

- m_1 = mass of incident deuteron,
 m_2 = mass of target tritium,
 m_n = mass of neutron,
 m_α = mass of alpha particle,
 E_1 = incident energy of deuteron, and
 Q = 17.6 MeV (emitted total kinetic energy).

When we obtain ϕ_n , the emitted neutron energy, E_n , is determined relativistically by the following equation:

$$E_n(E_1, \phi_n) = W_n - m_n, \quad (\text{III.3})$$

where,

$$W_n = \frac{1}{2} \{b \pm \sqrt{b^2 - 4ac}\}$$

$$a = (W_1 + m_2)^2 - (W_1 - m_1)^2 \cos^2 \phi_n,$$

$$b = (m_1^2 + m_2^2 + m_n^2 - m_\alpha^2 + 2m_2 W_1) (W_1 + m_2), \text{ and}$$

$$W_1 = m_1 + E_1 = \text{total energy of deuteron.}$$

In the course of determining the emitted neutron energy and angle, a statistical process is necessary. This calculation routine was originally programmed by Seki, et al.,⁽²⁸⁾ and installed in the MORSE-DD source routine. MCNP calculations used the calculated energy-angle distribution obtained by MORSE-DD.

The calculated energy and angular distribution of the emitted neutron is presented in Table III.1, where the angular mesh size is coarser compared with the one actually used. The table shows probabilities for each energy band and the integrated probability in each band is normalized to unity. The peak energy at the experimental hole is within the range 13.88 - 14.10 MeV. By using this energy/angular distribution of the D-T neutrons, Monte Carlo calculations [MORSE-DD(JAERI), MCNP(U.S.)] have been carried out to obtain the direct component into the experimental zone. In these calculations, the target assembly was included but the room walls were not taken into account. Accordingly, this direct neutron source component consists of virgin neutrons emitted from the D-T beam spot in the direction of the Li₂O assembly plus those that were collided in the RNT structure and then scattered in that direction. The normalized angular distributions are depicted in Fig. III.2 (JAERI) and in Fig. III.3 (U.S.), for within the angular range = 50°-103° (θ is the angle made

Table III.1 Energy and Angular Distribution of the Emitted (D,T) Neutron

E (MeV)	S(u) ^(b)	Angle $\mu = \cos \theta$ (a)						
		-0.940	-0.707	-0.259	0.259	0.707	0.940	1.0
upper								
15.49	0.302						0.293	0.707
15.25	1.666					0.010	0.700	0.290
15.01	4.174					0.241	0.587	0.172
14.78	7.641					0.517	0.406	0.077
14.55	9.293				0.085	0.798	0.111	0.006
14.32	9.469				0.746	0.250	0.003	0.001
14.10	9.225			0.070	0.930			
13.88	8.882	0.001	0.033	0.939	0.027			
13.67	7.880	0.049	0.376	0.575				
13.46	4.313	0.184	0.698	0.118				
13.25	1.193	0.559	0.441					
13.04	0.031	1.0						
12.84								
Total ^(c)		0.028	0.108	0.215	0.260	0.233	0.123	0.032

(a) θ is the angle with the D^+ beam.(b) Integrated for angle $\mu = \cos \theta$.

(c) Normalized to unity.

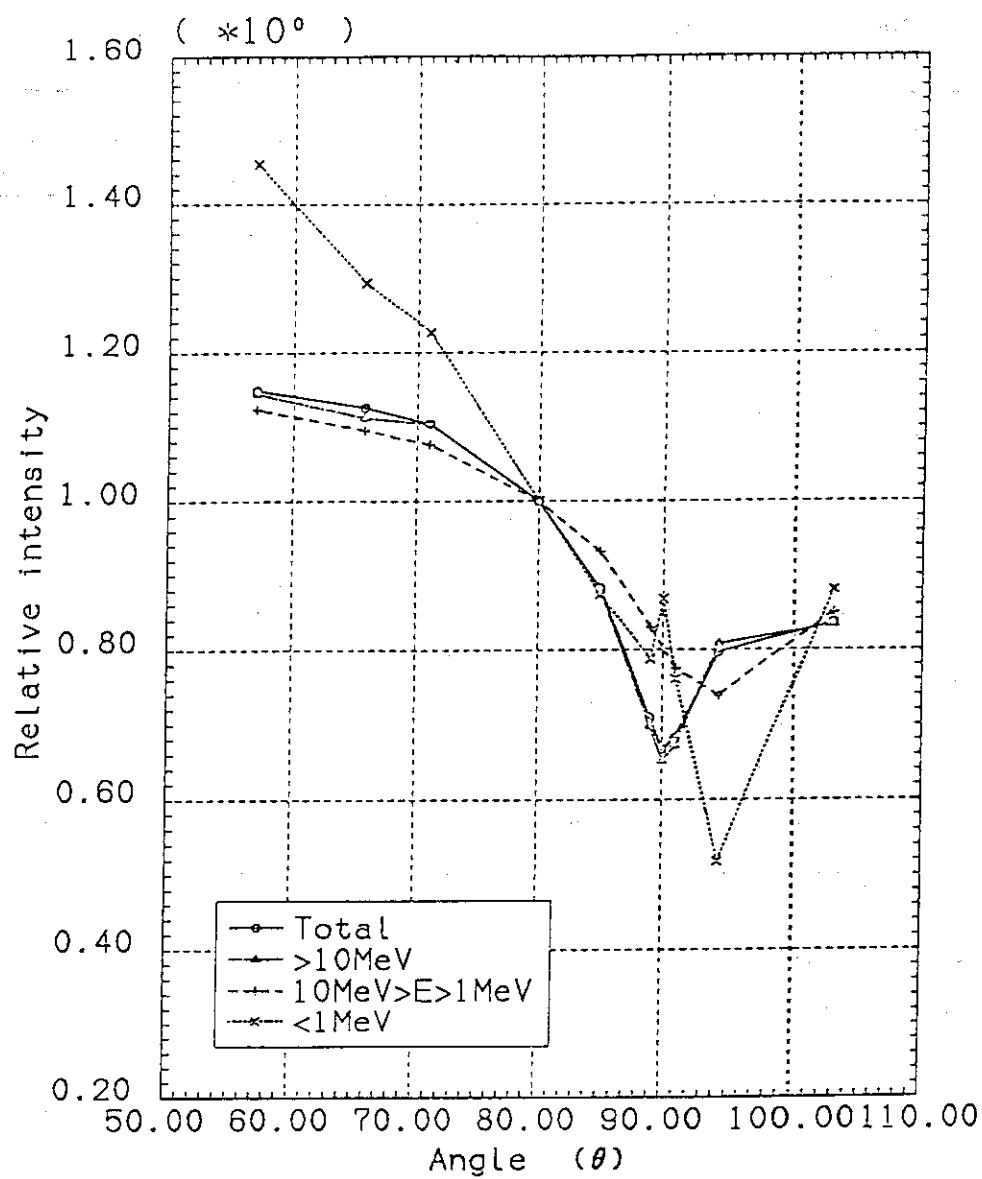


Figure III.2 Angular distribution of neutrons emitted from RNT. The distribution curves are normalized to unity at $\theta = 80$ degrees. (JAERI)

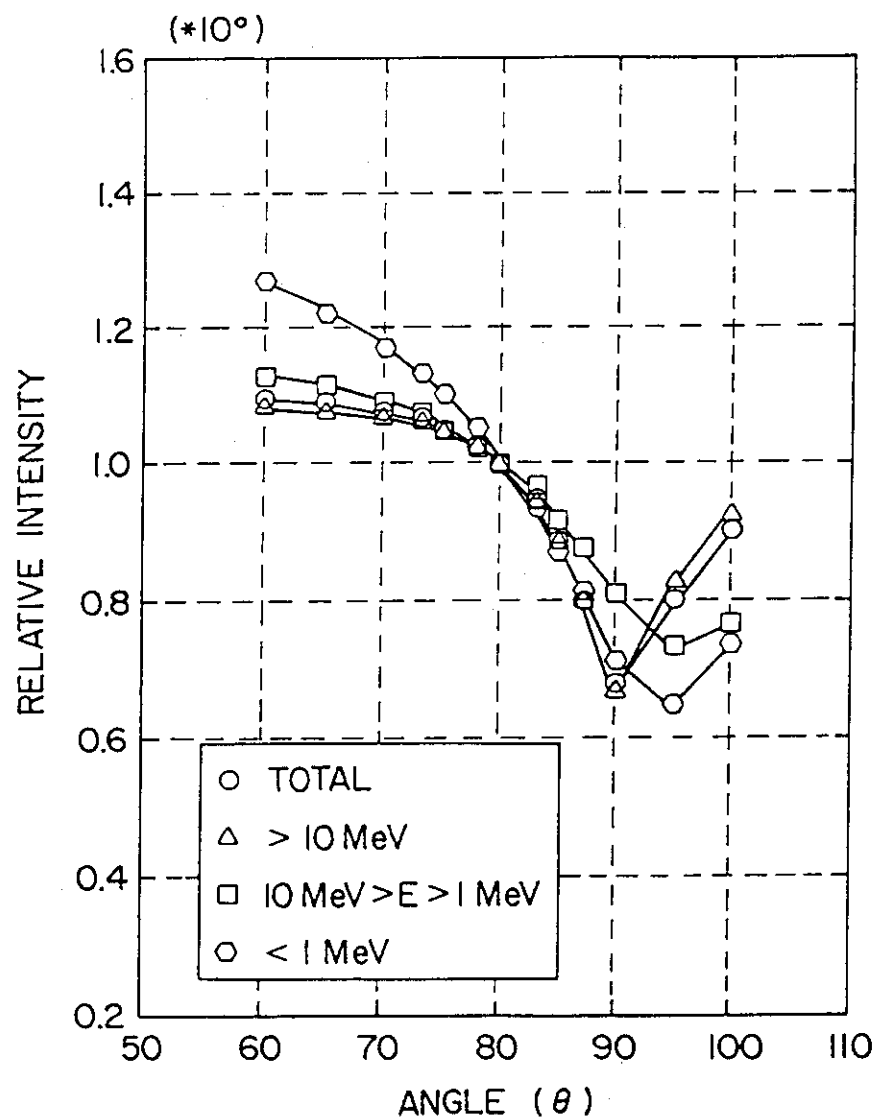


Figure III.3 Angular distribution of neutrons emitted from RNT (U.S.)

with the D+ beam. The center line of the experimental cavity is at $\theta = 80^\circ$). Similar angular dependencies can be observed between both calculations for most energy intervals. The angular distribution of this direct neutron source is shown relative to the one in the $\theta = 80^\circ$ direction and at different energy ranges. Note that more direct neutrons reach the right side of the experimental cavity ($\theta < 80^\circ$) than the left side ($\theta > 80^\circ$). Examining these two figures, one notices that at small angles ($\theta < 80^\circ$) the MCNP source strength is lower than the MORSE-DD calculated result, except at $10 \text{ MeV} > E > 1 \text{ MeV}$. The reverse is true at large angles ($\theta > 80^\circ$). However, it is important to know that the angle from the source to the edge of the mouth is about 9° with respect to the center of the experimental port. In this angular range, the distributions of relative source strength of MCNP and MORSE-DD calculations are consistent.

Strengths of direct source at the entrance to the experimental cavity are compared in Table III.2 for the energy ranges $E > 10 \text{ MeV}$ and $E > 1.2 \text{ MeV}$, as calculated by JAERI. These values show source strengths per unit solid angle times 4π . The table shows strong angular dependence across the entrance. The integral value 1.012 means that a multiplication occurs due to the (n,2n) reactions with the structure of the RNT. The absolute values of integrated sources for $E > 10 \text{ MeV}$, $10 \text{ MeV} > E > 1 \text{ MeV}$, and $1 \text{ MeV} > E$ are compared in Fig. III.4. The integrated absolute values calculated by MCNP for the direct neutrons are 0.04053 at $E > 10 \text{ MeV}$, 0.00308 at $10 \text{ MeV} > E > 1 \text{ MeV}$, and 0.00141 at $1 \text{ MeV} > E$ in the units of neutrons/steradian/source. Neutrons above 10 MeV are apparently dominant for the direct source from the RNT.

III.1.2 Neutron Source Spectrum at the Entrance to Experimental Cavity

The incident source distribution for the experimental hole is influenced by the RNT structural materials, and accordingly not flat across the hole, as was shown in Figs. III.2, III.3, and III.4. In addition, neutrons incident on the test module include an uncollided component and collided neutrons from the room walls and the rotating target materials. It is essential for the measurement and analysis to characterize the irradiation field where the experiments are conducted.

For that purpose, a series of experiments were carried out to measure the energy and angular distributions of neutrons around the target and their spatial distribution inside the room cavity. Measured and calculated values for these distributions were reported previously.⁽²⁹⁾ In addition, time-of-flight (TOF) spectrum measurements were performed in target room #1 (TR#1) at a distance of 17.445 m from the target assembly, as shown in Fig. III.5, with and without a collimator behind the experimental hole. The collimator was used in order to eliminate the scattered component by the RNT structure and by the room walls. The opening of the collimator was 50 mm in diameter (i.e., 50 mm ϕ). The NE213 counter used for that purpose was able to see an area of about 7 cm ϕ at the target through the collimator. In the case without the collimator, the experimental port between the first and second target rooms acts as a collimator whose opening is 42 cm ϕ . In this case, the detector can see the whole target assembly and

Table III.2 Source Neutron from Target Assembly (Source/ 4π)

Horizontal Position on mouth (cm)	Angle to D+ Beam, θ (degree)	E > 10 MeV	E > 1.2 MeV
37.6	71	0.972	1.078
0.0	80	0.881	0.976
-37.6	89	0.615	0.693
Integral		0.895	1.012

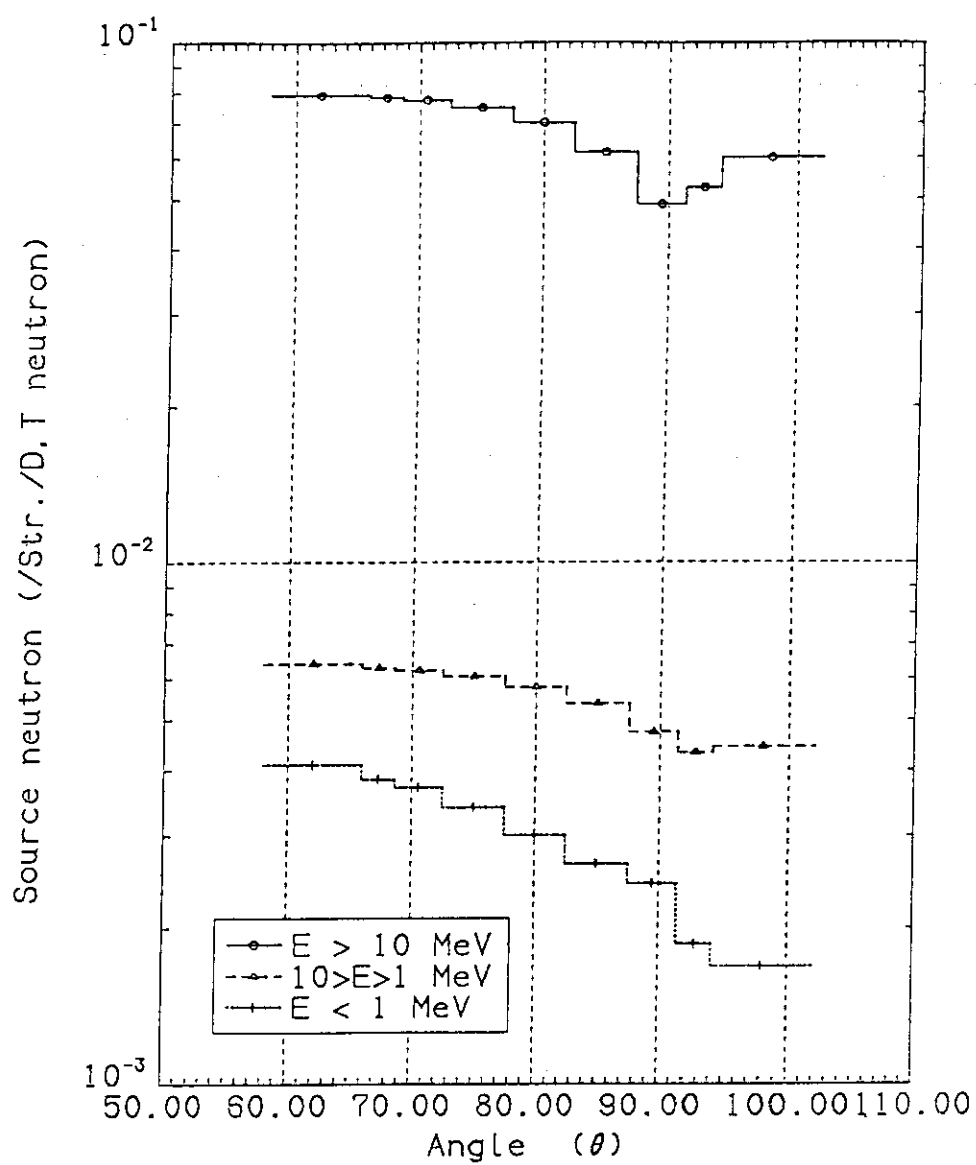


Figure III.4 Angular distribution of neutrons emitted from RNT (absolute value)

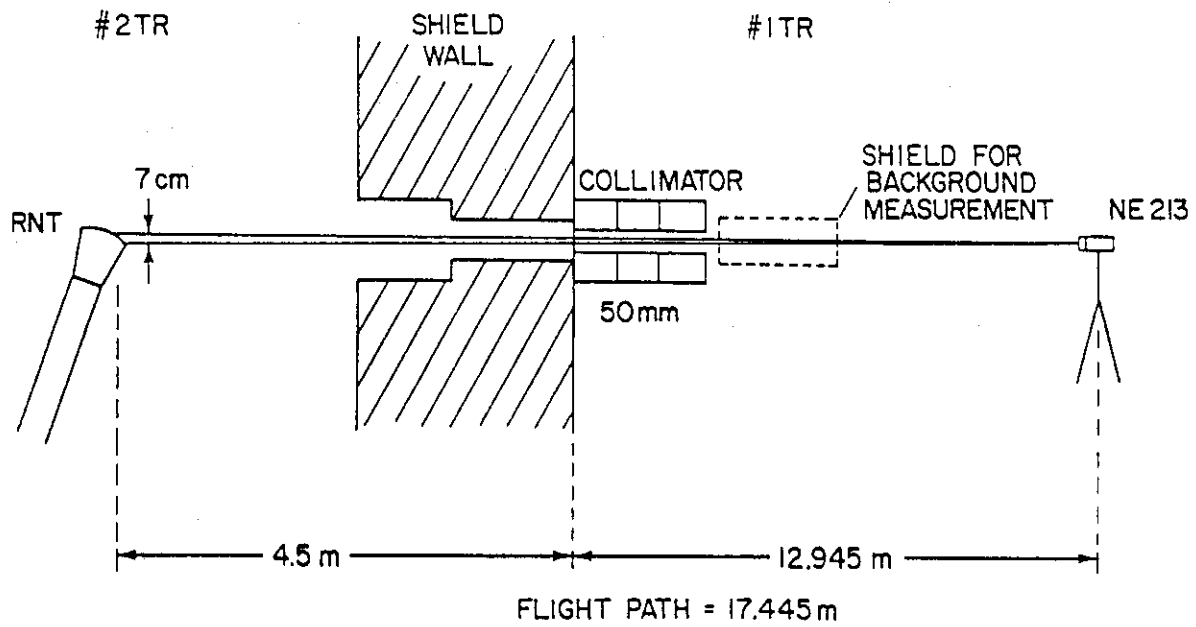


Figure III.5 Layout of the time-of-flight spectrum measurements

the area of 59 cm ϕ on the opposite side wall of the second target room. This measurement was also repeated for a flight path of 11.445 m.

Spectrum was also measured at the front surface of the Li₂O assembly by an NE213 spectrometer and a proton recoil counter (PRC). The first detector measured neutron spectrum energies above 1 MeV while the PRC was used to measure spectra below 1 MeV down to a few KeV. Two experiments were performed to measure the direct and room-scattered neutron spectra at the entrance center of the experimental port with the Li₂O assembly loaded in that port (assembly in). To measure the room-scattered component, a large shadow cone was placed between the target assembly and the detectors. In this case, only neutrons scattered by the room walls were detected. The direct component was detected by subtracting the room-scattered component from the measured spectrum without the shadow cone in place. These two experiments were repeated but without the Li₂O assembly inside the experimental port (assembly out).

Flux mapping at several locations on the horizontal and vertical axes at the front face of the Li₂O assembly was also performed by NE213 spectrum measurements and by measuring reaction rates in ²⁷Al, ⁵⁸Ni, and ¹⁹⁷Au foils placed at these locations. These experiments were necessary to measure the degree of asymmetry in the neutron field at the entrance of the test module. Details of these experiments can be found in Volume I of this report.

To compare spectrum prediction to the time-of-flight measurements, the calculated spectra should be smeared over the detector energy resolution. The resolution function, a Gaussian distribution, of the time-of flight method, is expressed as:

$$R(E-E') = A \exp(-(E-E')^2/2\sigma^2(E)),$$

where $\sigma(E)$ is the energy resolution which can be expressed as $\sigma(E) = 0.0277 \Delta t E^{3/2}/Z$, Z is the flight path, Δt is the time resolution of pulsed DT neutrons, E is the neutron energy at the peak of the Gaussian distribution, $(E-E')$ is the energy deviation, and A is the normalization constant.

For the case without the collimator, the MCNP modeling used by the U.S. is straightforward. All the geometrical details of the target assembly and the walls of room #2 were taken into account. Two point estimators were applied at the locations where the detectors were placed in the experiment i.e., at $Z = 17.445$ m and 11.445 m. As was mentioned in subsections II.1.3 and II.2.3, the thickness of the concrete room wall in the modeling is taken to be 60 cm in all the calculations which adequately represents the effect of the room walls.

The measured and calculated spectra at 17.44 m, without a collimator, are shown in Fig. III.6. The cross-section library used in the MORSE-DD calculation is the DDL/B4 (JAERI), while the RMCCS library, based on ENDF/B-V, is used in the MCNP calculations (U.S.). The calculated spectra show a good agreement with the measurements. The 14 MeV peak is well-predicted in both the MCNP

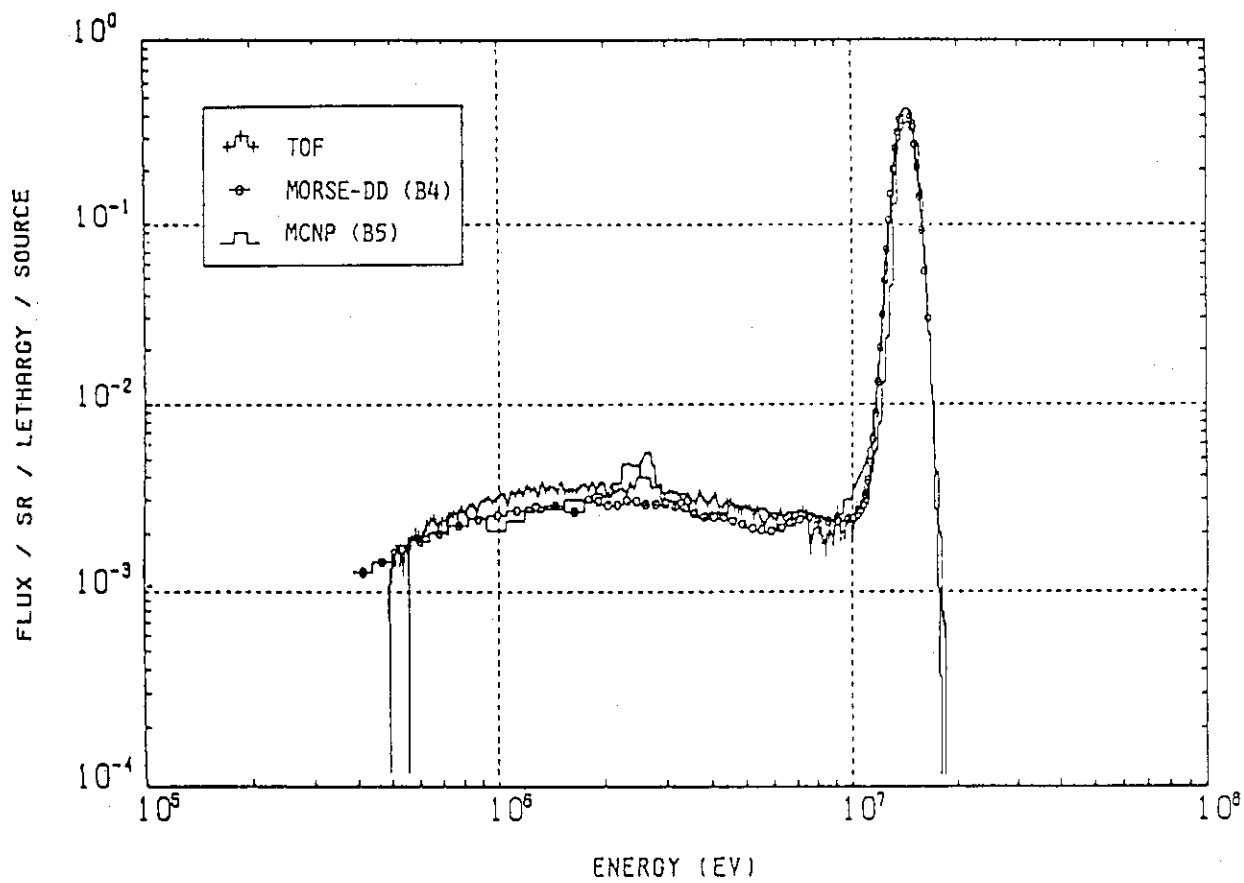


Figure III.6 Comparison of neutron spectrum for RNT between calculations and measurements by the TOF method, no collimator, $L = 17.445$ m

and MORSE-DD calculations. However, at energy between 10 and 14 MeV, the calculated spectrum is overestimated in both calculations. The reason for the discrepancy is not clear. (Probably the time resolution is not proper.) The small peak due to the (d,d) reaction is observed in the measured spectrum, but was not taken into account in the analysis. The small peak on the calculated spectrum by MCNP near 2.5 MeV, resulting from the background contribution predicted by the RMCCS library should not be confused with the DD neutron peak at ~2.5 MeV on the measured spectrum. This peak in the calculations was not shown in the MORSE-DD calculations although there is a dip at 1.8 MeV. The MORSE-DD calculations also underestimate the spectrum below 8 MeV due to underestimating the scattering component by the RNT target. Fig. III.7 shows the comparison between the MCNP calculations and measurements for the without-collimator case, and for $L = 11.445$ m.

In order to include the TOF with-collimator case in the same calculation as the without-collimator cases, the collimator geometry was not actually simulated. Instead, with all the geometry remaining the same, the tally in the Monte Carlo calculations was taken only from a small zone on the RNT, which can be seen by the detector through the collimator. Such a zone is approximated by the intersection of an $R = 7$ cm cylinder with the RNT. The cylinder has the same central axis as that of the experimental port, and the intersection zone is composed of the fusion neutron source (beam spot), copper, water, and stainless steel layers. A point estimator was applied at $Z = 17.445$ m to simulate the detector in the experiment. Two contributions (from neutrons interaction) were not tallied by the point estimator in the calculations. These components are neutrons bounced back from the RNT side wall, passing through the $R = 7$ cm zone without collisions and going to the detector, and neutrons reflected by the room wall and passing through the intersecting zone of $R = 7$ cm. Since most of the high energy neutrons are forward-peaked, and because the side-wall of the target assembly is thin, the error due to neglecting the first component (target-returned) is small. Neglecting the second component (room-returned) could cause some deviation on the calculated spectrum in the MeV energy regime, although its impact is still small.

Fig. III.8 shows the comparison of the calculated spectra with measurements for the with-collimator case, and for flight length of 17.445 m. Similar to the comparison in the without-collimator cases, the calculated spectra have larger shift values between 10 MeV and 8 MeV, even though the 14 MeV peak coincides with the measured one. As a large fraction of the indirect contribution is screened out by the collimator, the measured DD neutron peak at 2.5 MeV becomes more apparent, and the calculated background peak predicted by MCNP near 2.5 MeV diminishes. The calculated spectrum at energies between 0.8 MeV and 2.0 MeV in the MCNP calculation is lower than that of measurements.

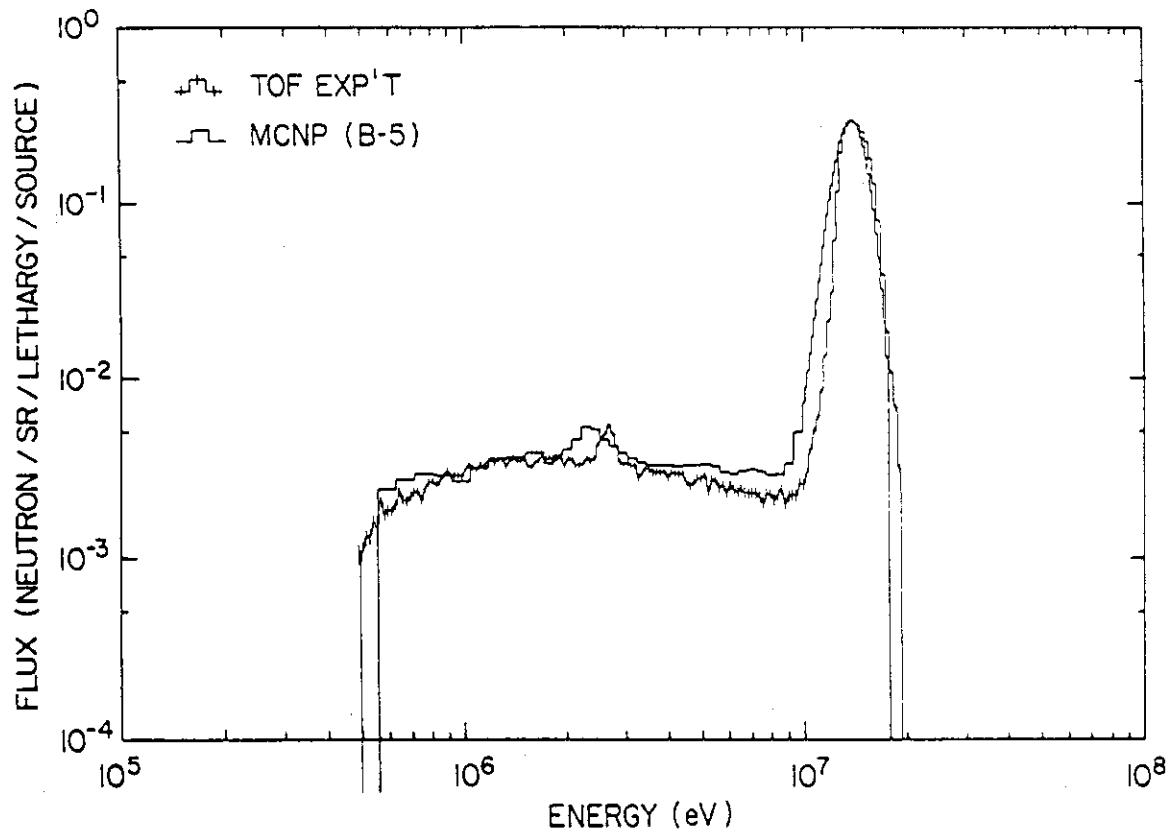


Figure III.7 Comparison of neutron spectrum for RNT between calculations and measurements by the TOF method, no collimator, $L = 11.445$ m

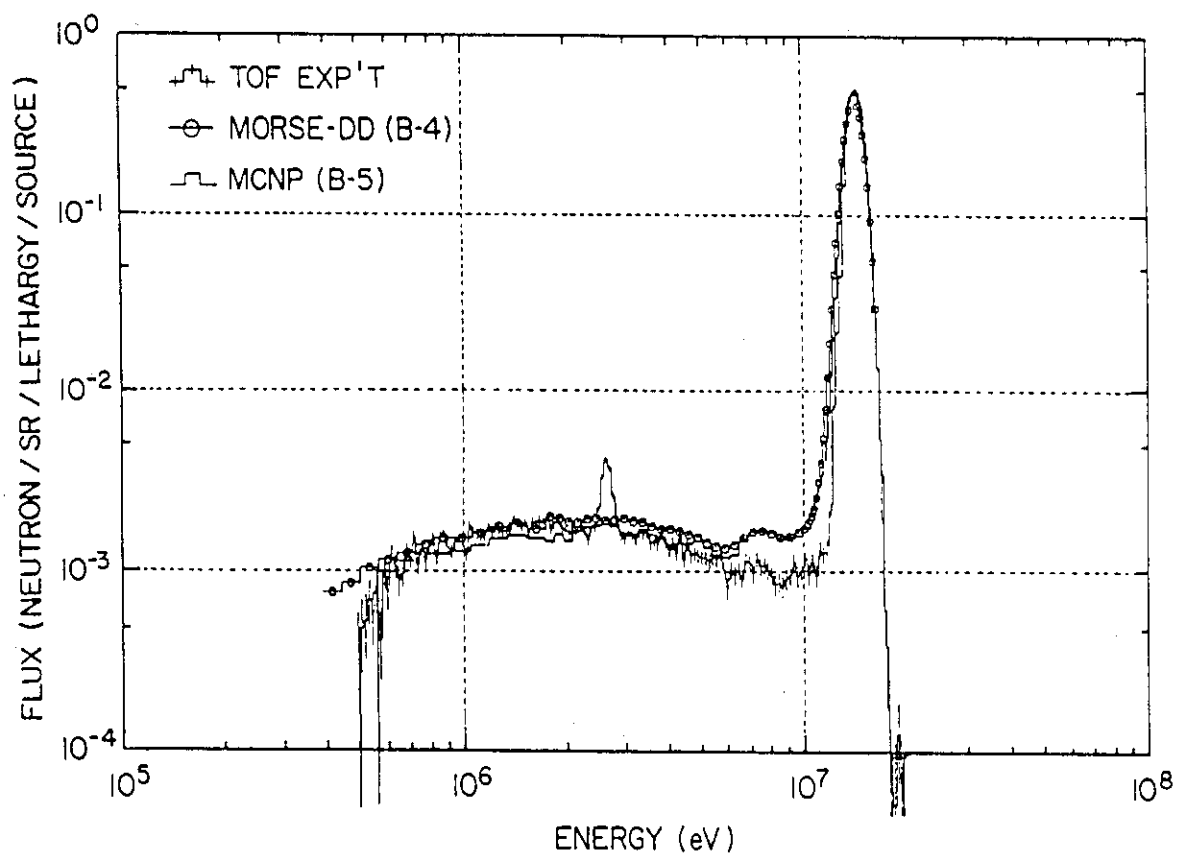


Figure III.8 Comparison of neutron spectra from RNT between calculation and measurement by the TOF method, with collimator, $L = 17.445$ m

The large discrepancy at energies near 10 MeV may be caused by the smearing process applied and/or the inadequate cross-sections used.

The accuracy of predicting the integrated fluxes is verified by examining the ratio of calculated to measured values (C/E), as shown in Table III.3. In the high energy region, ($E > 10$ MeV), the calculation agrees well with the measurements within the experimental errors for the TOF and the unfolding method. Note that the values obtained by the MCNP calculation is larger by $\sim 4\%$ than those obtained by JAERI. Neutrons with energies above 1.19 MeV are underestimated in the MORSE-DD calculations by $\sim 3\%$, but overestimated by $\sim 2\%$ in the MCNP calculations.

As mentioned above, two neutron source components were independently treated [the direct and indirect (room-returned) components] in the Monte Carlo calculations for the reference and the beryllium experiments (another calculational model was used in the first wall experiments, see Section II). We compared these neutron currents at the entrance to the experimental hole in Fig. III.9, as obtained by JAERI. We can see that the reflected neutrons are dominant below 1 MeV and have an essentially $1/E$ spectrum. On the other hand, neutrons that come directly from the RNT have a sharp peak around 14 MeV and rapidly decrease below 1 MeV. The neutron spectra measured at the entrance of the experimental hole with or without a shadow shield, by using an NE213 detector are helpful to evaluate the calculational accuracy of each source component above 1 MeV. A comparison is made in Fig. III.10, where we can see a good agreement between the measured and calculated spectra for both direct (without a shadow shield) and room-returned (with a shadow shield) components above 1 MeV. In the measurement, the NE213 detector was placed at a distance $Z = 248$ cm from the RNT and at the center of the experimental hole (with no Li_2O assembly in place).

In the above NE213 measurements, three cases were investigated by the U.S. One of the measurements was taken without any shielding material between the RNT and the detector. In the other two experiments, a small bar, and then a small and heavy-shadow shield, were placed on the central axis of the experimental port between the D-T source and the experimental hole, as was shown in Fig. III.10.

For the case where no shield was used, the MCNP modeling was the same as what had been modeled in the TOF without-collimator case. The only difference was the location of the detector. For the small-bar case, the reverse treatment of modeling TOF with-collimator was adopted. The tally to the point estimator was taken from all but the contribution from the direct fusion neutron source and the small intersectional zone. The diameter of the zone in this modeling was taken to be 7 cm. When the heavy-shadow shield was placed on the central axis of the experimental port, contributions from the whole target assembly and from a portion of the room to the detector were shielded out. In this case, approximation in the modeling by simply excluding the tally of the whole target assembly to the point estimator is not realistic. A separate calculation, including the heavy shield geometry and material in the modeling, was made. A similar smearing process using a Gaussian distribution, as in the TOF case, was

Table III.3 Comparison of Source Neutron Spectrum with Measurements (C/E)

Energy Range	T.O.F.(a)		NE213(b)	
	JAERI(c)	U.S.(d)	JAERI	U.S.
> 10 MeV	0.984	1.024	1.04(e) ($\pm 7\%$)(f)	1.08
> 1.19 MeV	0.968	1.023		

(a) without collimator

(b) (without collimator) - (with heavy shield)

(c) MORSE-DD calculations

(d) MCNP calculations

(e) $E > 8.3$ MeV

(f) experimental error

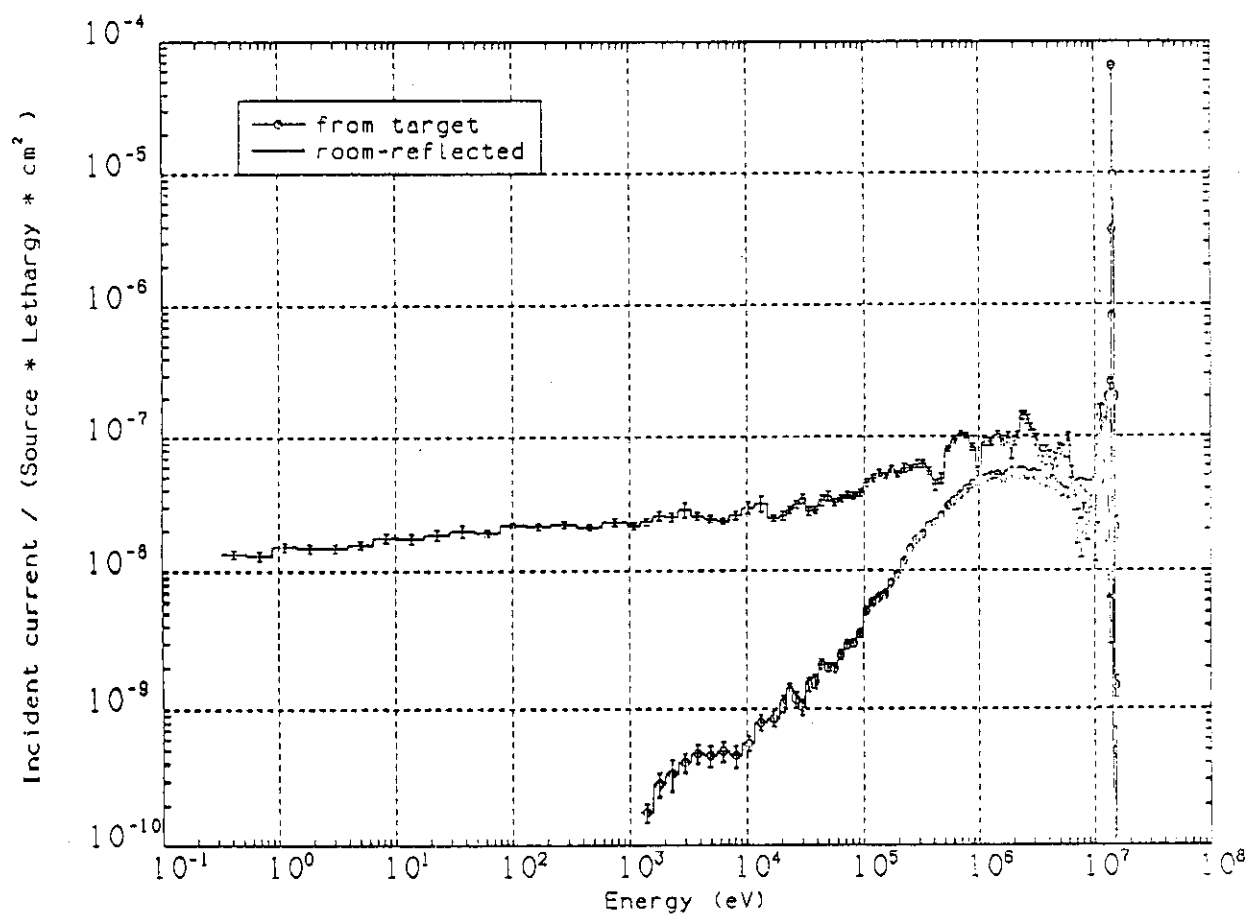


Figure III.9 Comparison of incident neutron current into the entrance of experimental hole

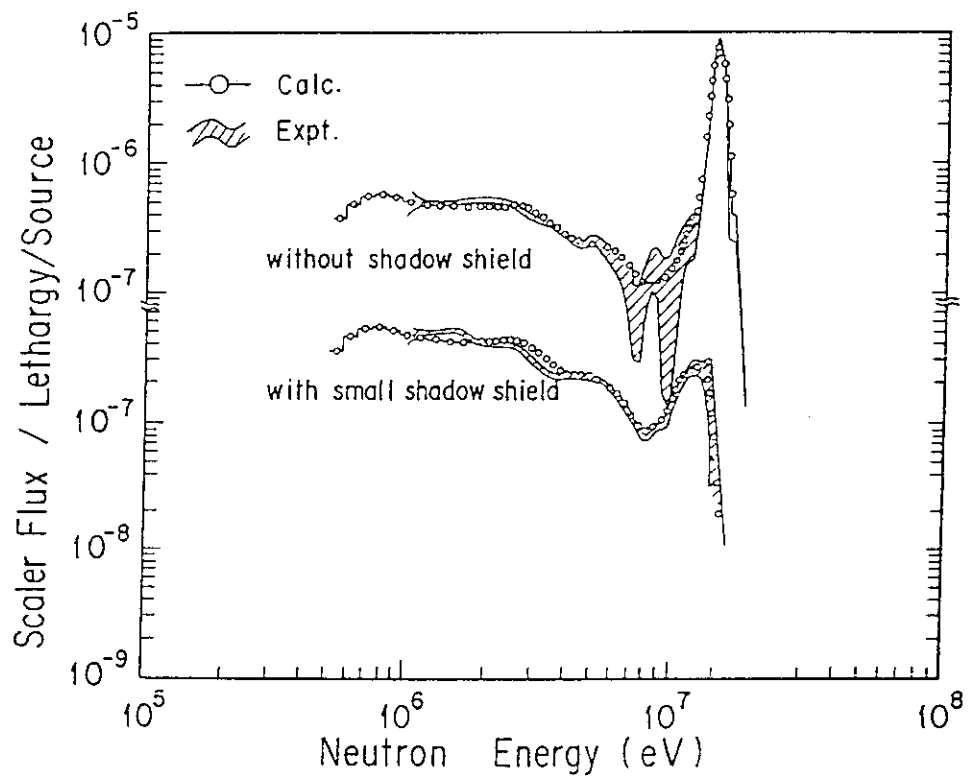


Figure III.10 Measured and calculated neutron spectra on the entrance of experimental hole with and without shadow shield (JAERI)

applied in the MCNP calculated spectra. Instead of using the resolution function, the energy error at each group, $\sigma(E)$, was obtained from the measured window values.

Comparisons of calculated spectra with measured results for NE213 cases are shown in Figs. III.11 to III.13. For all three cases, the agreement is reasonably good. The peak of DD fusion neutrons is not shown in the measured spectra due to a lower resolution of the NE213 detector. Lower values at about 0.9 to 2 MeV of the calculated spectra by the MCNP code are consistent with the results obtained in the TOF comparisons. In Fig. III.13, the MCNP evaluated spectrum is higher than the NE213 measurements at energies between 2 and 4 MeV. This is because a shadow cone, with a volume smaller than that of a shadow shield, was modeled. Extra contributions from the room-returned neutrons results in this discrepancy.

Due to the importance of the low-energy neutrons to the tritium production rate from the Li-6 inside the test assembly, and the limitation on the energy range of the NE213 detectors below 1 MeV, a proton recoil counter (PRC) provided by Argonne National Laboratory (ANL) was used to measure the low-energy spectrum in the energy range few KeV to 1 MeV. A PRC was placed at $Z = 248$ cm on the central axis of the experimental port (same location where the NE213 measurements were separately performed). Four cases were studied. These were combinations of with/without Li₂O assembly inside the experimental cavity, and with/without a specially designed shadow cone to shield the whole target assembly.

Figure III.14 shows the spectra in the case with the Li₂O assembly in and without a shadow cone in front of a detector. The calculations shown were performed by JAERI using the DDL/J3P1 library. The calculated values, using the multi-group set by MORSE-DD, were smeared using the same resolution as the NE213 detector although it is wider than that of the proton recoil counter; hence, a fine structure cannot be found in the calculated curve. The agreement between measurements and calculations is fairly good, but there are some discrepancies around several MeV, and at 1 MeV. The discrepancy at several MeV could be caused by the neutron component reflected by the Li₂O assembly. Below a few KeV, the PRC has large experimental errors. When a shadow cone was placed in front of the detector, only the reflected component was accounted for. Fig. III.15 shows the spectrum in this case. Except for the two dips that appear around 8 MeV and at 4 MeV, the calculated and measured spectra agree quite well. The discrepancy around 8 MeV is not significant because of the large statistical error in the measurement at that energy. The discrepancy at 4 MeV may be caused by the inadequate cross-sections of the composing materials of concrete, such as oxygen, and/or the statistical errors in the calculations.

The calculated and measured spectra without the assembly and the shadow cone are shown in Fig. III.16. The measured values are lower than the calculations by a few tens percent below 100 KeV. One possible cause of this discrepancy is that the MORSE-DD calculations underestimate the reflected neutron component by the concrete wall but overestimate the back-scattering component by the Li₂O assembly.

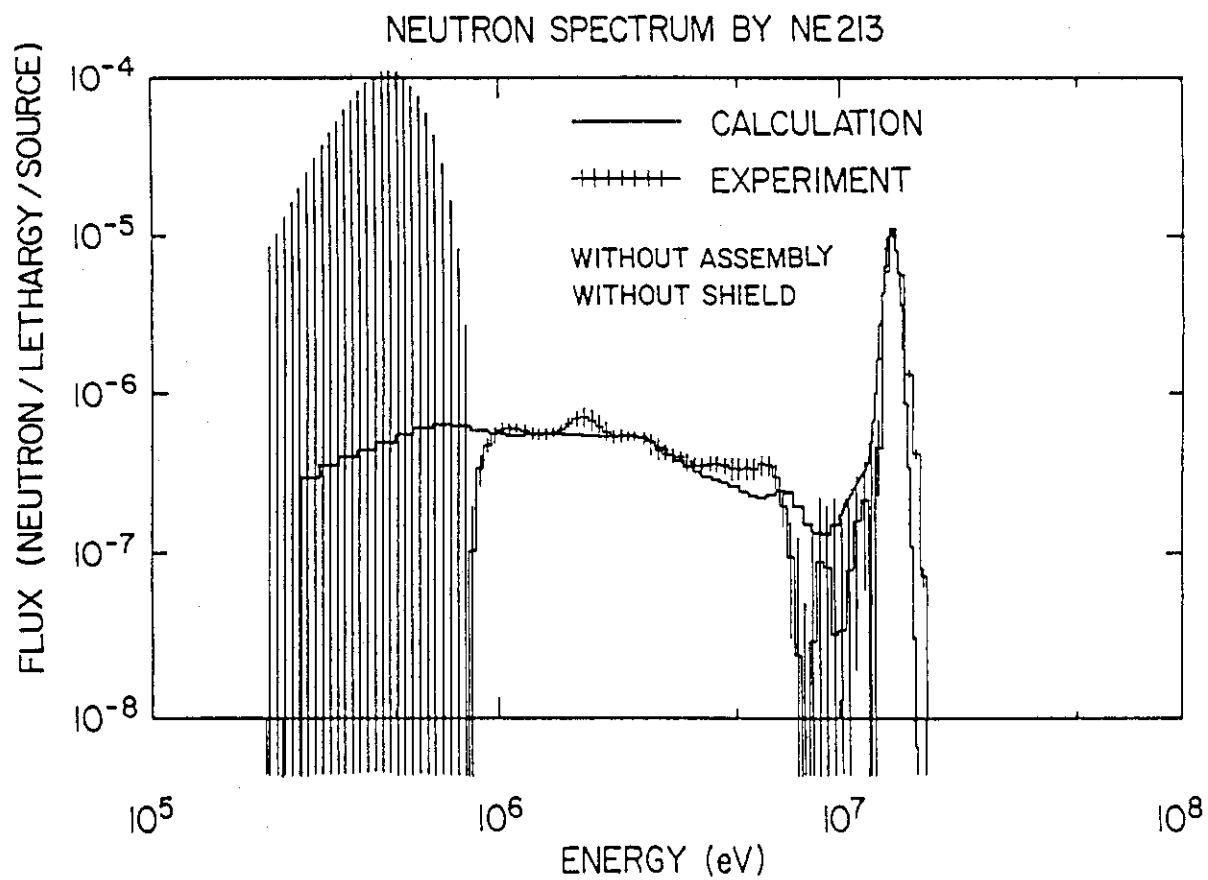


Figure III.11 Measured and calculated neutron spectrum on the entrance of experimental hole
(MCNP calculation, U.S.)

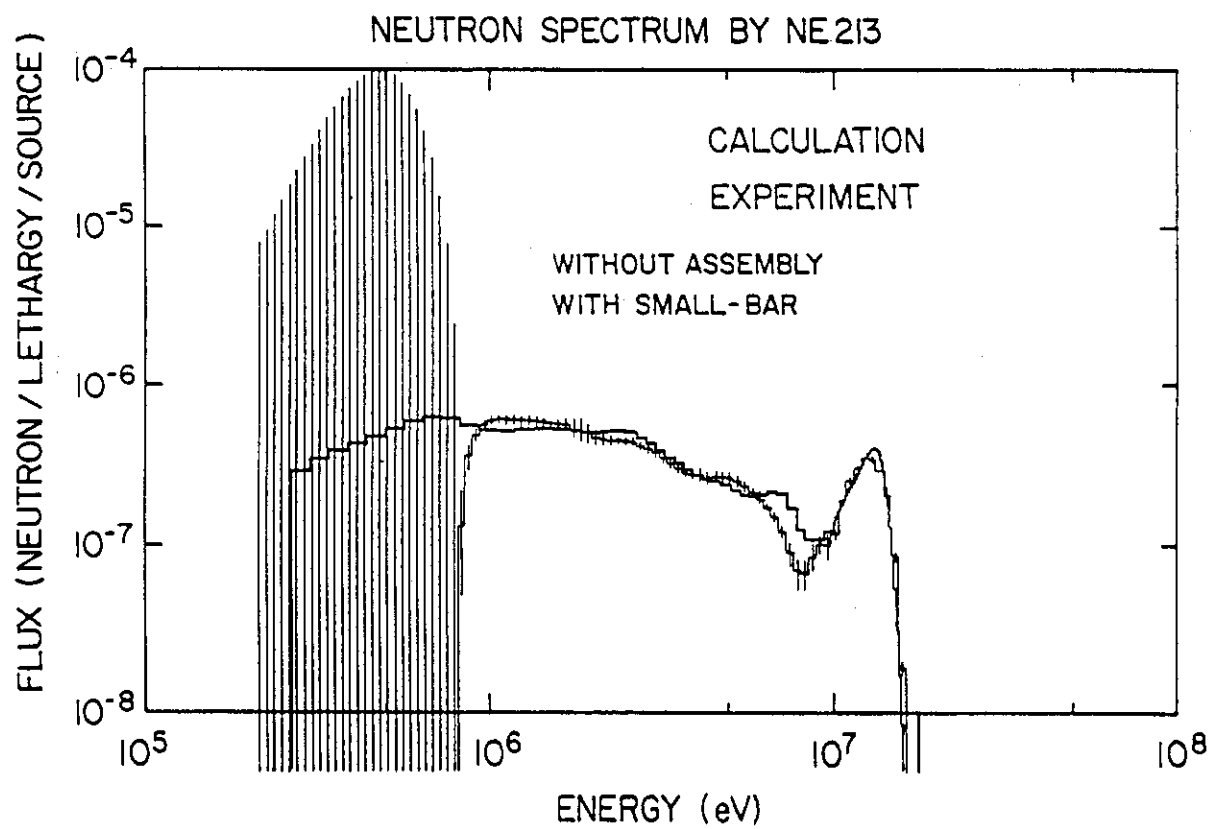


Figure III.12 Measured and calculated spectrum on the entrance of experimental hole with a small-bar between RNT and experimental hole (MCNP calculations, U.S.)

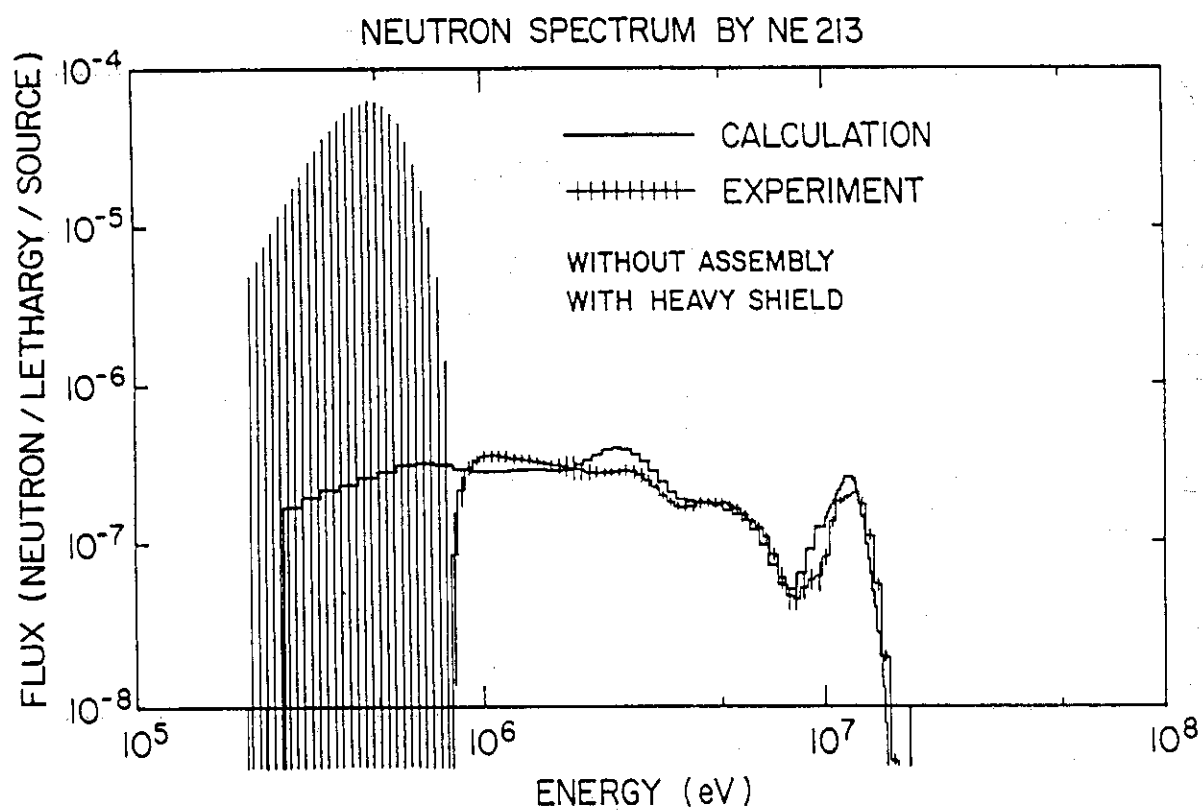


Figure III.13 Measured and calculated spectrum on the entrance of experimental hole with a heavy shield between RNT and the experimental hole (MCNP calculations, U.S.)

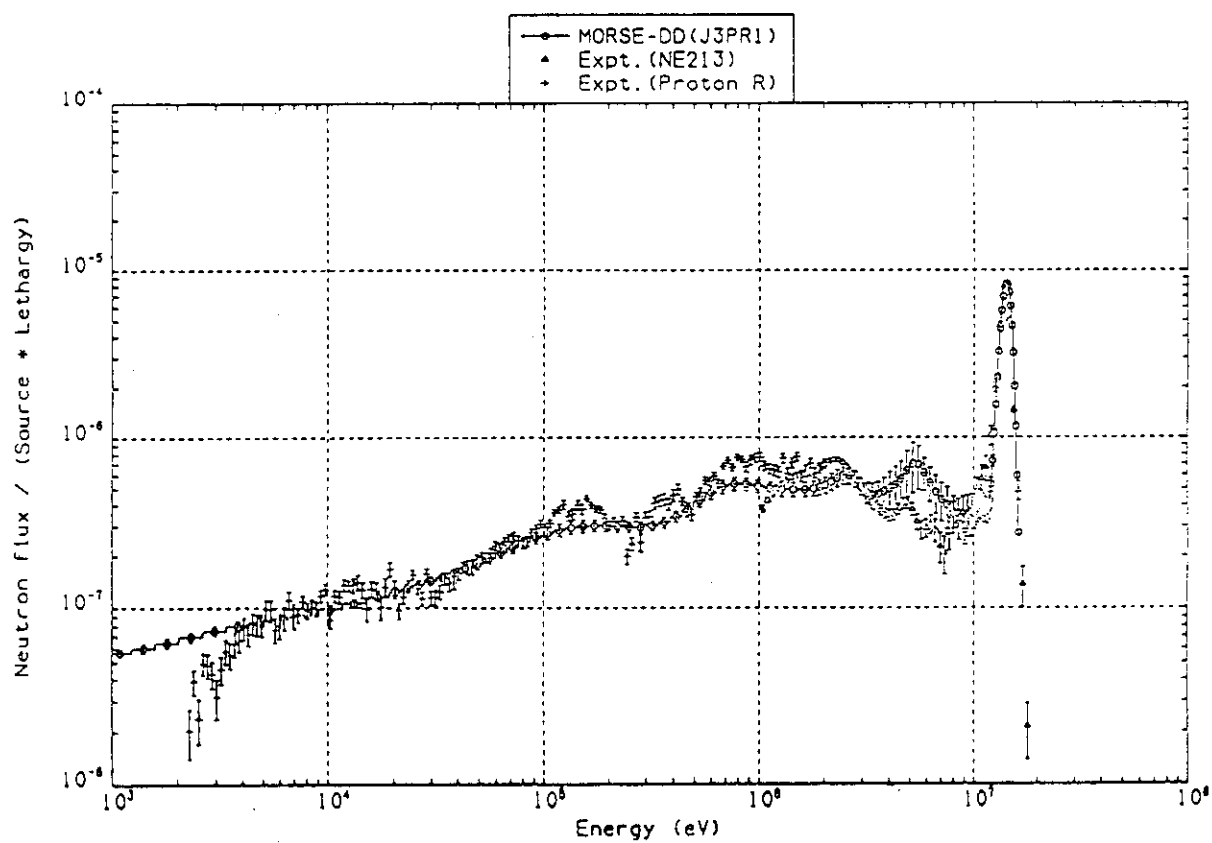


Figure III.14 Comparison of neutron spectra in front of the Li_2O assembly and with shadow cone out (JAERI)

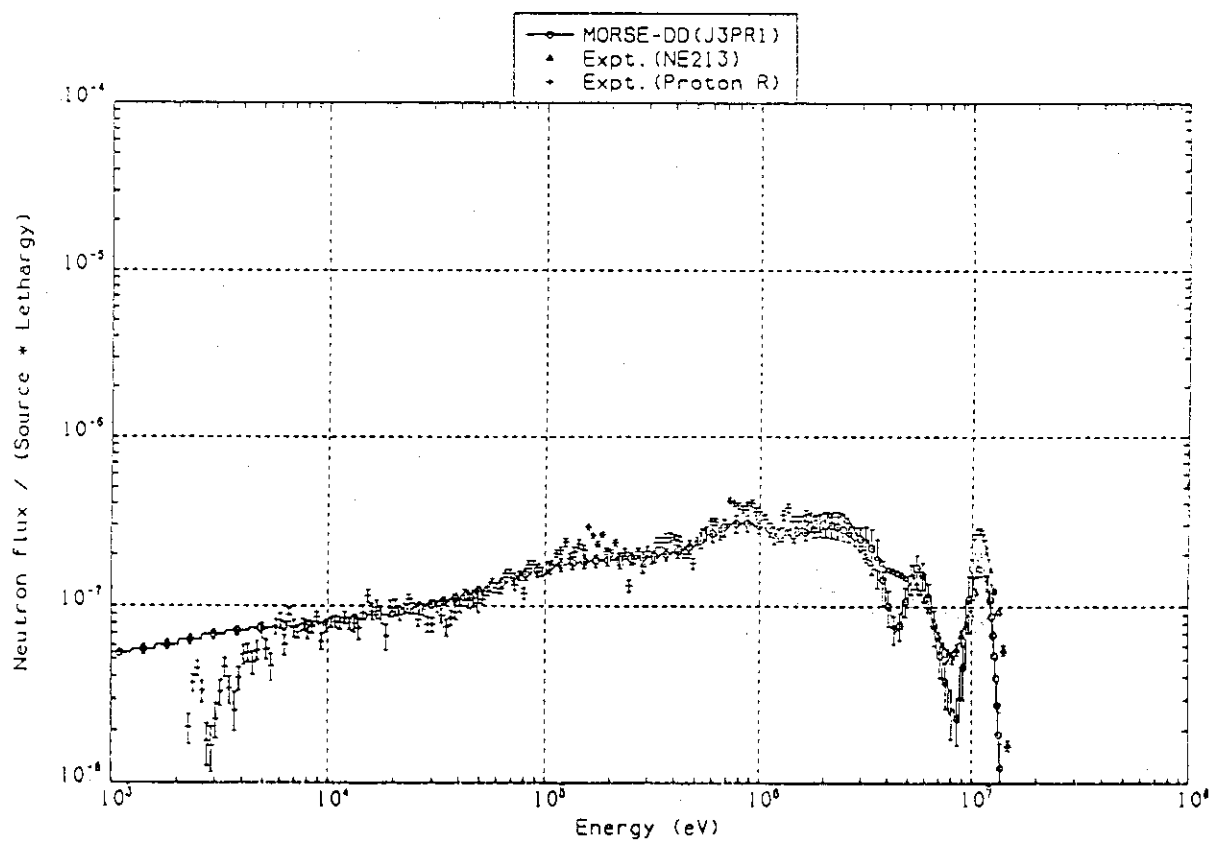


Figure III.15 Comparison of neutron spectra in front of the Li_2O assembly contributed from room returned neutrons (shadow cone in place, JAERI)

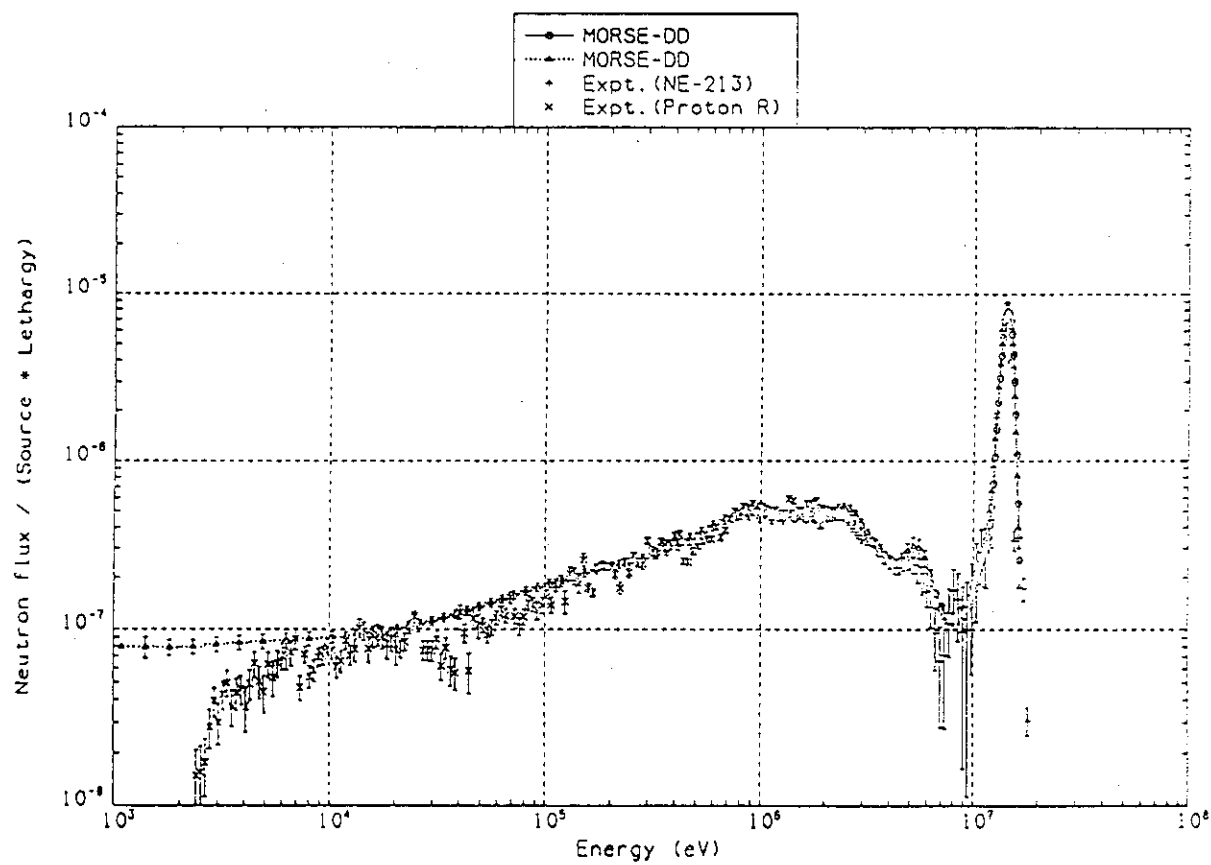


Figure III.16 Comparison of neutron spectra in front of experimental hole without the Li_2O assembly (assembly out, shadow cone out, JAERI)

These differences were cancelled in the spectrum shown in Fig. III.14. However, in order to confirm such an interpretation, a more elaborate investigation would be necessary. For instance, the fine structure that appears in the measured values in Fig. III.16 is not necessarily reasonable.

In the U.S. calculations performed by UCLA for the PRC experiments, the detailed geometry of the shadow cone was used in the MCNP Monte Carlo calculations along with the RMCCS pointwise library based on ENDF/B-V. Figures III.17 to III.20 show the comparisons of calculated spectra to measured spectra by the PRC and NE213 detectors. The PRC measured spectra are combined with the NE213 measured spectra for all four cases. The NE213 window values for the two cases where the Li_2O assembly was loaded into the experimental cavity were not used to smear the calculated values. However, the calculated spectra for these two cases were smeared only for the PRC energy range. For the cases where the Li_2O assembly was removed from the experimental port, the window values for smearing the calculated spectra at $E > 1$ MeV were taken from the measurements of NE213 with the heavy-shadow shield discussed earlier. Although the geometry of the heavy-shadow shield was different from that of the shadow cone, the window values were approximately equivalent due to a similar shielding effect to the detector.

The two cases where the Li_2O assembly was loaded in the experimental port are shown in Figs. III.17 and III.18, without and with the shadow-cone, respectively. In these two figures, the MCNP calculations are only shown within the PRC range (below 1 MeV). Also shown in Figs. III.17 to III.20 are the MORSE-DD results with the DDL/B4 library. Since the detector was placed in front of the mouth of the experimental port, neutrons reflected by the Li_2O assembly affect the shape of the spectrum, as was shown in Figs. III.14 and III.16. Large computational error was also introduced by these back-scattered neutrons. Large computation time is necessary to reduce the statistical errors associated with these slow neutrons. At energy value of about 250 KeV, the calculated characteristic dip due to resonance absorption in Li-6 agrees with that of the measurement in both Figs. III.17 and III.18. However, in JAERI's calculation, this dip was not shown (see Figs. III.14 and III.15). This is due to the resolution used by JAERI. In JAERI's calculation, the wide resolution of the NE213 detectors was used, so the dip becomes smooth. (The resolution of PRC was not used in the calculations shown in Figs. III.14 to III.16.) Without the shadow cone, and in the PRC energy range, the statistical errors by the MCNP calculated spectrum are still large at energy ranges 7 KeV - 50 KeV and above 100 keV. Nevertheless, in the other energy groups the statistical errors overlap with the experimental errors. When the shadow cone is included, the calculated spectrum is consistent with measurements at energies above 30 KeV. At energies lower than 30 KeV, the MCNP calculated spectrum is high, and the statistical error is large while the MORSE-DD results agree with the measurements above several KeV. Note also that the MCNP values and their statistical errors shown in Figs. III.17 and III.18 are larger than those obtained by the MORSE-DD calculations shown in Figures III.14 and III.15.

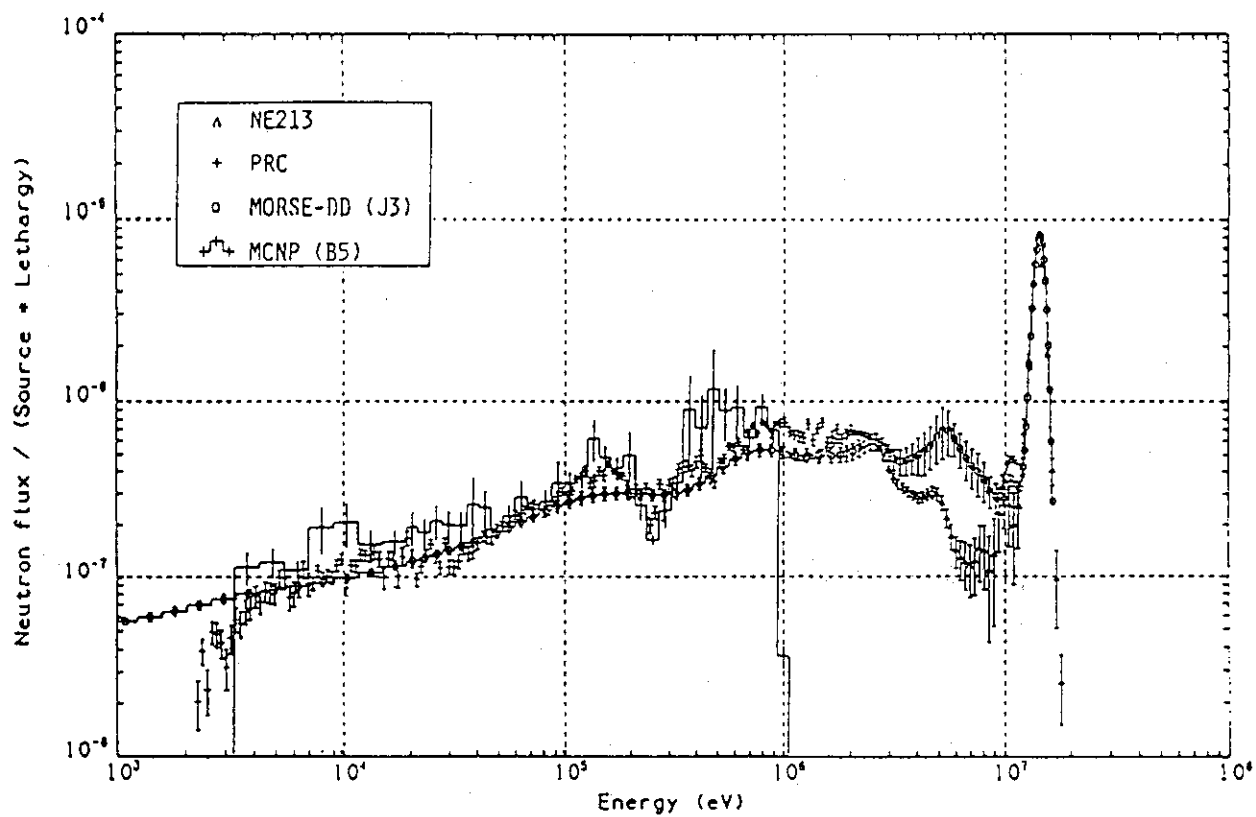


Figure III.17 Comparison of neutron spectra in front of the Li_2O assembly and with the shadow cone out (U.S.)

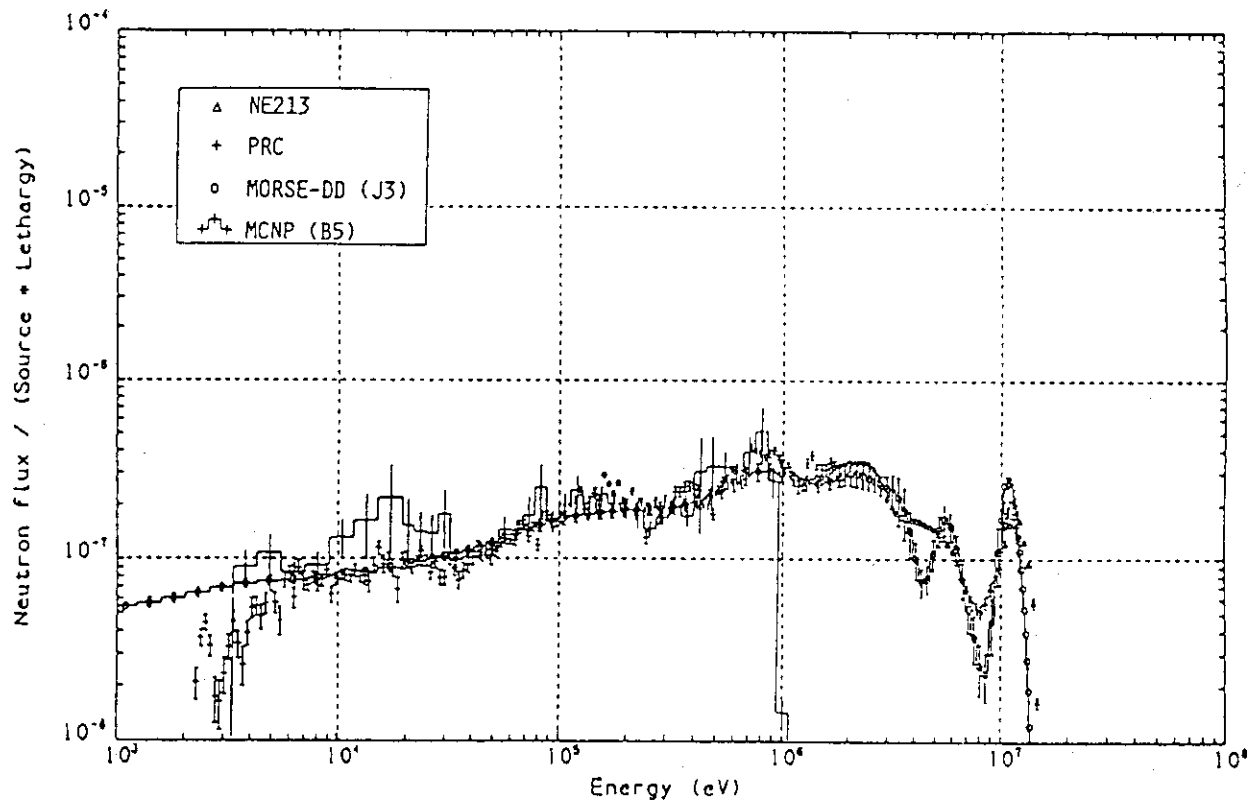


Figure III.18 Comparison of neutron spectra in front of the Li_2O assembly contributed from room returned neutrons (shadow cone in place, U.S.)

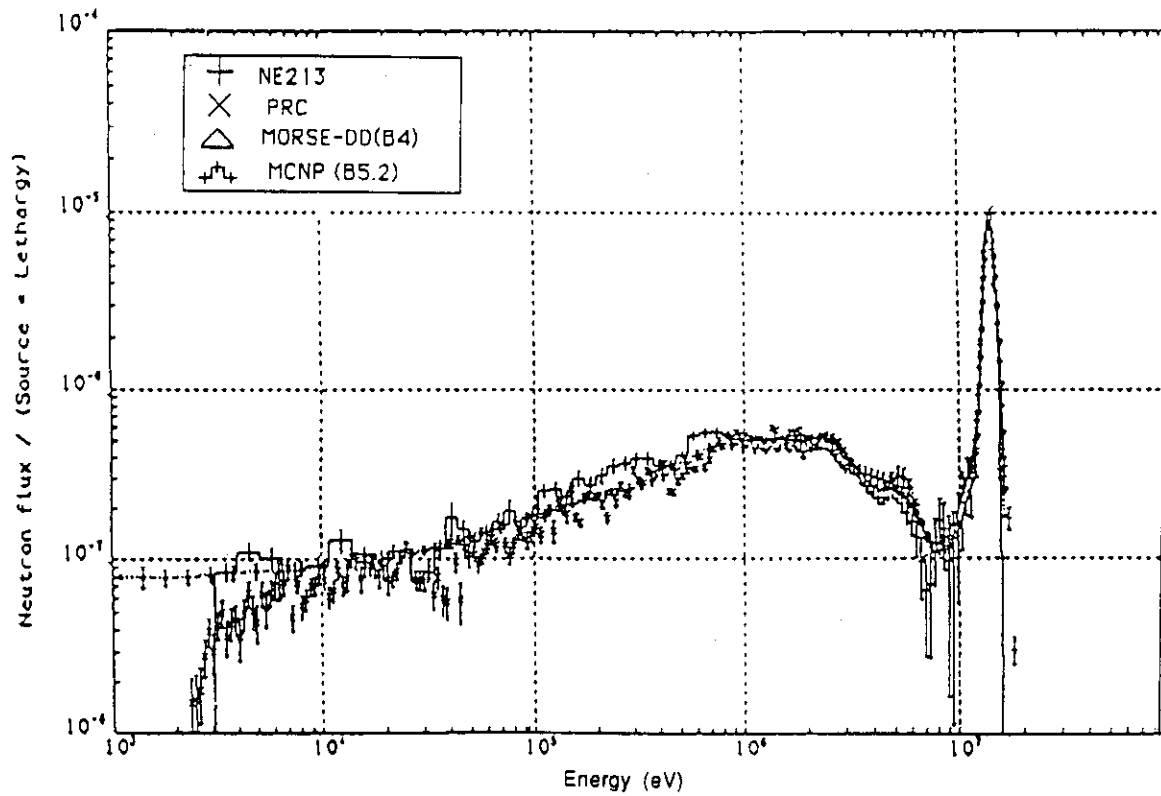


Figure III.19 Comparison of neutron spectra in front of the experimental hole without the Li_2O assembly, (assembly out, shadow cone out, U.S.)

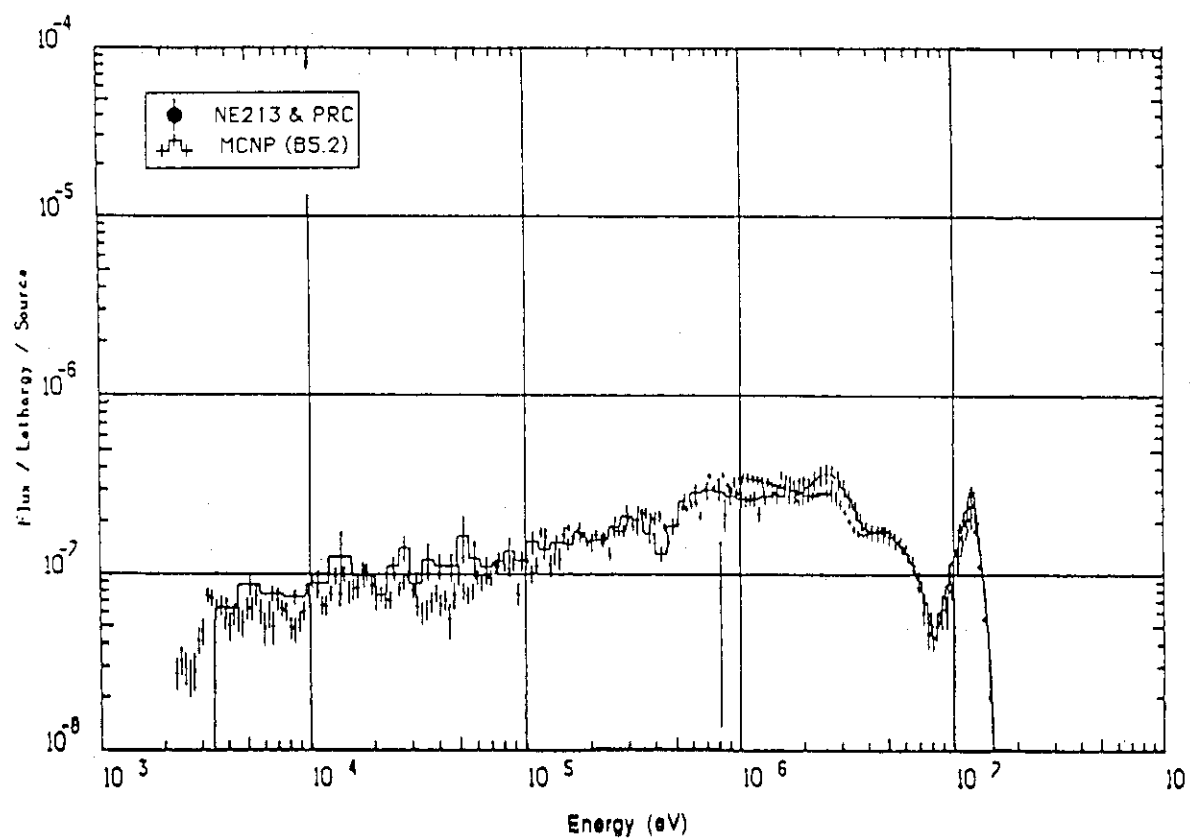


Figure III.20 Comparison of neutron spectra in front of the experimental hole without the Li_2O assembly (assembly out, shadow cone in, U.S.)

Without the Li_2O assembly and the shadow cone, the MCNP calculated spectrum has a trend very similar to the measurements in both the NE213 and the PRC energy ranges, as shown in Fig. III.19. However, in the PRC energy range, the calculated spectrum by MCNP is slightly larger than measurements (better agreement than in Fig. III.17). As was noted earlier, it seems that the back-scattered low-energy neutrons by the Li_2O assembly, when it is placed in the experimental hole, introduce large statistical error into the Monte Carlo calculations, as was noted in Fig. III.17. In the case where the shadow cone was used, the direct contribution to the detector is shielded out. The spectrum at energies greater than about 300 KeV is drastically reduced, as seen in Fig. III.20. The calculated spectrum has a good agreement with the measured values except in the energy range 30 to 60 KeV.

III. 1.3 Source Characterization by Integral Quantities (Flux Mapping)

Neutron field characteristics at the front surface of the Li_2O assembly have also been investigated by measuring several integral quantities. These include mapping data of integrated flux measured by an NE213 detector and several activation foils placed at various locations on the surface of the Li_2O assembly (see Volume I).

Fig. III.21 shows a horizontal distribution of an NE213 response, as obtained by JAERI, across the entrance of the experimental hole at $y = 0$, $z = 0$ (index "x" represents horizontal distance, index "y" represents vertical distance, and index "z" represents depth, all measured from the center of the front surface of the Li_2O assembly).

Though the calculations (MORSE-DD) give larger values by a few percent, the spatial shape is well predicted as shown in Fig. III.21. The values in the vertical direction $y = \pm 18$ cm at $x = 0$, (shown in the figure) agree with those at $y = 0$ cm. It was also shown that the neutron flux above 5 MeV is larger at locations $\theta < 80$ (x-distances are +ve) than the flux at locations $\theta > 80$ (x-distances are -ve) on the horizontal axis. However, on the vertical axis (y-direction), the neutron flux distribution is flat within 1%. This demonstrated the asymmetry of the neutron field in the horizontal direction as discussed in subsection III.1.2. This feature was also observed in the flux mapping experiments using the activation foils (see below) placed at the horizontal and vertical axes.

The activation reactions considered are $^{27}\text{Al}(n,\alpha)^{24}\text{Na}$, $^{58}\text{Ni}(n,2n)^{57}\text{Ni}$, $^{197}\text{Au}(n,2n)^{196}\text{Au}$, and $^{197}\text{Au}(n,\gamma)^{198}\text{Au}$. The first three reactions have threshold energies at about 4.9 MeV, 13 MeV, and 8.6 MeV, respectively. The last reaction has large resonance absorption cross-section at low-energy regime (less than 10 eV). Foils were placed in the horizontal and vertical directions on the surface of the Li_2O assembly at a distance of 235 cm from the RNT. In JAERI's calculation, the MORSE-DD code was used along with the DDL/J3P1 and the DDL/B4 libraries, respectively. As for the activation cross-sections, JAERI used those compiled from ENDF/B-IV. The U.S. used the MCNP code along with the RMCCS library. In order to cover the whole cross-section table length in the MCNP calculations, the cutoff energy was set at 10^{-10} MeV. The calculated fluxes were then multiplied by the activation cross-section

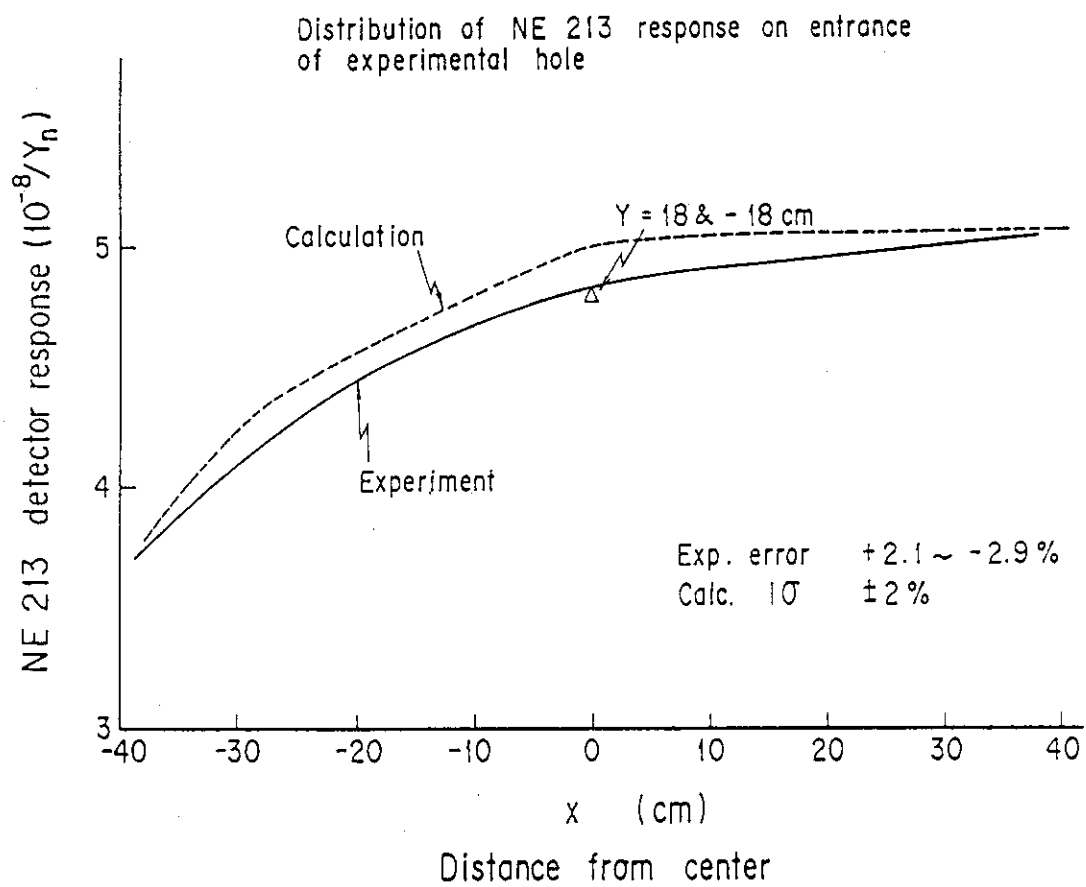


Figure III.21 Horizontal distributions of NE213 detector response

data for different reactions. The activation cross-section data bases applied in the MCNP calculation were the ENDL-73 library for ^{56}Ni , and the ENDF/B-V library for all other reactions.

The horizontal distribution of the reactions considered and the ratios of the calculated to measured values, C/E, are shown in Figs III.22 to III.29. As can be seen from the figures, both the calculated and measured values for all the threshold reactions are larger at the positive x direction ($\theta < 80^\circ$). This trend is the same as the one observed in one NE213 flux mapping. Note that the high reactions are almost caused by the direct neutrons coming from the RNT, which have an angular/energy dependence at the front surface of the Li_2O assembly in the horizontal direction (see Figures III.2 and III.3). For the $^{197}\text{Au}(n,\gamma)$ reaction, the relative standard deviations at all locations and the self shielding factor are large due to its high resonance cross-section peak at very low energy, as can be seen from Table III.4 that shows the MCNP calculation result. The measured $^{197}\text{Au}(n,\gamma)$ reaction rate was not corrected for the foil self-shielding effect although the thickness of foils are relatively large. Thinner gold foils should be used in future experiments. This reaction requires longer computational time to obtain a reasonable standard deviation in the calculations. Note also from this table that the standard deviations for all other reactions are within 3%. Although the calculated distribution for the $^{197}\text{Au}(n,\gamma)$ reaction is about three times as large as the measured values, the trend of both results is similarly flat. This comparison demonstrates that the distribution of the low-energy component of background flux in the horizontal direction is approximately uniform at the front surface of the experimental port.

For the $^{197}\text{Au}(n,2n)$ reaction rate shown in Fig. III.22, the measurements and the calculations agree within 10%. In JAERI's calculations, the DDL/B-IV library shows slightly better agreement as compared to the results obtained by the DDL/J3P1 library. The MCNP results with the RMCCS library are larger by $\sim 5\text{--}8\%$ than the MORSE-DD results and the C/E values vary between 1.03 and 1.13 (see Fig. III.23). The results for the $^{58}\text{Ni}(n,2n)$ reaction rate are presented in Figs. III.24 and III.25. The calculations performed by JAERI give consistently smaller values by about 10% as compared to the measurements at all locations. This is caused by the underestimation of the $^{58}\text{Ni}(n,2n)$ cross-section used by JAERI. Recent measurement made at FNS⁽³⁰⁾ showed larger values for that cross-section. However, in the MCNP calculation, the C/E values for the $^{58}\text{Ni}(n,2n)$ reaction rate is 0.91 - 1.00, as shown in Fig. III.25. Note that the cross-section values used in this case are obtained from the ENDL-73 activation cross-section library.

The results for the $^{27}\text{Al}(n,\alpha)$ foil activations are shown in Figs. III.26 and III.27. This reaction cross-section is usually adopted as a standard one, so its reliability is high. In the calculations, the results agree satisfactorily with measurements except for the range $15 < x < 25$ cm, especially at $x = 15$ cm (JAERI) and at $x = 25$ cm (U.S.). The reason for this discrepancy is not resolved but may be attributed to improper modeling of the RNT because such a deviation in the C/E values at $x > 15$ cm can

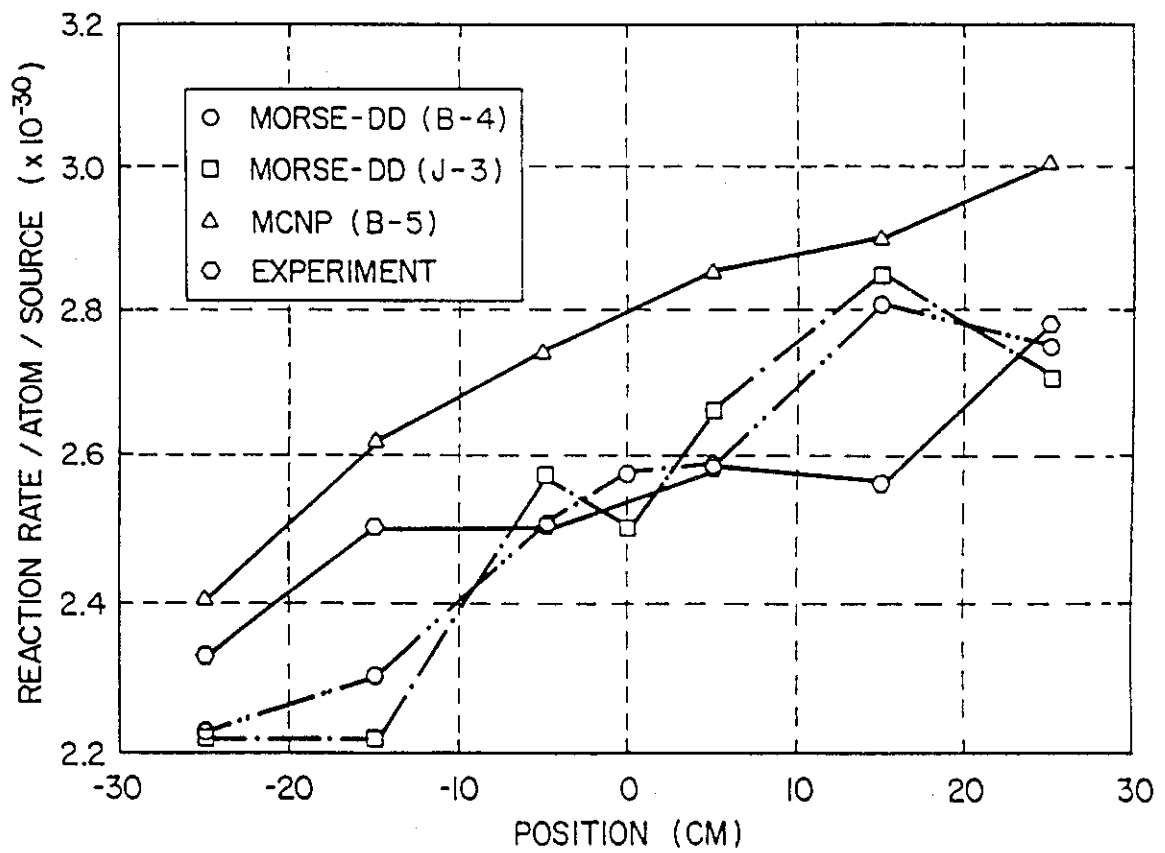


Figure III.22 Horizontal distribution of the $^{197}\text{Au}(n,2n)^{196}\text{Au}$ reaction rate on the front surface of the Li_2O assembly

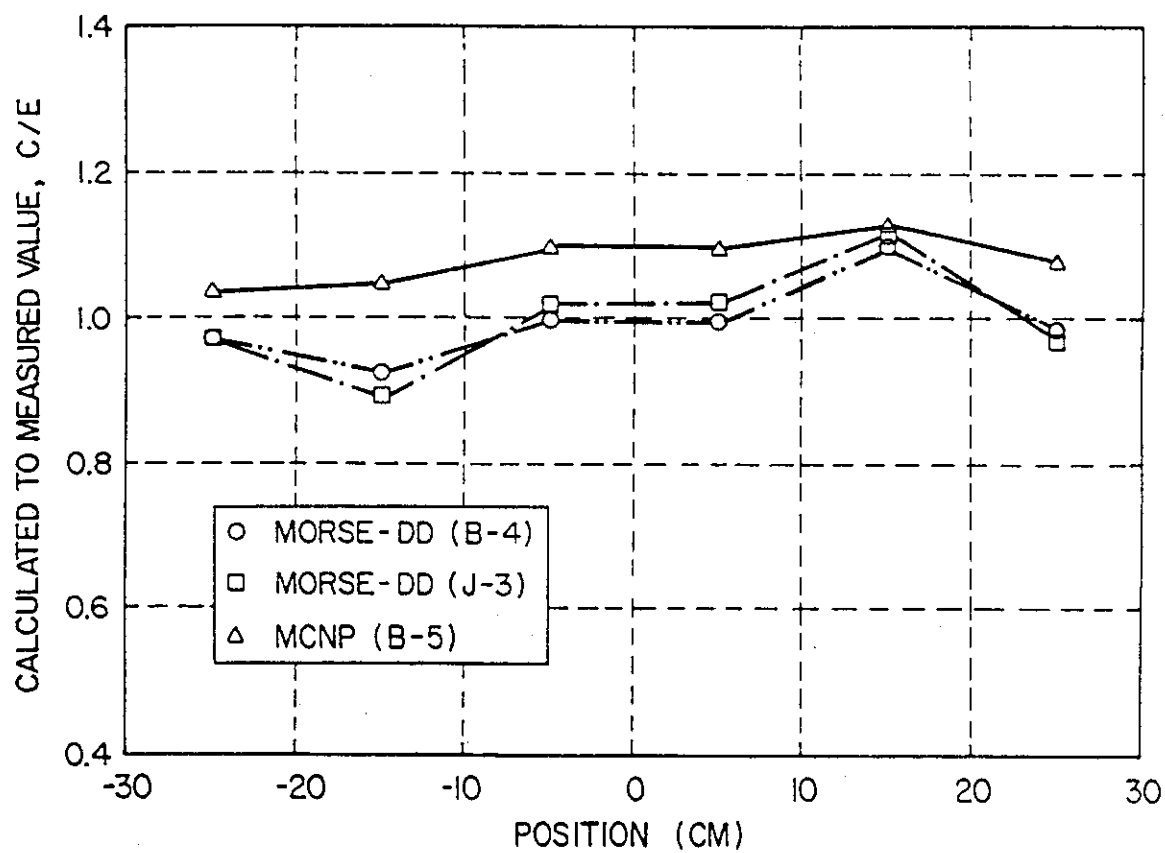


Figure III.23 C/E values of the $^{197}\text{Au}(n,2n)^{196}\text{Au}$ reaction rates on the front surface in the horizontal direction

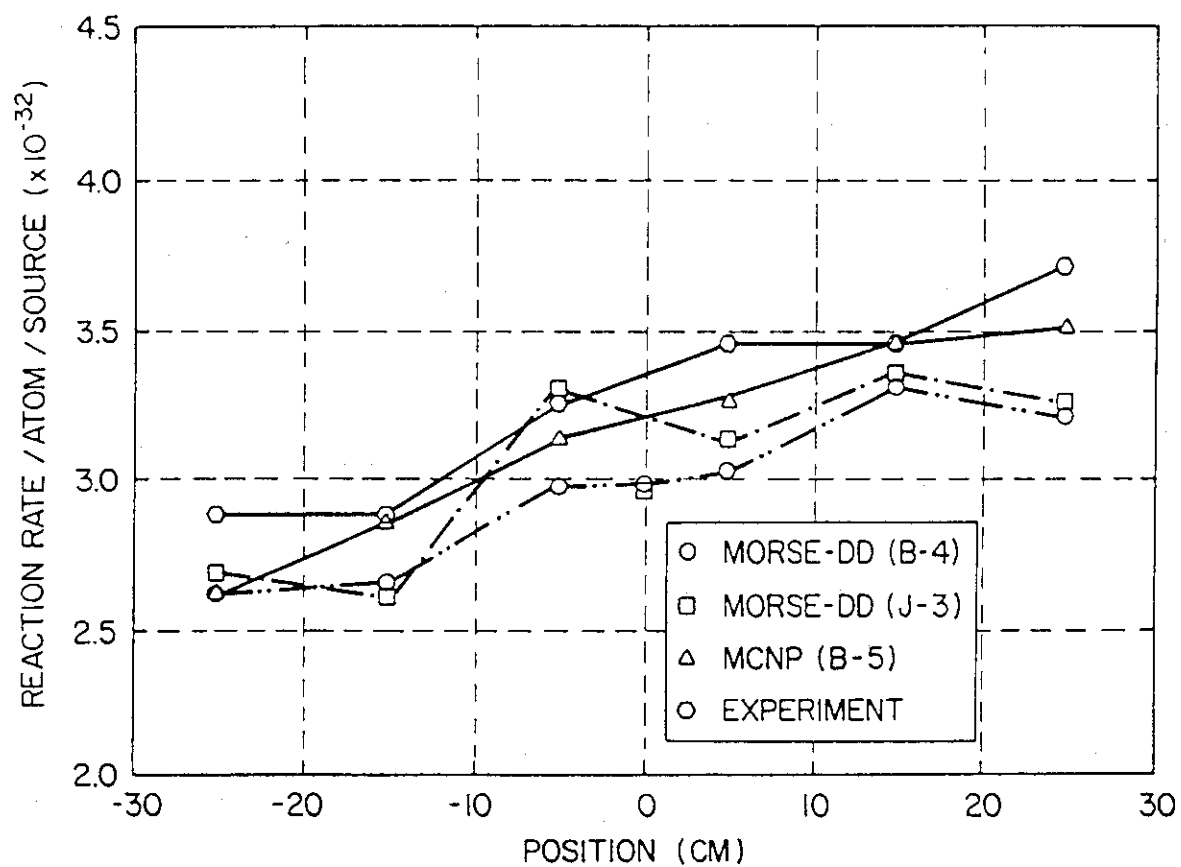


Figure III.24 Horizontal distribution of the $^{58}\text{Ni}(n,2n)^{57}\text{Ni}$ reaction rate on the front surface of the Li_2O assembly

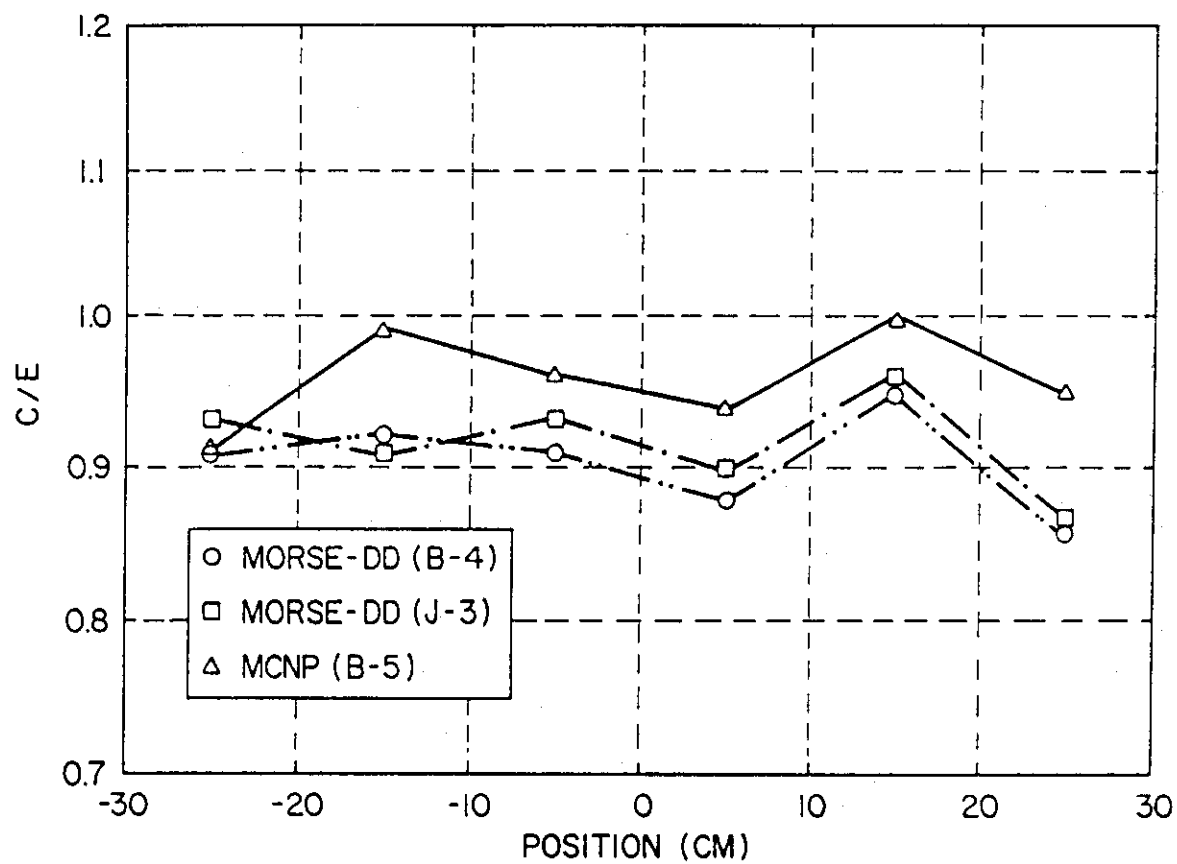


Figure III.25 C/E values of the $^{58}\text{Ni}(n,2n)^{57}\text{Ni}$ reaction rate on the front surface in the horizontal direction

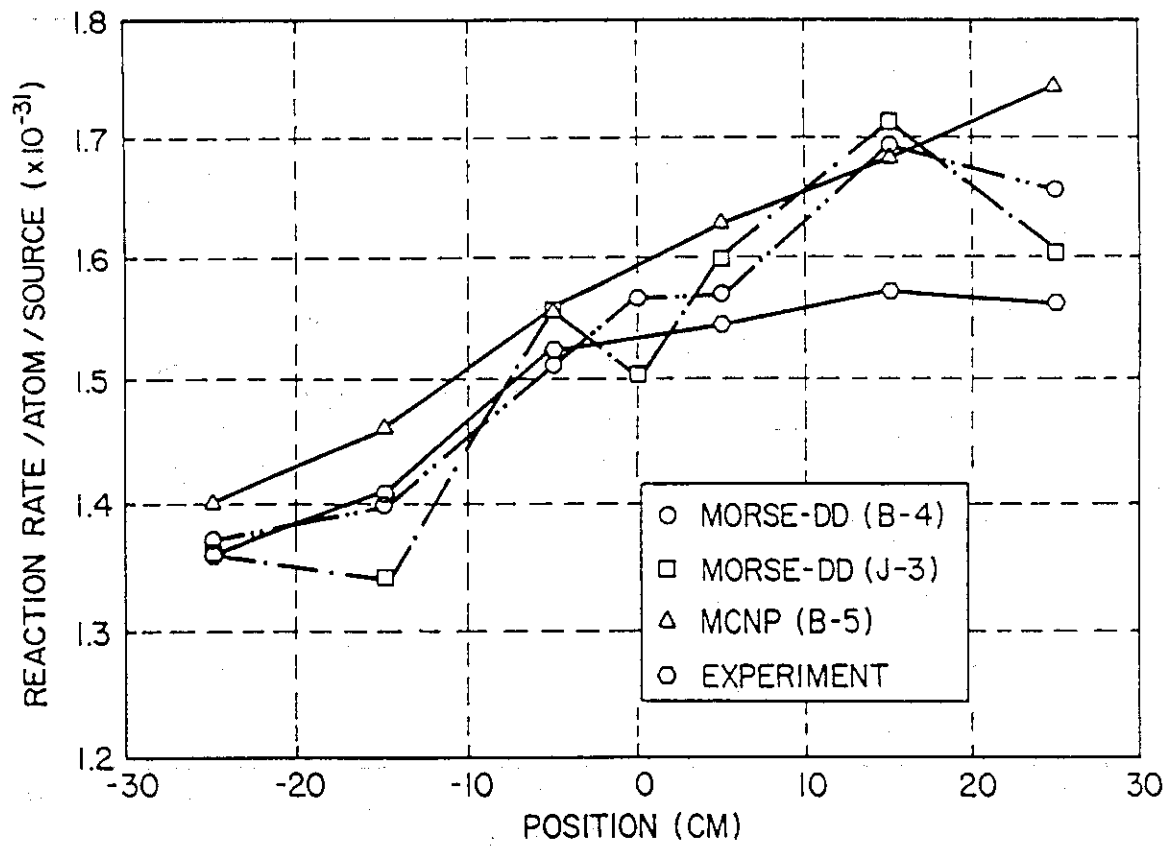


Figure III.26 Horizontal distribution of the $^{27}\text{Al}(n,\alpha)^{24}\text{Na}$ reaction rate on the front surface of the Li_2O assembly

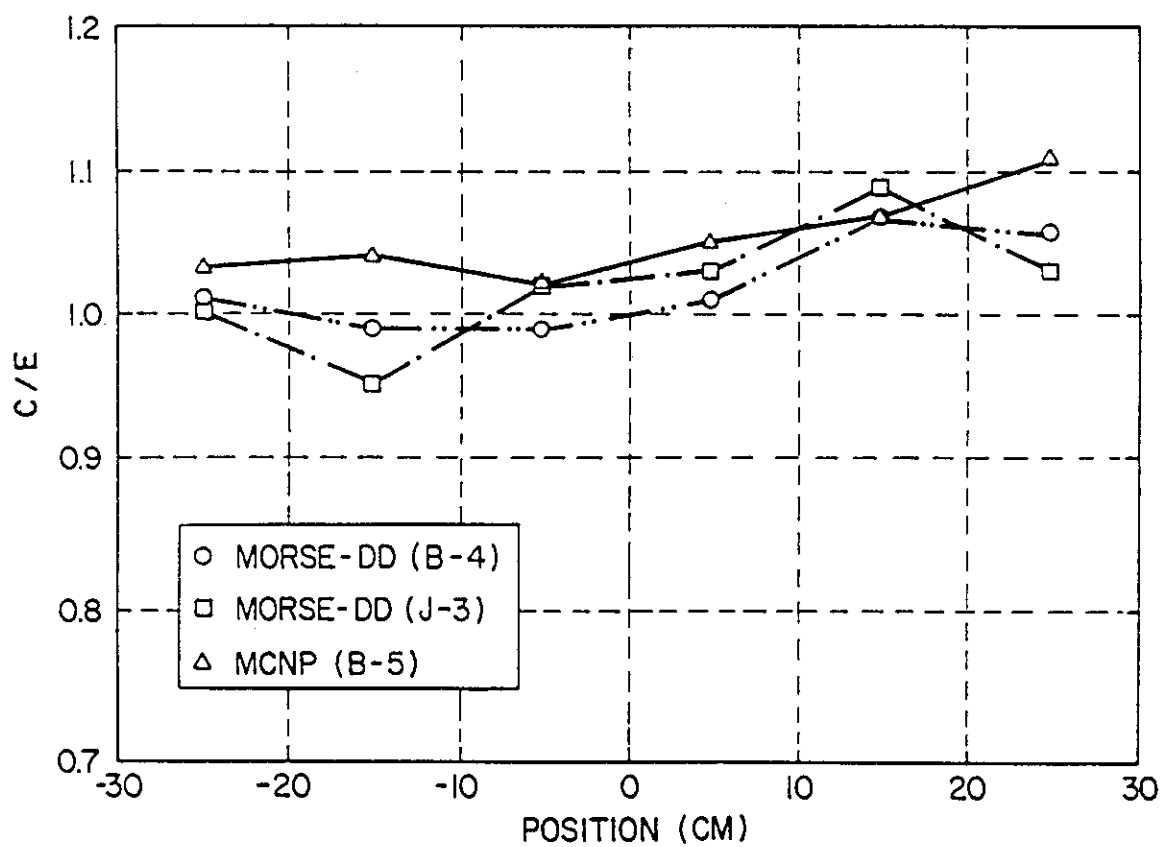


Figure III.27 C/E values of the $^{27}\text{Al}(n,\alpha)^{24}\text{Na}$ reaction rate on the front surface in the horizontal direction

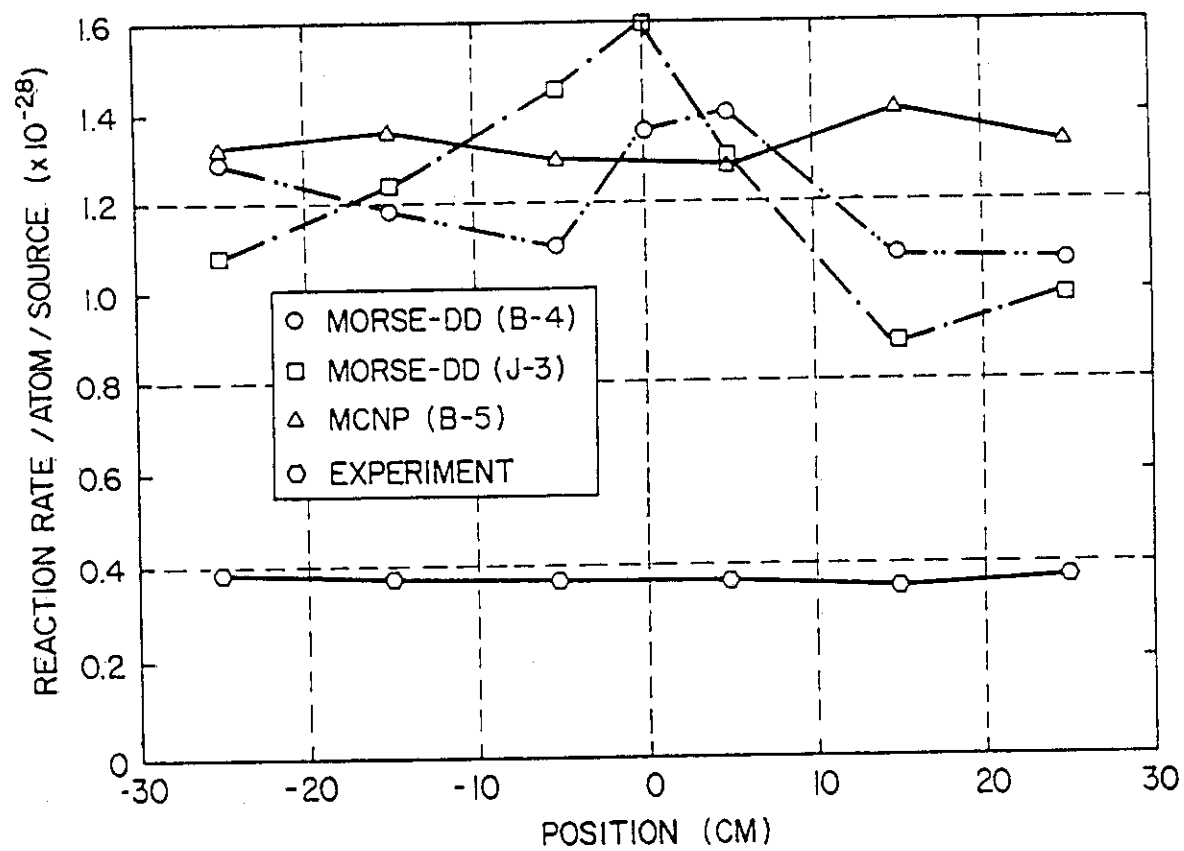


Figure III.28 Horizontal distribution of the $^{197}\text{Au}(n,\gamma)^{198}\text{Au}$ reaction rate on the front surface of the Li_2O assembly

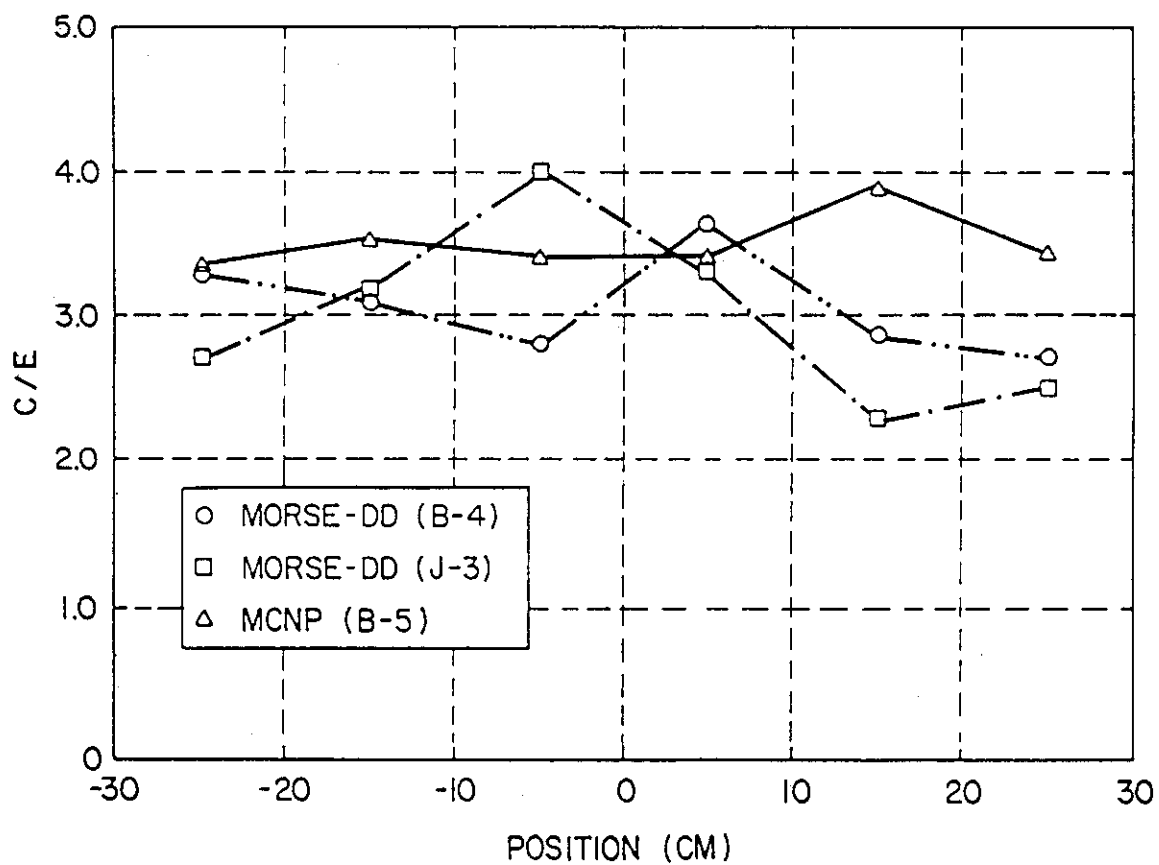


Figure III.29 C/E values of the $^{197}\text{Au}(n,\gamma)^{198}\text{Au}$ reaction rate on the front surface in the horizontal direction

be observed for all reactions. Note in particular that in the C/E distributions of the $^{27}\text{Al}(n,\alpha)$ and $^{197}\text{Au}(n,2n)$ reactions (Figs. III.26, III.27, III.22, and III.23), all the values are greater than unity in the U.S. calculations. This is qualitatively consistent with the C/E comparison of the integrated flux in the TOF experiments (see Table III.3). In the horizontal direction, the deviation of the C/E distribution for these two reactions increases in the positive x-direction. The overestimation in the direction of positive x's is possibly caused by improper RNT modeling and the nuclear data base of the RNT materials.

In Figs. III.30 to III.33, we show the results obtained from foils put in the vertical direction. In this direction, the direct source distribution is not distorted by the target structure at any particular range. The results are shown in Figs. III.30 and III.32 for the absolute values and in Figs. III.31 and III.33 for the C/E values, for the $^{58}\text{Ni}(n,2n)$ and $^{27}\text{Al}(n,\alpha)$ reaction rates. As can be seen from the former two figures, the reaction rates show flat distributions as discussed earlier. In JAERI's calculations, the C/E values for the $^{58}\text{Ni}(n,2n)$ reaction rate is about 10% smaller than unity, the same observation as in the horizontal case. For the $^{27}\text{Al}(n,\alpha)$ reaction rate, the C/E values are almost unity and the DDL/B4 library gives a larger fluctuation compared with the DDL/J3PI library. The C/E values for that reaction are also close to unity ($C/E = 1.01 - 1.06$) in the U.S. calculations, as can be seen from Fig. III.33 and from Table III.5. To decrease the discrepancies by more than 5%, we need to measure and reevaluate these dosimetry cross-sections.

In conclusion, the source characteristics are well predicted for almost all the measurements, e.g., spectra and reaction rates by both JAERI and the U.S. The calculated models and the results give an adequate input source for analyzing the in-system experiments. Only the low-energy component below several KeV has not yet been characterized. It will, however, affect the tritium production rate from ^6Li only at the surface region of the Li_2O assembly.

Table III.4 Horizontal Distribution of Various Reaction Rates (U.S. Calculations)

X	$^{27}\text{Al}(n,\alpha)$	$^{58}\text{Ni}(n,2n)$	$^{197}\text{Au}(n,2n)$	$^{197}\text{Au}(n,\gamma)$
-25	1.40-31* (0.012)** (1.36-31)† 1.03*†	2.62-32 (0.008) (2.88-32) 0.91	2.40-30 (0.010) (2.33-30) 1.03	1.31-28 (0.08) (3.93-29) 3.33
-15	1.46-31 (0.018) (1.41-31) 1.04	2.86-32 (0.010) (2.88-32) 0.99	2.62-30 (0.016) (2.50-30) 1.05	1.36-28 (0.108) (3.85-29) 3.53
-5	1.56-31 (0.021) (1.52-31) 1.02	3.13-32 (0.009) (3.25-32) 0.96	2.74-30 (0.018) (2.50-30) 1.10	1.30-28 (0.081) (3.85-19) 3.38
+5	1.63-31 (0.016) (1.55-31) 1.05	3.26-32 (0.010) (3.46-32) 0.94	2.85-30 (0.013) (2.58-30) 1.10	1.29-28 (0.095) (3.83-29) 3.37
+15	1.69-31 (0.020) (1.58-31) 1.07	3.46-32 (0.008) (3.46-32) 1.00	2.90-30 (0.014) (2.56-30) 1.13	1.40-28 (0.095) (3.80-29) 3.68
+25	1.75-31 (0.031) (1.57-31) 1.11	3.51-31 (0.009) (3.71-32) 0.95	3.01-30 (0.024) (2.78-30) 1.08	1.34-28 (0.093) (3.89-29) 3.44

*Calculated value by MCNP

**Calculated fractional standard deviation (FSD)

†Measured value

*†C/E value

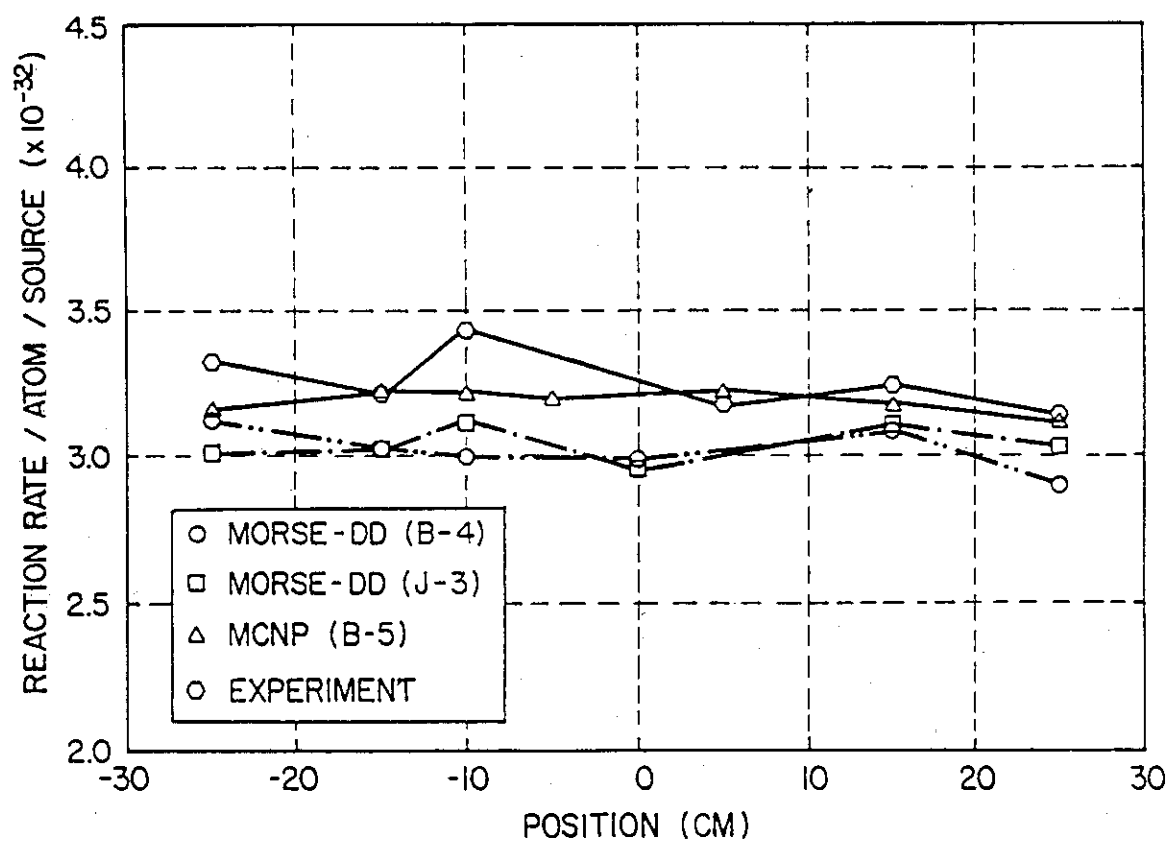


Figure III.30 Vertical distribution of the $^{58}\text{Ni}(n,2n)^{57}\text{Ni}$ reaction rate on the front surface of the Li_2O assembly

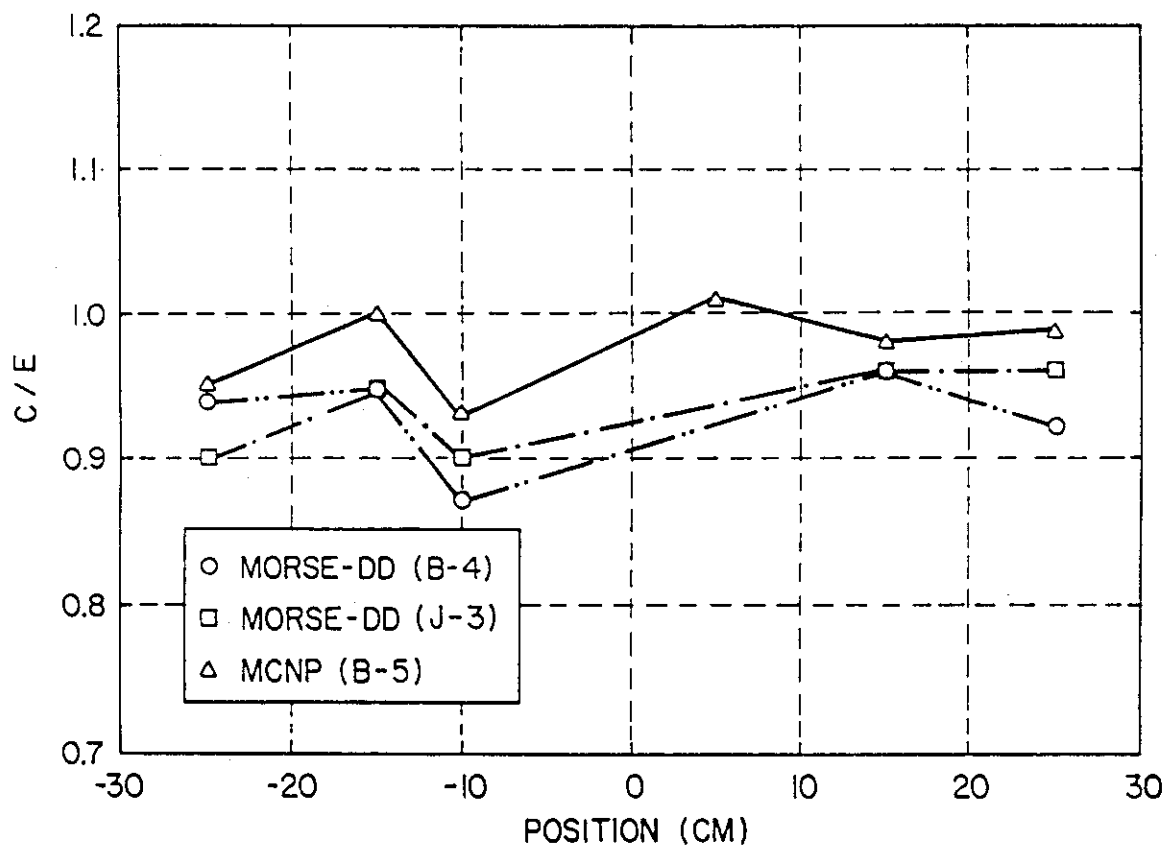


Figure III.31 C/E values of the $^{58}\text{Ni}(n,2n)^{57}\text{Ni}$ reaction rate on the front surface in the vertical direction

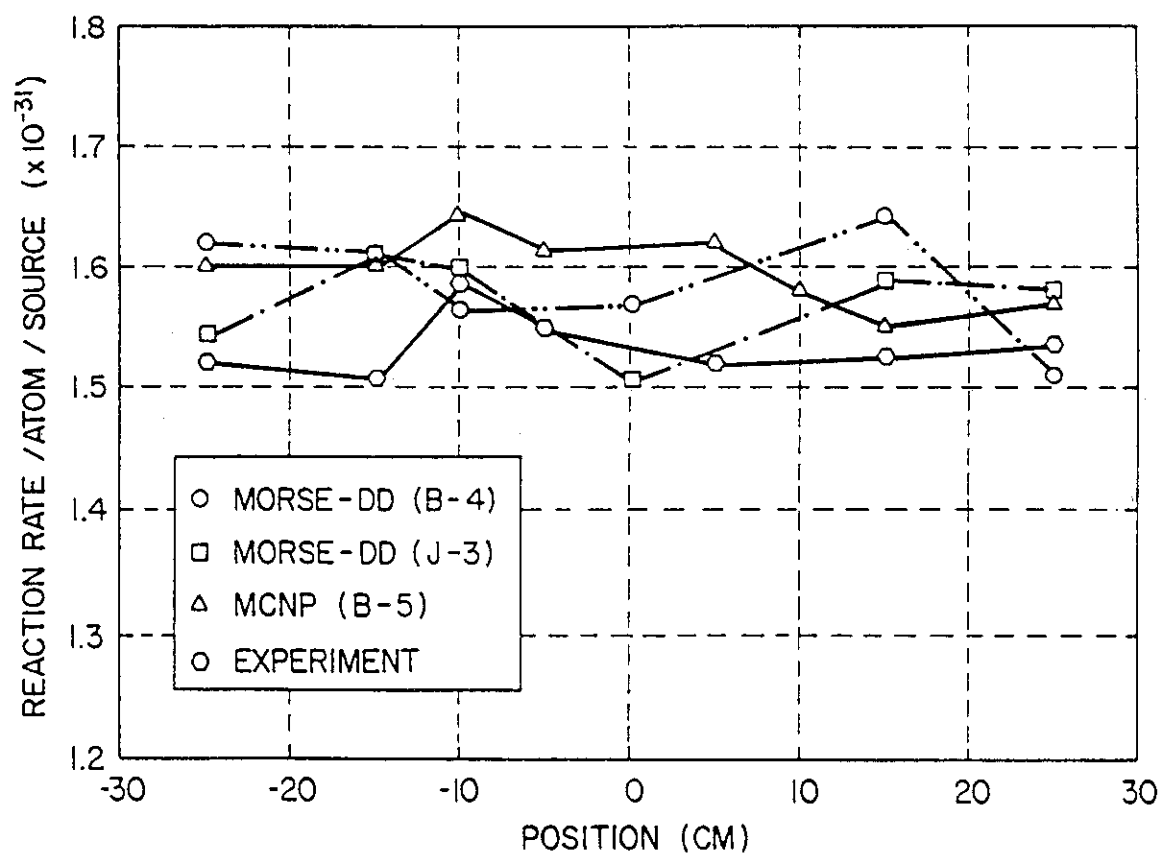


Figure III.32 Vertical distribution of the $^{27}\text{Al}(n,\alpha)^{24}\text{Na}$ reaction rate on the front surface of the Li_2O assembly

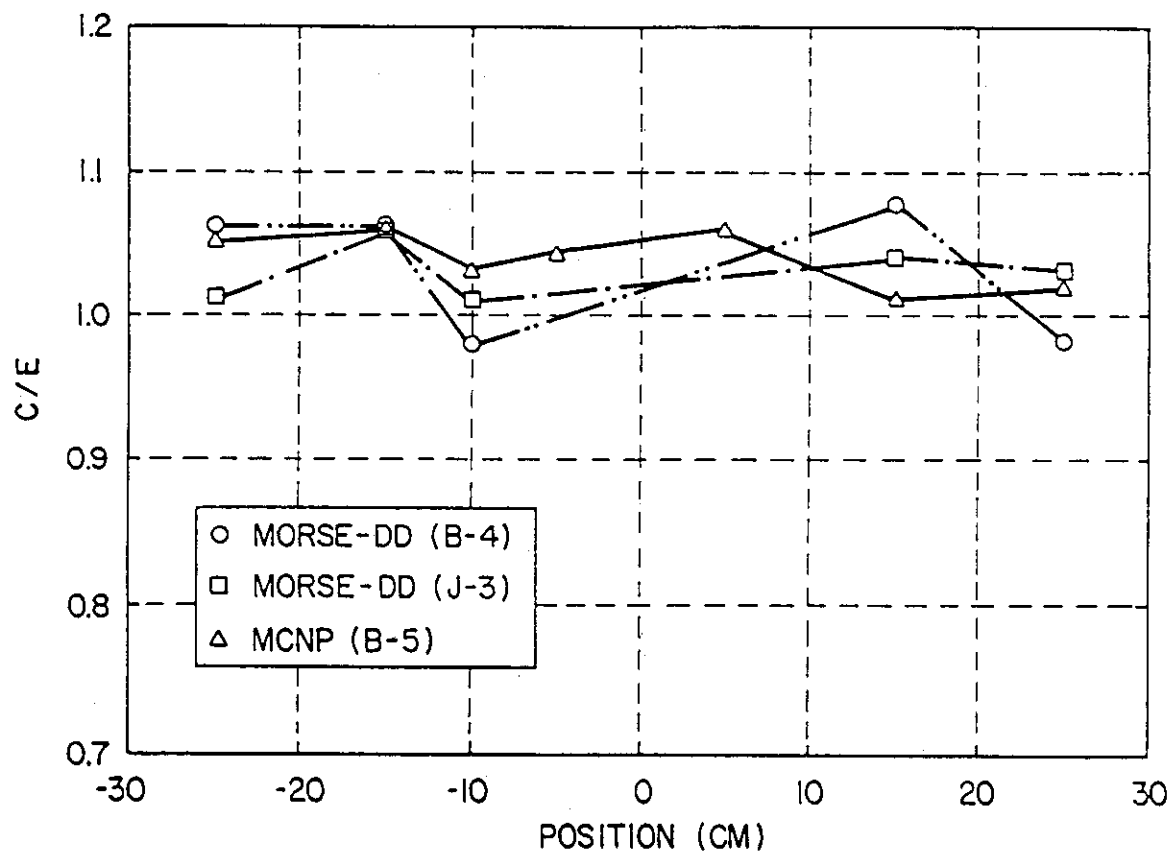


Figure III.33 C/E values of the $^{27}\text{Al}(n,\alpha)^{24}\text{Na}$ reaction rate on the front surface in the vertical direction

Table III.5 Vertical Distribution of Various Reaction Rates (U.S. Calculations)

X	$^{27}\text{Al}(n,\alpha)$	$^{58}\text{Ni}(n,2n)$	$^{197}\text{Au}(n,2n)$	$^{197}\text{Au}(n,\gamma)$
-25	1.60-31* (0.016)** (1.52-31)† 1.05*†	3.16-31 (0.008) (3.32-31) 0.95	2.80-30 (0.010)	1.25-28 (0.080)
-15	1.60-31 (0.030) (1.51-31) 1.06	3.22-31 (0.015) (3.21-31) 1.00	2.91-30 (0.025)	1.23-28 (0.077)
-10	1.64-31 (0.018) (1.59-31) 1.03	3.20-31 (0.011) (3.43-31) 0.93	2.84-30 (0.016)	1.30-28 (0.091)
-5	1.61-31 (0.012) (1.55-31) 1.04	3.19-31 (0.008)	2.80-30 (0.011)	1.33-28 (0.078)
+5	1.62-31 (0.016) (1.52-31) 1.06	3.20-31 (0.010) (3.17-31) 1.01	2.82-30 (0.015)	1.31-28 (0.082)
+10	1.58-31 (0.028)	3.20-31 (0.011)	2.82-30 (0.015)	1.31-28 (0.082)
+15	1.55-31 (0.016) (1.53-31) 1.01	3.17-31 (0.011) (3.24-31) 0.98	2.72-30 (0.014)	1.36-28 (0.086)
+25	1.57-31 (0.016) (1.54-31) 1.02	3.13-31 (0.007) (3.15-31) 0.99	3.73-30 (0.013)	1.41-28 (0.120)

*Calculated value by MCNP

**Calculated fractional standard deviation (FSD)

†Measured value

*†C/E value

IV. TRITIUM PRODUCTION RATES

The potential for tritium breeding in various breeding materials is a key design issue in the neutronics field of fusion reactors. Various blanket designs using potentially accepted breeders have been proposed. However, the uncertainty in the tritium production rate (TPR) in these breeders has hardly been verified experimentally in an engineering mockup system. The Phase I experiments and their analyses were the first investigation of tritium production rates in a relatively prototypical system. Since the calculational models and the methods applied were described in Section II, this section discusses the results of the analysis and comparison with measurements for TPR by ${}^6\text{Li}$, ${}^7\text{Li}$ and natural lithium.

IV.1 The Reference Li_2O Experiment

The tritium production rates of ${}^6\text{Li}$ (T_6) and ${}^7\text{Li}$ (T_7) were measured with Li-metal detectors, Li_2O -pellet detectors, and with Li-glass detectors (for on-line measurements). The NE213 scintillation counter was applied as an indirect method to measure T_7 . The T_7 values were obtained by multiplying the NE213 measured spectra with the ${}^7\text{Li}(n,n'\alpha)t$ cross-section. Since the NE213 measurements are available at energies above about 1 MeV, this technique cannot be applied to the T_6 measurement.

In measuring T_6 , the finite thicknesses of the detectors used caused a self-shielding effect to the low-energy part of the neutron spectrum, and therefore to the integrated values. Much effort has been devoted to correcting for the self-shielding effect.⁽³¹⁻³⁴⁾ Special difficulty was found in the front part of the Li_2O assembly, where the low-energy room-return neutron component dominates the direct component. The T_6 produced by the room-return neutrons decreases rapidly and exponentially along the Z direction within the first few centimeters. More discussion on this point will follow.

IV.1.1 Tritium Production Rate from ${}^6\text{Li}$ (T_6)

The absolute values of T_6 are shown in Fig. IV.1. It includes the measured values obtained by Li_2O pellets, Li-glass and Li-metal detectors. Also shown are the calculated values using the MORSE-DD and DOT3.5 codes (JAERI). The divergence among measurements and calculations is larger at the front region and at deep locations ($Z > 50$ cm). In the intermediate region, T_6 decreases slowly with distance and the agreement among the various measuring methods is good. The absolute values seem to agree well with each other, as shown in Fig. IV.1 (plotted in a log linear scale) although it appears that the calculations overestimate T_6 . Since our target accuracy in predicting the TPR is less than 5% in the case of the Li_2O breeder, which has a marginal breeding ratio, it is more practical to use the C/E values (ratio of calculation to measurement) in the intercomparison. It should be noted that the importance of the accuracy in C/E values is not uniform throughout the assembly. Greater importance (weight) is given to the front region for TPR because the contribution from this region to the absolute value of the TPR is larger than the contribution from the back region.

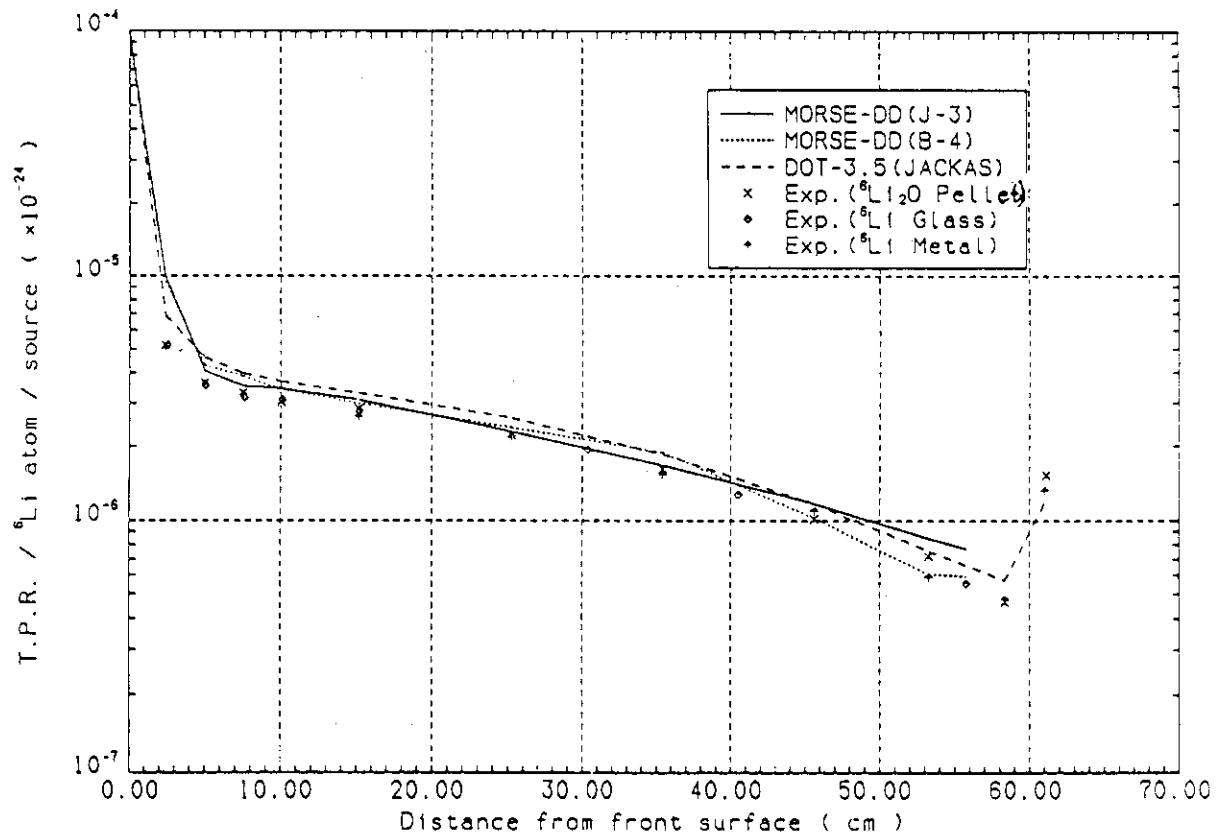


Figure IV.1 Distribution of tritium production rate by ${}^6\text{Li}$ in the reference system

To intercompare the various measuring techniques in the C/E scale, Fig. IV.2 shows the C/E values for these techniques using the calculational results obtained with DOT3.5 and the JACKAS cross-section library (see Section II). In the region $Z < \sim 5$ cm and $Z > 50$ cm, the divergence between the measuring techniques is large; therefore it is inappropriate to discuss the prediction accuracy of various calculational methods in this region. In the region, ~ 5 cm $< Z < 50$ cm, the C/E values lie within a width of 10% deviation from unity for all measuring techniques.

In the following, we compare the C/E values obtained by various codes and nuclear data libraries for each measuring technique. Fig. IV.3 shows the C/E values obtained by MORSE-DD with the DDL/J3P1 library, DOT3.5 with the JACKAS library, MCNP with the RMCCS library, and DOT4.3 with the MATXS6 library. As in the DOT4.3 calculations, in the MCNP calculations, the latest evaluation for ^7Li cross-sections obtained by Young⁽¹⁹⁾ in the T-2 group at LANL was used. Except for the range $Z < 5$ cm, the divergence in the C/E values is about 15% among the four calculations. As for the comparison between the results obtained by the MORSE-DD and DOT3.5 codes, the difference is less than 7% in the region 10 cm $< Z < 40$ cm. MORSE-DD gives closer values of C/E to unity, although the difference gets larger at the front surface. This difference was reduced by introducing the room-returned component of the incident neutron source calculated by MORSE-DD into the DOT calculation. A notable tendency in the C/E values is that all the calculations overestimate the measured values by 5~25% in the system at locations $Z > 5$ cm and in the bulk of the Li_2O assembly. The fractional standard deviation (FSD) of the MORSE-DD calculations is large at the back locations. In the region $Z < 5$ cm, the gradient of the TPR distribution is very steep and the interpolation formula used to obtain the calculated values at locations corresponding to the exact measuring points affects the C/E values, e.g., ~ 10 -14%.

Note also from Fig. III.3 that the C/E values for T_6 evaluated by the DOT codes are within 1.10-1.28 throughout the assembly, except at the front locations ($Z = 0$ -5 cm) where large deviations from unity are found ($C/E = 0.80$ -1.4). One notices from the figure that the C/E values obtained by the U.S. using the DOT4.3 code are 2-10% larger than those obtained with the DOT3.5 code (JAERI) at $Z > 10$ cm. The experimental values used in Fig. IV.3 are corrected for the self-shielding effect. This effect results from flux depression inside the finite-size enriched ^6Li samples used to measure T_6 . Even after the correction, large deviations from the experimental values are obtained near the front surface. This is also true in the Monte Carlo calculations case where the C/E values obtained by the MCNP code (U.S.) are 1.12-1.80 at front locations, but are 1.02-1.10 at locations $Z > 10$ cm. The C/E values obtained by the MORSE-DD code (JAERI) show the same trends and are larger than the MCNP values by 2 to 8%, especially at the front and back locations. At the front surface, the C/E values obtained by the MORSE-DD code are as large as 3 ($C/E = 1.4$ at $Z = 55$ cm).

The tendency of the C/E values for the Li_2O pellets is similar to that for the Li-glass detectors, as shown in Fig. IV.4. The reason for the large C/E values at the back region beyond $Z = 55$ cm could be the underestimation of self-shielding factors where the contribution from the soft-energy neutrons that are

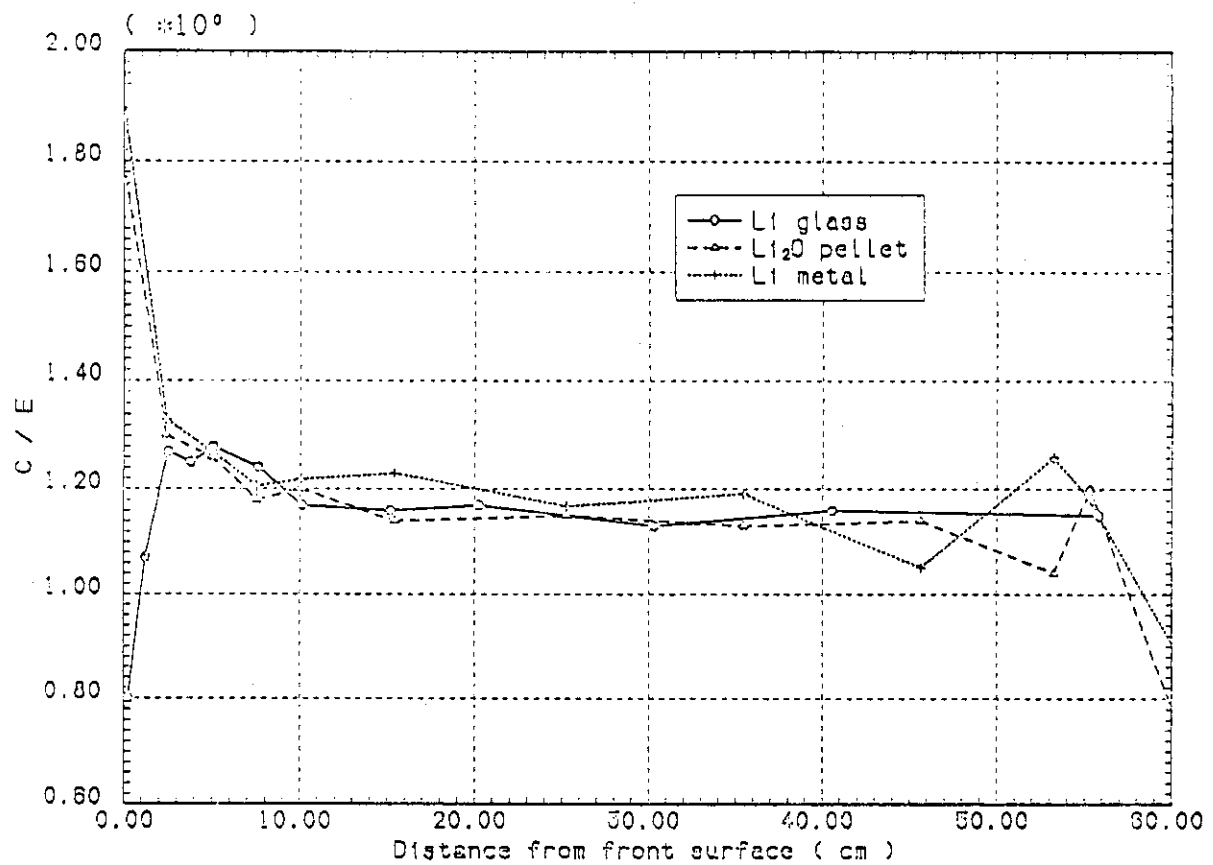


Figure IV.2 C/E values for T_6 in the reference system calculation: DOT 3.5 with JACKAS

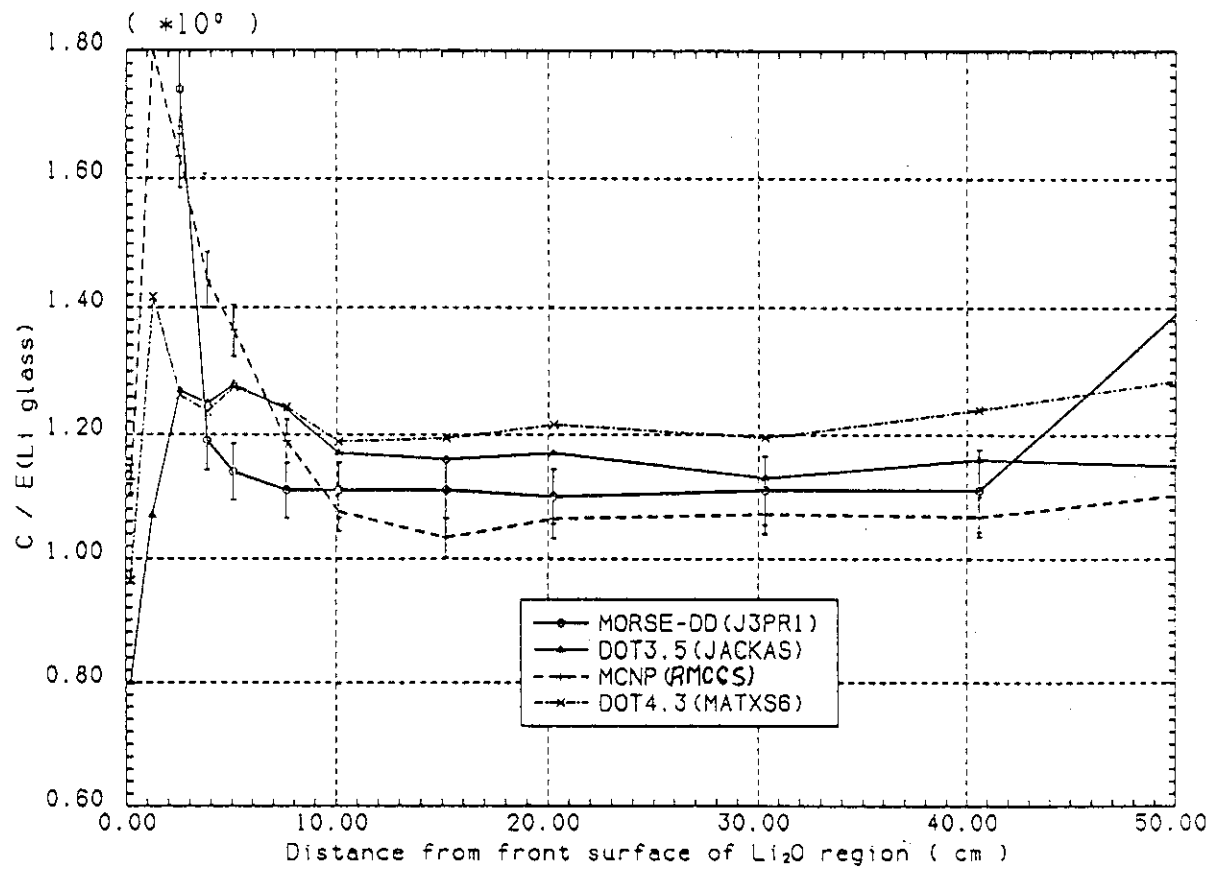


Figure IV.3 Comparison of C/E values for T_6 in the reference system. Measured values were obtained by a Li-glass detector.

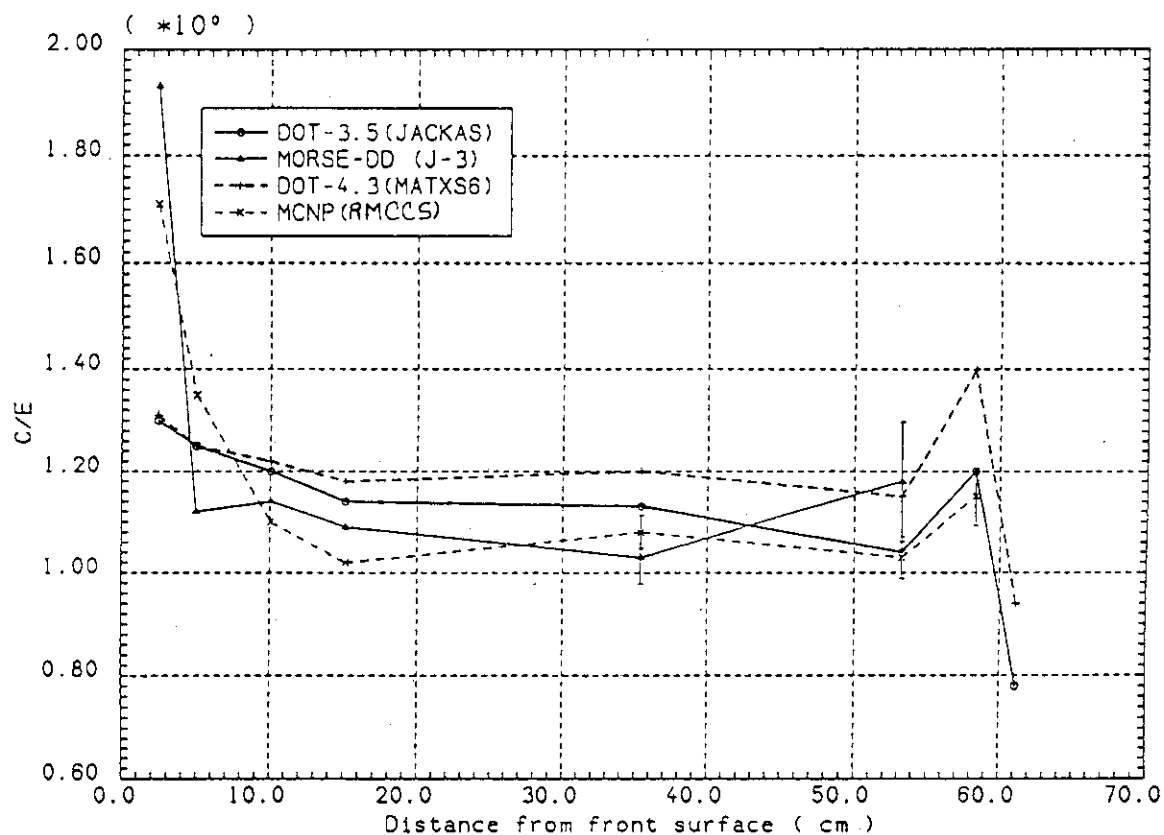


Figure IV.4 Comparison of C/E values for T_6 in the reference system. Measured values were obtained by Li_2O pellets.

reflected from the surrounding concrete of the back wall was not accounted for. Note from Fig. IV.4 that the number of measuring points in the middle region may be too small to discuss the results in detail, as for the Li-glass case shown in Fig. IV.3.

Fig. IV.5 compares the values of C/E for T_6 as measured by the Li-metal samples. This case shows a tendency similar to the C/E features obtained by the other measuring methods throughout the whole region. In this case, MORSE-DD also shows a large fluctuation in the back region beyond $Z = 45$ cm, as is the case with the MCNP code. Also note that the deterministic codes give larger C/E values in the middle region than those obtained by the Monte Carlo codes.

In order to investigate the source of the discrepancy between the calculations and measurements at the front region, an experiment was performed to confirm the low-energy component of the input source. By setting a large shadow cone between the RNT and the Li_2O system, the direct component from the RNT was removed and the TPR was measured in the system. Fig. IV.6 shows the results of both the measurements and the calculations. In the figure, three types of TPR profiles are plotted, namely, the total T_6 , T_6 due to the direct component of the incident neutrons from the RNT, and T_6 due to the indirect room-returned component. First, the total TPR as predicted by the MORSE-DD code is overestimated, as discussed earlier. Second, the contribution to T_6 from the room-returned component generally agrees with the measurement up to $Z = 30$ cm. This fact means that the calculation of the room-returned component, which is larger than the direct component in the region $Z < 8$ cm, is accurately predicted by MORSE-DD. The difference between calculations and measurements for T_6 that is contributed from the direct component is almost constant throughout the Li_2O assembly. This difference is the main cause of the discrepancy observed in the total TPR, which is about 10~15%. That is, the discrepancy in the total T_6 is caused by the uncertainty in the prediction of the direct component of the neutron source, which is overestimated. The discrepancy in the absolute number of these neutrons is small as discussed in Section III on TOF experiment. Therefore, the soft neutrons, which mainly contribute to T_6 , would be overestimated in their slowing-down and transport processes. A similar conclusion can be drawn from Fig. IV.7, which compares the same measurements to the calculations performed by DOT/JACKAS. The uncertainties in the cross-sections of Li could cause such a discrepancy, if the measurements have no systematic errors. This point needs further investigation in the Phase II experiments and analysis. As shown in Figures IV.3 to IV.5, the largest discrepancy between the measurements and calculations is observed at the front region ($Z < \sim 5$ cm). In this region, T_6 decreases rapidly with distance from the front of the Li_2O assembly, as seen in Fig. IV.7 (e.g., one and a half order-of-magnitude decrease). Such a decrease is caused by the rapid absorption of the room-returned soft neutrons. The measurements shown in Figures IV.6 and IV.7 were corrected for self-shielding effect by applying the correcting factors that correspond to the measuring techniques used, but these factors are large at front locations (up to a factor 2~3) and the associated uncertainties in their values seem to be large. In Phase II experiments, the geometrical arrangements were chosen to decrease the uncertainty in the low-energy component as much as possible.

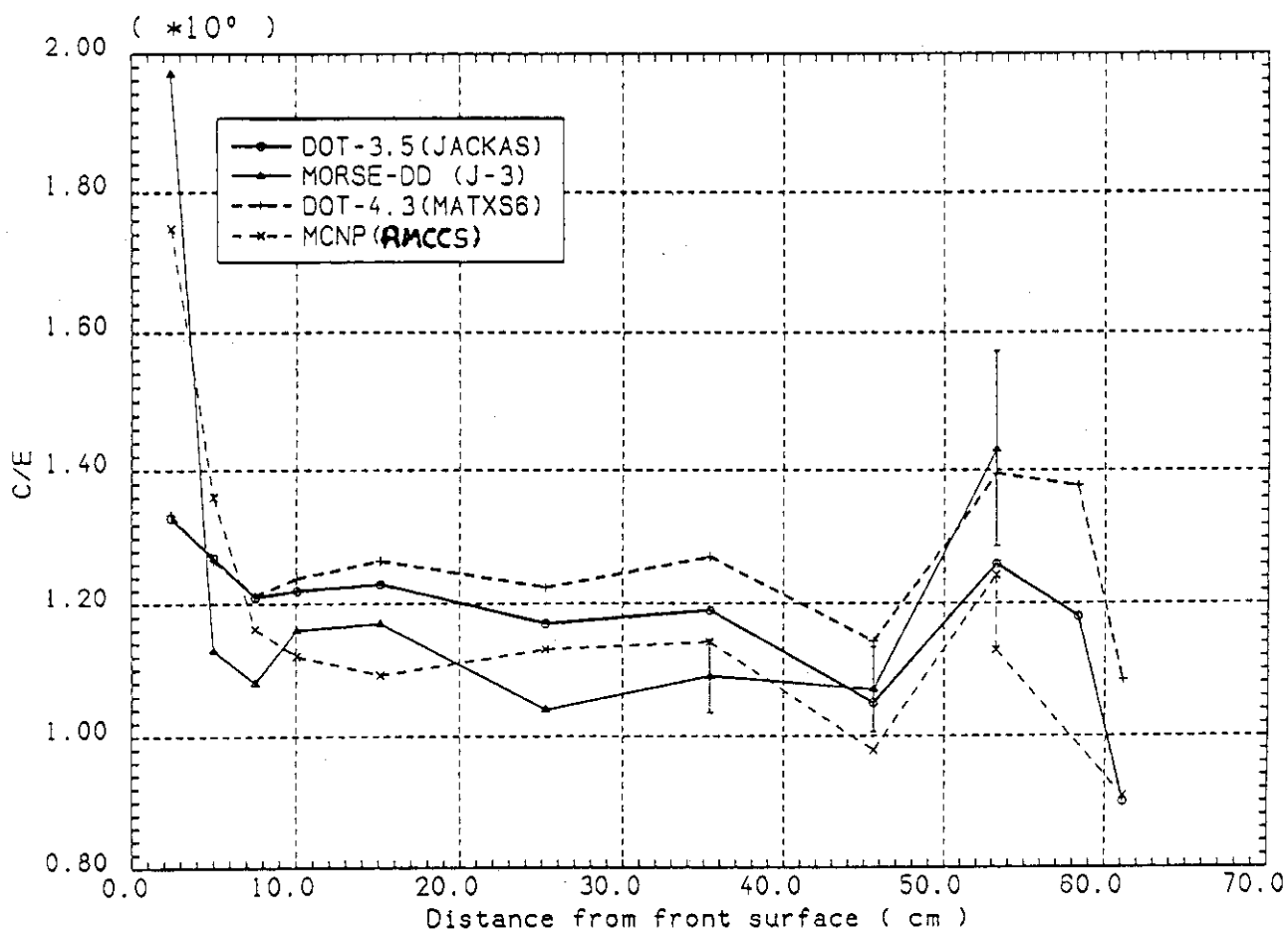


Figure IV.5 Comparison of C/E values for T_6 in the reference system. Measured values were obtained by Li-metal detectors.

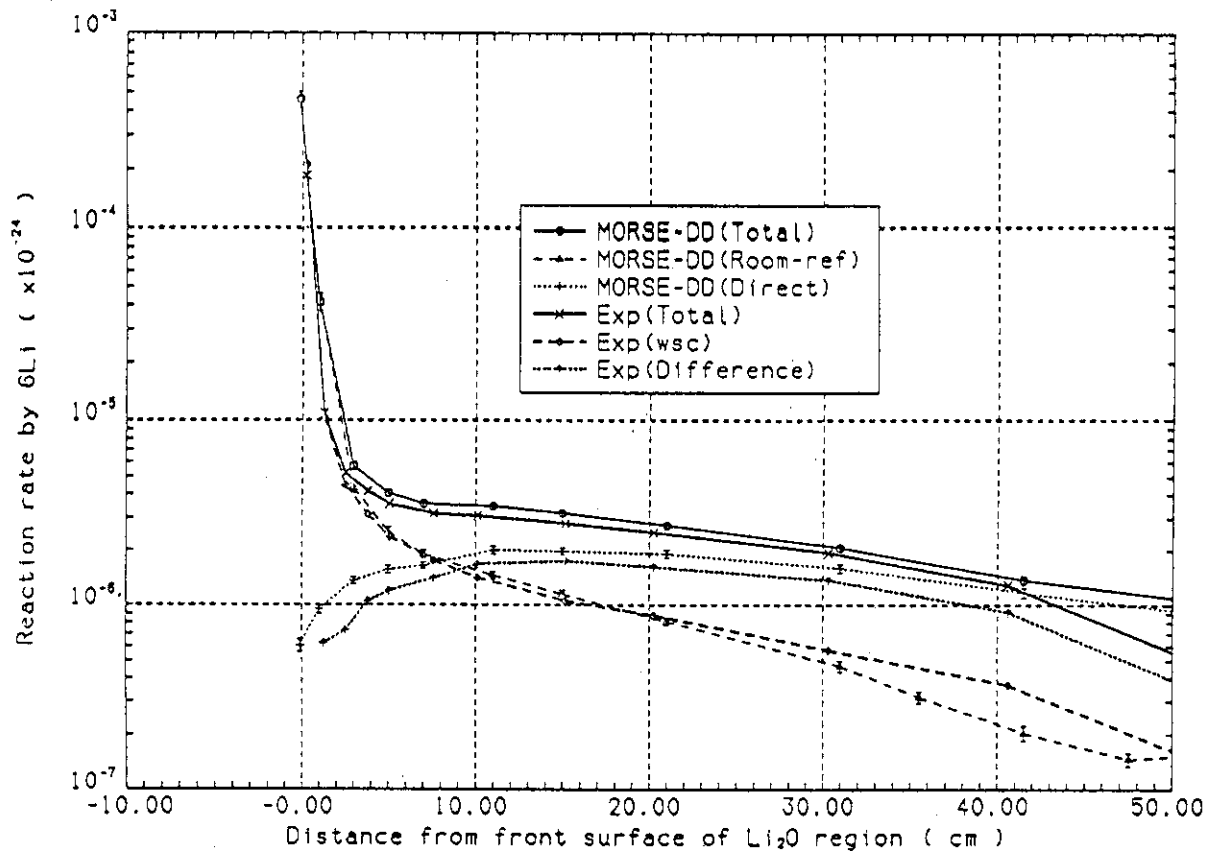


Figure IV.6 Components contributing to T_6 in the reference system. Measured values were obtained by Li-glass detectors and calculations were performed by MORSE-DD.

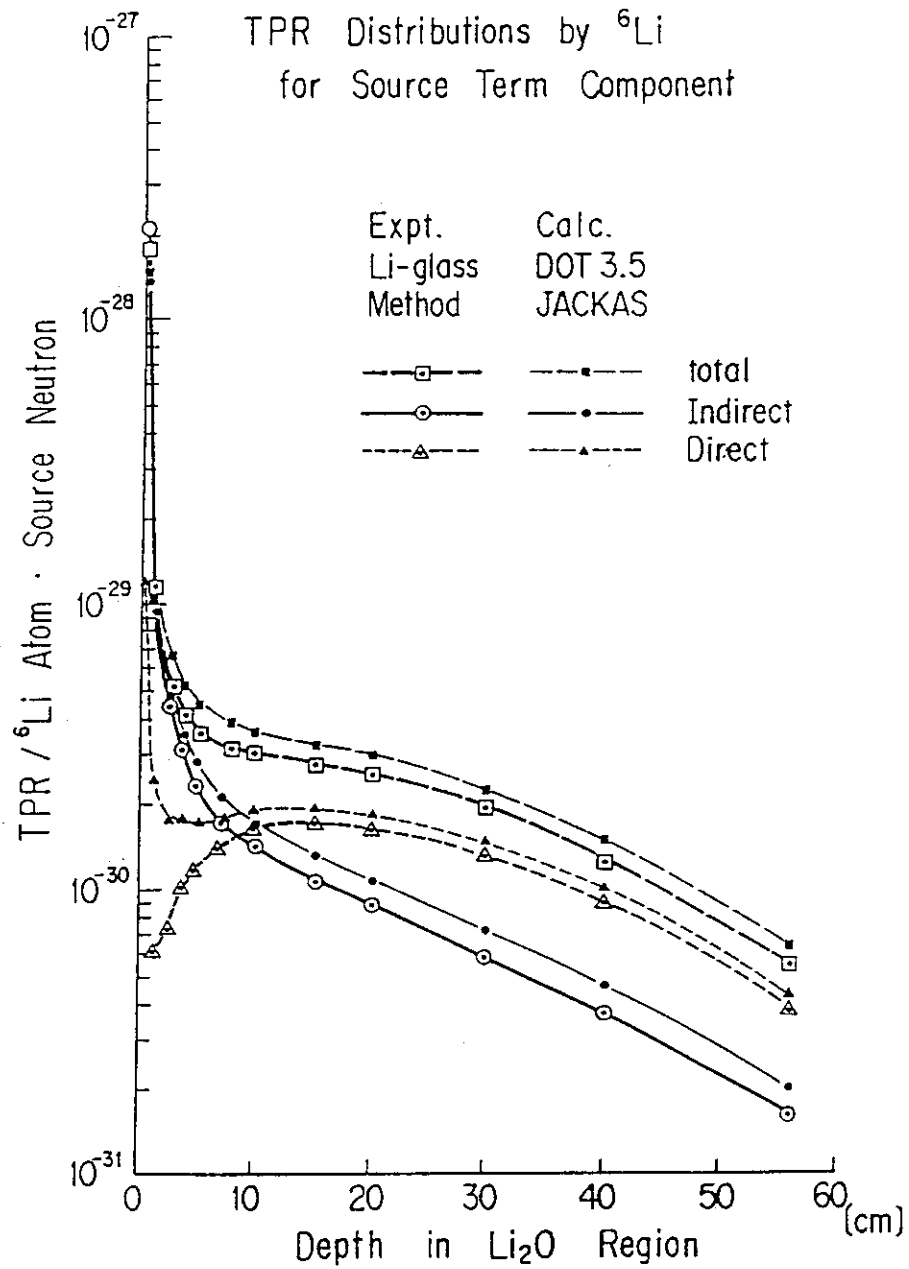


Figure IV.7 Components contributing to T_6 in the reference system. Measured values were obtained by Li-glass detectors and calculations were performed by DOT3.5/JACKAS.

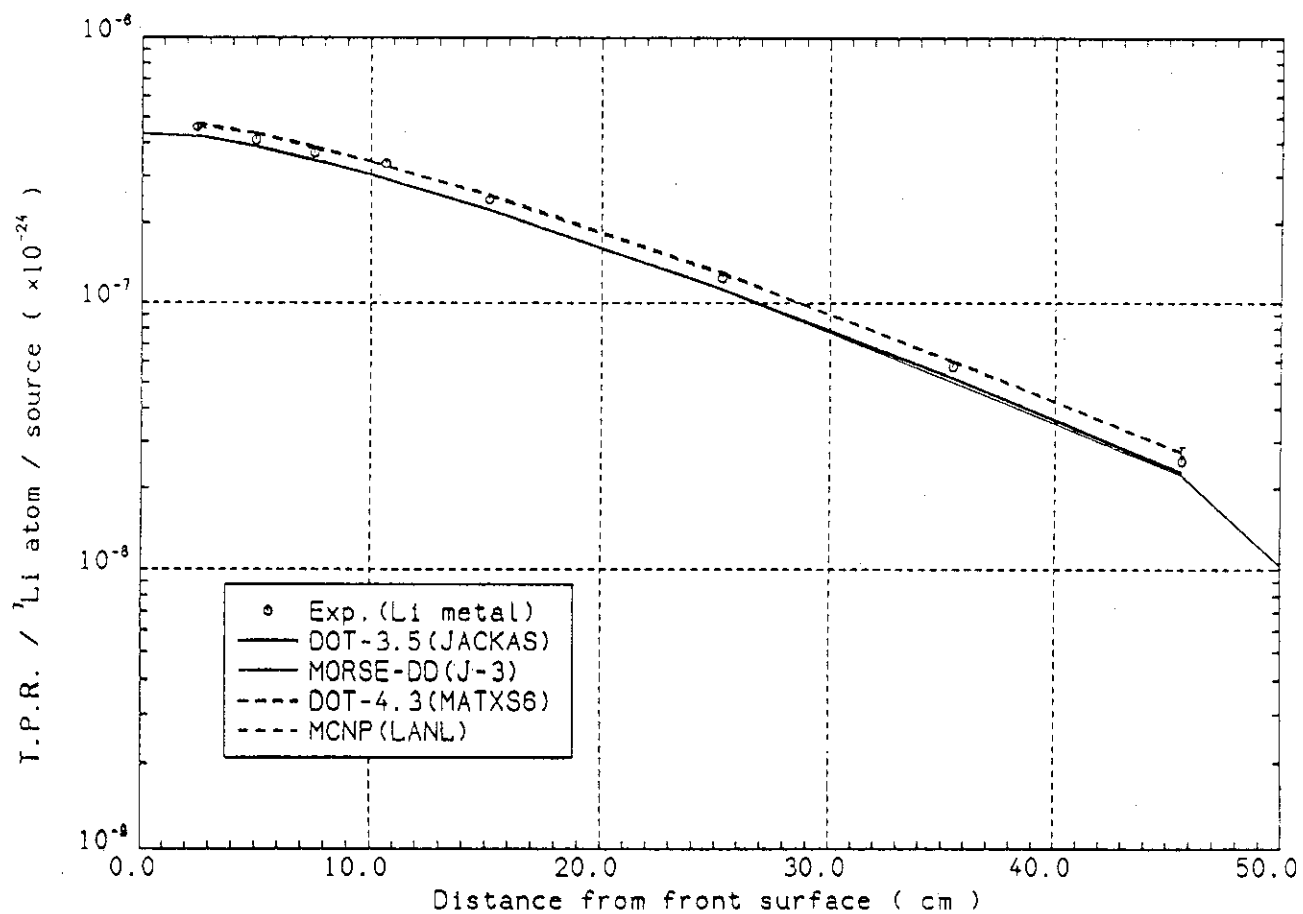
IV.1.2 Tritium Production Rate from ^7Li (T_7)

The absolute values for T_7 are shown in Fig. IV.8, as predicted by calculations and as measured by the Li-metal detectors. The slope of T_7 profile with distance from the front surface is steeper than that of T_6 . Note that ^7Li contributes less to the total TPR as compared to the contribution from ^6Li in most blanket designs. In this reference experiment, T_7 is smaller than T_6 by an order-of-magnitude, as can be seen from Figures IV.7 and IV.8.

Since tritium production from ^7Li is due to the reaction of $^7\text{Li}(n,n'\alpha)t$, which has a high threshold energy, T_7 is thus sensitive to the 14 MeV flux peak. Fig. IV.9 compares the C/E values as obtained by two measuring methods, namely the NE213 indirect method and the Li-metal method. Calculations are performed by the DOT3.5 code along with the JACKAS library. A systematic difference is observed between the two measuring methods, which amounts to about 10%; nevertheless, the spatial dependence of that difference is small. As discussed in Volume I, the NE213 indirect method is affected by the uncertainty in the reaction cross-section used, although the NE213 method shows better agreement (C/E ~ 1.02), as shown in Fig. IV.9, with JAERI's calculation using the 2-D model. Thus, it appears from the C/E values for the Li-metal detectors that the JENDL/3PR1 or 2 libraries underestimate T_7 by 7~10%, which is attributed to the cross-section $^7\text{Li}(n,n'\alpha)t$.

A comparison of the C/E values is also shown in Fig. IV.10, where several codes and nuclear data libraries are used, and the measured values are those obtained by Li-metal detectors. The JAERI results using the JENDL/3PR1 or 2 libraries give lower C/E values by 10%, as compared to unity. On the other hand, the U.S. values are higher than unity by 1~8%. Such an extreme discrepancy is mainly attributed to the difference in the tritium production cross-section of ^7Li . As shown in Fig. IV.11, the $^7\text{Li}(n,n'\alpha)t$ cross-section adopted by JENDL/3PR1 or 2 is 10% or more smaller at 14 MeV compared with that evaluated by Young (T-2 group at LANL). Further accurate measurements and re-evaluation for this cross-section are needed in order to accurately predict T_7 .

The intercomparison between codes and libraries for the C/E values of T_7 is also shown in Fig. IV.12 for the NE213 indirect method. The C/E values are 1.12-1.18 and are 1.00-1.04 as obtained by the U.S. and JAERI, respectively, using the 2-D calculational model. The curves for the C/E values are flat in this case, which suggests that there is a systematic difference of about 12-18% between the JAERI and U.S. calculations, where the U.S. values are generally larger. This again is attributable to the difference in the evaluations of the $^7\text{Li}(n,n'\alpha)t$ cross-section mentioned above. The trend observed in the 2-D calculations is also apparent in the Monte Carlo calculations. Note also from Fig. IV.12 that the ENDF/B-V, version 1, evaluation for ^7Li (denoted B-5 in the figure), gives a 10-15% larger T_7 , as compared to results obtained from the T-2 group (Young's) evaluation. This is also clear from Fig. IV.13, where the measured values obtained by the Li-metal detectors are compared with the U.S. calculations.

Figure IV.8 Tritium production rate by ${}^7\text{Li}$ in the reference system

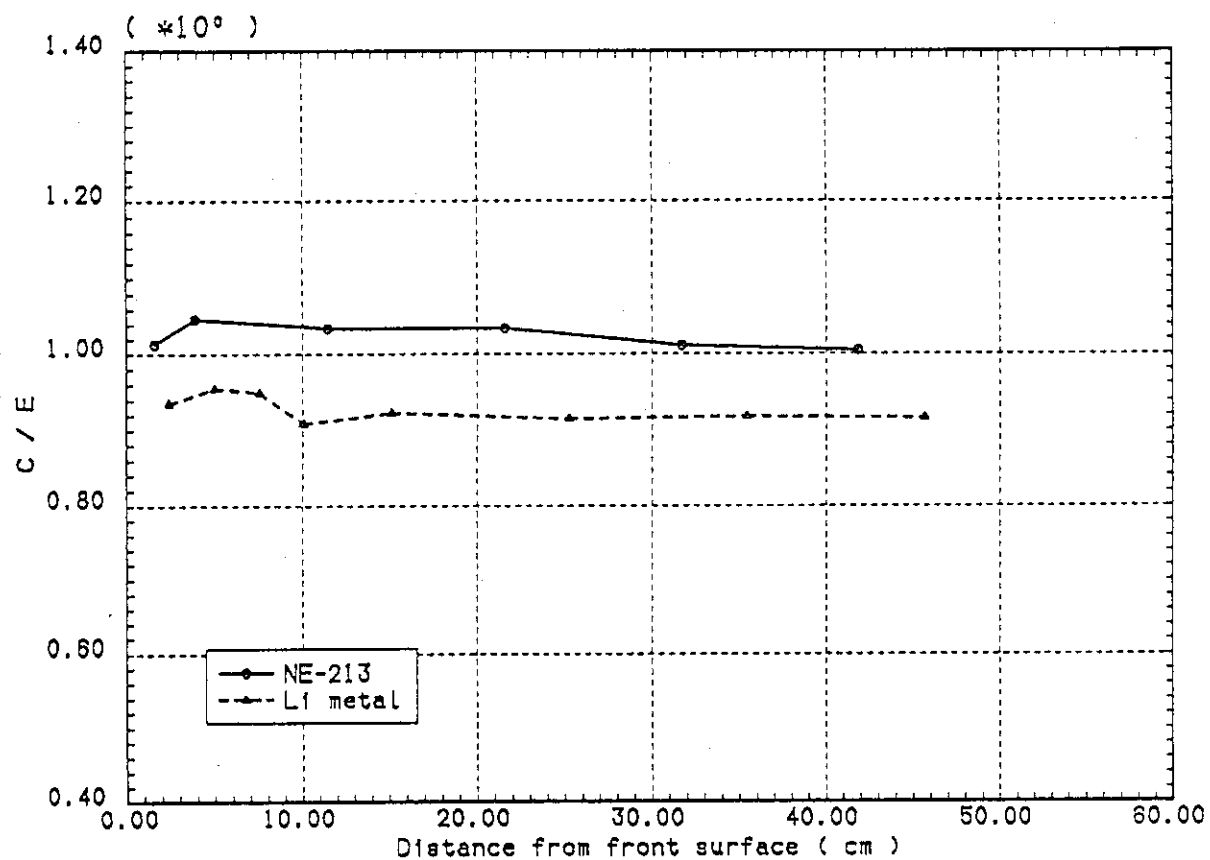


Figure IV.9 Comparison of C/E values for T_7 in the reference system based on calculations performed by DOT3.5 with JACKAS library

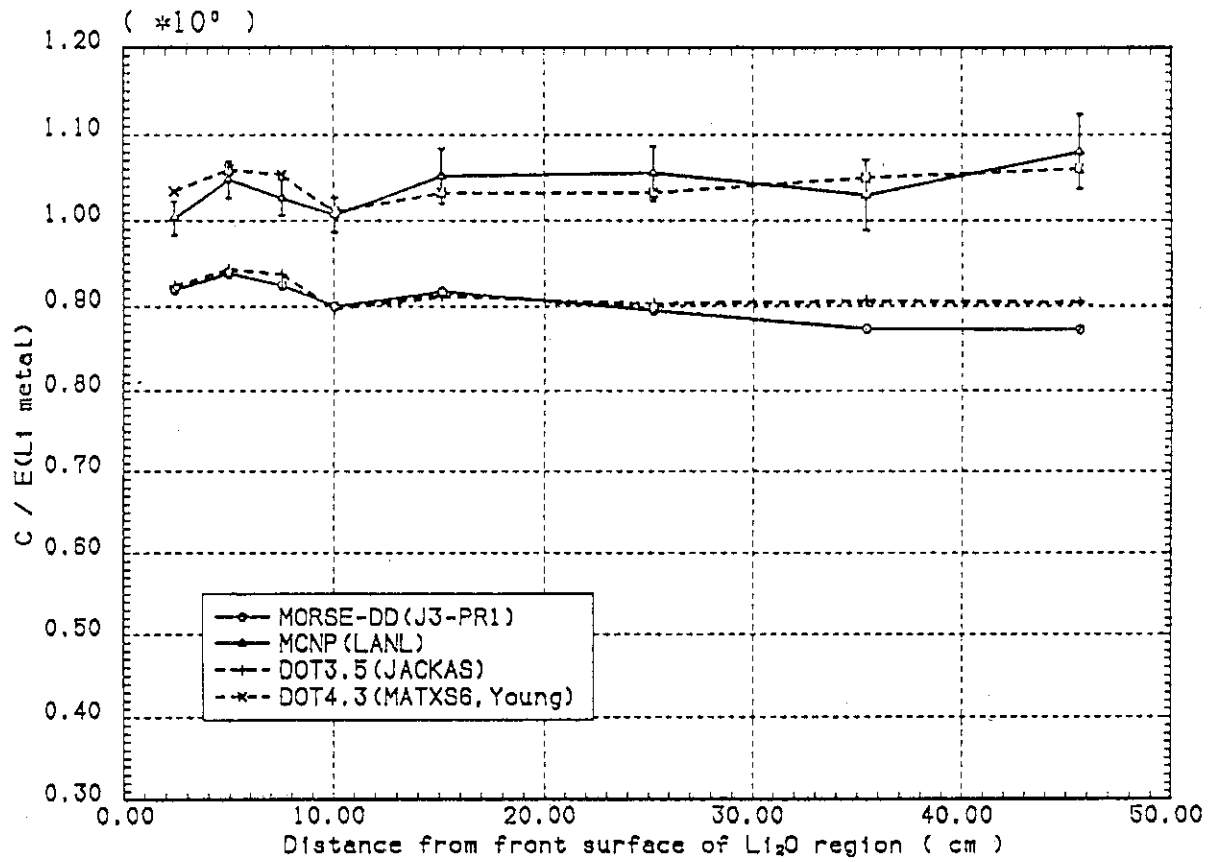


Figure IV.10 Comparison of C/E values for T7 in the reference system. Experimental values were obtained by Li-metal dectectors.

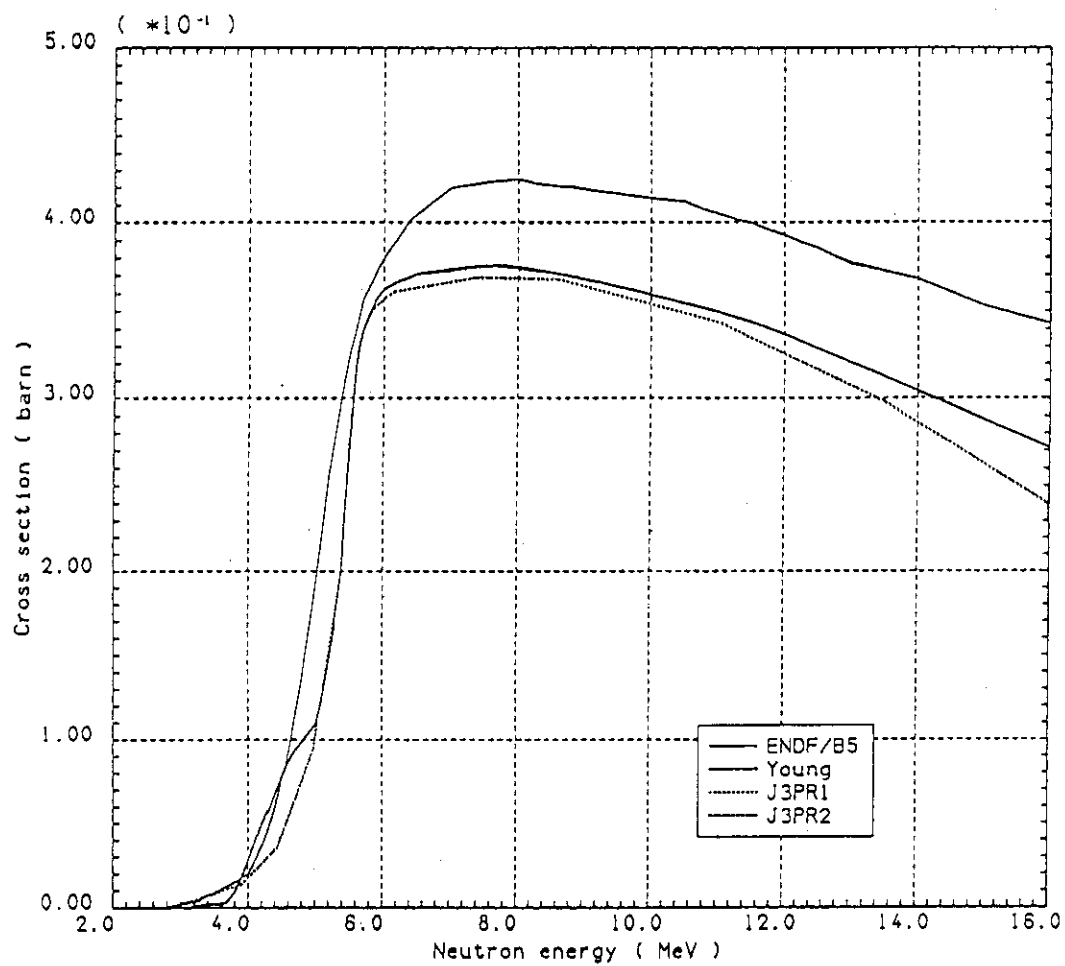


Figure IV.11 Comparison of cross-sections for ${}^7\text{Li}(n,n'\alpha)t$ reaction

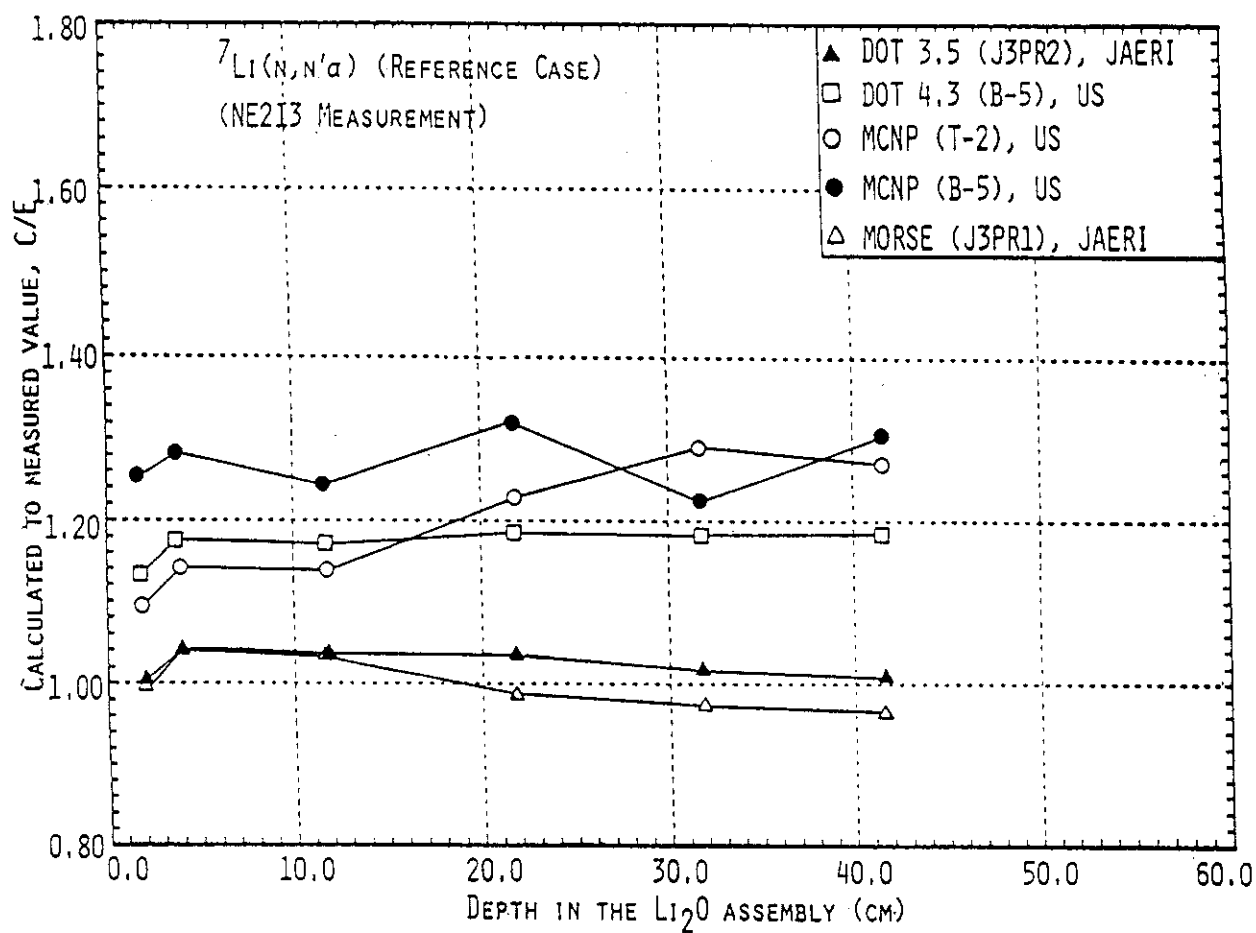


Figure IV.12 The C/E values for T7 in the reference system using the NE213 indirect method

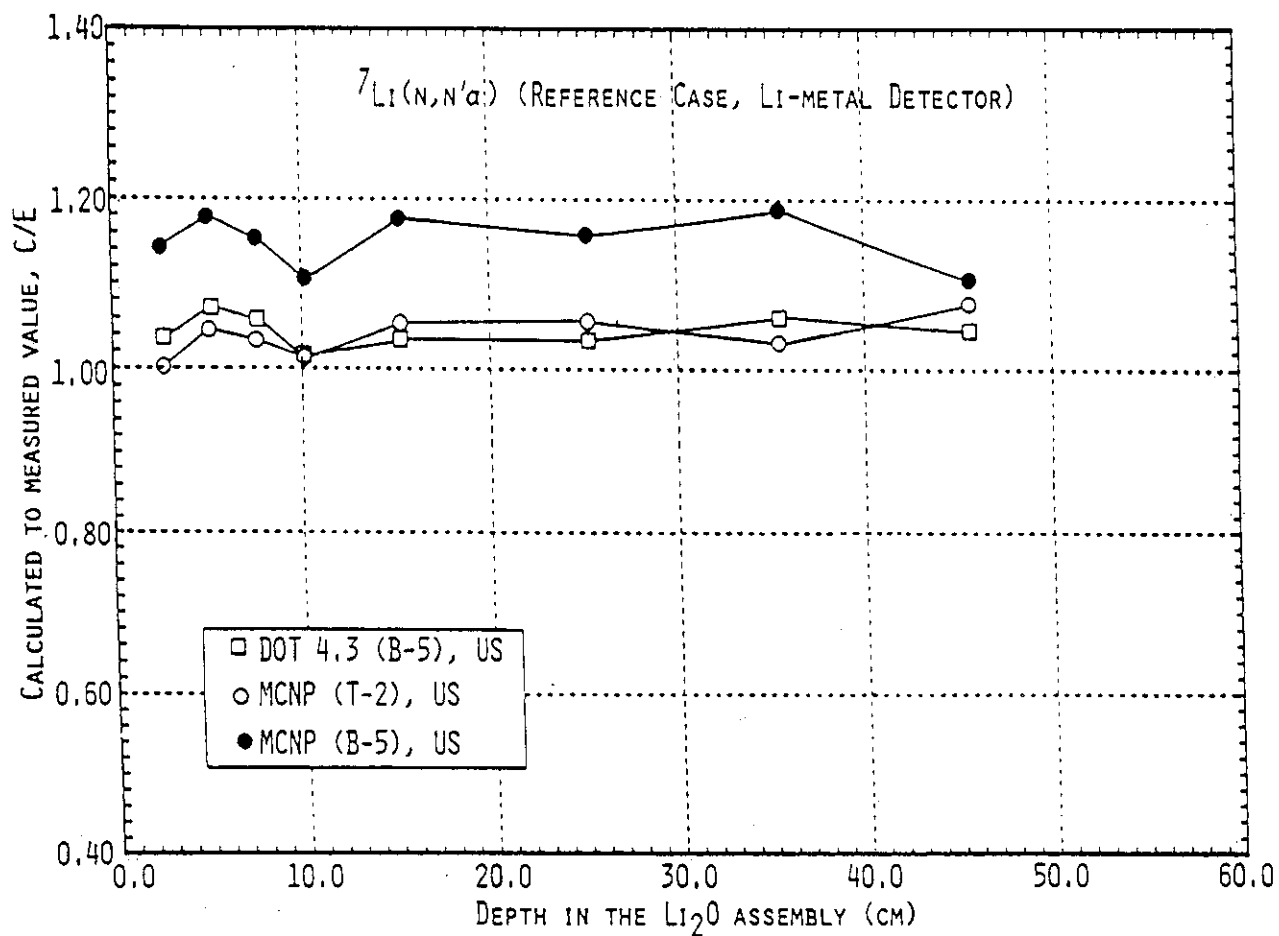


Figure IV.13 The C/E values for T7 in the reference system using Li metal detectors (U.S. calculations)

IV.2 First Wall Experiments

IV.2.1 2-D Analysis

The impact of including a first wall and a polyethylene layer that simulates a coolant channel on tritium production rates was studied both analytically (JAERI: DOT3.5/JACKAS; U.S.: DOT4.3/MATXS6) and experimentally (T_6 : Li-glass on line measurements, T_7 : NE213 indirect method). Both T_6 and T_7 profiles will decrease upon including an 0.5-cm stainless steel (SS) layer in front of the Li_2O assembly. This decrease is more pronounced in the 1.5-cm SS case. As predicted by the U.S., and in comparison to the reference system, the decrease in T_7 is about 5% and 15% throughout the Li_2O assembly in the 0.5-cm SS and the 1.5-cm SS cases, respectively (see Fig. IV.14 and Table IV.1). Thus, the decrease shows some linearity with respect to the first wall thickness. On the other hand, the decrease in the local values for T_6 , relative to the reference system, is much larger at locations just behind the first wall (40% decrease in the 0.5-cm SS case and 70% decrease in the 1.5-cm SS case) while the decrease is less pronounced at deeper locations (3% and 5% decrease in the 0.5-cm and 1.5-cm SS cases, respectively, at $Z > 15$ cm (see Fig. IV.15 and Table IV.2).

The inclusion of a 0.5 cm-thick polyethylene (PE) layer behind the first wall tends to further decrease the local values of T_6 and T_7 . The additional decrease in T_7 is almost constant throughout the assembly and is about 3-5% and 2-4% in the 0.5 cm-thick and 1.5 cm-thick SS cases, respectively. As for T_6 , and at locations $Z < 3$ cm, the additional decrease is ~5%, while it is 2-5% at locations $Z > 15$ cm. However, at locations $3 \text{ cm} < Z < 15 \text{ cm}$, and in comparison to the reference case, the local T_6 values are larger by 1-2% and 2-6% in the 0.5 cm-thick and the 1.5 cm-thick SS cases, respectively. The calculations performed by JAERI show similar changes in the local values of T_6 and T_7 relative to the reference system. This is shown, for example, in Fig. IV.16 for T_6 in the 0.5 cm-thick SS system (with and without PE layer) where the JAERI calculations generally overestimate these relative changes (by 2-10%) as compared to the U.S. calculations (see also Table IV.2).

The C/E values for T_6 are shown in Fig. IV.17 for the case where the PE layer is not included and as calculated by both JAERI and the U.S. using the 2-D model. The measurements were performed by the Li-glass on-line method and are corrected for self-shielding effect. As shown, the deviation in the C/E values from unity is more pronounced in the 0.5 cm-thick SS case as compared to the 1.5 cm-thick case. As in the reference case, the discrepancies with the experimental values are large at front locations ($Z < 10$ cm) while the C/E values are around 1.10 and 1.25 in the JAERI and U.S. calculations, respectively, throughout the bulk of the Li_2O assembly. The predictions for T_6 , as obtained by the U.S., are larger than those obtained by JAERI, as shown in Figures IV.17 and IV.18 and as introduced in Table IV.3.

The observations that the inclusion of a first wall and PE layer tends to improve the C/E values can be seen from Fig. IV.19, as obtained by JAERI's 2-D model. As shown, the C/E values agree fairly well with each other in the range, $10 \text{ cm} < Z < 41 \text{ cm}$, but the divergence increases at $Z = 20 \text{ cm}$. Also

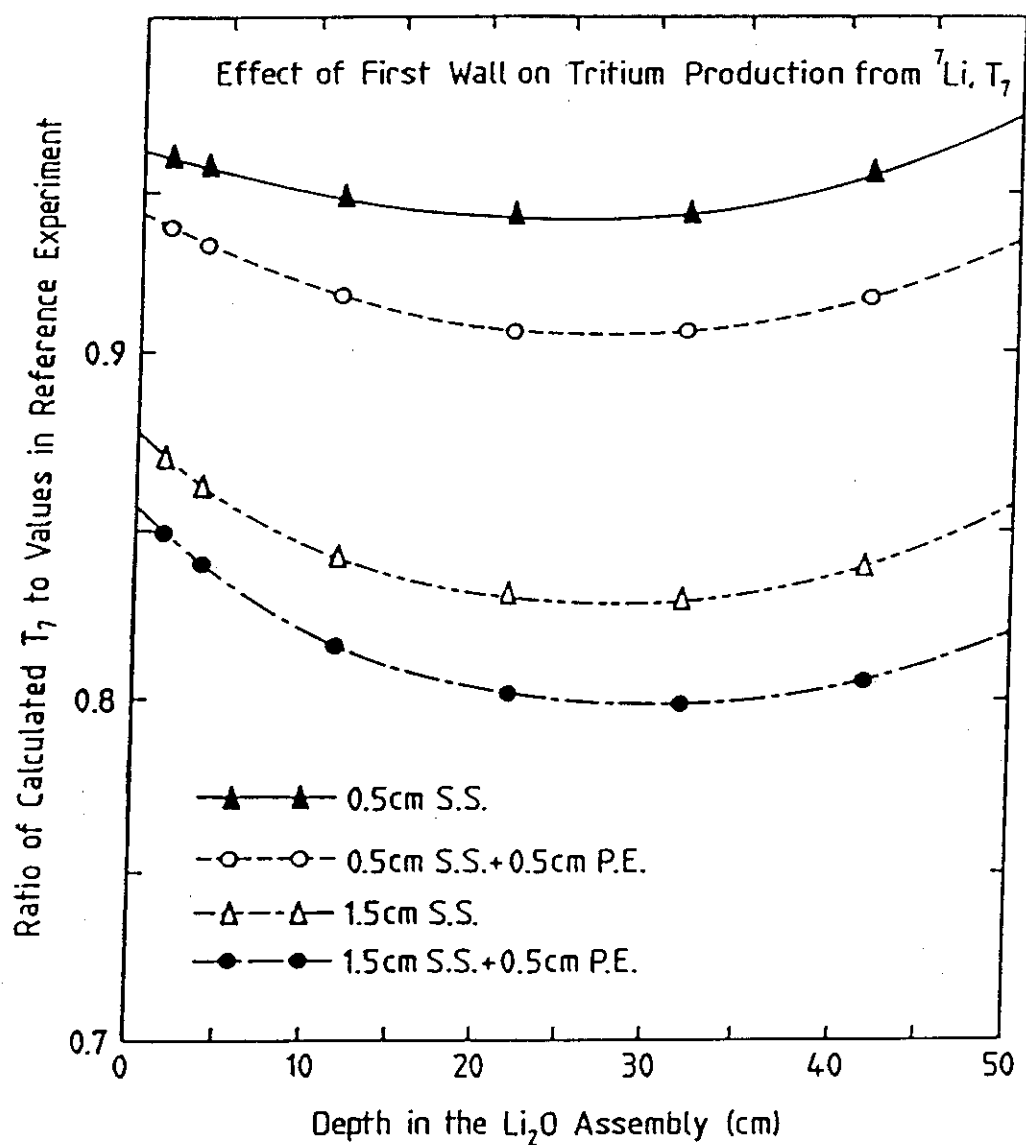


Figure IV.14 Effect of first wall on tritium production from ${}^7\text{Li}$, T_7 (U.S. calculation: DOT4.3/MATXS6)

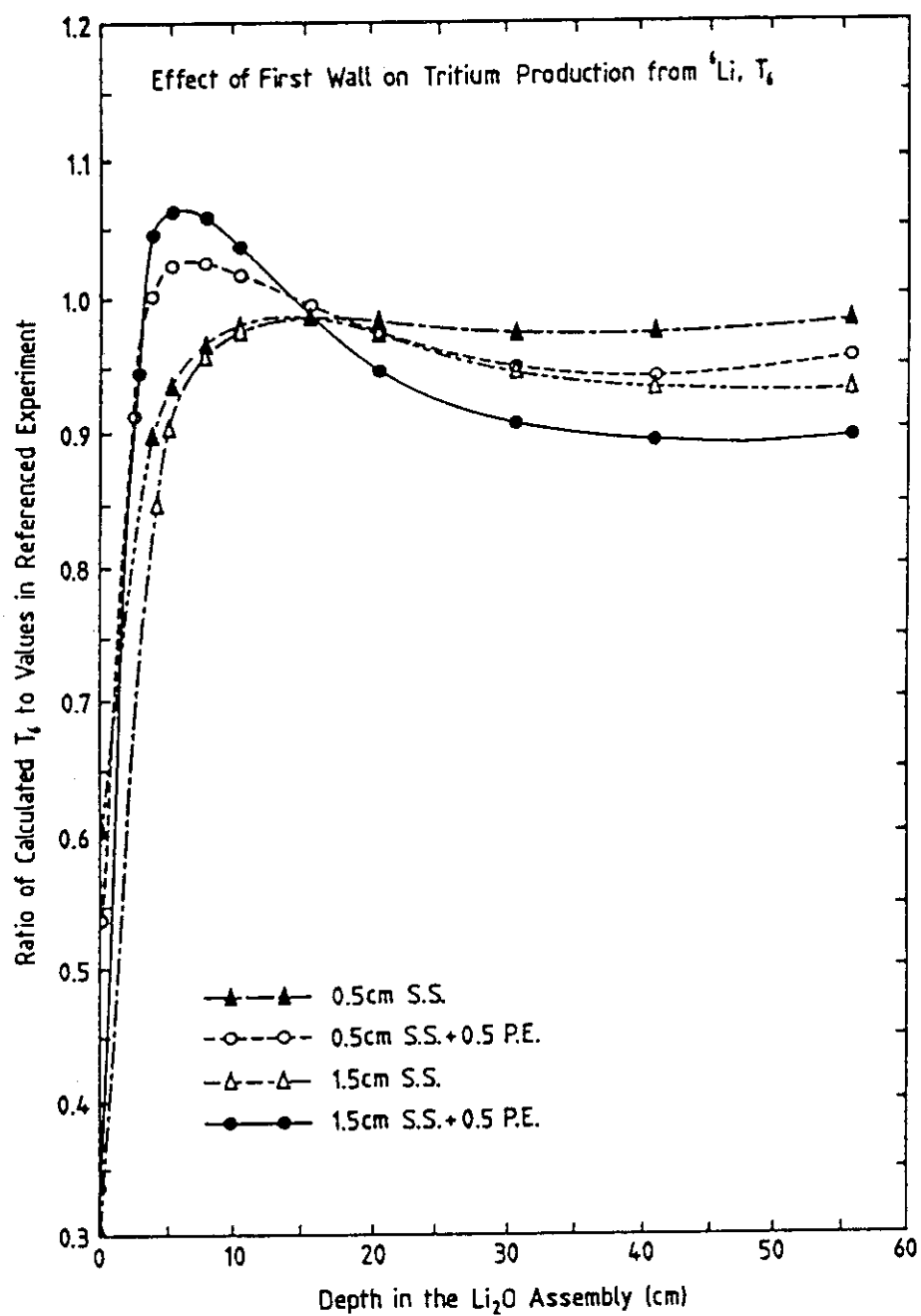


Figure IV.15 Effect of first wall on tritium production from ${}^6\text{Li}$, T_6 (U.S. calculation: DOT4.3 /MATXS6)

Table IV.1 Ratio of the Calculated Tritium Production Rate from ^7Li to the Values in the Reference Li_2O Assembly^(a)

Location (cm)	0.5 cm SS	1.5 cm SS	0.5 cm SS 0.5 cm PE	1.5 cm SS 0.5 cm PE
1.60	0.955	0.866	0.937	0.842
3.88	0.950	0.855	0.928	0.834
11.47	0.943	0.838	0.915	0.813
21.59	0.940	0.830	0.907	0.800
31.71	0.938	0.826	0.903	0.795
41.85	0.937	0.823	0.900	0.791

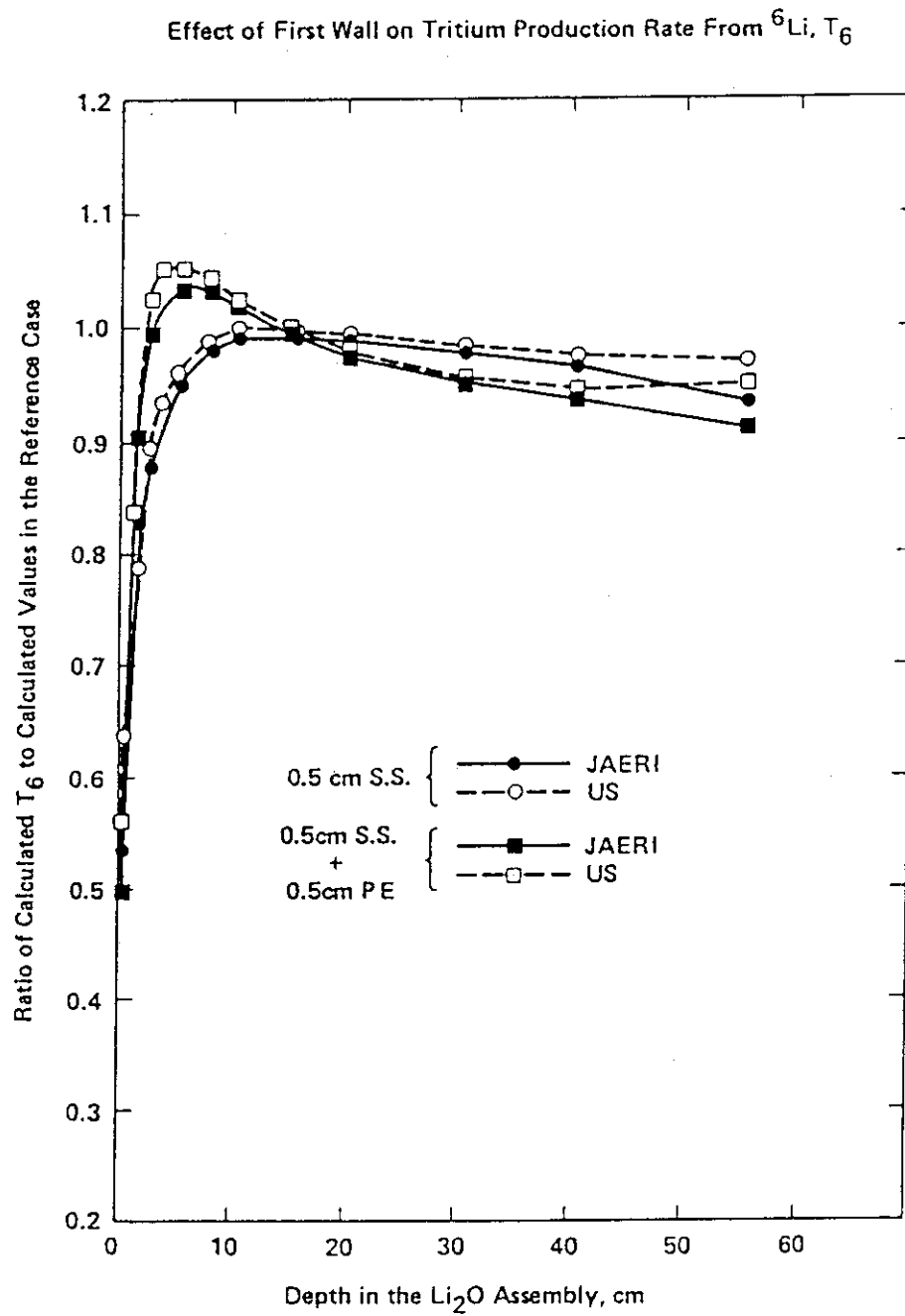
(a) Calculation performed using DOT4.3 + GRTUNCL, MATXS6 Library (80-n, ENDF/B-V), and Young's evaluation for $^7\text{Li}(n,n'\alpha)t$ cross section.

Table IV.2 Ratio of Calculated Tritium Production Rate
From ${}^6\text{Li}$, T_6 , to the Reference Experiment

Location (cm)	0.5 cm S.S.		1.5 cm S.S.		0.5 cm S.S. 0.5 cm PE		1.5 cm S.S. 0.5 cm PE	
	U.S.(a)	JAERI(b)	U.S.	JAERI	U.S.	JAERI	U.S.	JAERI
0.25	0.635	0.536	0.327	0.261	0.569	0.497	0.352	0.297
1.26	0.784	0.826	0.568	0.592	0.839	0.908	0.754	0.840
2.53	0.896	0.879	0.800	0.736	1.026	0.994	1.057	1.023
3.81	0.936	---	0.883	---	1.052	---	1.096	---
5.06	0.959	0.949	0.930	0.893	1.056	1.032	1.099	1.087
7.61	0.984	0.979	0.978	0.961	1.044	1.032	1.076	1.076
10.12	0.994	0.989	0.994	0.985	1.028	1.019	1.045	1.045
15.20	0.996	0.991	0.992	0.986	0.999	0.993	0.993	0.989
20.24	0.993	0.987	0.979	0.971	0.980	0.974	0.957	0.951
30.38	0.984	0.976	0.952	0.941	0.959	0.952	0.916	0.908
40.45	0.977	0.966	0.934	0.917	0.948	0.937	0.895	0.882
55.72	0.970	0.933	0.916	0.884	0.941	0.910	0.880	0.851

(a) DOT4.3/MATXS6 calculations

(b) DOT3.5/JACKAS calculations

Figure IV.16 Effect of first wall on tritium production rate from ${}^6\text{Li}$, T_6

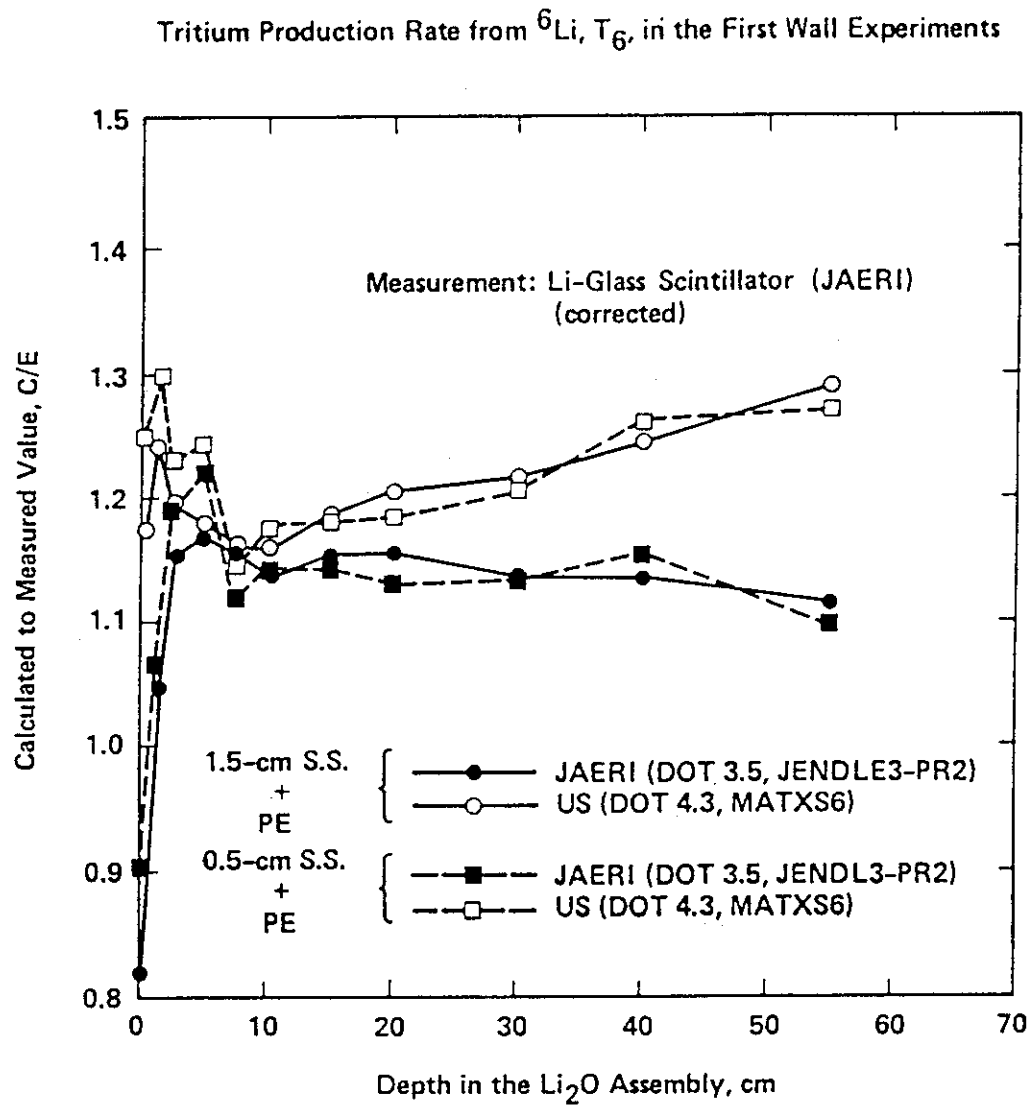


Figure IV.17 The C/E values for tritium production rate from ${}^6\text{Li}$, T_6 in the first wall experiment without a polyethylene layer (2-D model)

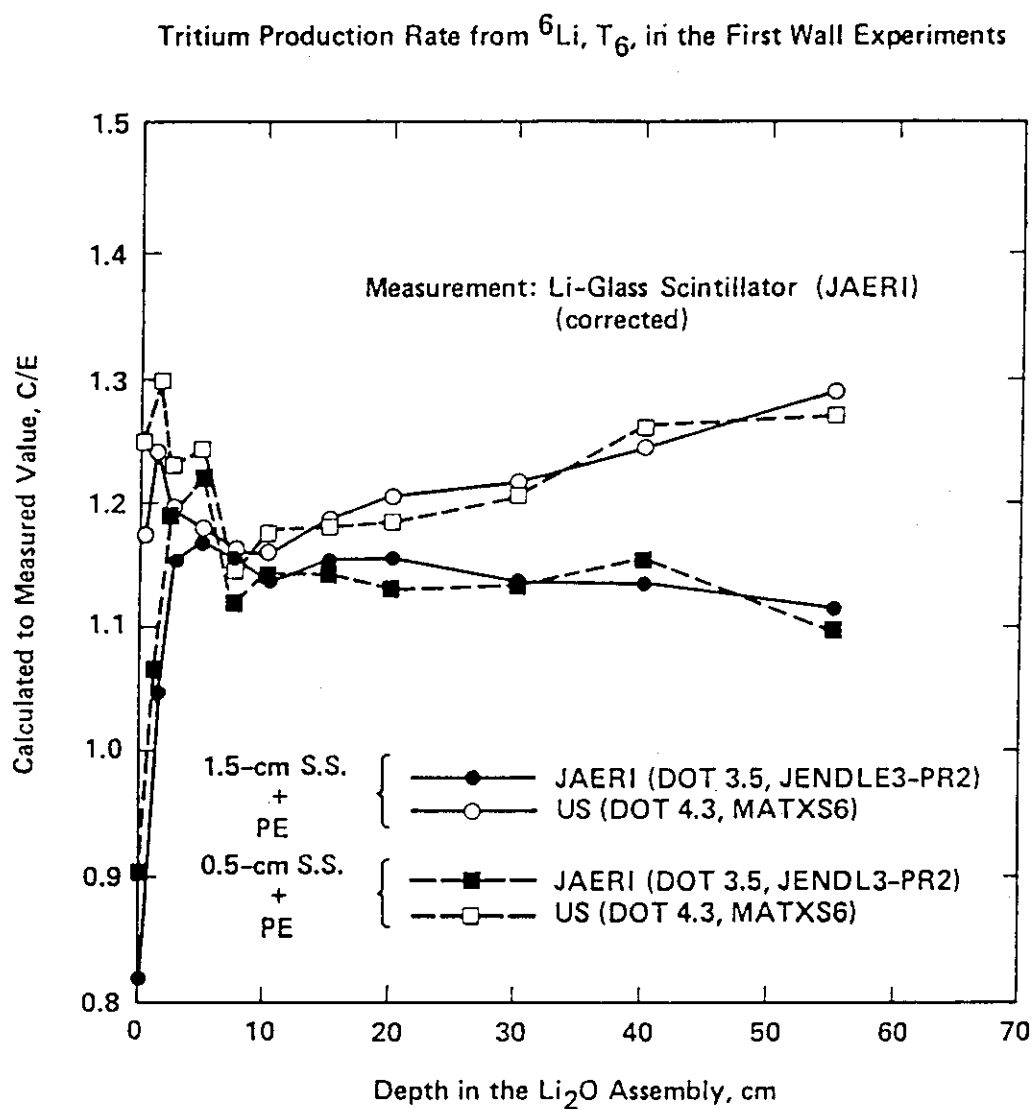


Figure IV.18 The C/E values for tritium production rate from ${}^6\text{Li}$, T_6 in the first wall experiments, with a polyethylene layer (2-D model)

Table IV.3 Calculated to Measured Values for Tritium Production Rate
From ${}^6\text{Li}$ In the First Wall Experiment along the Central Axis (a),(b)

Location (cm)	Reference		0.5 cm S.S.		1.5 cm S.S.		0.5 cm S.S. 0.5 cm PE		1.5 cm S.S. 0.5 cm PE	
	U.S.	JAERI	U.S.	JAERI	U.S.	JAERI	U.S.	JAERI	U.S.	JAERI
0.25	0.965	0.801	1.028	0.719	1.125	0.746	1.252	0.906	1.171	0.819
1.26	1.415	1.073	1.344	1.072	1.309	1.033	1.305	1.069	1.240	1.046
2.53	1.263	1.265	1.260	1.238	1.251	1.125	1.227	1.192	1.193	1.157
3.81	1.236	1.252	---	---	---	---	---	---	---	---
5.06	1.275	1.279	1.274	1.264	1.235	1.189	1.245	1.221	1.179	1.170
7.61	1.245	1.235	1.217	1.202	1.145	1.116	1.141	1.119	1.166	1.157
10.12	1.188	1.167	1.192	1.166	1.166	1.135	1.172	1.142	1.159	1.139
15.20	1.194	1.160	1.198	1.157	1.206	1.165	1.185	1.143	1.189	1.151
20.24	1.216	1.170	1.217	1.163	1.251	1.193	1.183	1.130	1.208	1.154
30.38	1.196	1.132	1.221	1.147	1.208	1.129	1.209	1.136	1.215	1.139
40.45	1.247	1.158	1.258	1.154	1.252	1.142	1.261	1.157	1.242	1.136
55.72	1.294	1.152	1.269	1.086	1.305	1.121	1.270	1.093	1.292	1.113

(a) Experimental values are corrected for self-shielding effect

(b) U.S.: MATXS6 Library (ENDF/B-V, 80-g), JAERI: JENDL3-PR2 (125-g)

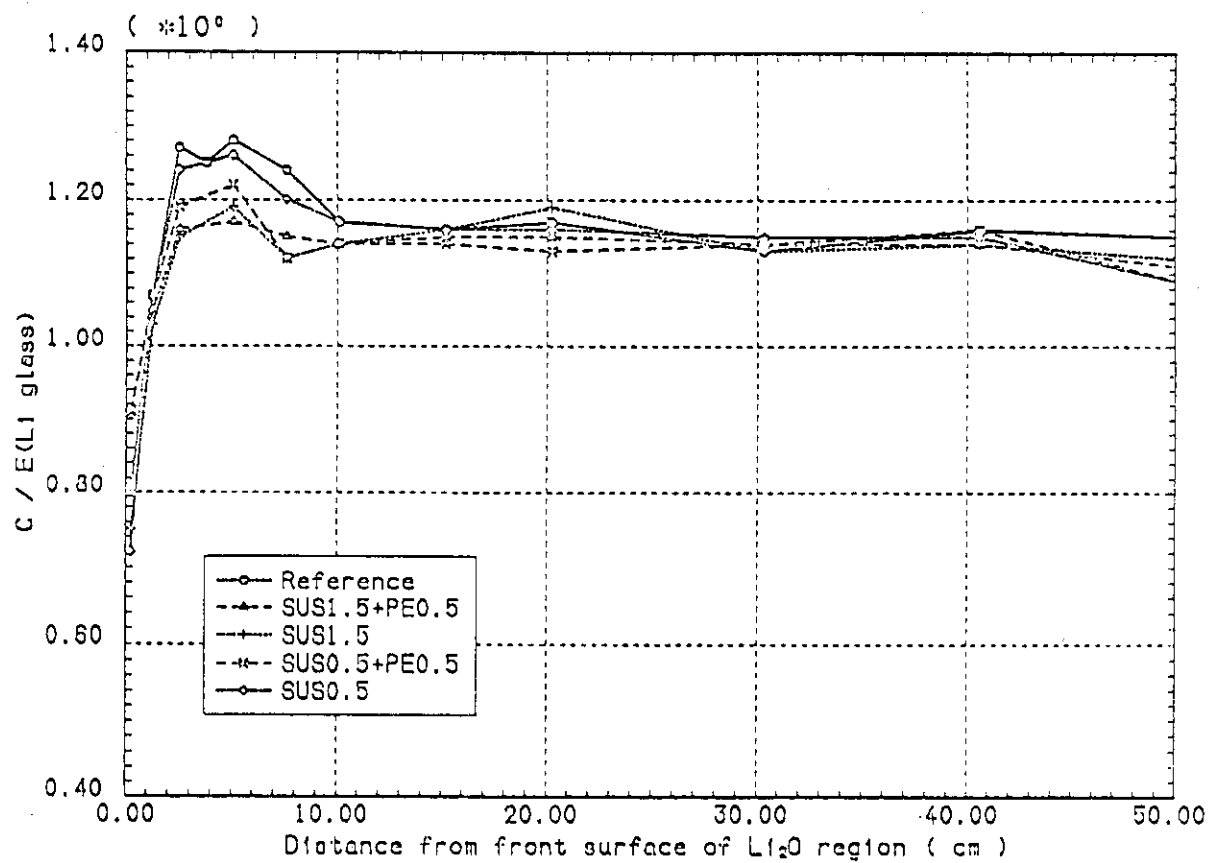


Figure IV.19 C/E values for T_6 in the first wall experiments, based on the calculated values by DOT3.5/JACKAS (JAERI)

note from Fig. IV.19 that the C/E of the reference case shows the largest values in the region $2\text{ cm} < Z < 10\text{ cm}$, and that the existence of a polyethylene slab in addition to the 0.5 cm first wall reduces C/E values by about 5% in this region. The fluctuation of the C/E values for the case with a 1.5 cm thick first wall is rather large over the system.

As mentioned earlier, the predictions for T_6 obtained by the U.S. are larger than those obtained by JAERI. The ratios of the calculated T_6 by the U.S. to the corresponding values by JAERI are shown in Table IV.4 and depicted in Fig. IV.20. At $Z > 5\text{ cm}$, the calculations of the U.S. are larger by 2-15% than JAERI's calculations and the largest discrepancies occur at back locations in all the systems considered. These discrepancies also get larger at front locations ($Z < 5\text{ cm}$), especially for the 1.5 cm-thick SS case. Sources of these discrepancies could be attributed to the fact that the MATXS6 library used by the U.S. has fewer groups (80-g) and different weighting functions than the JACKAS library (125-g) used by JAERI. In a parallel analysis, it was demonstrated that a fewer-group library (e.g., MATXS5, 30-g) gives ~10% larger T_6 values than those obtained by a relatively finer-group library such as MATXS6.

A comparison with calculations for the TPR from ${}^7\text{Li}$ is presented in Figures IV.21 and IV.22. The C/E values increase at the front region ($Z < 5\text{ cm}$) but decrease with increasing distance from the surface. The agreement between the measurements and calculations performed by JAERI are satisfactory for all cases. The C/E values are 1.02-1.05 in all the first wall and reference experiments. The corresponding values obtained by the U.S. are 1.13-1.18, and it seems that the larger values obtained by the U.S. (~11-13% difference) are basically due to the difference in the ${}^7\text{Li}(n,n'\alpha)t$ cross-section used by both parties, as was mentioned earlier. As was discussed in the reference case, however, the measured values may have some uncertainties. The NE213 method determines T_7 by using the measured neutron flux and the group cross-sections, hence systematic errors due to ${}^7\text{Li}(n,n'\alpha)t$ cross-sections may be involved in this method.

IV.2.2 Monte Carlo Analysis

In the Monte Carlo analysis performed by the U.S. (ORNL) using the MCNP and the MORSE codes, five configurations were considered, namely the reference experiment, and the four configurations of the first wall experiment (see Table IV.5). The calculational model used in these calculations was described in Section II.

The measured and calculated tritium production rates from ${}^6\text{Li}$ in the experimental configurations given in Table IV.5 is compared in Figures IV.23 to IV.27. In the figures, the open circles are the measured data and the solid and dashed histograms are the calculated TPR rate obtained from MORSE and MCNP, respectively. The curve connecting the measured data points is included only to show the trend in the measured TPR rate and has not been fitted to the data. The experimental uncertainties in the measured data are small (~2-3%) and correspond, approximately, to the size of the circles. The error bars on the histograms indicate plus and minus one standard deviation in the tritium production rate in the front of the Li_2O assembly. The measured and calculated data are normalized to one source neutron per ${}^6\text{Li}$ atom.

Table IV.4 Ratios of the Calculated T_6 by U.S. to the Calculated T_6 by JAERI in the First Wall Experiments^(a)

Location (cm)	Reference	0.5 cm S.S.	1.5 cm. S.S.	0.5 cm SS 0.5 cm PE	1.5 cm S.S. 0.5 cm PE
0.25	1.206	1.430	1.508	1.382	1.430
1.26	1.321	1.254	1.268	1.221	1.186
2.53	0.998	1.026	1.086	1.030	1.031
3.81	0.998	----	----	----	----
5.06	0.997	1.008	1.039	1.019	1.008
7.61	1.007	1.018	1.026	1.019	1.008
10.12	1.017	1.022	1.027	1.027	1.018
15.20	1.029	1.035	1.036	1.036	1.033
20.24	1.040	1.046	1.049	1.046	1.046
30.38	1.057	1.065	1.070	1.064	1.066
40.45	1.077	1.090	1.096	1.089	1.093
55.72	1.124	1.168	1.164	1.162	1.161

(a) Calculation; U.S., DOT4.3, MATXS6 ((80-g), B5
JAERI, DOT3.5, JENDL-3PR2 (125-g)

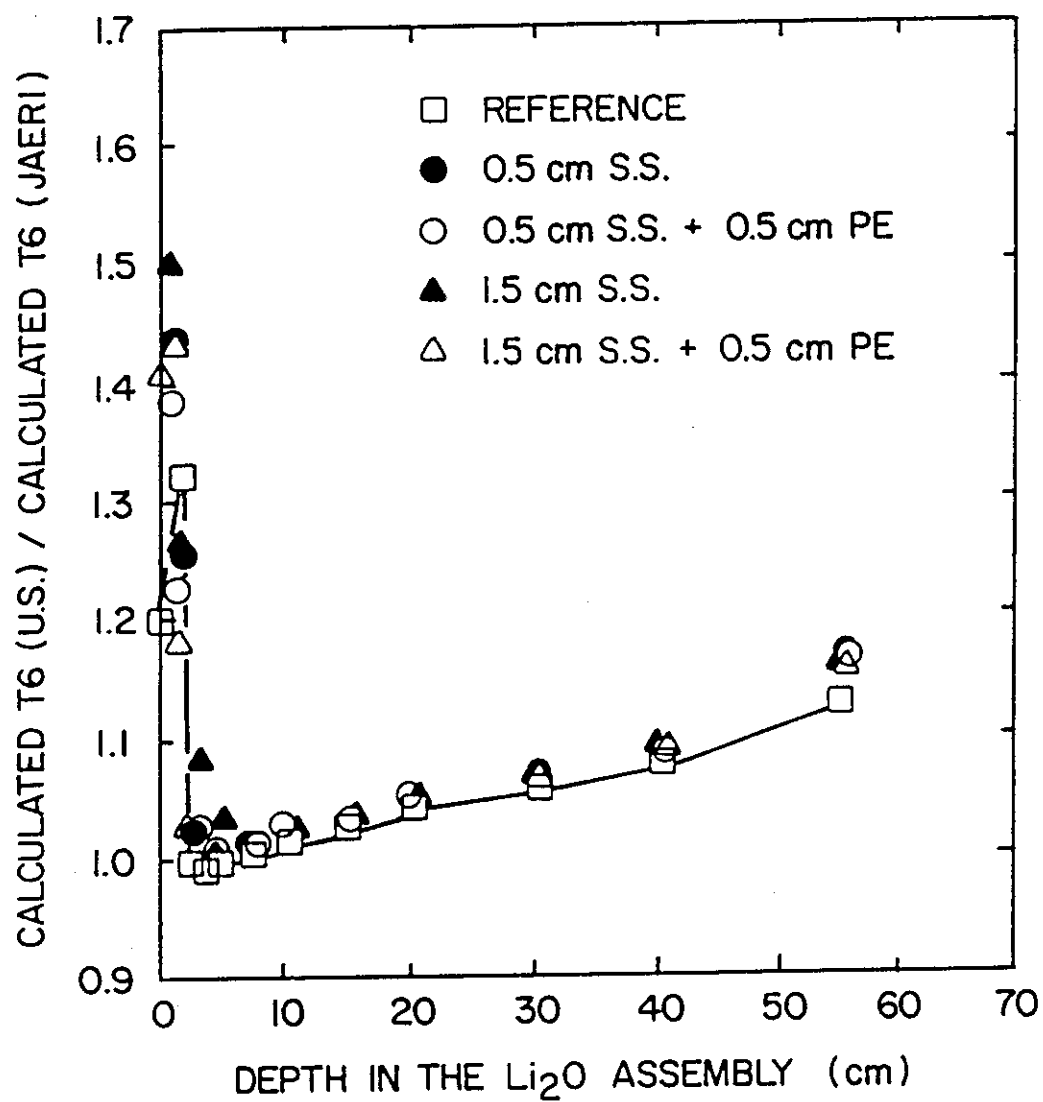


Figure IV.20 Ratio of the calculated T_6 by U.S. to calculated T_6 by JAERI in the first wall experiments (2-D model)

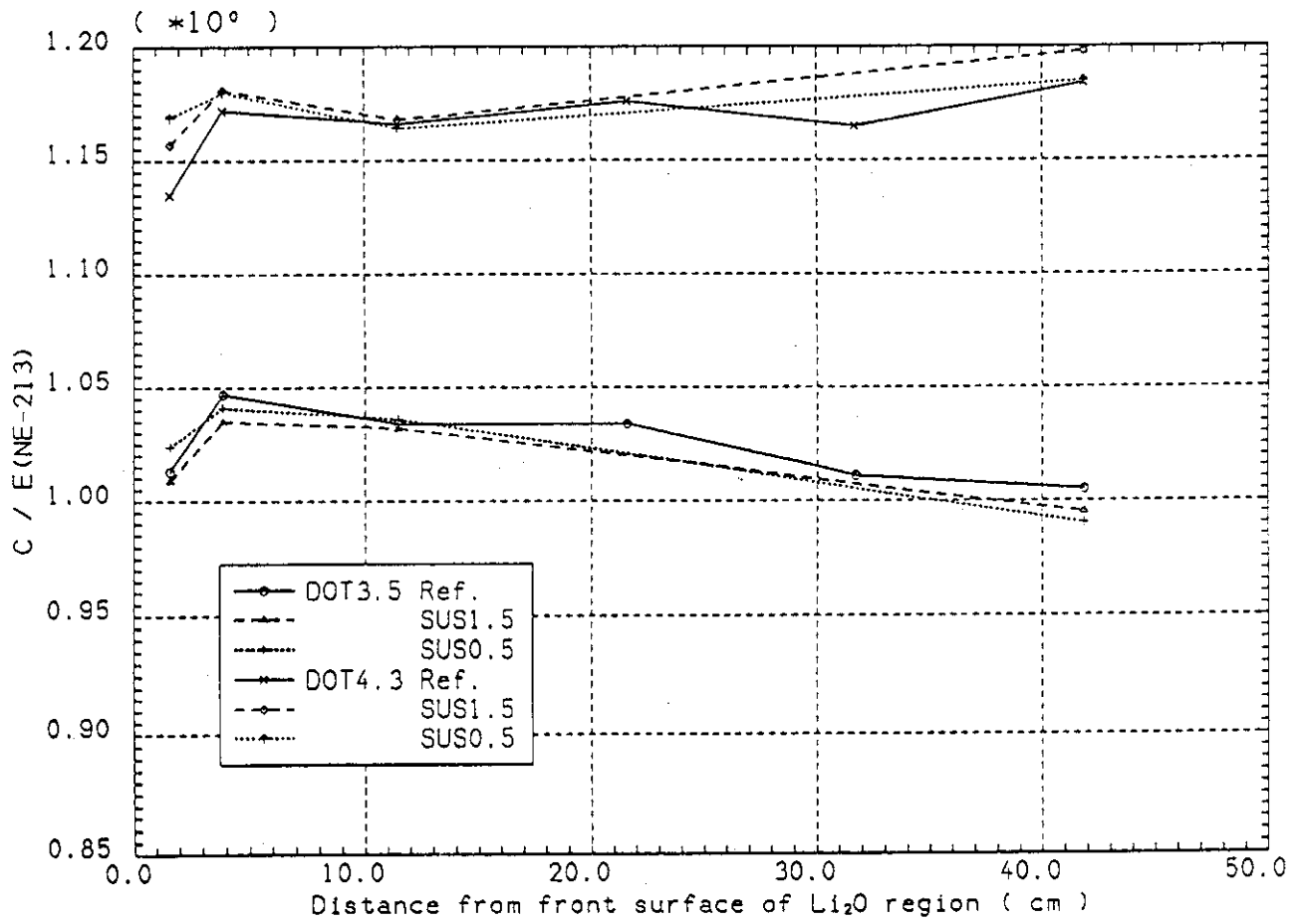


Figure IV.21 C/E values for T7 in the first wall experiments (without a coolant channel)

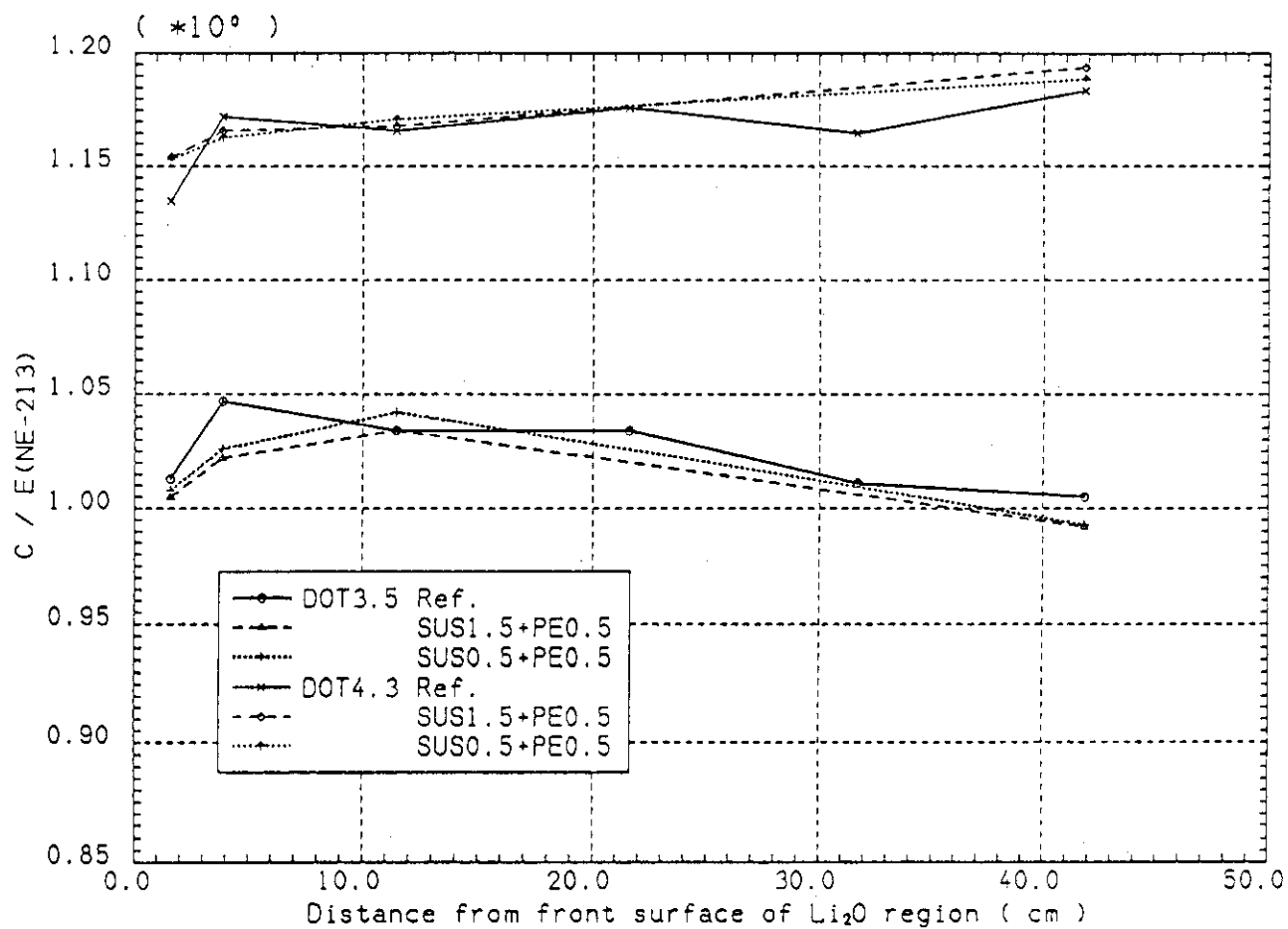


Figure IV.22 C/E values for T7 in the first wall experiments (with a coolant channel)

Table IV.5 Experimental Configurations Used in the Monte Carlo Analysis for the First Wall Experiments

Configuration	SS-304 (cm)	Polyethylene (cm)	Li ₂ O Assembly (cm)
1	-	-	61.0
2	0.5	-	61.0
3	1.5	-	61.0
4	0.5	0.5	61.0
5	1.5	1.5	61.0

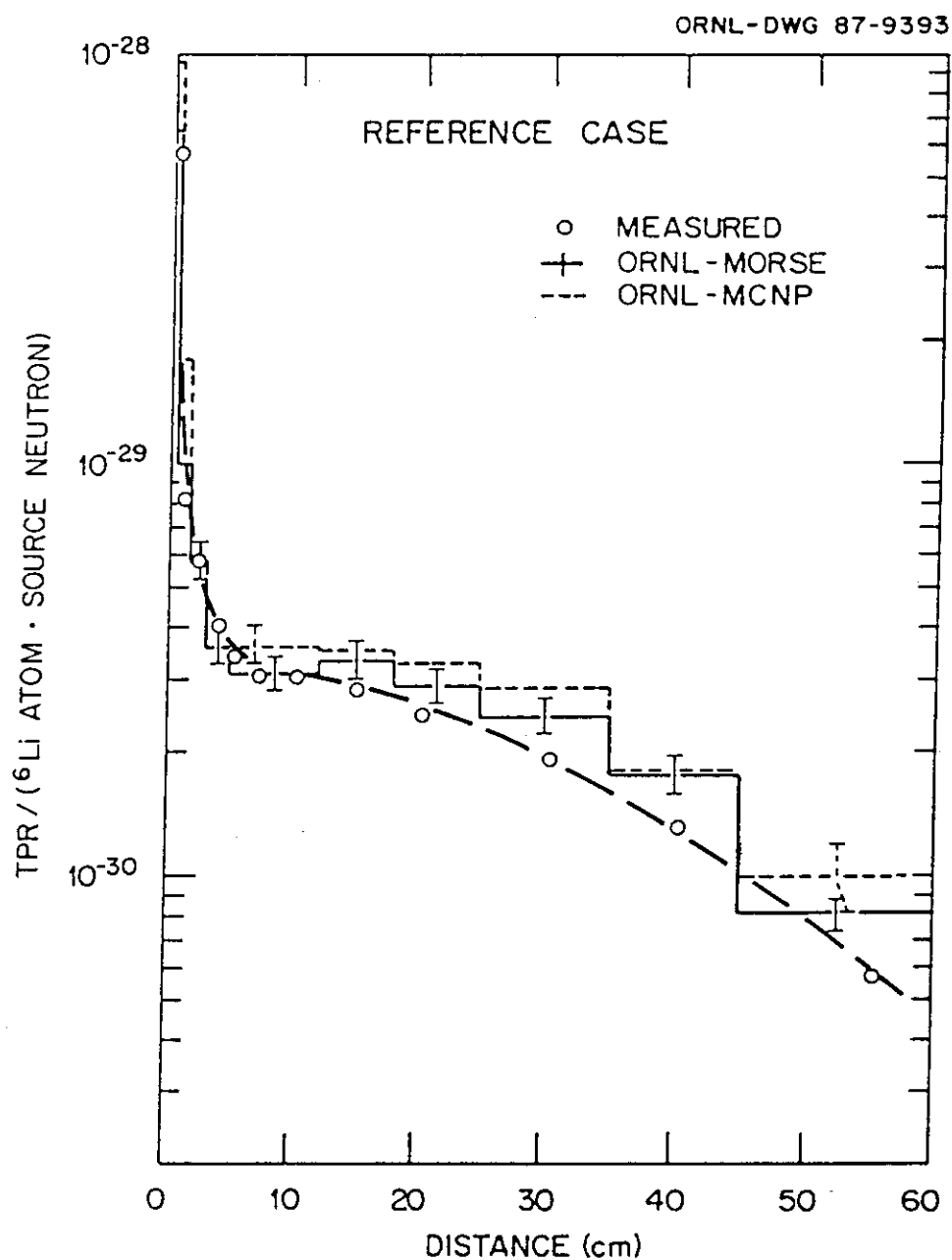


Figure IV.23 Profile of TPR from ${}^6\text{Li}$ in the reference system (U.S.: ORNL calculations)

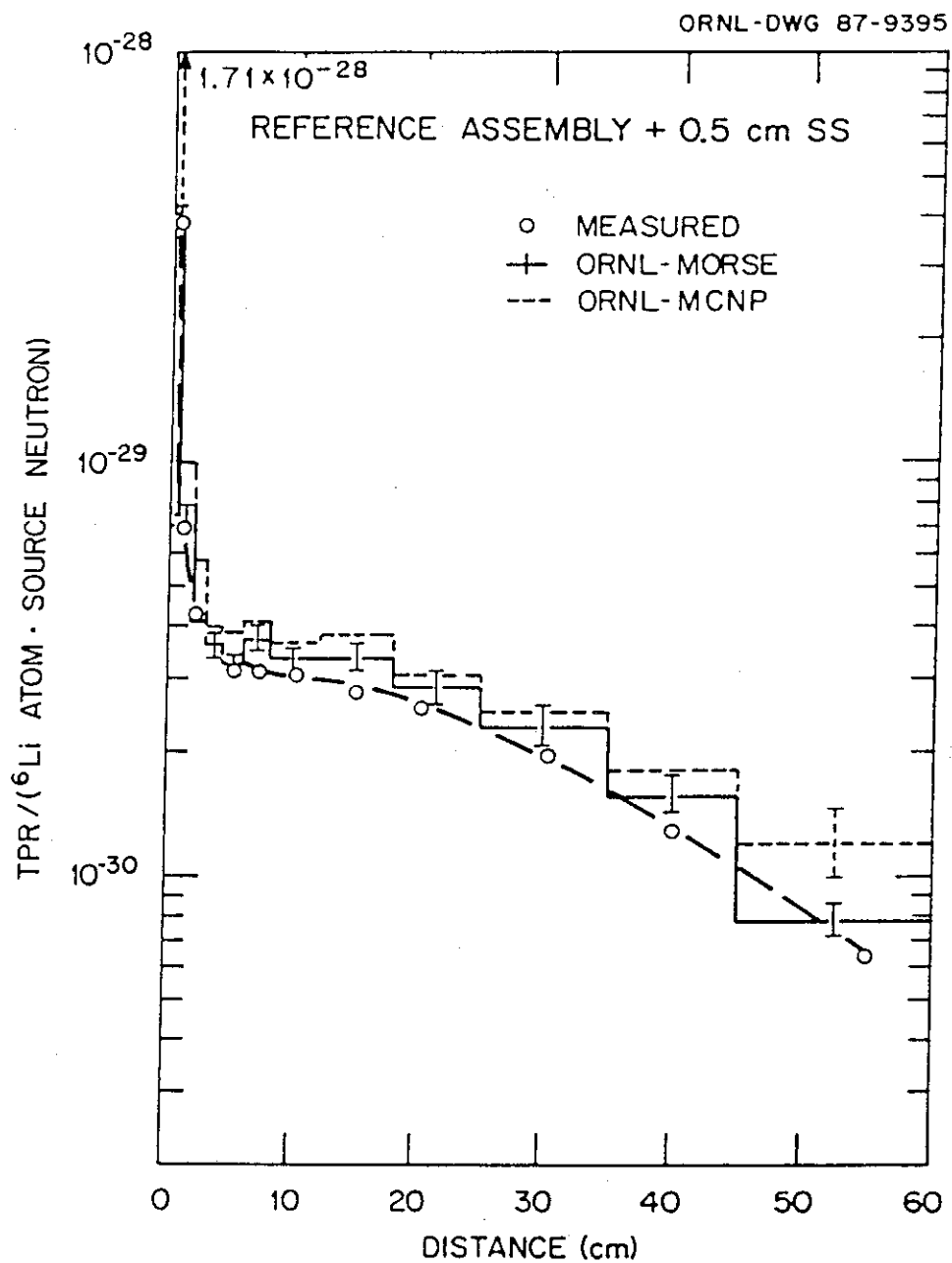


Figure IV.24 Profile of TPR from ${}^6\text{Li}$ in 0.5 cm SS first wall system (U.S.: ORNL calculations)

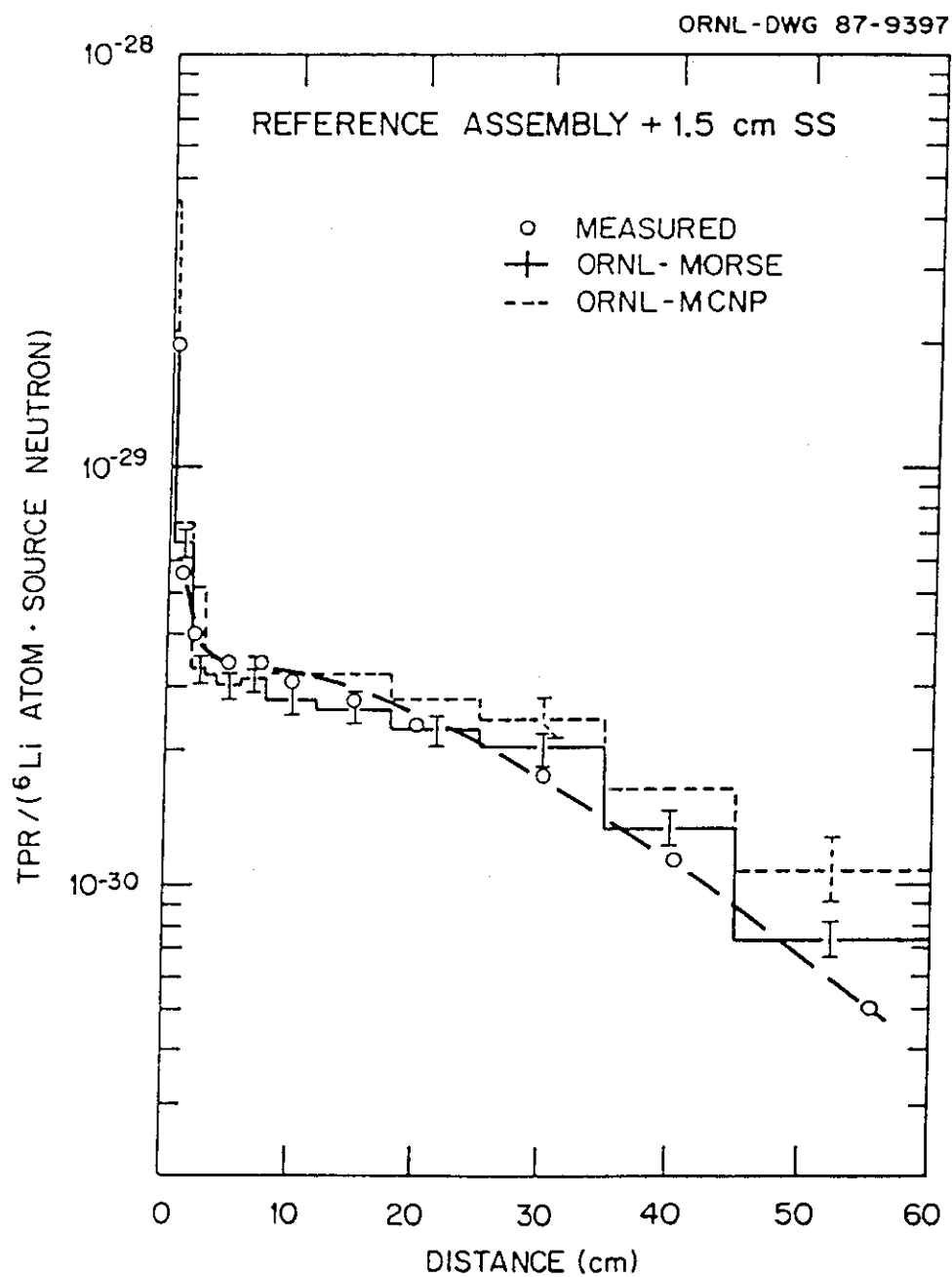


Figure IV.25 Profile of TPR from ${}^6\text{Li}$ in the 1.5 cm SS first wall system (U.S.: ORNL calculations)

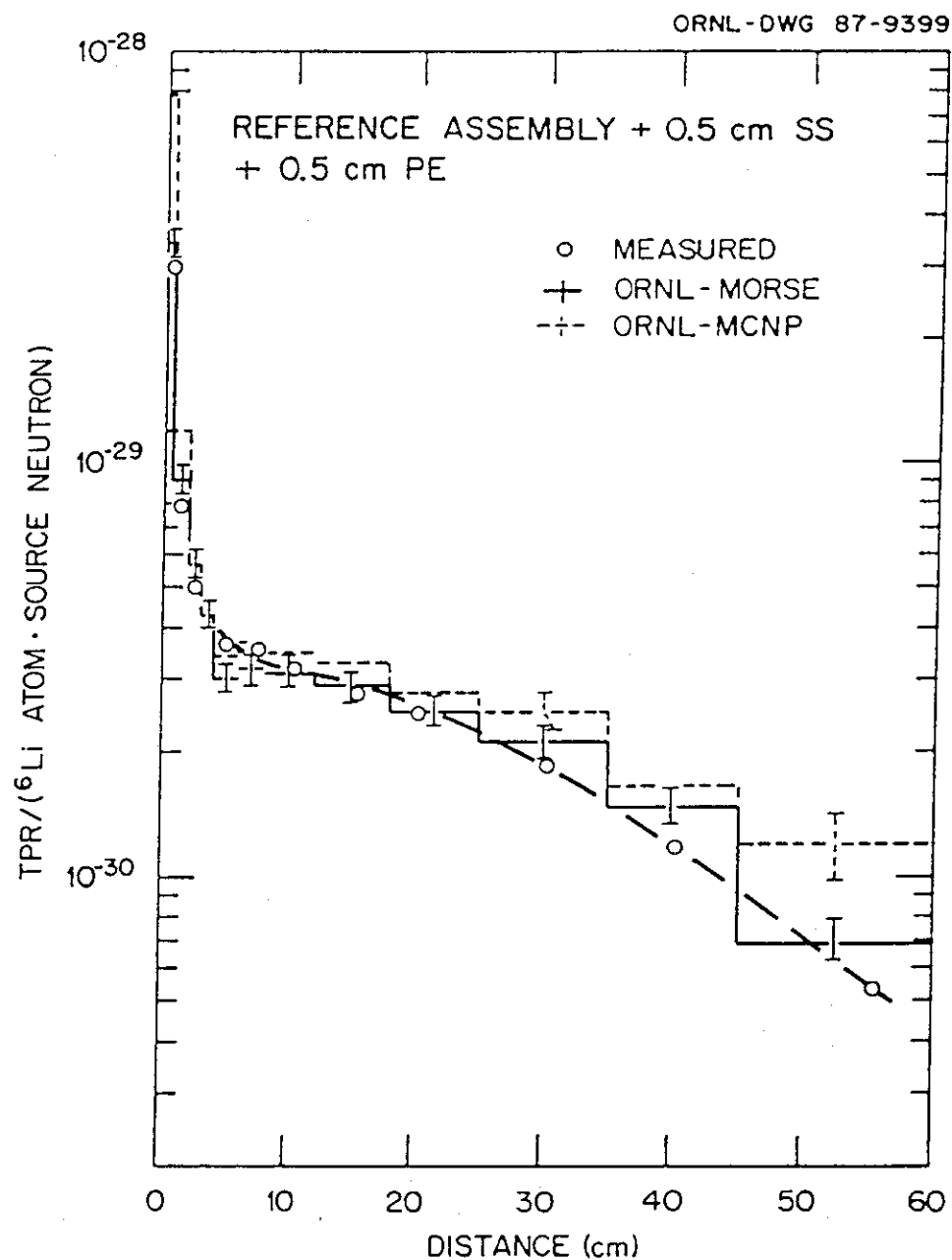


Figure IV.26 Profile of TPR from ${}^6\text{Li}$ in the 0.5 cm + 0.5 cm PE first wall system (U.S.: ORNL calculations)

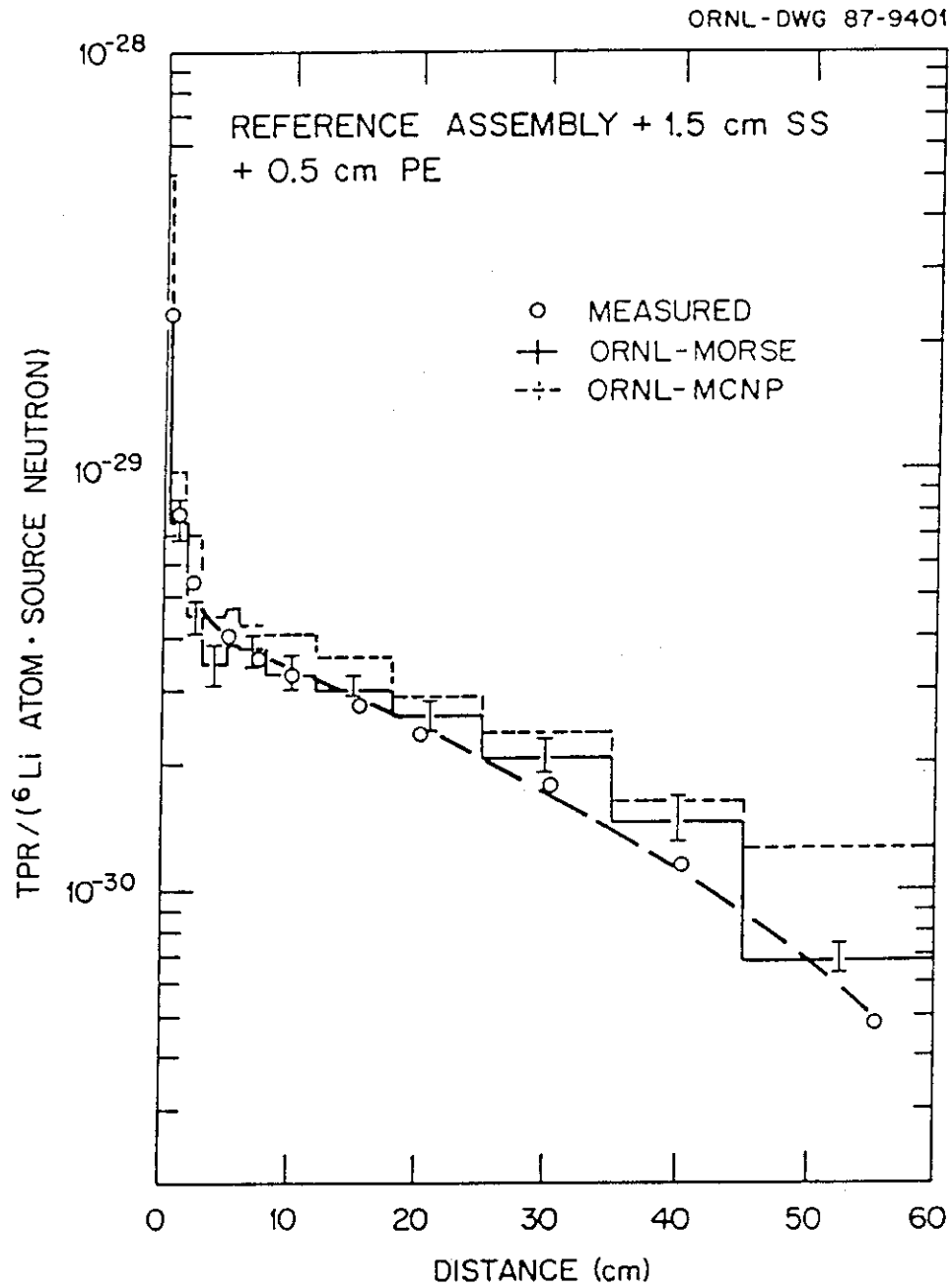


Figure IV.27 Profile of TPR from ${}^6\text{Li}$ in the 1.5 cm SS + 0.5 cm PE first wall system (U.S.: ORNL calculations)

The spatial distribution of the TPR in ${}^6\text{Li}$ is essentially the same for all of the experimental assemblies. The TPR decreases by approximately an order-of-magnitude in the first 10 cm of the Li_2O and then decreases more gradually over the remaining thickness. The same behavior is observed in the calculated data.

The calculated T_6 using the MORSE code is in reasonably good agreement with the measured data over the first 10 cm in the Li_2O assembly for all of the experimental configurations. The MCNP code, on the other hand, overpredicts the measurement at very shallow depths in the Li_2O (< 2.5 cm) and then falls into reasonable agreement at depths between 2.5 and ~ 15 cm. Both calculations overpredict the tritium production from a depth of 20 cm to the rear of the assembly. The calculated data are systematically higher than the measured data, although they agree with each other, within statistics, at distances into the blanket between 10 and ~ 45 cm. MCNP consistently overpredicts both the MORSE and the measured data at the rear of the Li_2O assembly.

The calculated to experimental (C/E) ratios for the MORSE data are shown in Figures IV.28 to IV.32. The MCNP data were not included in these comparisons to minimize confusion in the plotted results and because the C/E ratios show essentially the same trend. The error bars on the data in Figures IV.28 to IV.32 reflect the range in the C/E values imposed by the standard deviations in the calculated data. For the preponderant number of points, the C/E ratio indicates that MORSE reproduces the measurement within nominally 20%. The largest differences between the estimated and measured tritium production data occur at distances greater than 20 cm into the breeding assembly.

The measured and calculated tritium production rates from neutron reactions with ${}^7\text{Li}$ are compared in Figures IV.33 to IV.37. The data points and the histograms have the same meanings as discussed above. These data have also been normalized to one source neutron and per ${}^7\text{Li}$ atom.

The calculated T_7 as a function of distance in the Li_2O assembly reproduces the measured data in shape, but not in magnitude, in all of the experimental configurations except for the case with 0.5 cm of stainless steel (Fig. IV.34). The MORSE and MCNP data consistently overpredict the measurements. However, this may arise in part from the selection of the estimator dimensions used in the collision density and track length estimation; in the two codes (see details in Section II). The interval dimensions were selected to bracket the detector locations for the ${}^6\text{Li}$ assembly, particularly since both sets of calculated data are in reasonably good agreement with each other.

Finally, for completeness, the calculated-to-experimental ratios for the T_7 are compared in Figures IV.38 to IV.42. The C/E values are, in some cases and for specific detect locations, larger than desired and probably due to the selection of the histogram interval size.

The MORSE and MCNP codes reproduce both the ${}^6\text{Li}$ and ${}^7\text{Li}$ measurements in shape. Differences in magnitude may be attributed to a number of causes. The geometry of the experiment challenges a Monte Carlo analysis. The volume of the Li_2O assembly is small compared to the volume of the

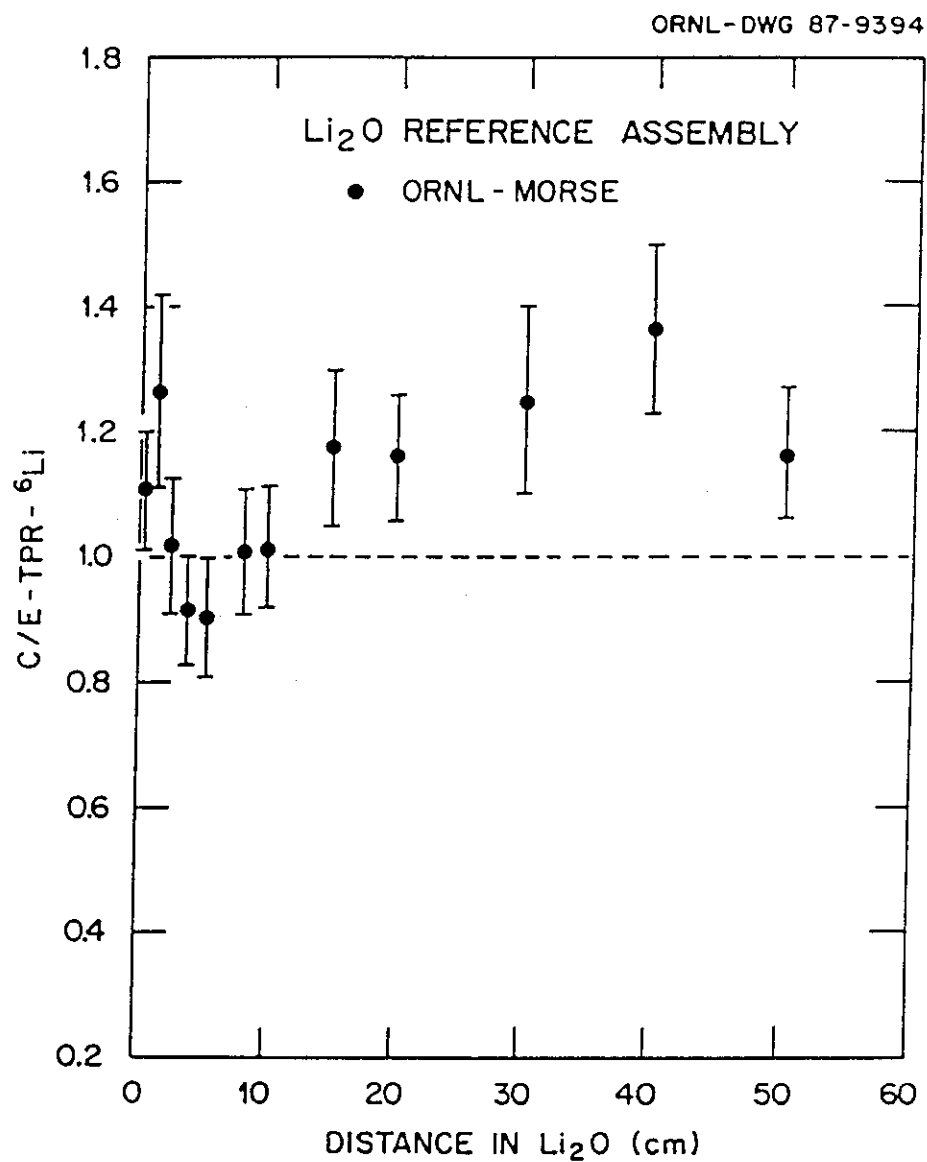


Figure IV.28 C/E values for T₆ in the reference system (U.S.: ORNL calculations)

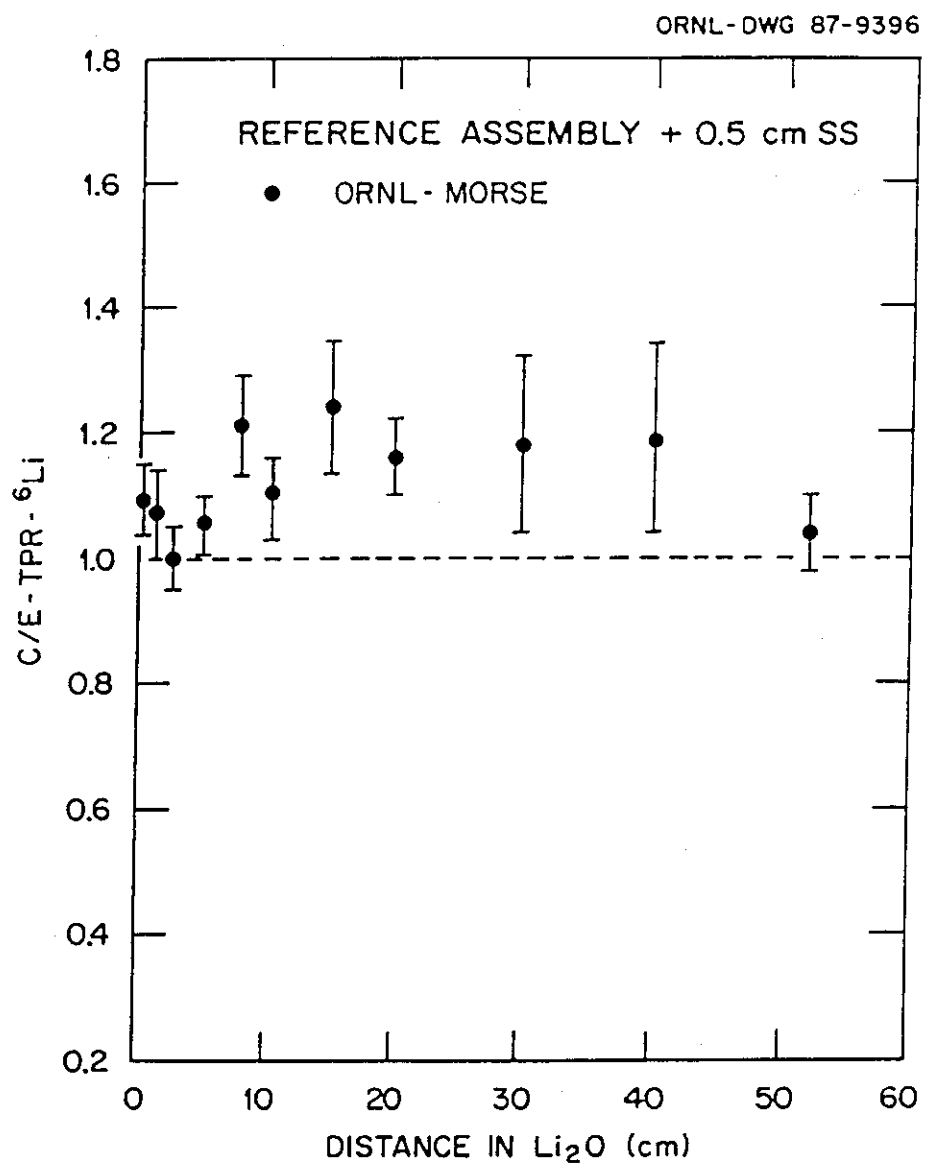


Figure IV.29 C/E values for T_6 in the 0.5 cm SS first wall system (U.S.: ORNL calculations)

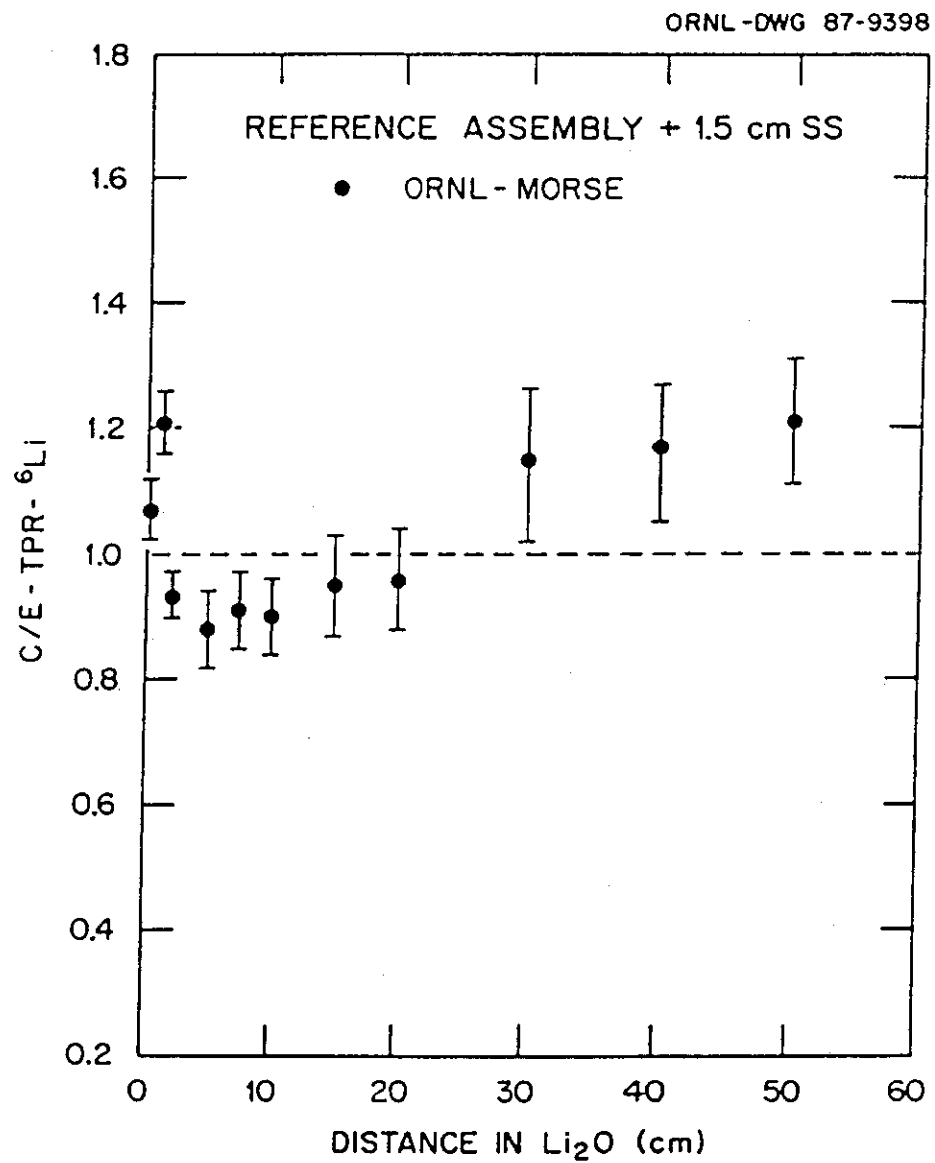


Figure IV.30 C/E values for T_6 in the 1.5 cm SS first wall system (U.S.: ORNL calculations)

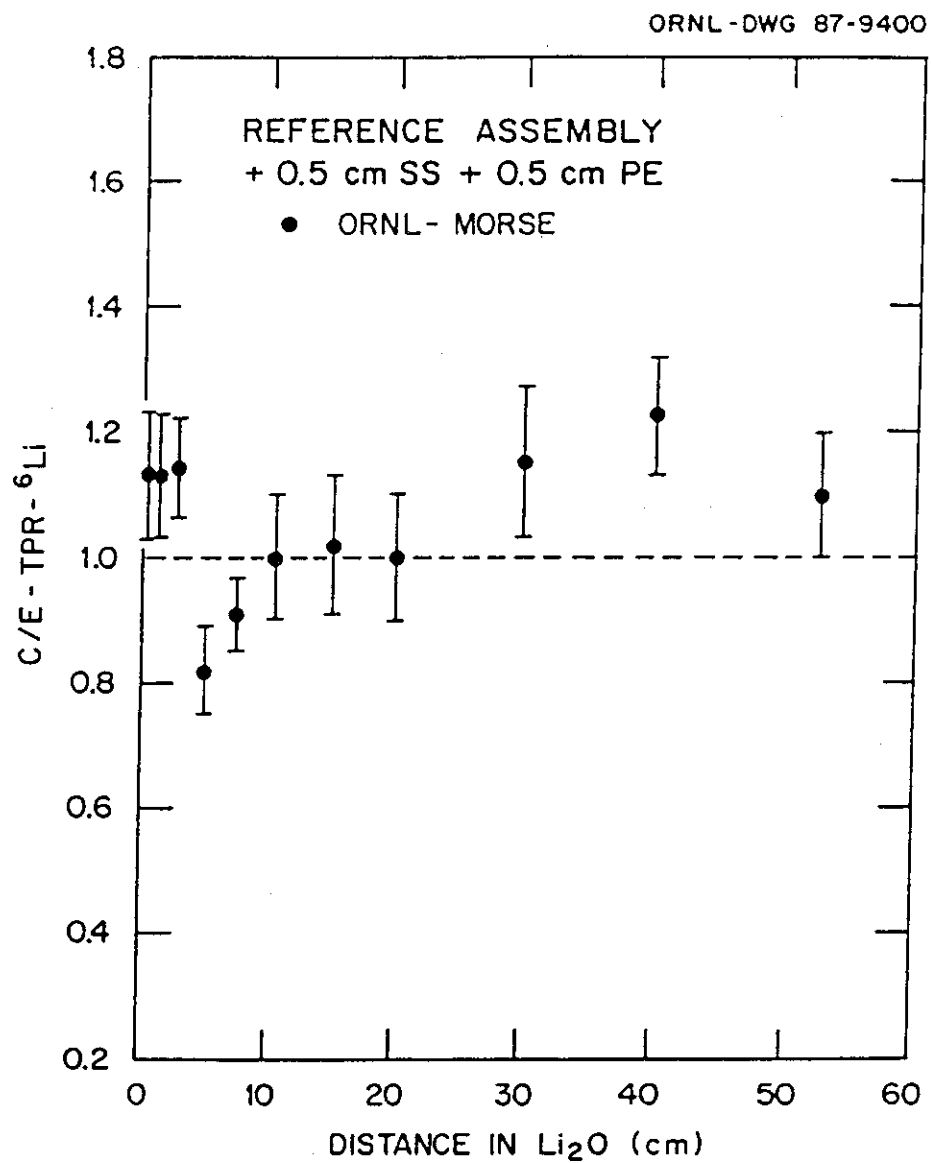


Figure IV.31 C/E calculations for T_6 in the 0.5 cm SS + 0.5 cm PE first wall system (U.S.: ORNL calculations)

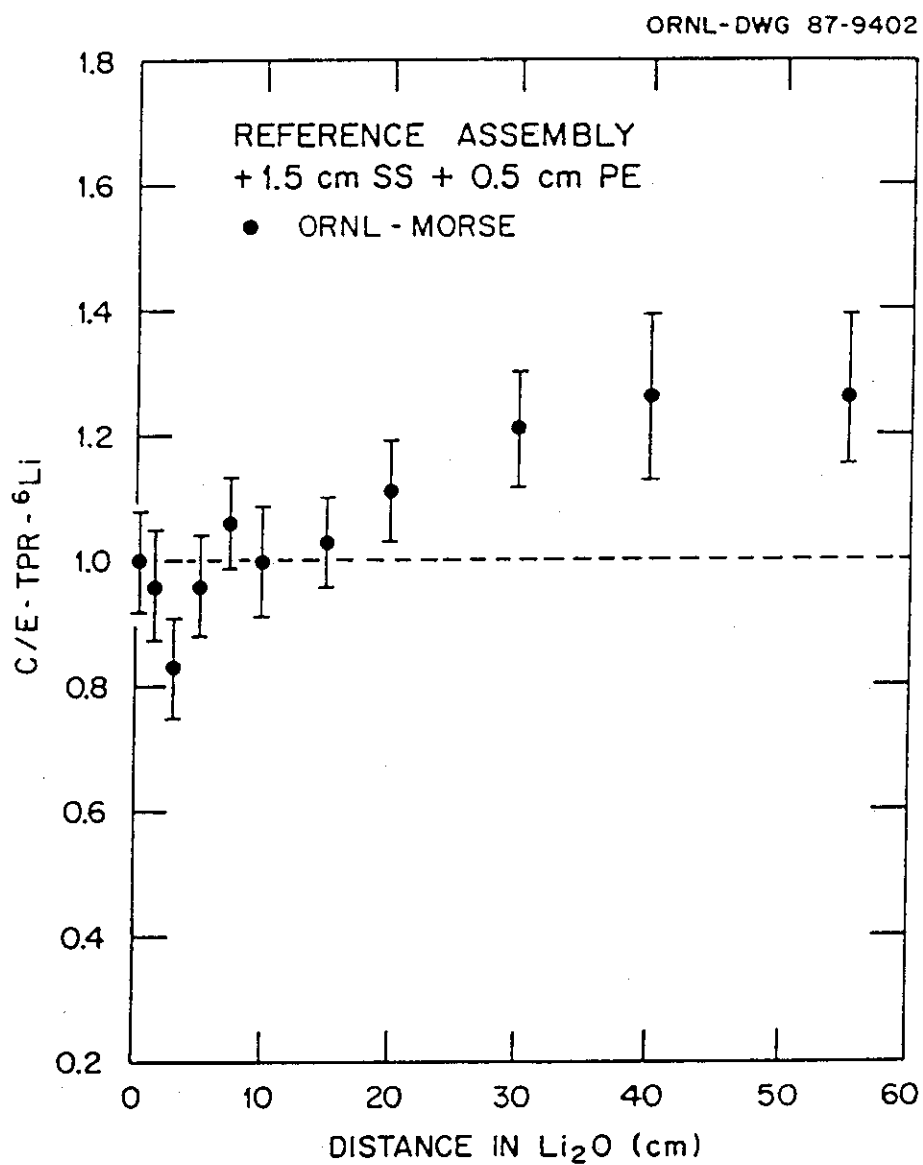


Figure IV.32 C/E values for T₆ in the 1.5 cm SS + 0.5 cm PE first wall system (U.S.: ORNL calculations)

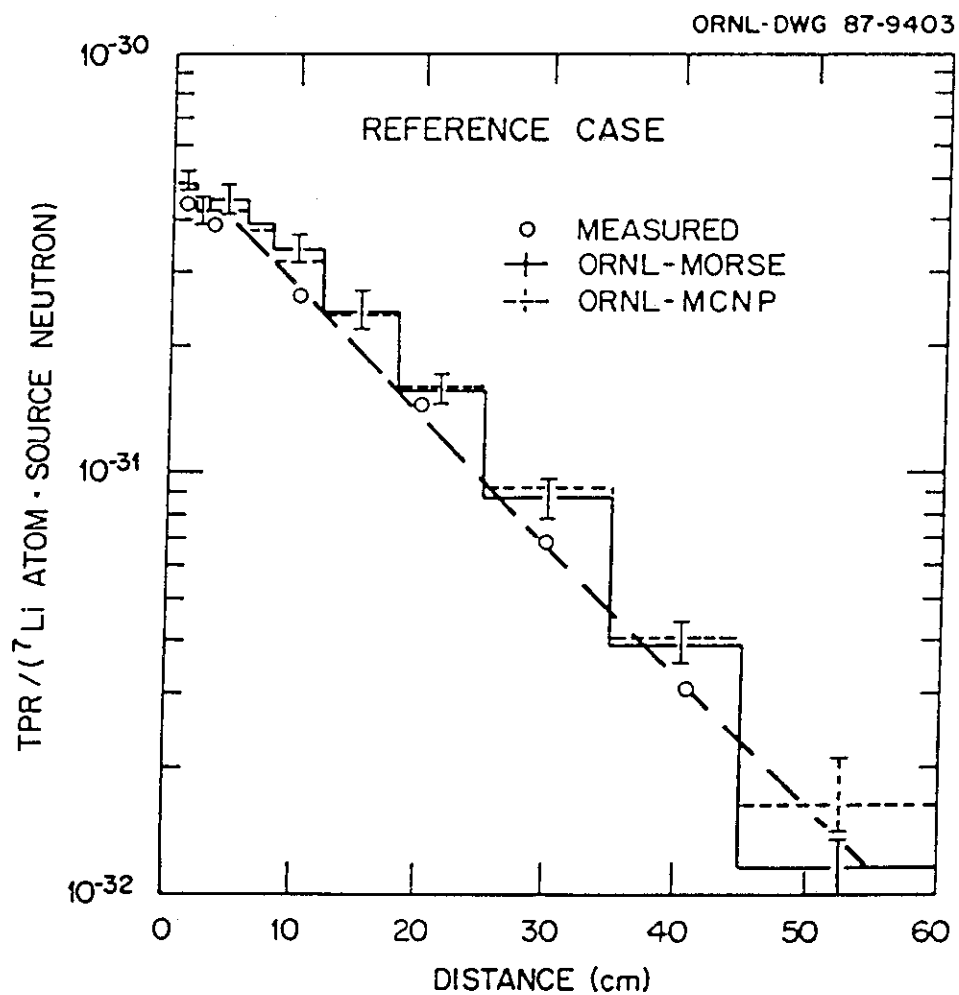


Figure IV.33 Profile for TPR from ${}^7\text{Li}$ in the reference system (U.S.: ORNL calculations)

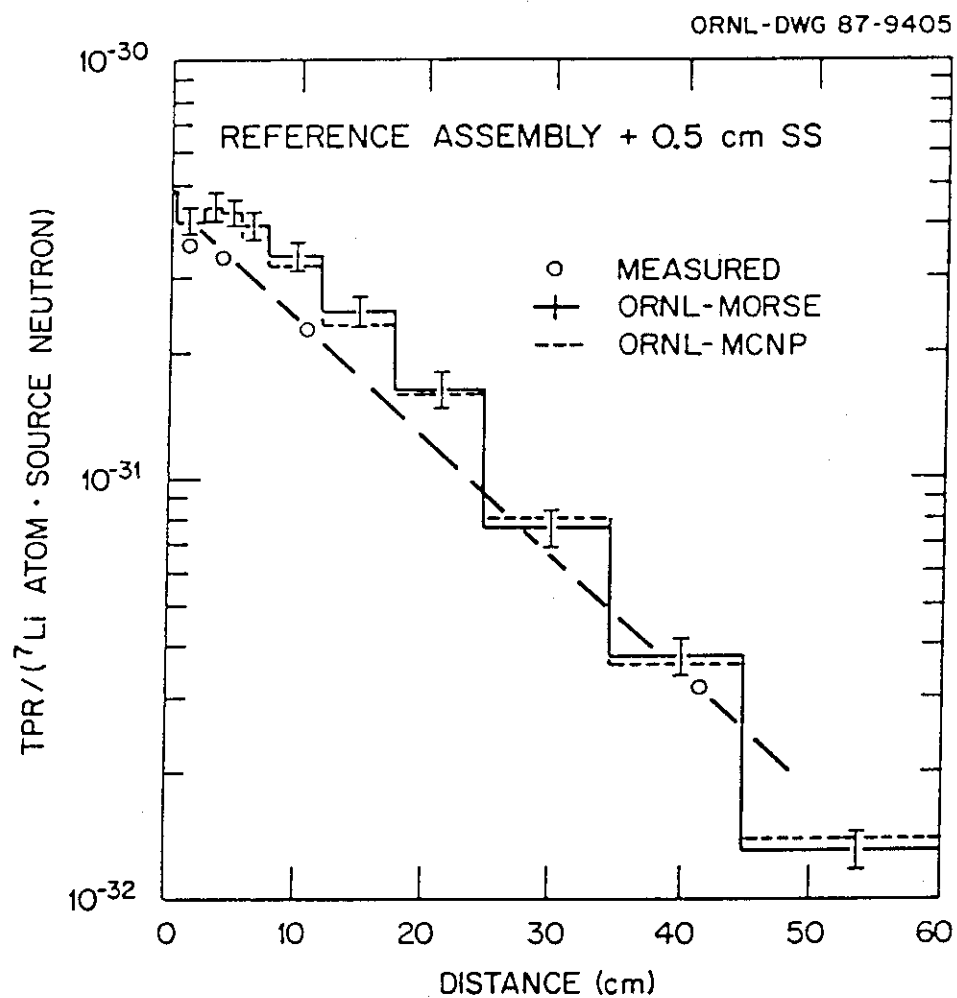


Figure IV.34 Profile of TPR from ${}^7\text{Li}$ in the 0.5 cm SS first wall system (U.S.: ORNL calculations)

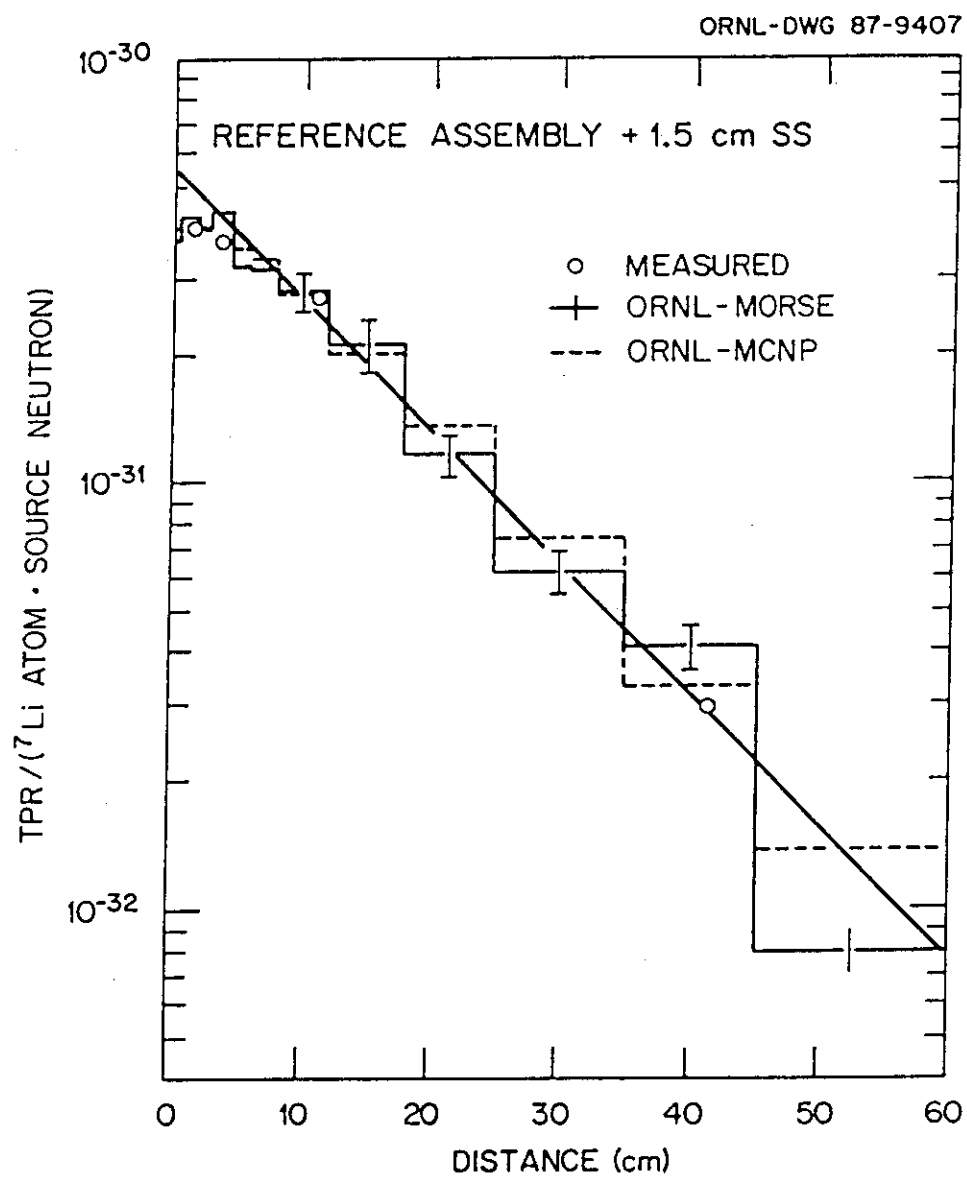


Figure IV.35 Profile of TPR from ${}^7\text{Li}$ in the 1.5 cm SS first wall system (U.S.: ORNL calculations)

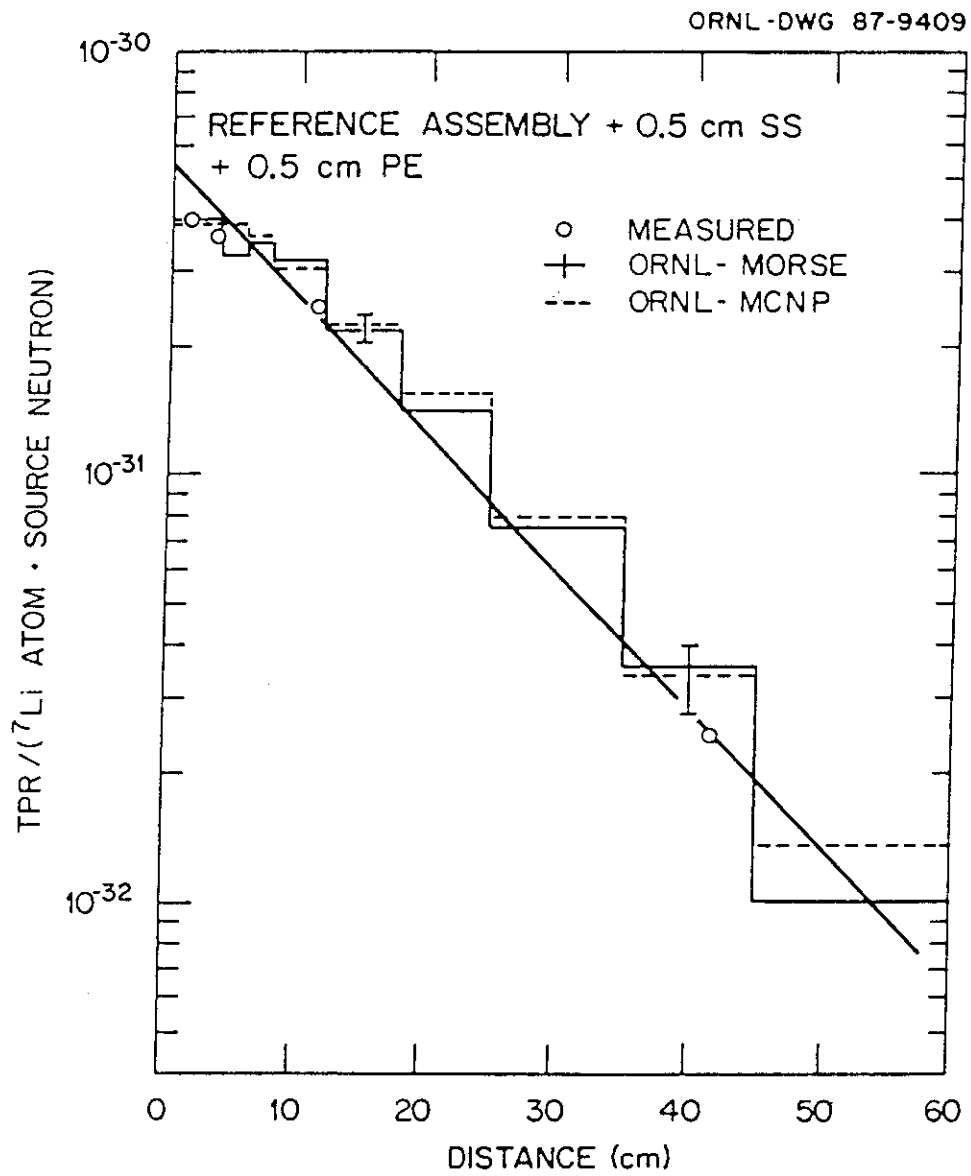


Figure IV.36 Profile of TPR from ${}^7\text{Li}$ in the 0.5 cm SS + 0.5 cm PE first wall system (U.S. ORNL calculations)

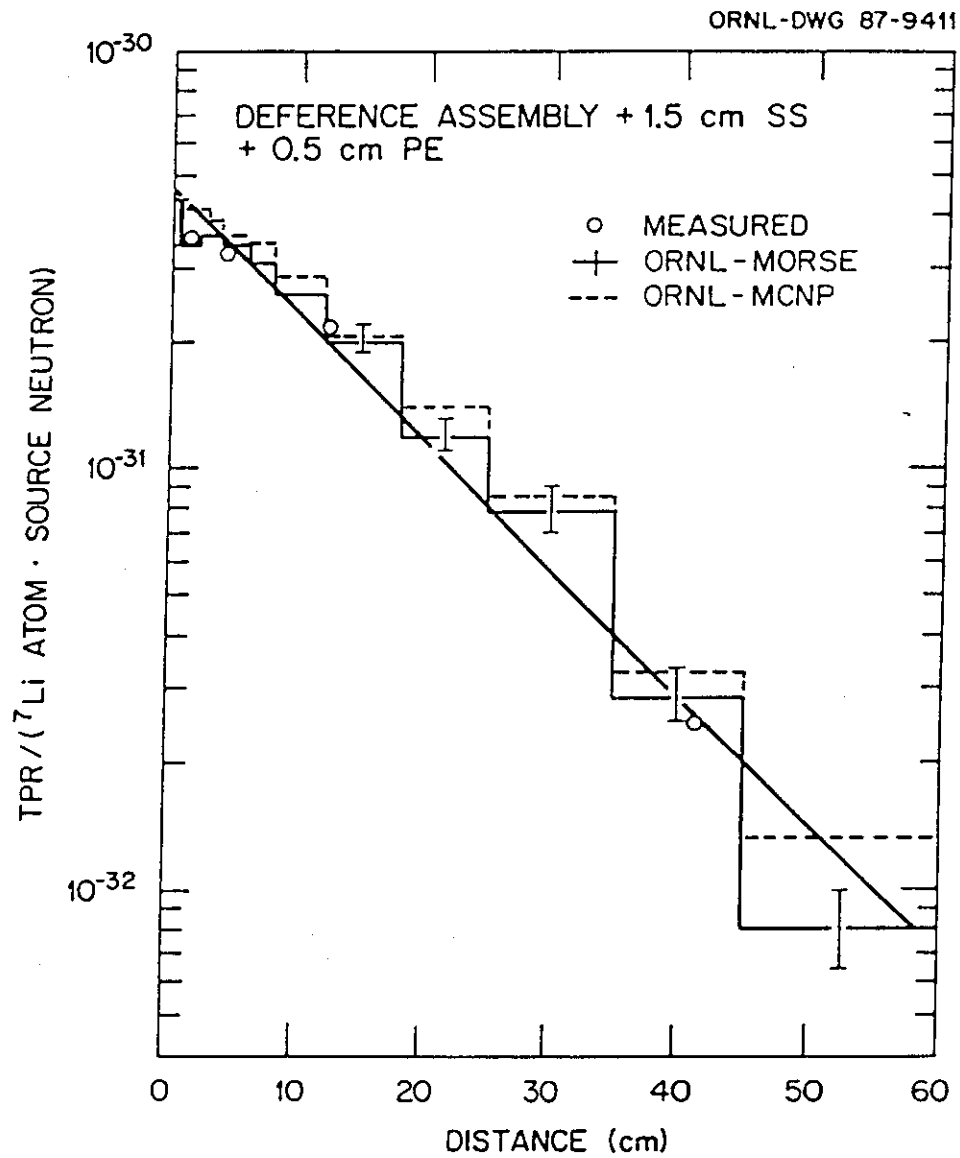


Figure IV.37 Profile of TPR from ^7Li in the 1.5 cm SS + 0.5 cm PE first wall system (U.S.: ORNL calculations)

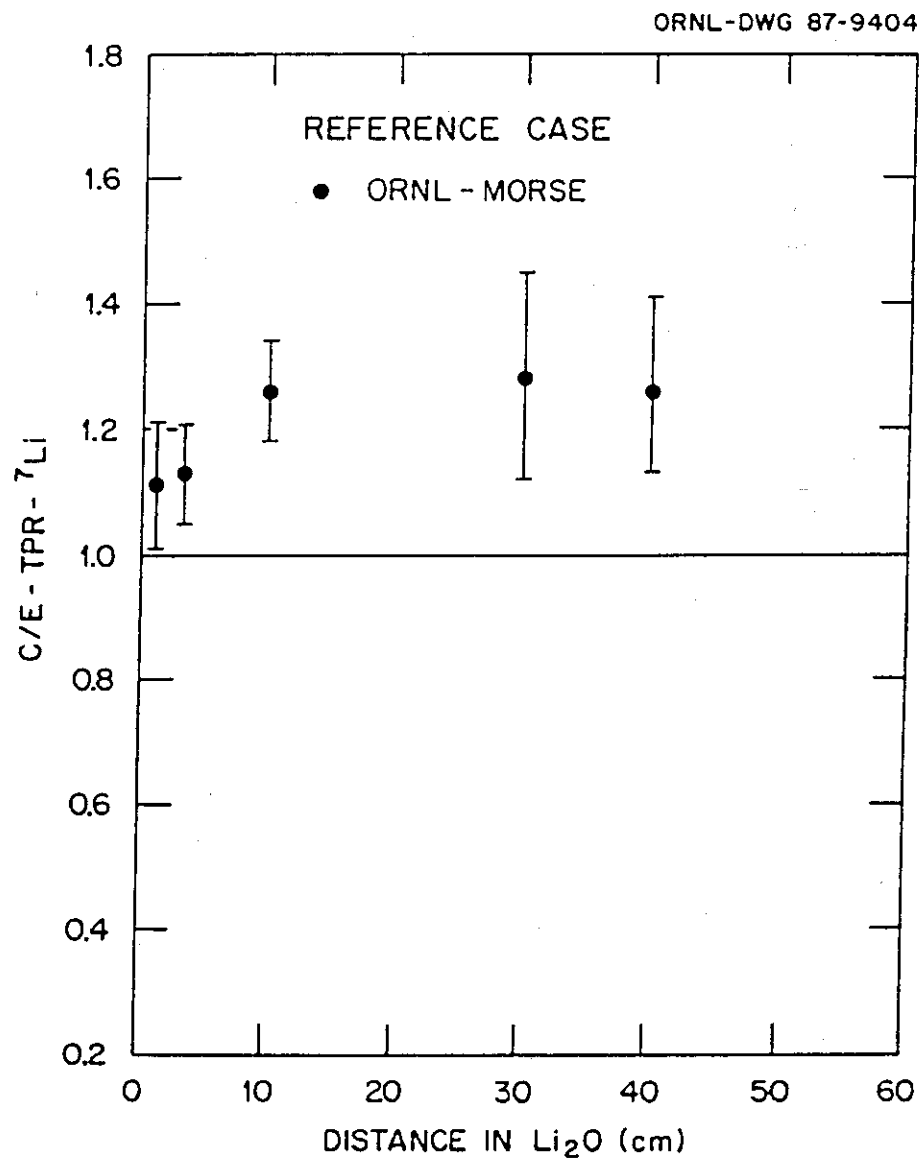


Figure IV.38 C/E values for T_7 in the reference system (U.S.: ORNL calculations)

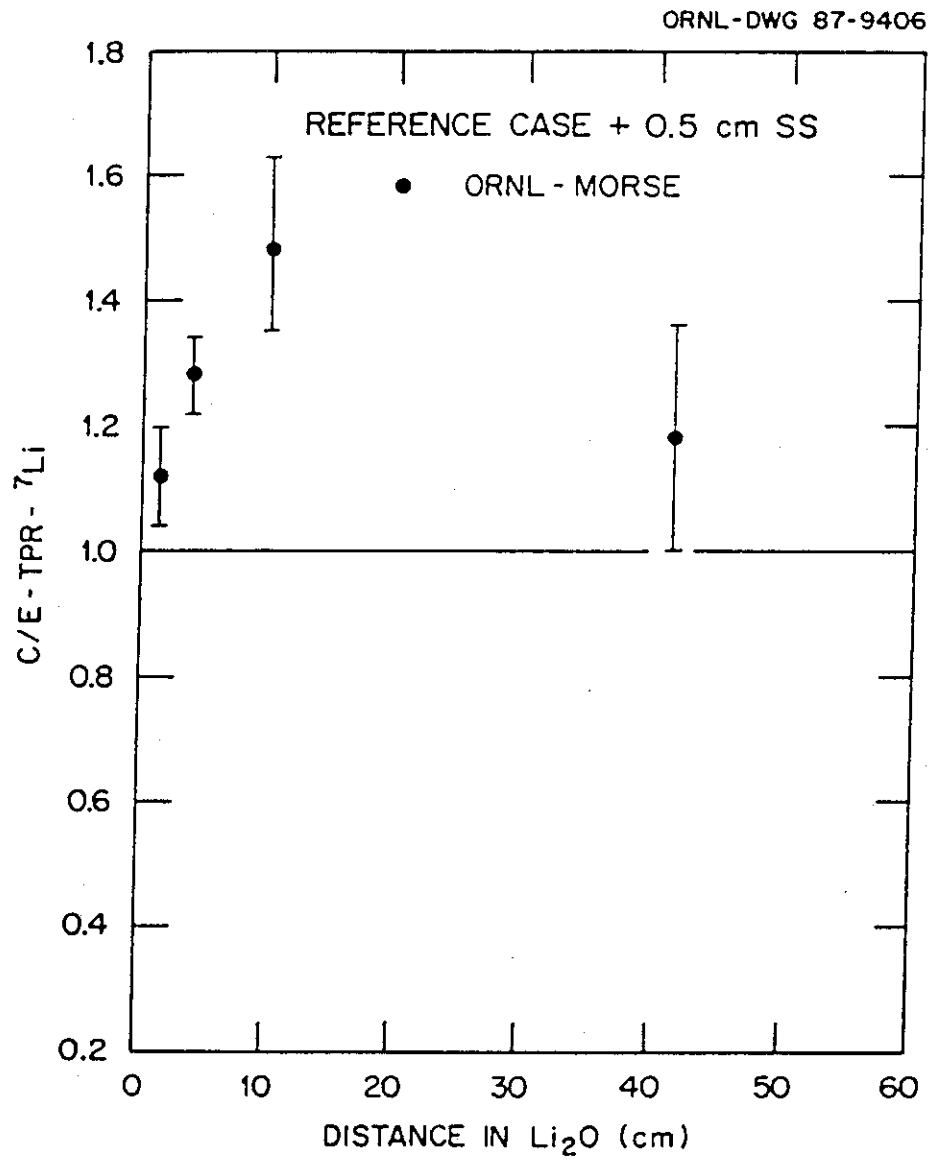


Figure IV.39 C/E values for T_7 in the 0.5 cm SS first wall system (U.S.: ORNL calculations).

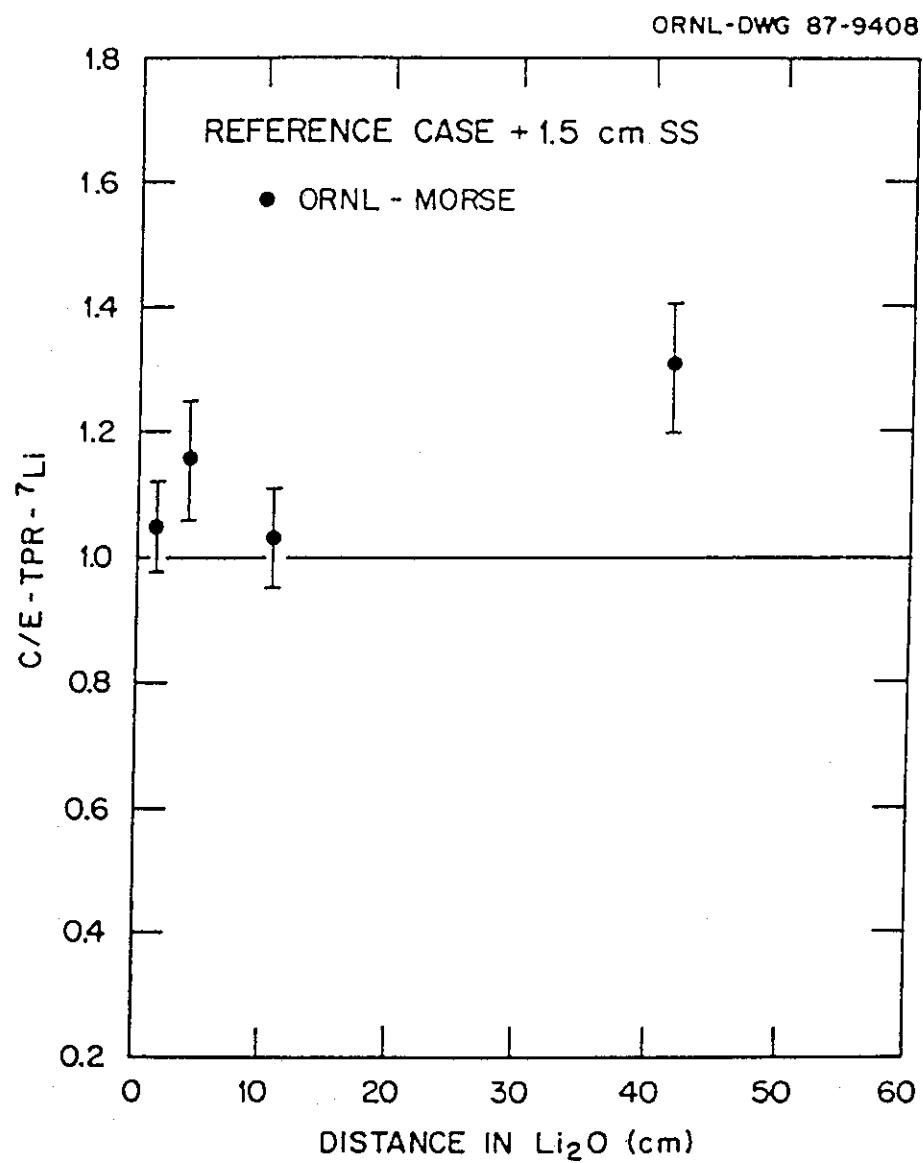


Figure IV.40 C/E values of T_7 in the 1.5 cm SS first wall system (U.S.: ORNL calculations)

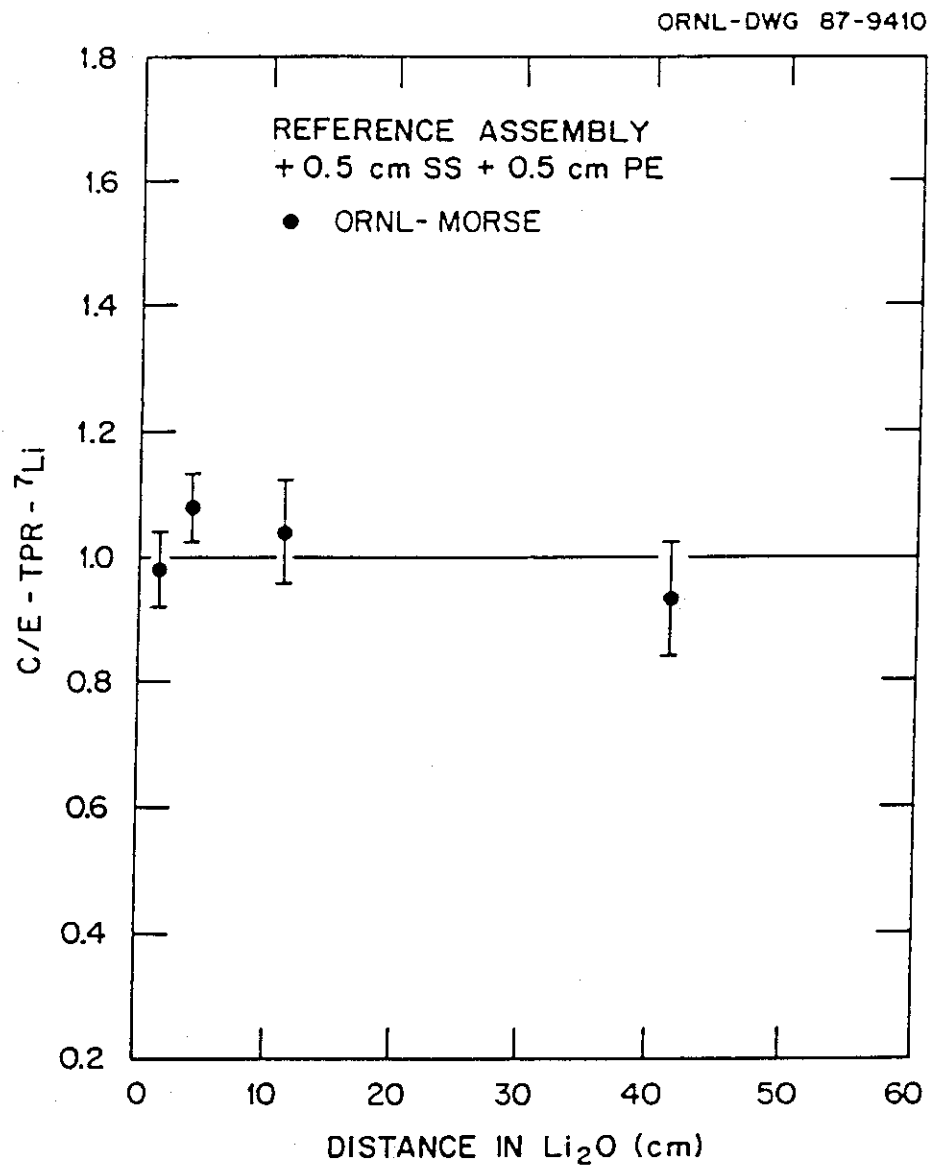


Figure IV.41 C/E values for T_7 in the 0.5 cm SS + 0.5 cm PE first wall system (U.S. ORNL calculations)

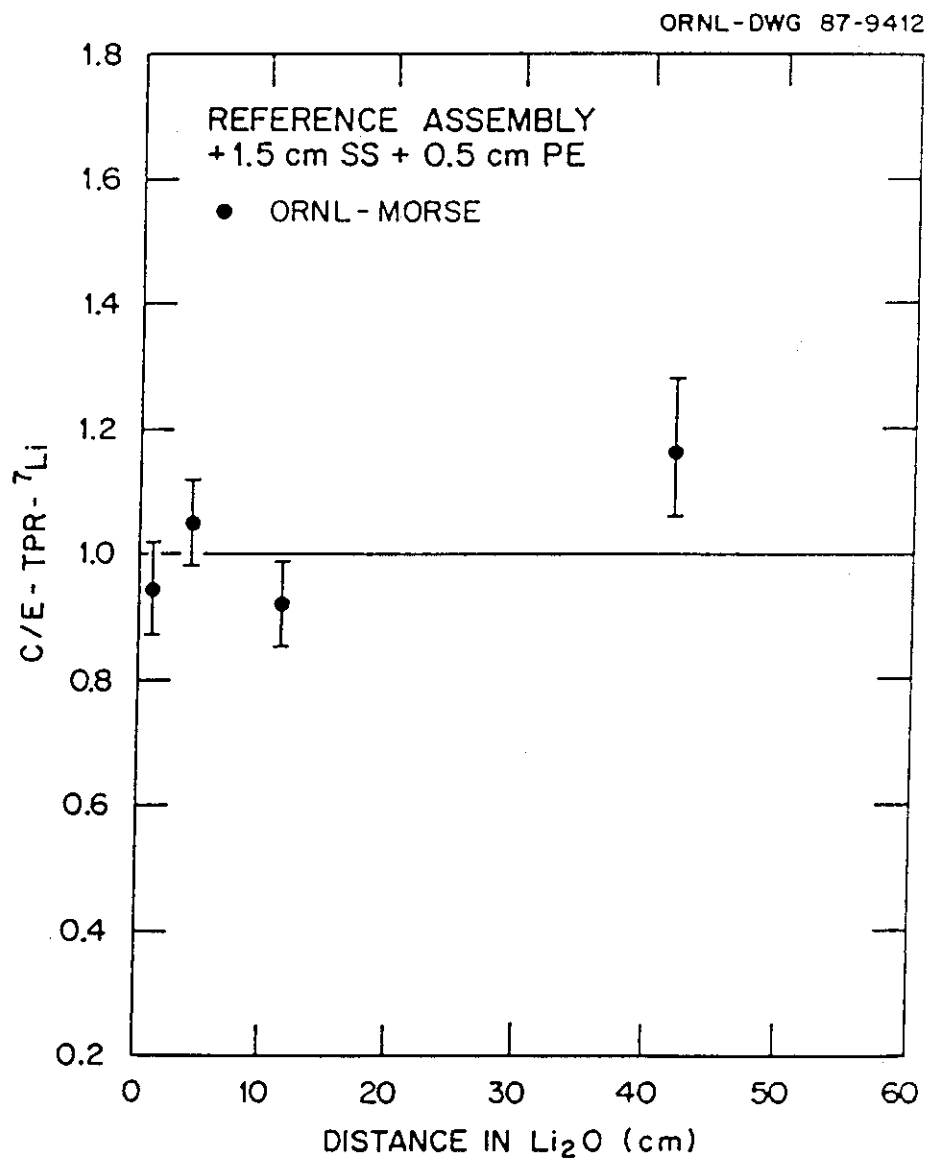


Figure IV.42 C/E values for T_7 in the 1.5 cm SS + 0.5 cm PE first wall system (U.S.: ORNL calculations)

the experimental room. The fraction of source neutrons reaching the surface of the Li_2O assembly is small, so biasing techniques were imposed to achieve reasonable statistics in the estimation of the tritium breeding. As in all analyses where biasing is used, the results may be, in part, influenced by the procedures used to sample from the neutron source distribution.

Additionally, differences between the calculated and measured results may arise, at least in the case of the MORSE analysis, from the use of multi-group cross-section data. Representing the ^6Li tritium production thermal cross-section in this format may lead to the rather large differences in the MORSE and MCNP predictions of the ^6Li tritium production at the front of the Li_2O assembly. The estimates of T_6 using the MCNP code are reasonably consistent with those obtained by the UCLA (U.S.) group using the same code for the reference experiment. However, the differences in the source sampling procedure and the representation of the experiment room geometry used at ORNL and UCLA may account for some of the differences observed among the calculated results for the reference experiment.

IV.3 The Beryllium Neutron-Multiplier Experiments

The effect of a neutron multiplier on the TPR has been investigated by setting a beryllium region at the front of the Li_2O system. Three experimental configurations have been considered: a) a 5 cm-thick beryllium front region; b) a 10 cm-thick beryllium front region; and c) a 5 cm-thick Li_2O + 5 cm-thick beryllium front region. The last configuration is called a beryllium-sandwiched system.

The measured values of the neutron multiplication effect on T_6 are presented in Fig. IV.43, which compares the ratio of the T_6 measured values obtained by the Li-glass detectors to those of the reference experiment. The location $Z = 0$ cm corresponds to the boundary of the beryllium and the Li_2O region. The multiplication is obtained at the zone $2 \text{ cm} < Z < 30 \text{ cm}$ and the effect is proportional to the thickness of the beryllium in these experiments. Net multiplication can be achieved up to $Z < 27\sim 32 \text{ cm}$. Comparing the 5 cm beryllium system with the Be-sandwiched system, the former gives larger multiplication over the system (the contribution from the 5 cm-thick Li_2O region in front of the beryllium is not taken into account). The corresponding calculated multiplication ratios as obtained by DOT3.5, MORSE-DD (JAERI) and MCNP (U.S.) are shown in Figures IV.44 and IV.45, respectively. The trend of the spatial dependence is similar to the experimental results, but the absolute values are underestimated by about 20% in the region $Z < 30 \text{ cm}$ when DOT3.5-JACKAS was used, while MORSE-DD results underestimate them in the region $Z < 15 \text{ cm}$. The trend of the multiplication effect is fairly different between MORSE-DD and MCNP predictions in the region $Z < 20 \text{ cm}$. Apparently, the peak value obtained by MCNP is considerably underestimated and the location is shifted backward as compared to the measurements.

All the results mentioned above are compared in Fig. IV.46. As shown in Fig. IV.46, and in the neighborhood of the surface of the Li_2O system, the multiplication is less than 1 because the soft neutrons reflected from the room wall are absorbed in the front beryllium or the front Li_2O + Be layers, contrary to the reference experiment in which such a component directly contributes to T_6 in this region. For example, including a 5 cm Be layer causes a decrease in T_6 by a factor of 0.3 at $Z = 0.25 \text{ cm}$. The corresponding

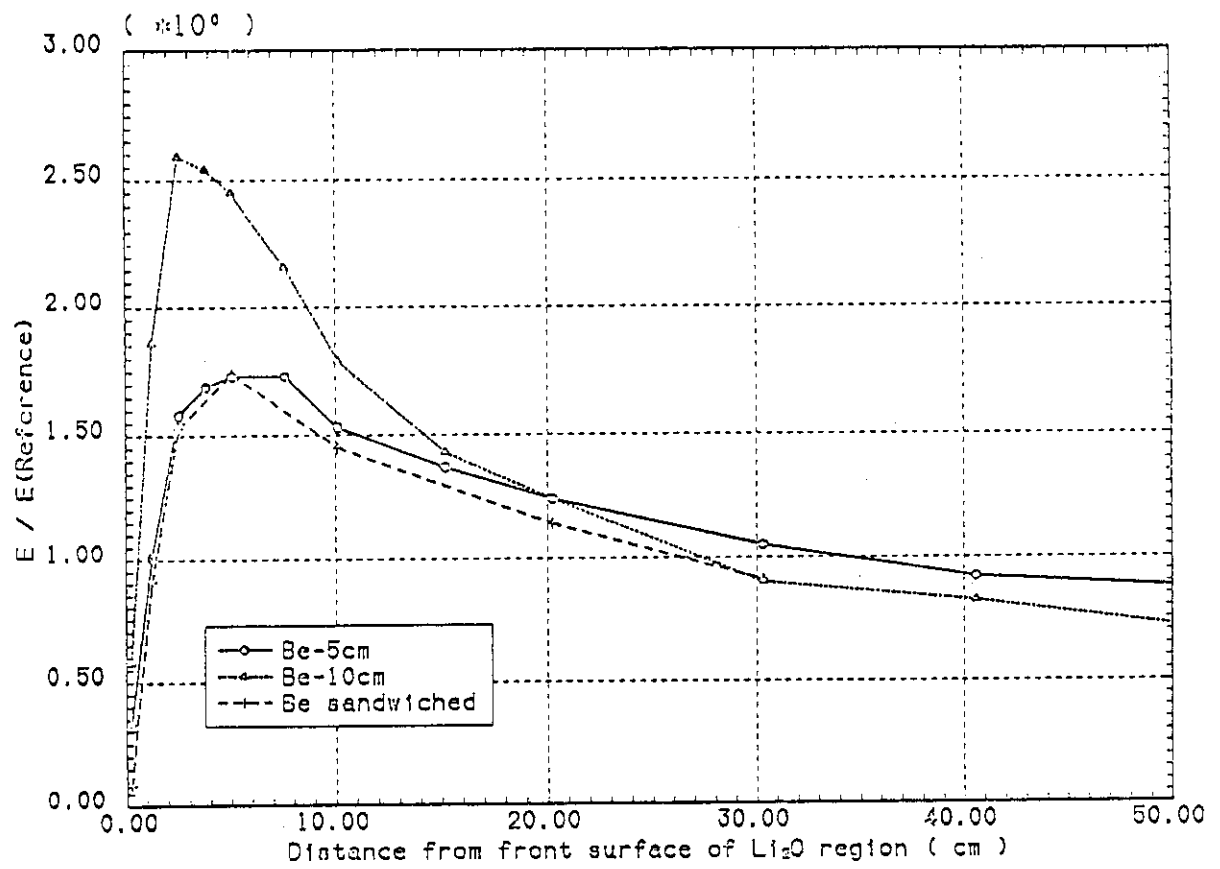


Figure IV.43 Neutron multiplication effect of Be on T_6 measured by Li-glass detectors

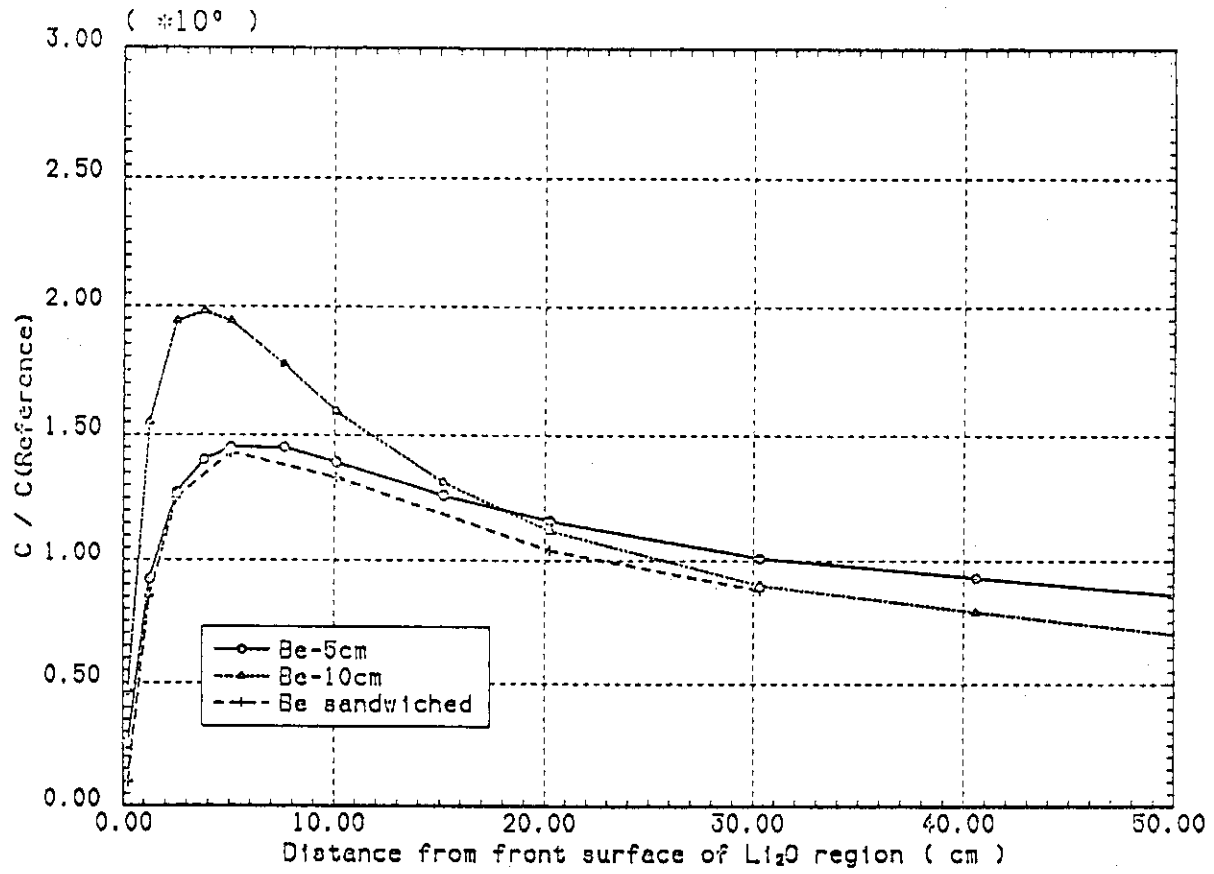


Figure IV.44 Neutron multiplication effect of Be on T_6 as calculated by DOT3.5 with JACKAS library

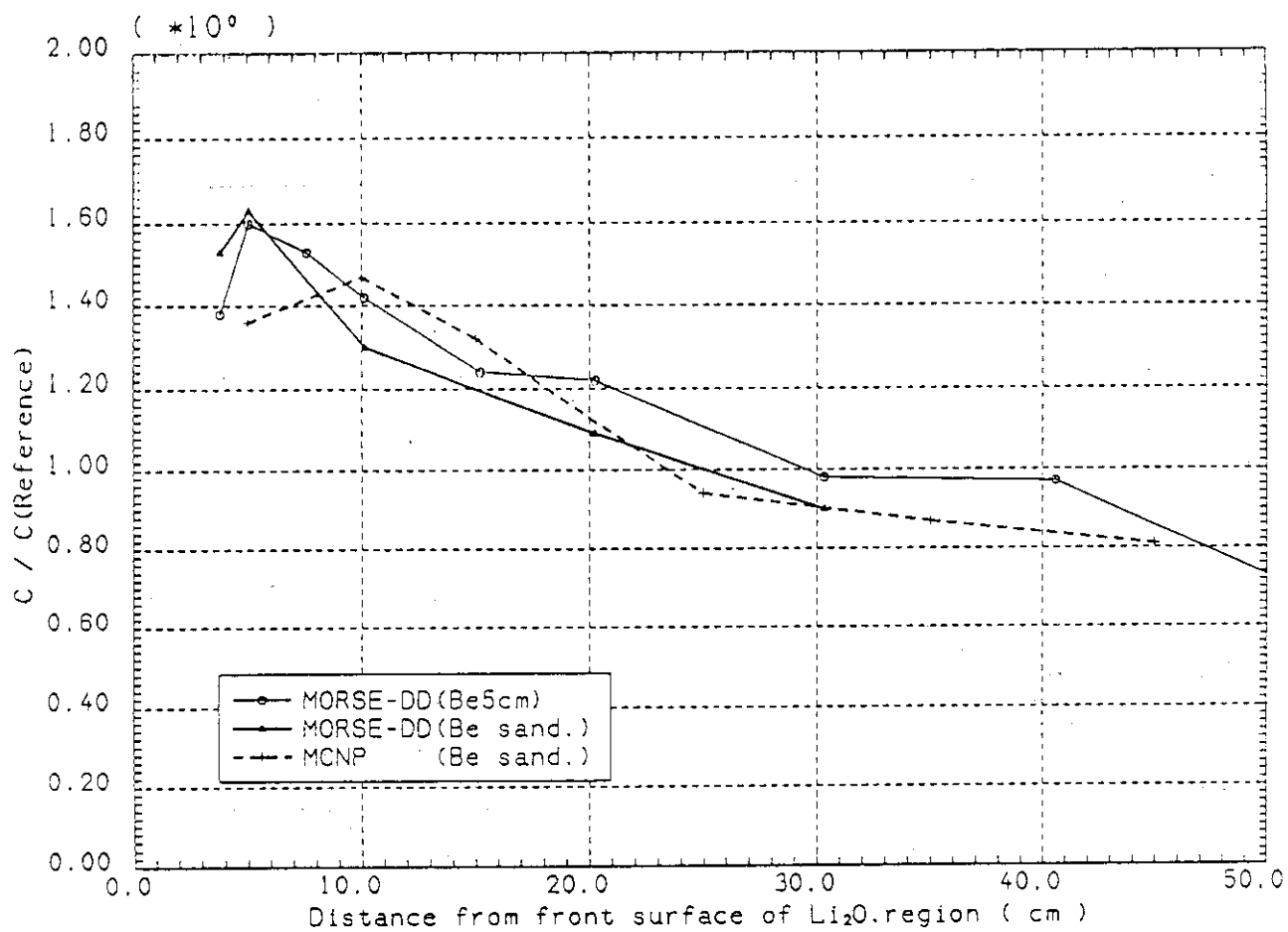


Figure IV.45 Neutron multiplication effect of Be on T_6 as calculated by the Monte Carlo method

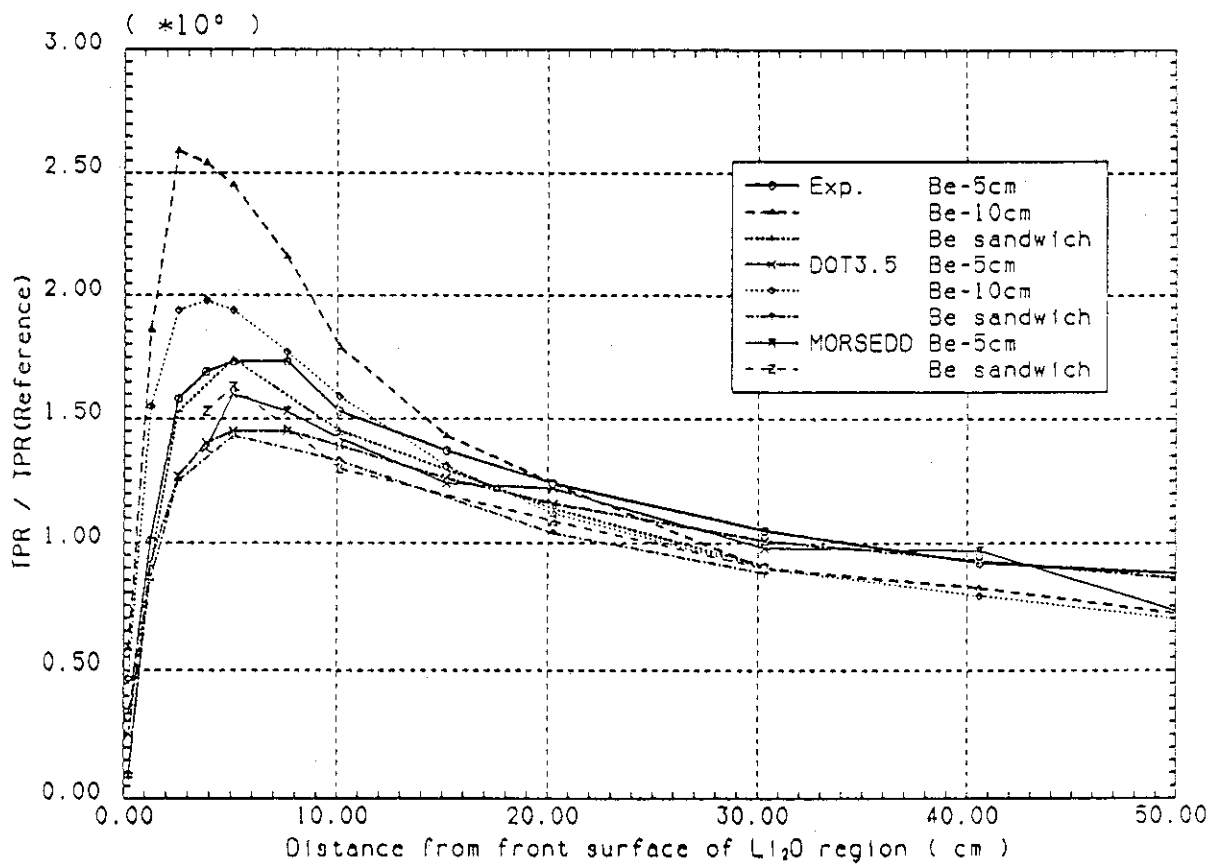


Figure IV.46 Comparison of Be neutron multiplication effect on T_6 , between measurements and calculations (JAERI)

decrease in the 10 cm Be and the beryllium-sandwiched systems are by factors of 0.5 and 0.2, respectively. The predictions of that decrease by DOT calculations are of the same order of magnitude. The T_6 values also decrease at deeper locations ($Z > 30$ cm). The inclusion of a beryllium layer tends to decrease the high-energy component of incident neutrons through the $\text{Be}(n,2n)$ reactions that can reach the rear zone of the Li_2O assembly and contributes to T_6 upon encountering slowing-down processes. Both experimental and analytical results show that the decrease in T_6 at $Z = 50$ cm is by a factor of ~ 0.9 and 0.7 in the 5 cm Be and 10 cm Be cases, respectively. But, as mentioned before, at $2 \text{ cm} < Z < 30 \text{ cm}$, the local T_6 is larger than the reference case in all the beryllium configurations considered. For example, at $Z = 5$ cm, the experimental ratio for the 10 cm Be case is about 2.5. The analytical prediction with the DOT code for this ratio is lower (~ 2). The experimental predictions for this ratio at $Z = 5$ cm in the 5-cm Be and the Be-sandwiched cases are similar and are 1.7, and again calculated ratios are lower (~ 1.4). The increase in T_6 at the locations $2 \text{ cm} < Z < 30 \text{ cm}$ is due to the increase in neutron population resulting from the $\text{Be}(n,2n)$ reactions. These neutrons are absorbed mainly by ^6Li at these locations after being slowed down. The discrepancy in the region $2 \text{ cm} < Z < 30 \text{ cm}$ between measurements and calculations will impact the predictive accuracy of the breeding ratio in fusion blankets that utilize beryllium as a multiplier.

The C/E values, as calculated by the U.S. and JAERI using the deterministic method, are shown in Figures IV.47 and IV.48, respectively. The experimental values are corrected for the self-shielding effect. Both the U.S. and JAERI results show an increase in the C/E values as one proceeds toward the back locations. At $Z = 55$ cm, the C/E value obtained by the U.S. is ~ 1.3 , while it is ~ 1.13 in JAERI's calculations in both the 5 cm and 10 cm Be systems. Large deviation from unity is also apparent at locations just behind the beryllium zone. The same trend is found in the Be-sandwiched system. The C/E values in this case are close to the values found in the 5-cm Be system. However, in JAERI's calculation, the discrepancies in the Be-sandwiched system are much larger in the front Li_2O and Be, zones as shown in Fig. IV.48. Note also that the prediction by the U.S. for T_6 is larger by about 10-15% in the bulk zone of the Li_2O assembly as compared to JAERI's results. In addition, the deviation in the C/E values from unity is more pronounced in the 5-cm Be system as compared to the results in the 10-cm Be system. This observation was also true in the first wall experiments. Note that the C/E values just behind the beryllium zone are less than unity, as predicted by the DOT calculations. The reason for this feature at $Z \sim 0$ cm is not clear. Such a tendency is not observed in the calculations performed by MORSE-DD, as seen in Fig. IV.49. This discrepancy may come from the calculational model used, such as the size of mesh intervals, the methodology applied to the solution method, or the processing method for the beryllium cross-sections. Like the results in the DOT calculations, the MORSE-DD calculations also give high C/E values in the beryllium region for the Be-sandwiched case, although the FSD in the calculations is not small.

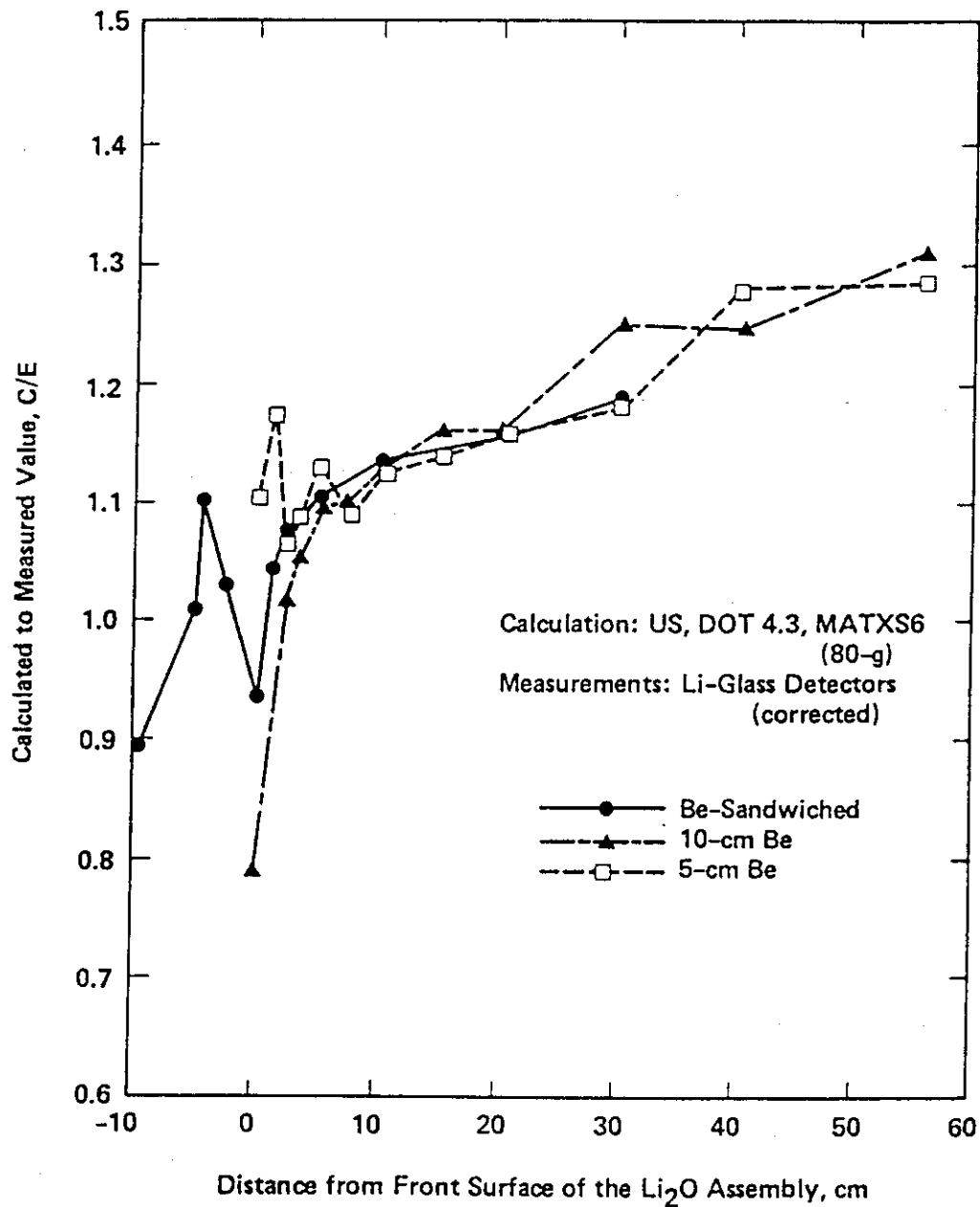
Tritium Production Rate from ${}^6\text{Li}$, T_6 , in the Beryllium Experiments

Figure IV.47 C/E values for tritium production rate from ${}^6\text{Li}$, T_6 , in the beryllium experiments (2-D model, U.S. calculations)

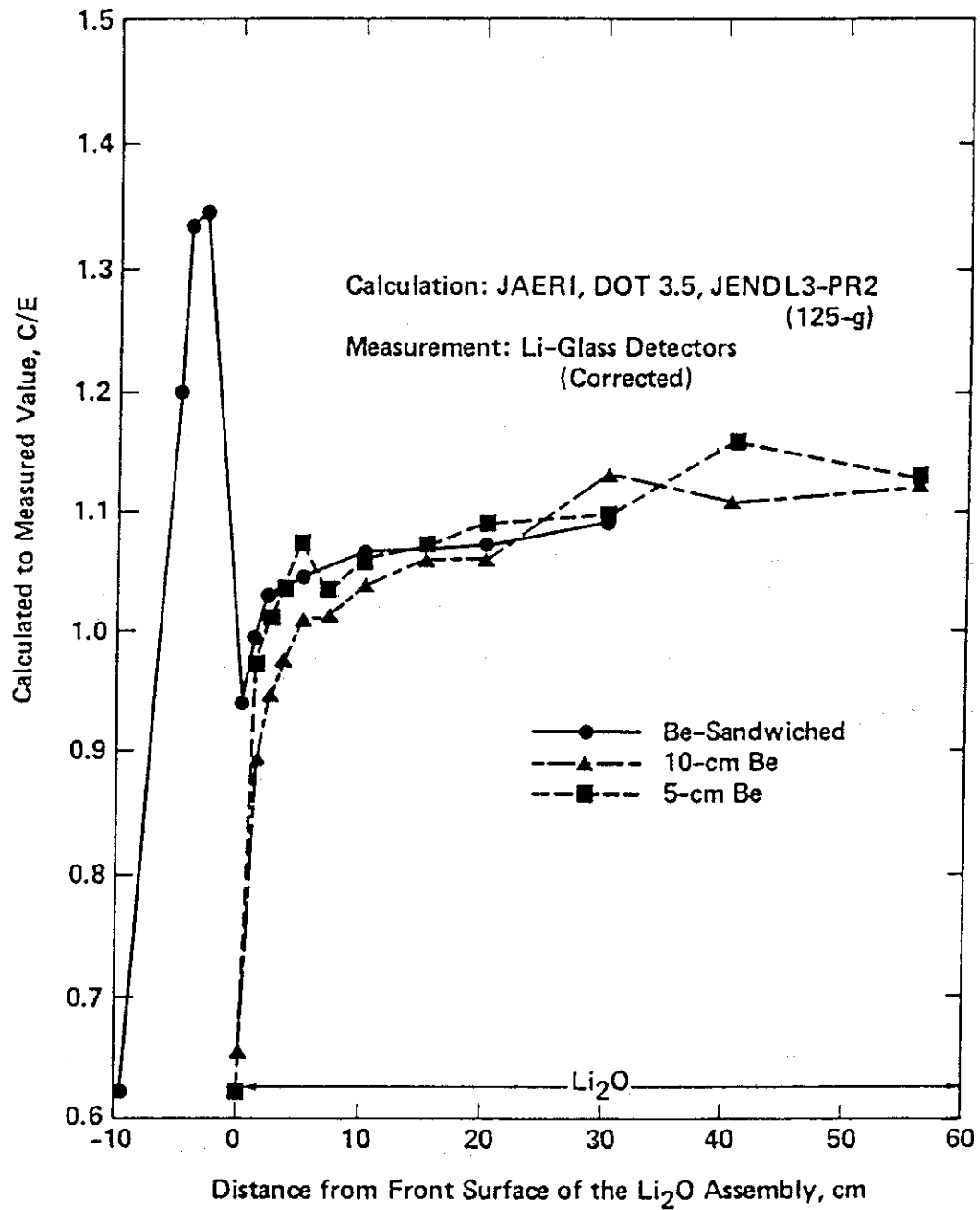
Tritium Production Rate from ${}^6\text{Li}$, T_6 , in the Beryllium Experiments

Figure IV.48 C/E values for tritium production rate from ${}^6\text{Li}$, T_6 , in the beryllium experiments (2-D model, JAERI calculations)

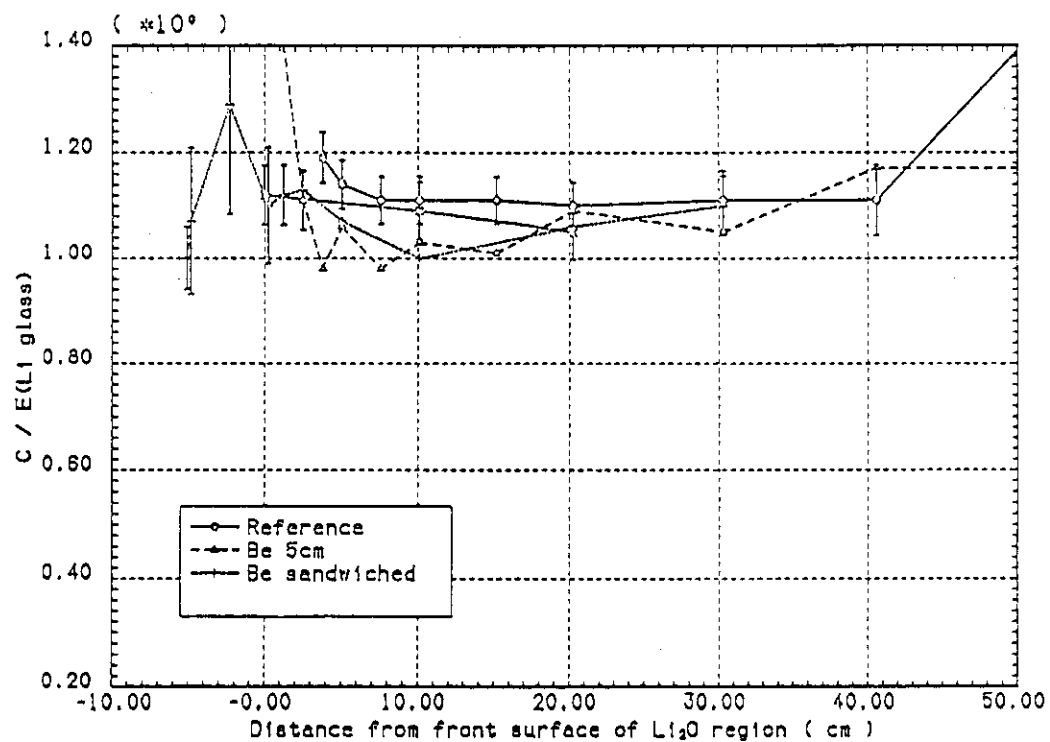


Figure IV.49 Comparison of C/E values for T_6 between experiments with and without Be multiplier (calculation: MORSE-DD with DDL/J3P1, experiment: Li glass)

A comparison between the C/E values for T_6 in the Be-sandwiched system as obtained by the Monte Carlo and the discrete ordinates methods is shown in Fig. IV.50. The C/E values, as obtained by the MORSE-DD and MCNP codes, are larger than the corresponding values obtained by the DOT code at $Z = 0 - 5$ cm behind the Be zone, but the values agree with JAERI's DOT results within 2-7% in the rest of the Li_2O test module. The discrepancies in the C/E values between the MCNP and the MORSE-DD calculations is very large in the front Li_2O layer. The reason for these large discrepancies may be due to the interpolation scheme and the estimators location and dimension applied to the calculated T_6 values at the locations where measurements were taken. At the boundaries between the Be layer and the adjacent Li_2O layer, the T_6 profiles are very steep and the interpolated values are sensitive to the number of neighboring points used in the interpolation. A log-linear interpolation scheme was used in both the U.S. and JAERI calculations.

The dependence of the C/E values on the techniques used to measure T_6 is presented in Fig. IV.51, based on the DOT3.5 calculations (JAERI) for the Be-sandwiched system. (Note that no self-shielding convected values were obtained for the Li-metal detectors inside the Be zone, therefore; the C/E values with this method are excluded in the figures in the Be zone). While divergence is very large in the beryllium region and in the front Li_2O zone, it is within 10~15% for the rest of the Li_2O system. When we compare Fig. IV.2 (reference system) with Fig. IV.51, we observe that the C/E values are closer to unity in the sandwiched system at locations far from the Be zone, and the difference among the measured values is similar in magnitude in both systems at these locations. However, there is a large divergence in the C/E values in the Be zone and the front Li_2O zone. To investigate the source of the difference in the C/E values among the various measuring techniques at these locations, we compared the self-shielding correction factors applied to the measured values obtained by each technique. The values are presented in Fig. IV.52 for the sandwiched case. It should be noted that in the asymptotic region (far from the interface between the Be zone and the Li_2O assembly) two calculated factors and one experimentally-derived factor agree well, but the experimentally-derived values for the Li-metal method are 10% less than the calculated values by Youssef and Mori in the range a few cm $< Z < 20$ cm behind the Be zone. The calculations show that the factors almost saturate at $Z = 10$ cm, while the experimental values gradually increase up to $Z = 30$ cm. (The self-shielding factors for $^6\text{Li}_2\text{O}$ pellets were calculated by Mori and Yamaguchi using independent methods and their results were quite similar. We show only those obtained by Mori.) If we consider that the density of ^6Li in the pellet detectors and their dimensions are larger than those in the metal detectors, the discrepancy between the calculations and the experimentally-derived values could be explained in the Li_2O assembly. However, there were no experimentally-derived values in the Be zone and it is clear that the experimental values in this zone (which has a very soft neutron spectrum as compared to that in the back Li_2O zone) are highly dependent on the measuring techniques used and on the calculated self-shielding correction factors applied.

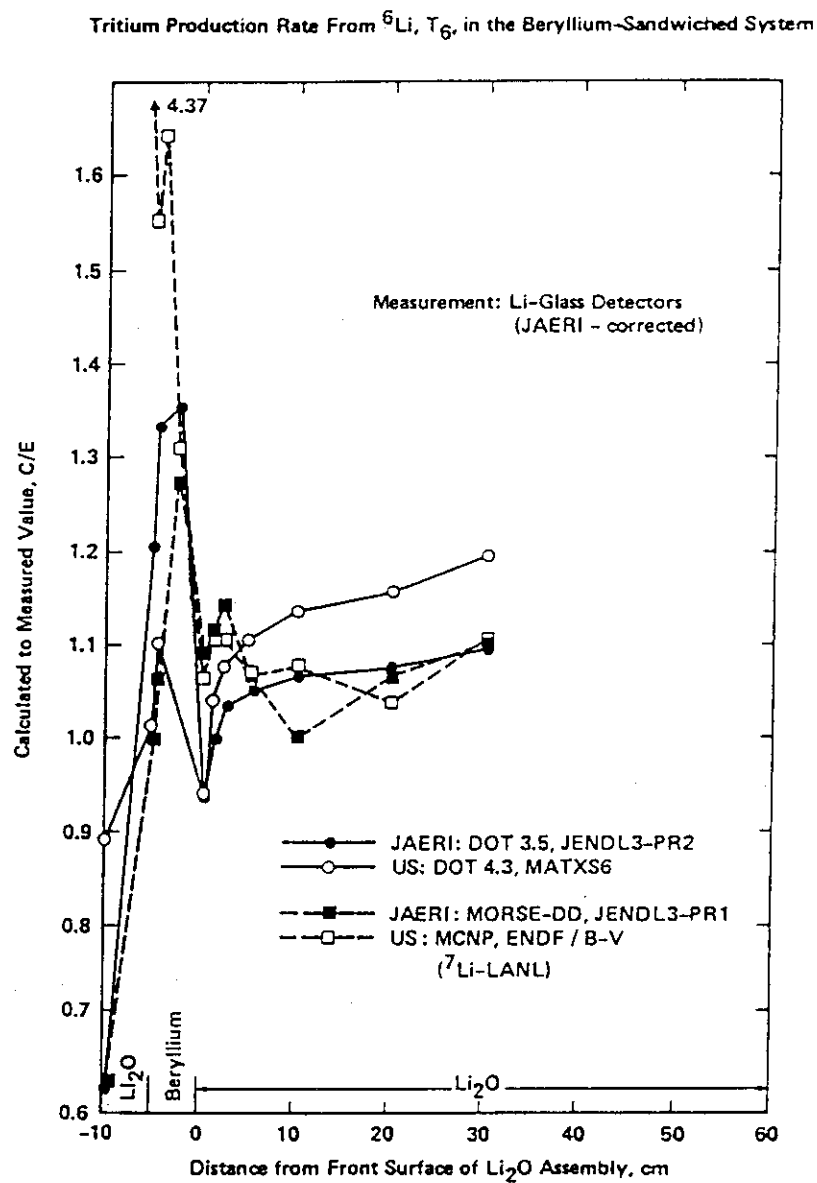


Figure IV.50 C/E values for tritium production rate from ${}^6\text{Li}$, T_6 in the Be-sandwiched system obtained by various codes and libraries

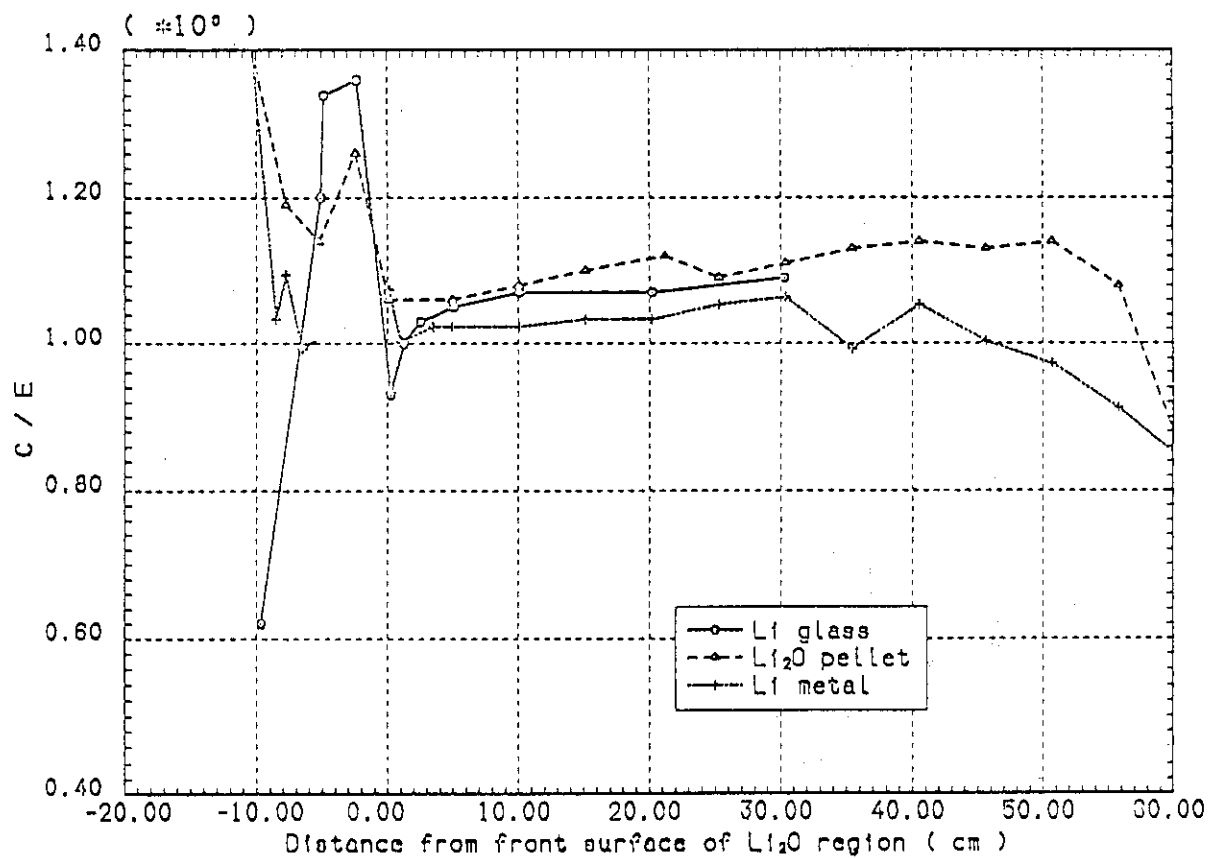


Figure IV.51 C/E values for T_6 in Be-sandwiched system based on the calculated values by DOT 3.5 with JACKAS library

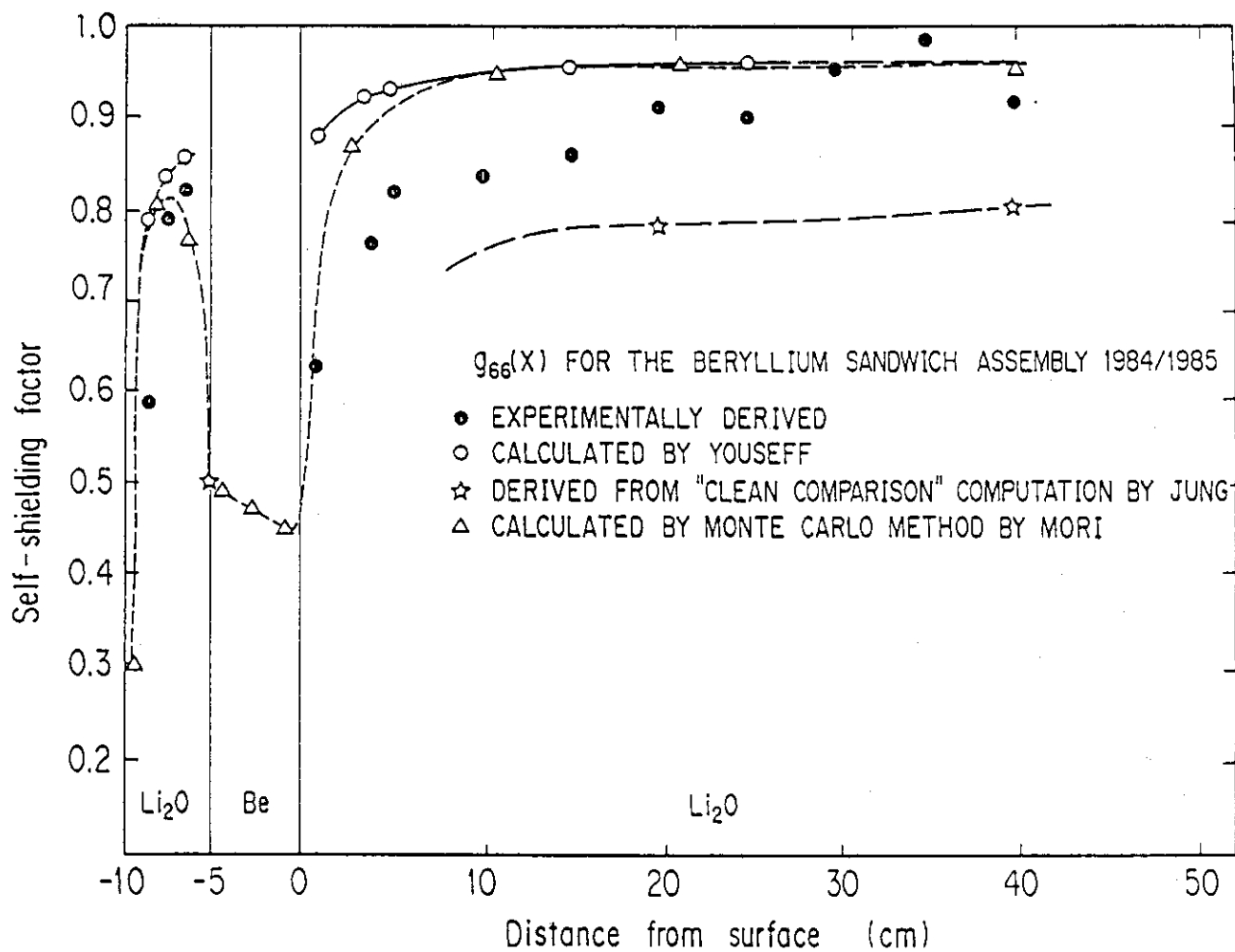


Figure IV.52 Comparison of self-shielding factors for ${}^6\text{Li}$ (n,α) reaction in Be-sandwiched system

A comparison between the C/E values in the Be-sandwiched system, as obtained by the DOT calculations and the Monte Carlo method, is shown in Figures IV.53 and IV.54, respectively, based on the experimental values obtained by the Li₂O-pellet and Li-metal detectors, respectively. Also shown in these figures, for comparison, are the C/E values in the reference system. The overestimation of the C/E values as obtained by DOT3.5 calculations are within 10-15% in the reference and the Be-sandwiched systems and the ones obtained by DOT4.3 are about 20% at $Z < 10$ cm. The C/E values at $Z < 5$ cm in the reference system are large for the reasons discussed earlier. In the front Li₂O zone in the Be-sandwiched system, the C/E values as obtained by both parties are also similar and, again, the deviation from unity is large (up to 40%). The discrepancy between the JAERI and U.S. calculations is also large (up to 30%) in the beryllium zone even after correcting for the self-shielding effect using the same correction factors that were obtained by JAERI for the Li₂O-pellet detectors. The discrepancy between JAERI and U.S. calculations obtained by the Monte Carlo method is within 10% in the Be-zone and larger in the front Li₂O zone of the Be-sandwiched systems, as shown in Fig. IV.54, where the C/E values are compared with the Li-metal detectors.

The C/E values, as obtained by the DOT calculations using the measured values obtained by the Li-metal detectors are also shown in Fig. IV.55, where JAERI's results show closer values to unity at $Z > 3$ cm, and, again, the predictions of the U.S. calculations are larger than JAERI's by 10-15%. Note that the measured values shown in Fig. IV.55 are corrected for self-shielding effect. As was observed in Fig. IV.52, the self-shielding factors depend on the calculation method applied and the neutron spectrum at sample locations. The Monte Carlo method was used by JAERI to derive these factors, while the methods based on the original work of Bothe and Hanna⁽³⁴⁾ were used by the U.S.

In Fig. IV.56, the C/E values for T₆ are shown for the cases where the corrected experimental values obtained by the Li-metal detectors are used (U.S.)^E_{corr} and those by the Li₂O pellet detectors (JAERI)^E_{corr}, and with the U.S. and JAERI's calculated values [(U.S.)^C, (JAERI)^C]. The calculations are based on the DOT3.5 and DOT 4.3 codes with the respective libraries. Large C/E values are apparent at the front surface of the front Li₂O layer (C/E ~2.4 with Li₂O pellet samples and ~5.5 with the Li-metal samples). It seems that the combination of JAERI's calculated values for T₆ and experimental values obtained by the U.S. using the Li-metal samples, gives, on the average, the closest C/E curve to unity.

The neutron multiplication effect on T₇, as obtained through measurements by the NE213 indirect method, is shown in Fig. IV.57, where the ratios to the experimental values in the reference system are displayed at various locations. Since beryllium has a large (n,2n) cross-section and since the secondary neutrons have low energies, the multiplication factor is always less than unity. The sandwiched case gives 30-40% lower local multiplication factors than the 5 cm-thick beryllium case. The results calculated by the MORSE-DD code are shown in Fig. IV.58. Though the calculations slightly underestimate these factors in the sandwiched case, the overall prediction accuracy is satisfactory, as seen in Figures IV.57 and IV.58.

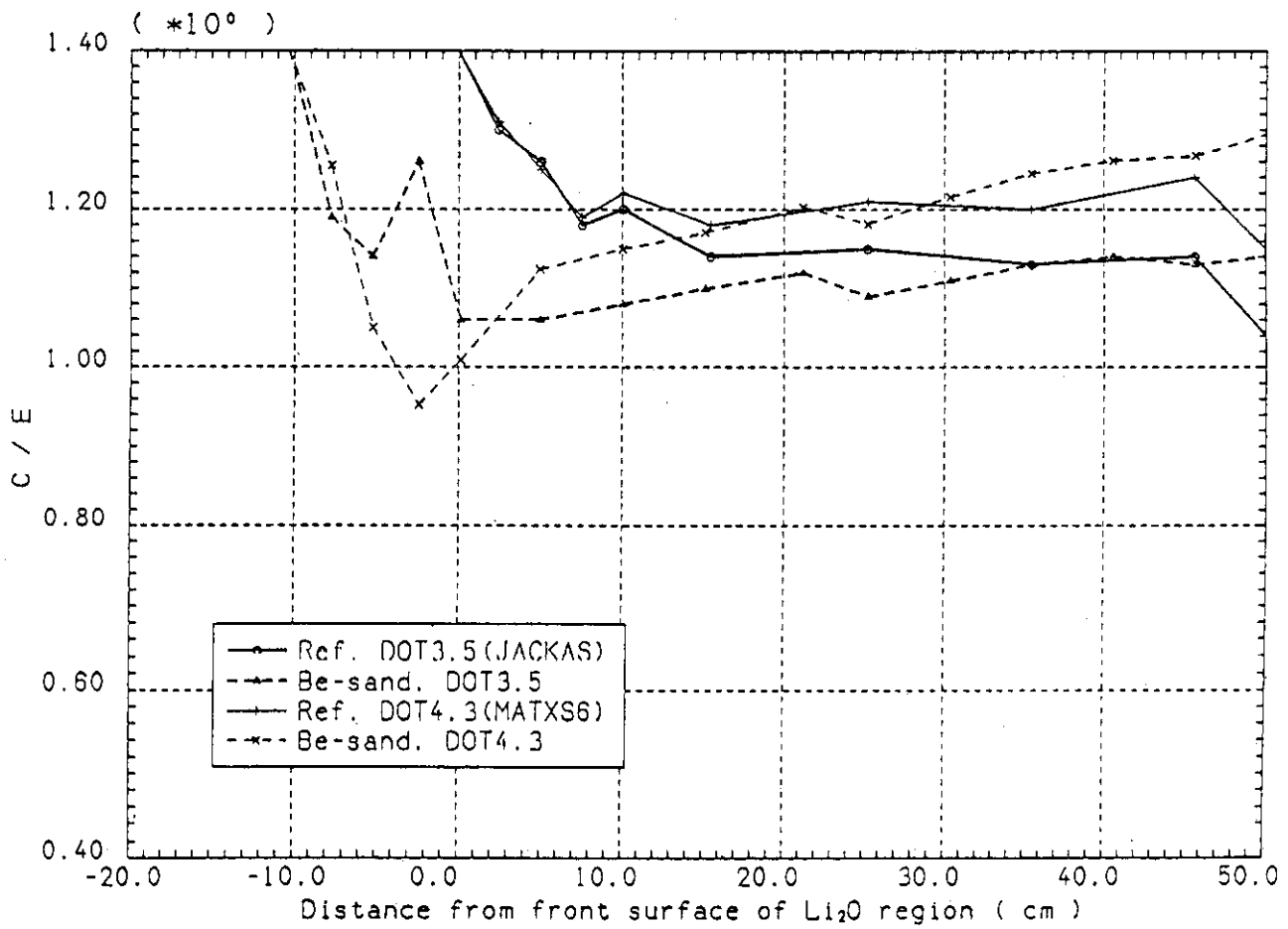


Figure IV.53 Comparison of C/E values for T_6 in the reference and the Be-sandwiched systems based on experimental values obtained by the Li_2O -pellet detectors

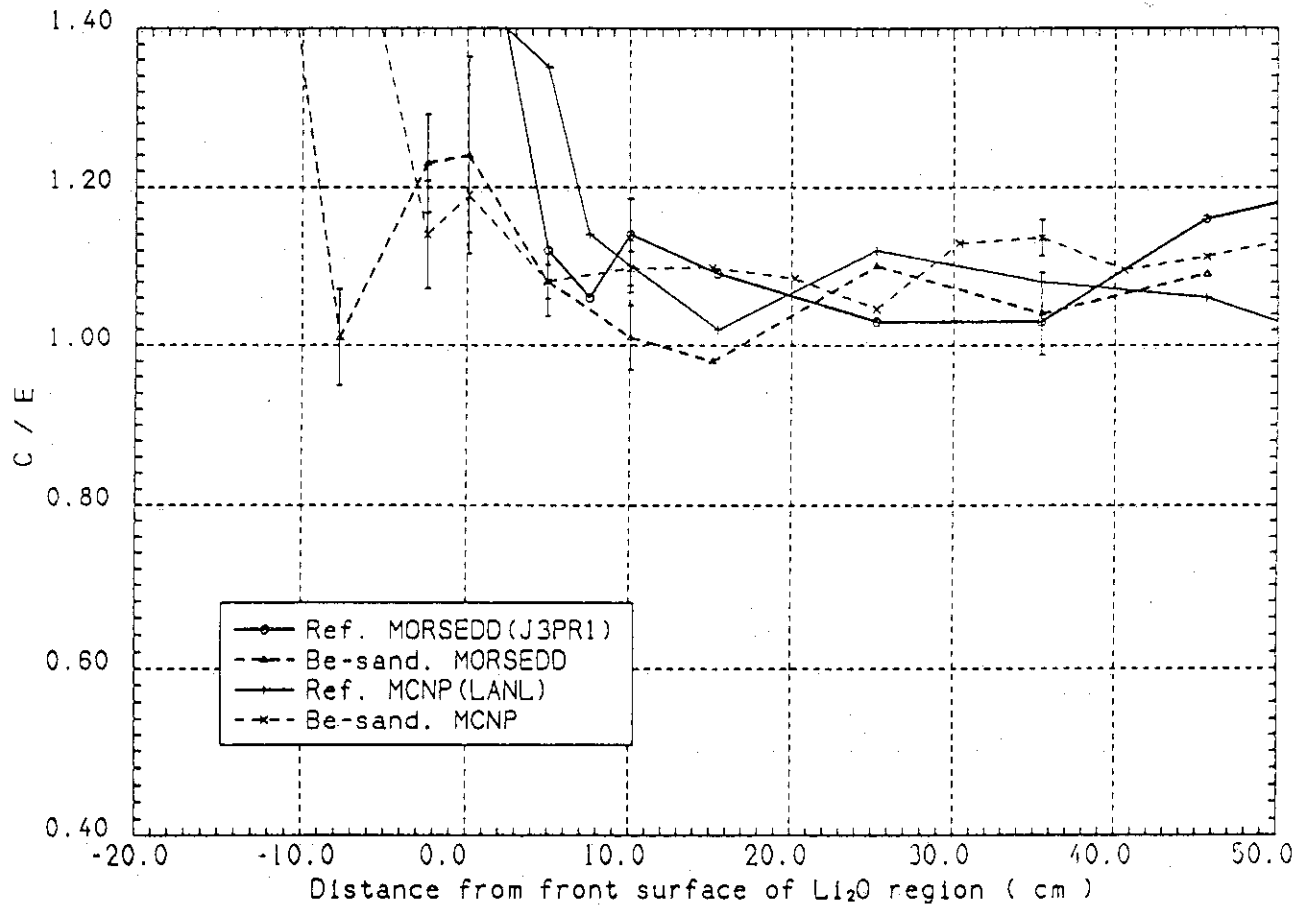
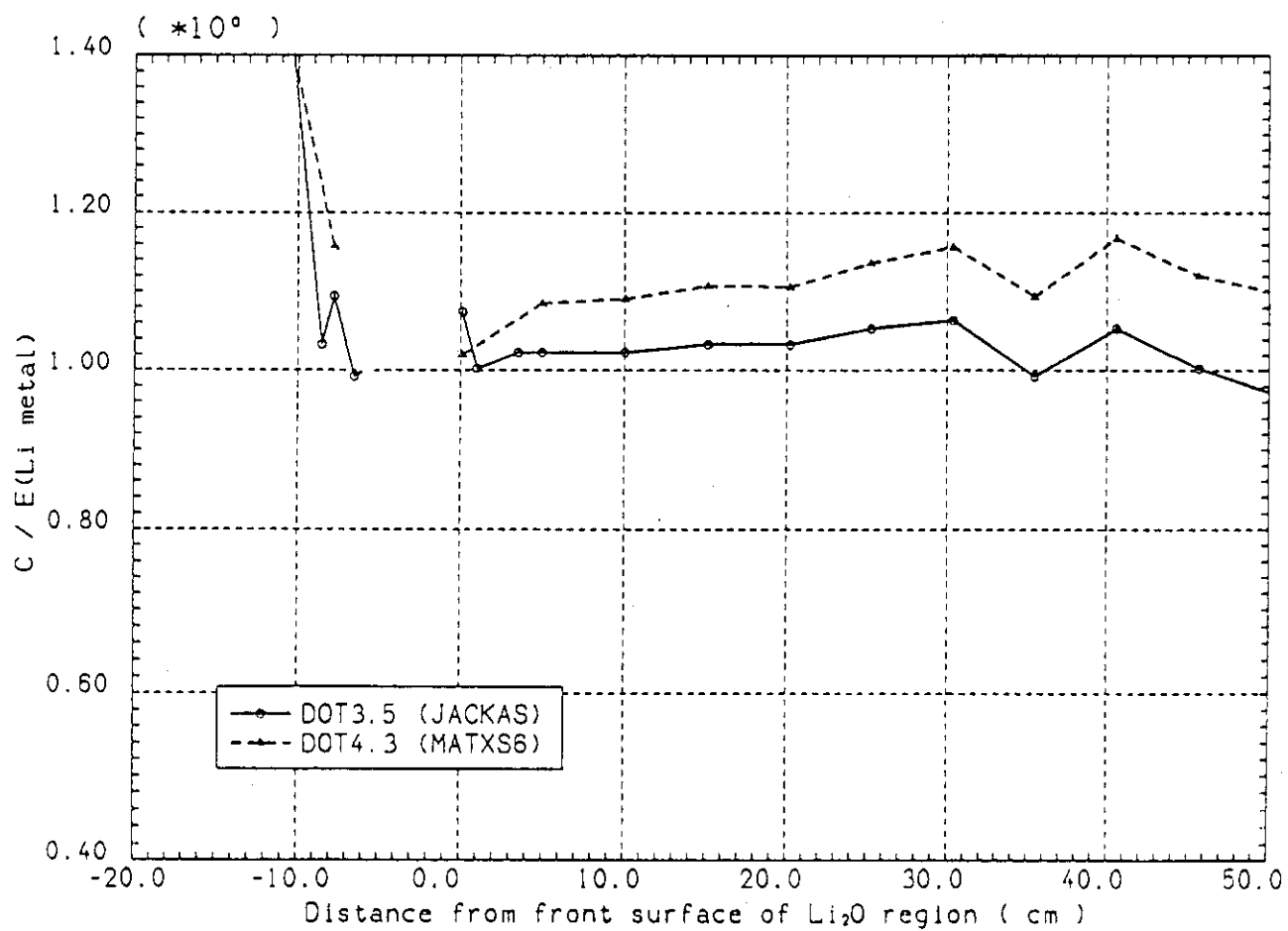


Figure IV.54 Comparison of C/E values for T_6 in the reference and the Be-sandwiched systems based on experimental values obtained by the Li-metal detectors

Figure IV.55 C/E of TPR by ^6Li in Be-sandwiched system (Li-metal)

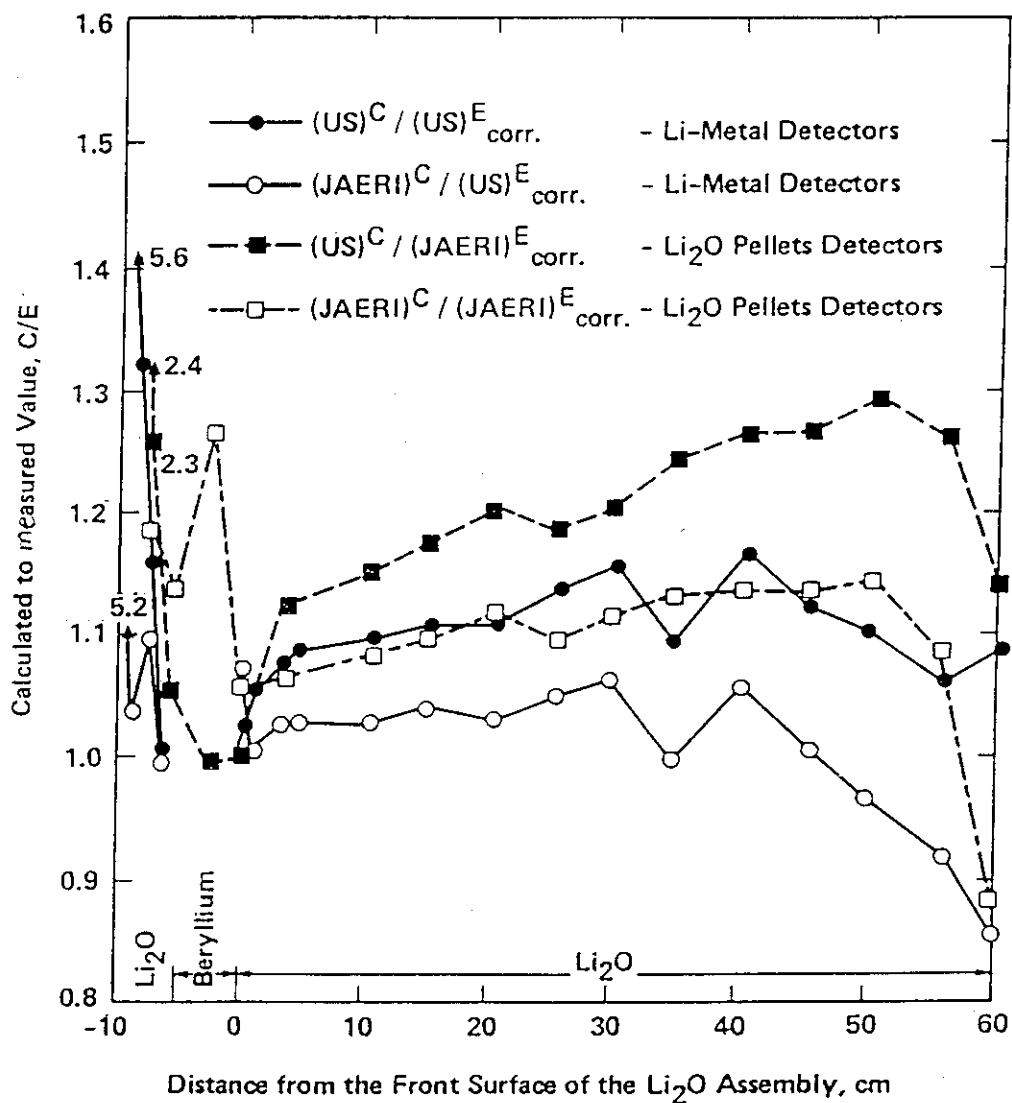
Tritium Production Rate From ${}^6\text{Li}$, T_6 , in the Beryllium-Sandwiched System

Figure IV.56 C/E values for tritium production rate from ${}^6\text{Li}$, T_6 in the Be-sandwiched system based on DOT calculations and Li-metal and Li_2O pellet measurements

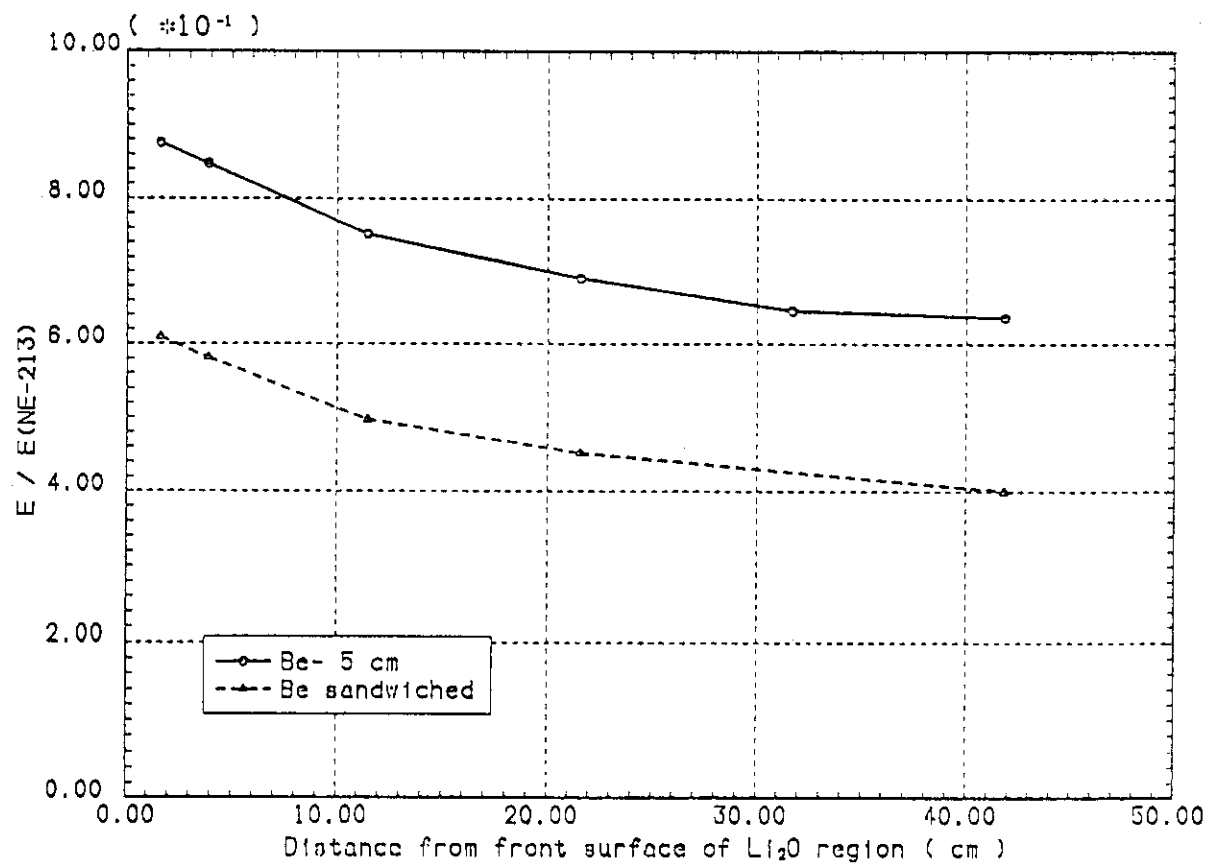


Figure IV.57 Neutron multiplication effect of Be on T₇ measured by the NE213 indirect method (DOT3.5/JACKAS calculations)

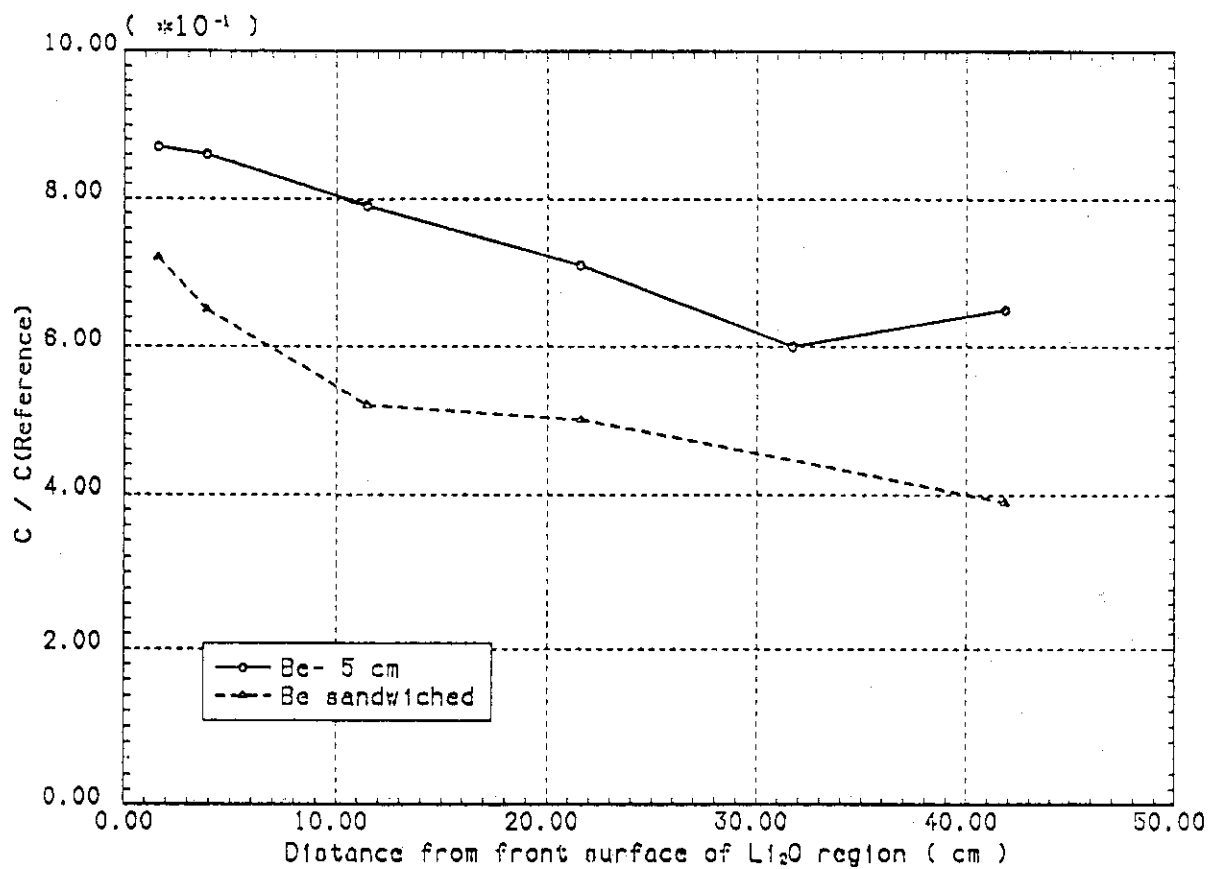


Figure IV.58 Neutron multiplication effect of Be on T₇ calculated by MORSE-DD with DDL/J3P1 evaluation

The C/E values of T_7 measured by the NE213 method are compared in Fig. IV.59 for the reference, the 5 cm-thick beryllium, and the Be-sandwiched systems. The 5 cm-thick beryllium case shows the lower C/E values (about 3-8% less than unity) when the DOT3.5 code was used, but larger values are obtained by the MORSE-DD code, except at the location $Z = 32$ cm, though the divergence in the calculations is not small. In the sandwiched case, on the other hand, the C/E values ($C/E = 1.04-1.06$) obtained by the DOT3.5 code are larger than 10% or more than those obtained in the 5 cm-thick beryllium case. Only the C/E values, as calculated by DOT3.5, are shown in Fig. IV.60, which includes the values obtained in the reference and three beryllium cases. The experimental values are based on the NE213 method. As shown in the beryllium-sandwiched and the reference cases, the C/E values are higher by 10% than those obtained in the other cases. The same features are also shown in Fig. IV.61. Such an inconsistency suggests that some kinds of systematic errors have been involved in the NE213 measurements. These measurements are discussed in detail in Volume I. Another inconsistency between measuring techniques can be observed in Fig. IV.62, showing the C/E values for NE213 and the Li-metal methods in the Be-sandwiched system, as calculated by both JAERI and the U.S., using the deterministic method. Results obtained by the Li-metal method show divergence over the whole Li_2O region; nevertheless, the C/E values in this case are lower, on average, than those obtained by the NE213 method. The reason for this discrepancy has not been resolved at present. Note from this figure that the curves with the NE213 method are flat as in other experiments. The C/E values obtained by JAERI are 1.05, while those obtained by the U.S. are 1.18-1.28. As for the Li-metal method, the large variation in the C/E curves with this method is due to the way the T_6 and T_7 were measured. A pair of natural lithium and 6Li -enriched samples, a pair of 6Li -enriched and 7Li -enriched samples, and a pair of 7Li -enriched and natural lithium samples were used at those locations denoted a, b, and c on the figure, respectively. After corrections were made for self-shielding effect in each sample type, the T_6 and T_7 measured values were derived simultaneously for a given pair of samples. It was shown that the derived T_7 values were sensitive to the specifications (dimension, size, atomic weight percentage, etc.) of the samples used, particularly for the 6Li -enriched samples.

Code and library intercomparison for the C/E values of T_7 is shown in Fig. IV.63 for the Be-sandwiched system using the measured values obtained by the NE213 indirect method. The features of the curves shown are similar to those found in the reference system (see Fig. IV.12) and the same remarks regarding the 7Li (n,n' α)t cross-section of the JENDL3 calculation can also be applied in this case. Note that if the measured values by the Li-metal method were used instead, the C/E values would have been lowered by 10-15%.

The C/E values of TPR obtained for natural lithium are shown in Fig. IV.64, where the calculations are obtained by DOT3.5. In the region $0 < Z < 35$ cm, both the Li_2O pellet (JAERI) and the Li-metal (U.S.) methods agree well with each other, but at deeper locations, the experimental errors in the Li-metal

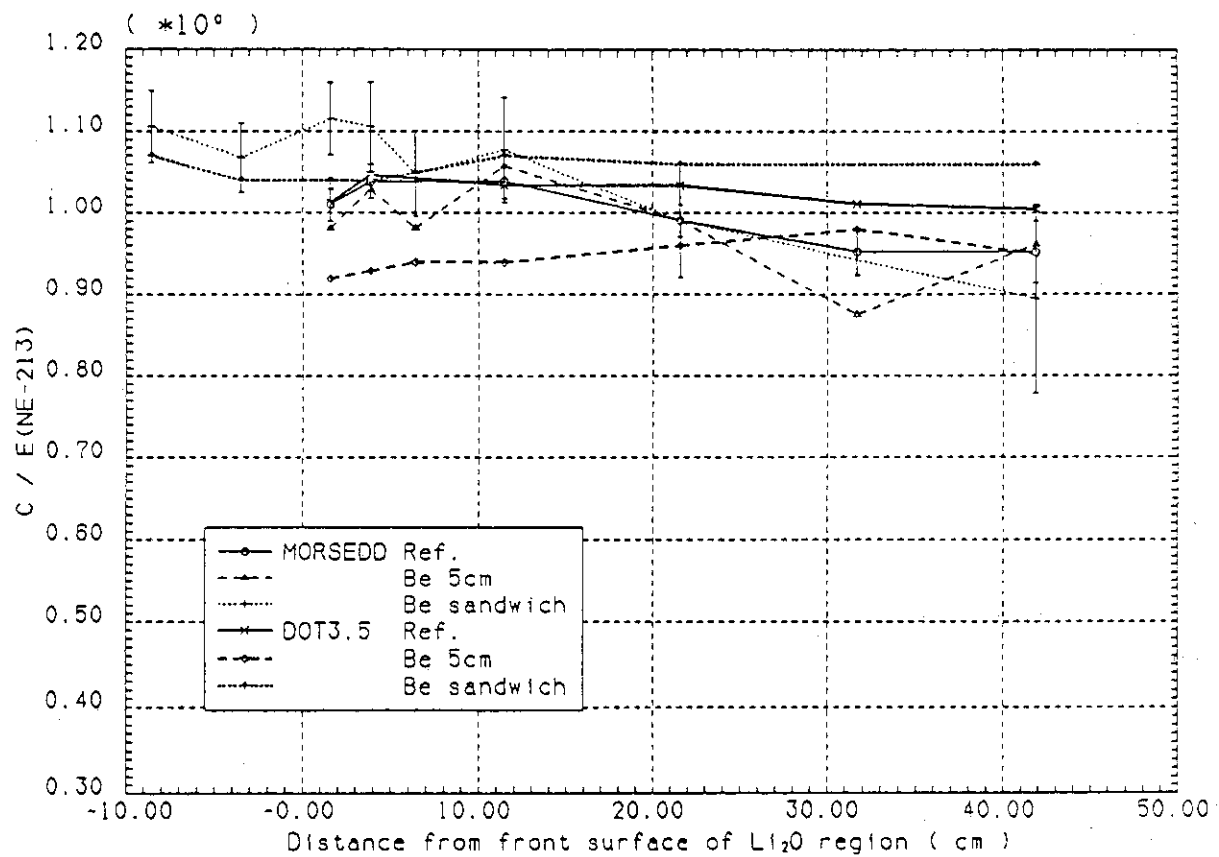


Figure IV.59 Comparison of C/E values for T7 based on experimental values obtained by the NE213 indirect method

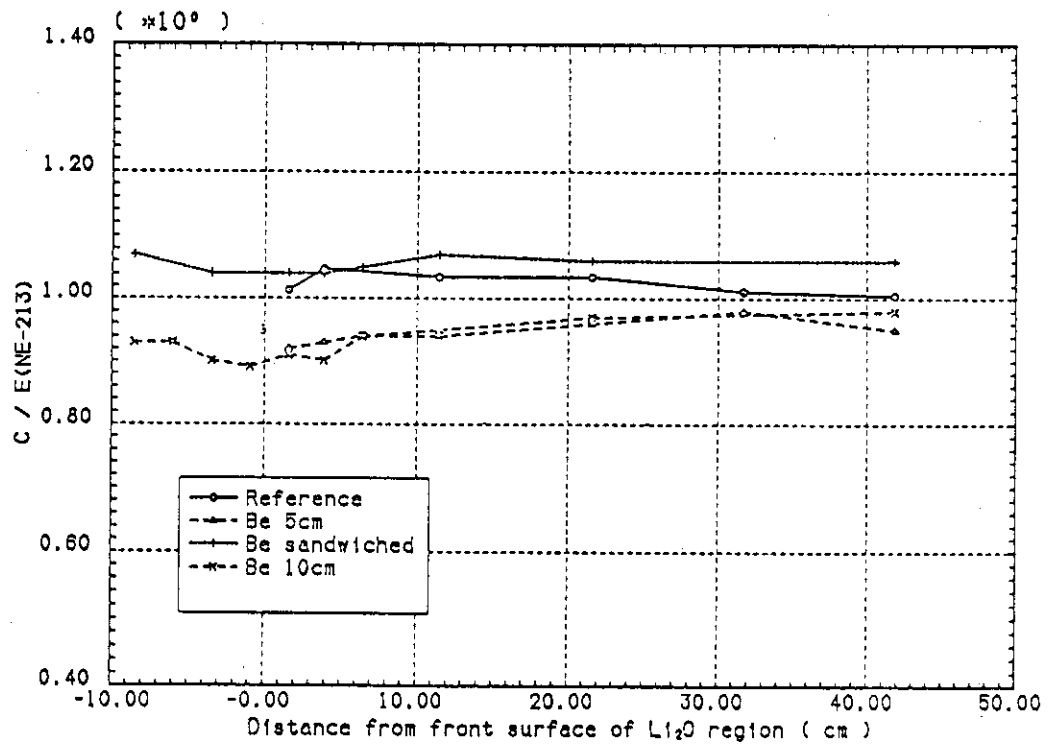


Figure IV.60 Comparison of C/E values for T7 between experiments with and without Be multiplier (experiment: NE213 detector, calculation: DOT3.5 with JACKAS)

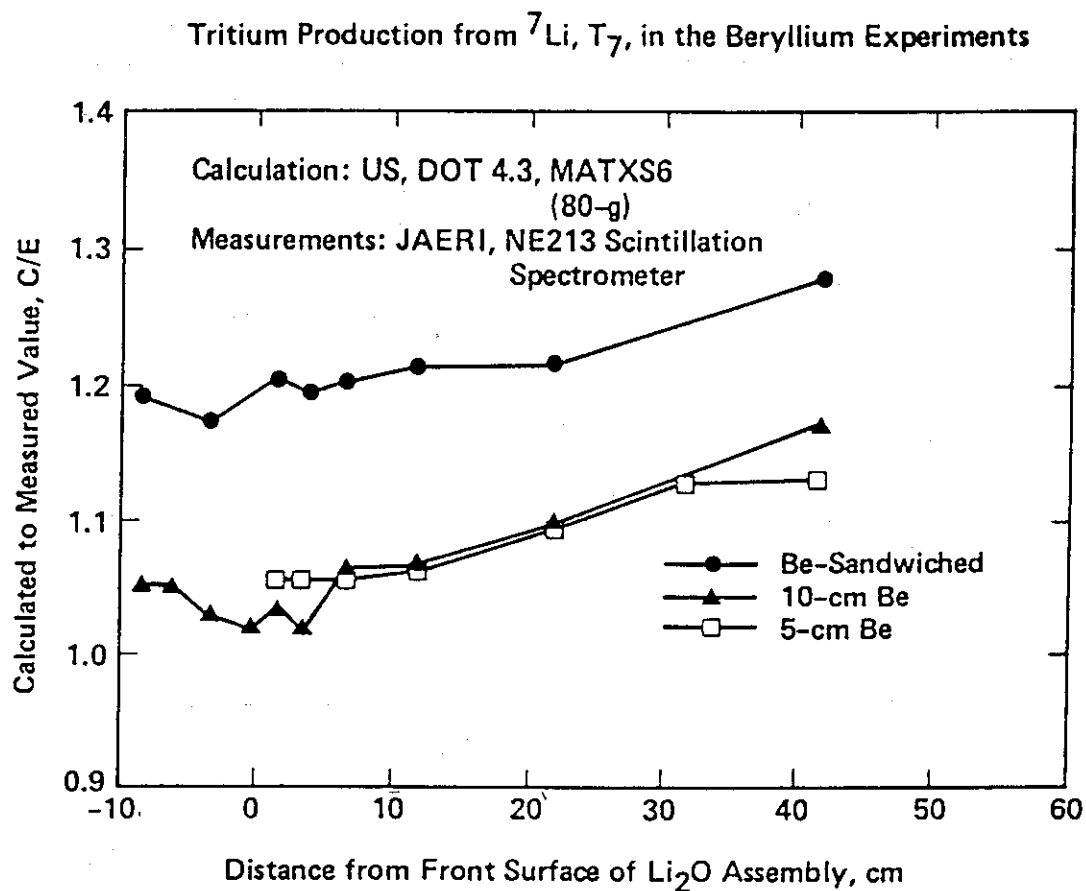


Figure IV.61 C/E values for tritium production from ${}^7\text{Li}$, T_7 in the beryllium experiments (experiment: NE213 detectors, calculation: DOT4.3/MATXS6)

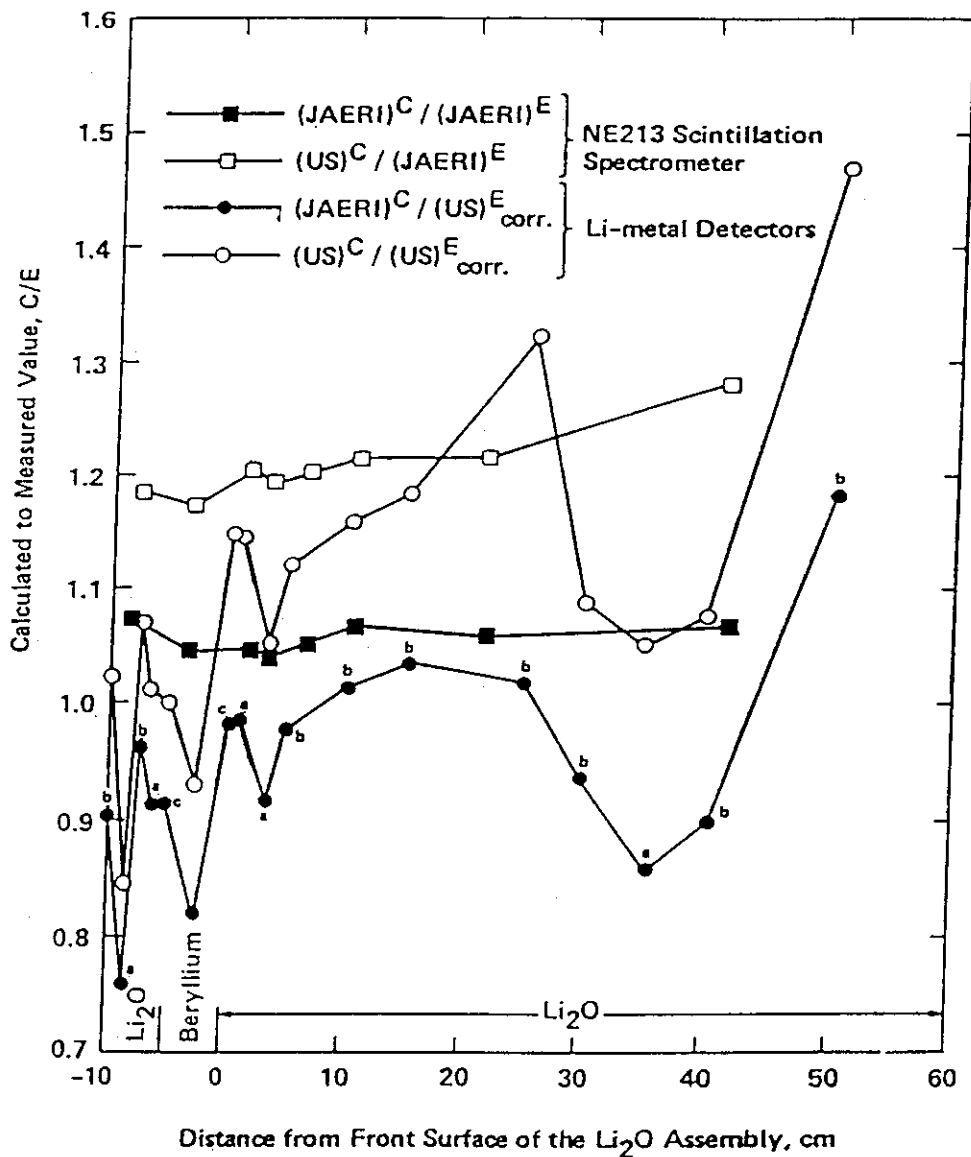
Tritium Production Rate from ${}^7\text{Li}$, T_7 , in the Beryllium-Sandwiched System

Figure IV.62 C/E values for tritium production rate from ${}^7\text{Li}$, T_7 , in the beryllium-sandwiched system using two measuring techniques (DOT calculations)

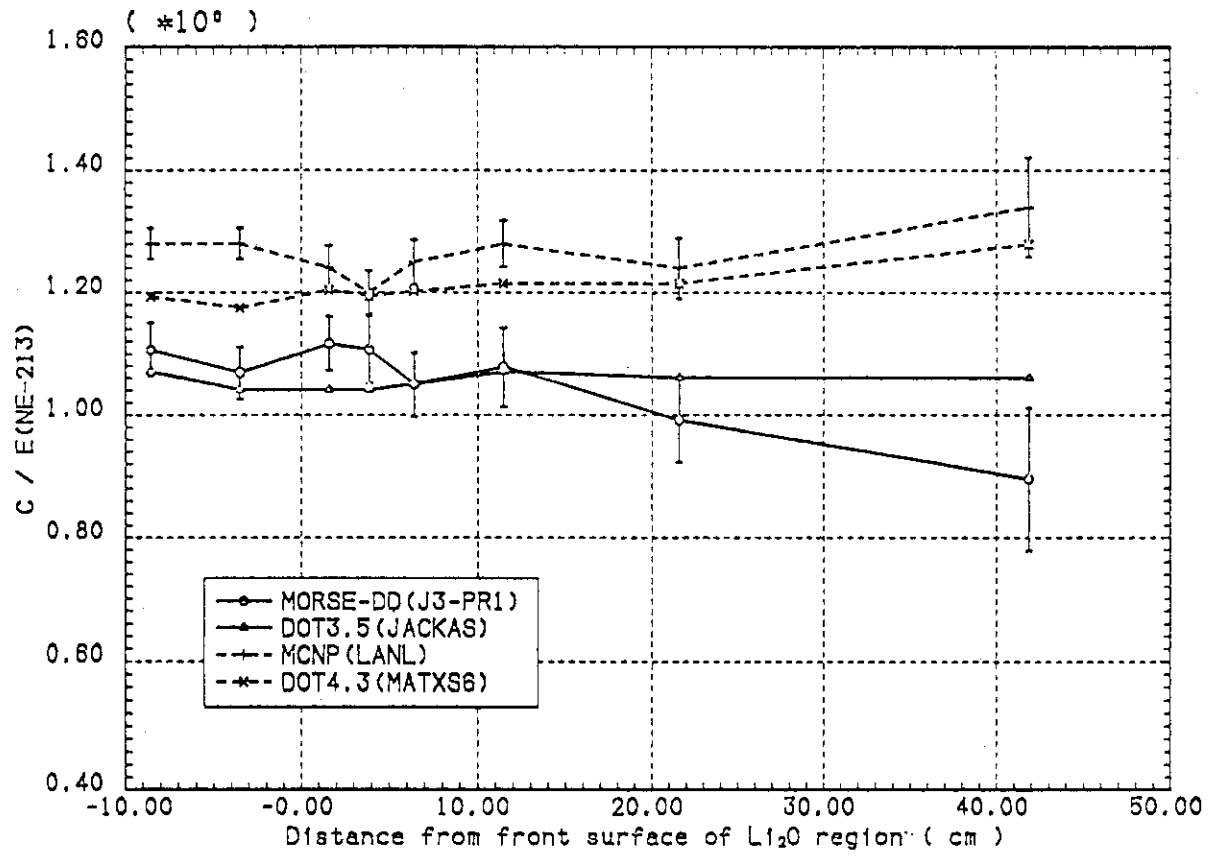


Figure IV.63 Comparison of C/E values for T_7 in Be-sandwiched system based on experimental values by the NE213 indirect method

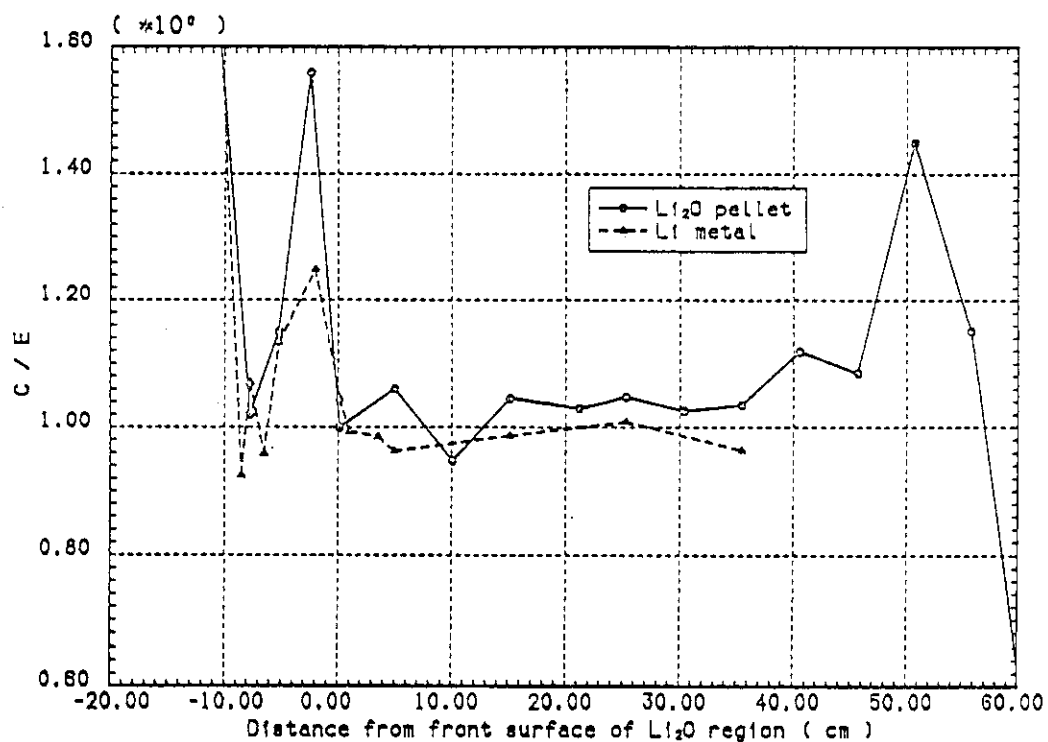


Figure IV.64 Comparison of C/E values for T_N in Be-sandwiched system between experiments with Li_2O and Li metal detectors based on the calculation performed by DOT3.5 with JACKAS library (JAERI)

measurements are large (not shown). It is interesting to note that the peaks in the C/E values are commonly predicted by the two measuring methods in the beryllium region at $Z = -2$ cm, similar to the case of T_6 . The C/E values for the TPR of natural lithium, as obtained by the DOT4.3 calculations (U.S.) are also shown in Fig. IV.65. Again, one can see that the U.S. predictions are larger by 10-15% than JAERI's predictions in the back of the Li_2O assembly.

Tritium Production Rate from Natural Lithium
in the Beryllium-Sandwiched System

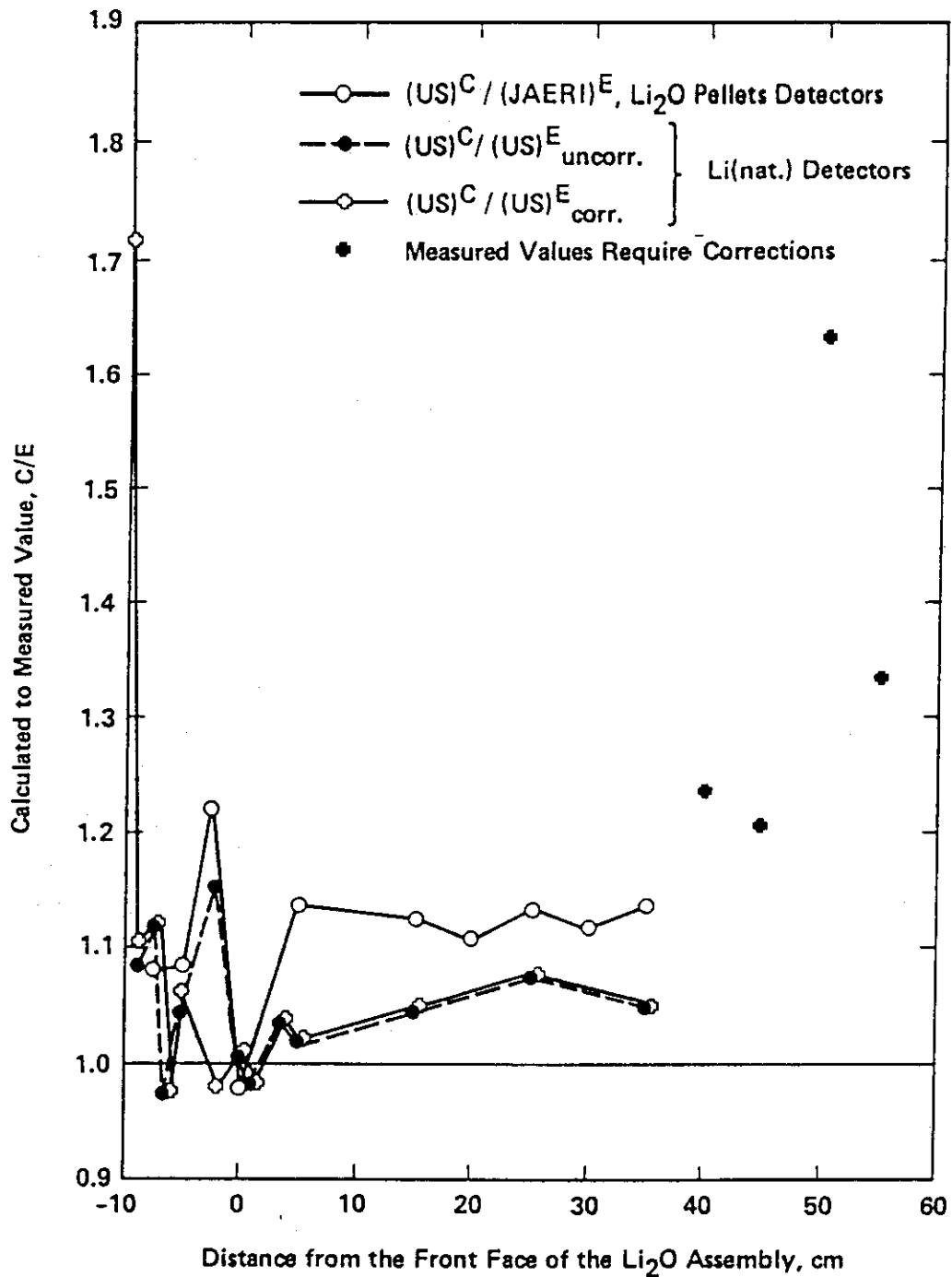


Figure IV.65 Tritium production rate from natural lithium in the beryllium-sandwiched system

V. REACTION RATES OF ACTIVATION FOILS

V.1 Reference System

Reaction rates of activation foils have been measured in the off-central drawer of the Li₂O assembly in addition to the TPR measurements. Among the many reaction types, we selected the following reactions in the reference system and in the beryllium-sandwiched system, where threshold energies are shown in brackets:

$^{27}\text{Al}(n,\alpha)^{24}\text{Na}$	(6 MeV),
$^{58}\text{Ni}(n,p)^{58}\text{Co}$	(2 MeV),
$^{58}\text{Ni}(n,2n)^{57}\text{Ni}$	(12.5 MeV),
$^{197}\text{Au}(n,2n)^{196}\text{Au}$	(8 MeV), and
$^{197}\text{Au}(n,\gamma)^{198}\text{Au}$	(0 eV).

These cross-sections are illustrated in Fig. V.1. The $^{58}\text{Ni}(n,2n)^{57}\text{Ni}$ cross-section has the highest threshold energy and the C/E values for this reaction are shown in Fig. V.2 for the reference system. Shown in this figure and subsequent figures are results based on both the deterministic and the Monte Carlo methods. In JAERI calculations using DOT3.5 code, the library used was based on ENDF/B-IV. Also shown in this figure are the MCNP results based on both the latest evaluation for ^7Li cross-sections (T-2 evaluations) and the evaluation of ENDF/B-V, Version 1(B5). The MORSE calculations were performed using the DDL/J3P1 library. As shown in Fig. V.2, the $^{58}\text{Ni}(n,2n)$ reaction rate is fairly underestimated by both ENDF/B-IV and JENDL3/PR1 or 2 files in JAERI's calculations. The deviation from unity increases inside the test assembly with increased distance. The results using the former file agree within several percent, but JENDL3/PR1 gives smaller values in the back locations. Concerning this reaction cross-section, new measurements were carried out at the FNS and the results show larger values for that cross-section.⁽³³⁾ Therefore, the C/E values as obtained by JAERI would be improved if the new cross-section was used.

In the U.S. calculations, the cross-section of $^{58}\text{Ni}(n,2n)$ applied in both MCNP calculations is from ENDL-73. Both MCNP(B5) and MCNP(T-2) calculated C/E distributions are lower than unity. The MCNP(T-2) calculated C/E values are consistently higher than those by MCNP(B5), particularly at the back locations. This is due to the fact that the $^7\text{Li}(n,\alpha)t$ cross-section, as evaluated by Young of the T-2 group at LANL, is smaller than that in Version 1 of the ENDF/B-V. This means that neutrons that have high energy have a better chance to reach the back locations with the T-2 evaluation than those with the B-5, Version 1 evaluation. Therefore, the calculated $^{58}\text{Ni}(n,2n)$ reaction rates are larger at these locations. As shown, the C/E values vary from 0.82 to 0.95 in the MCNP(T-2) calculations, and 0.60 to 0.92 in the MCNP(B5) calculations. The common dip shown in all the C/E distributions at $Z = 10$ cm suggests that

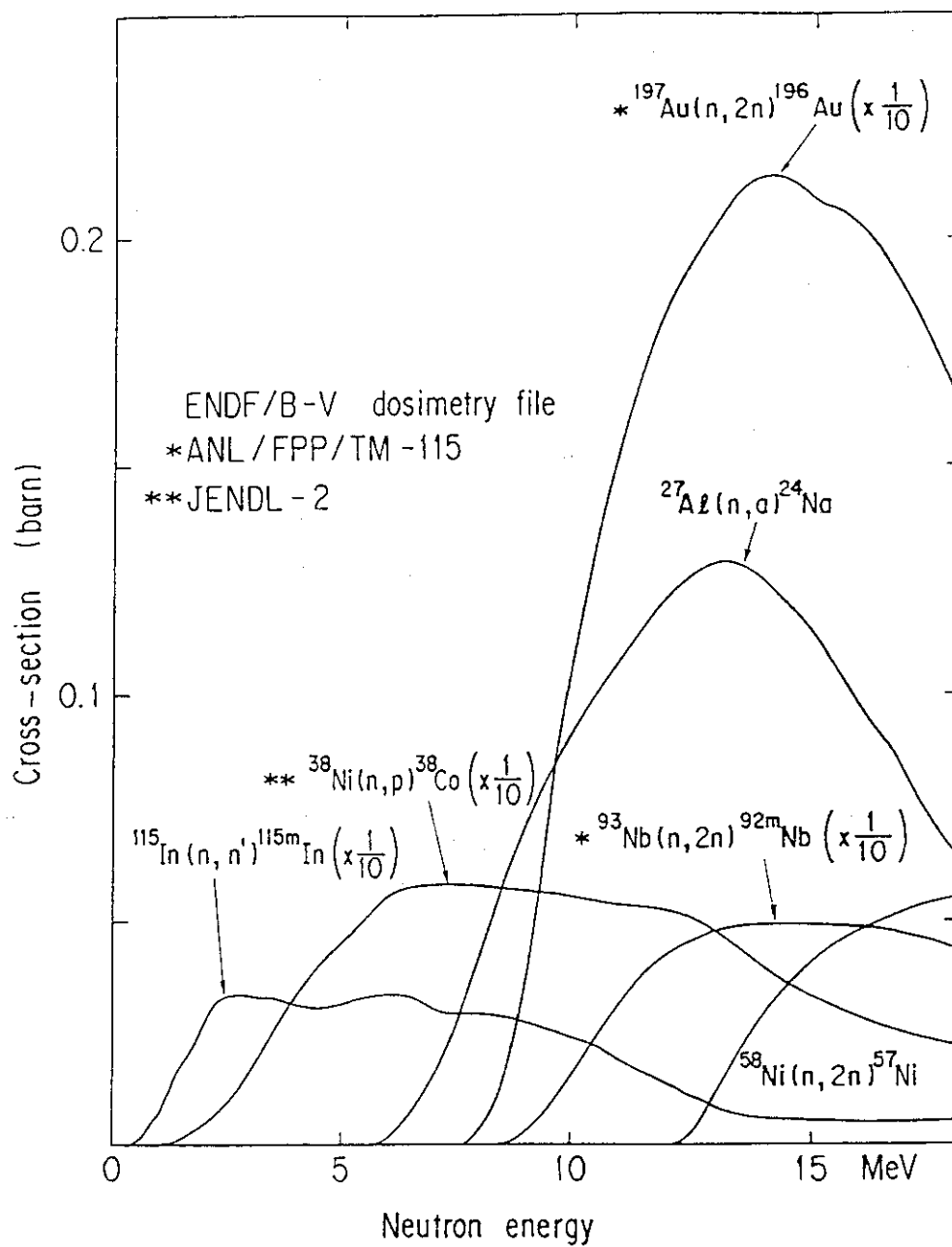
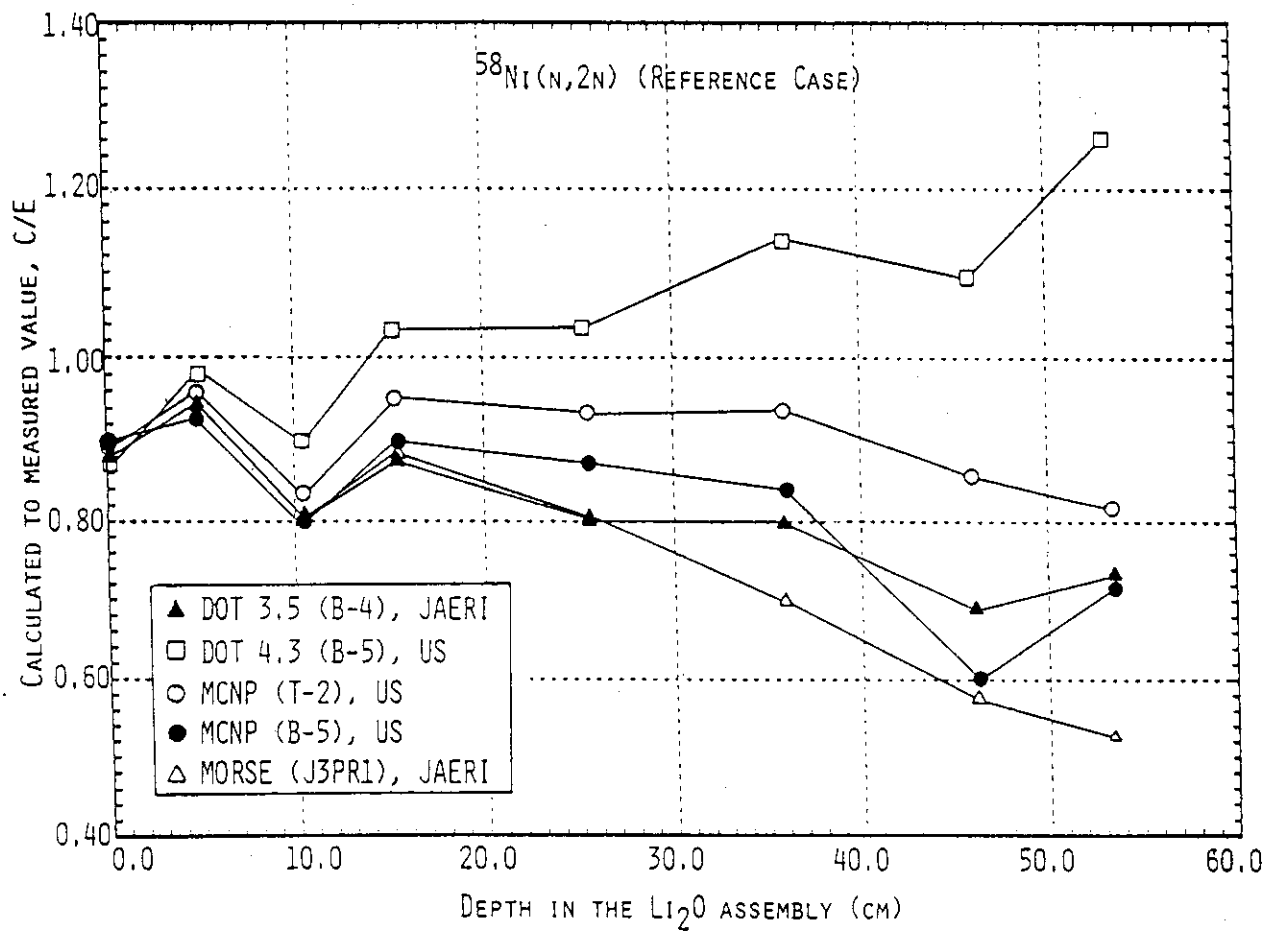


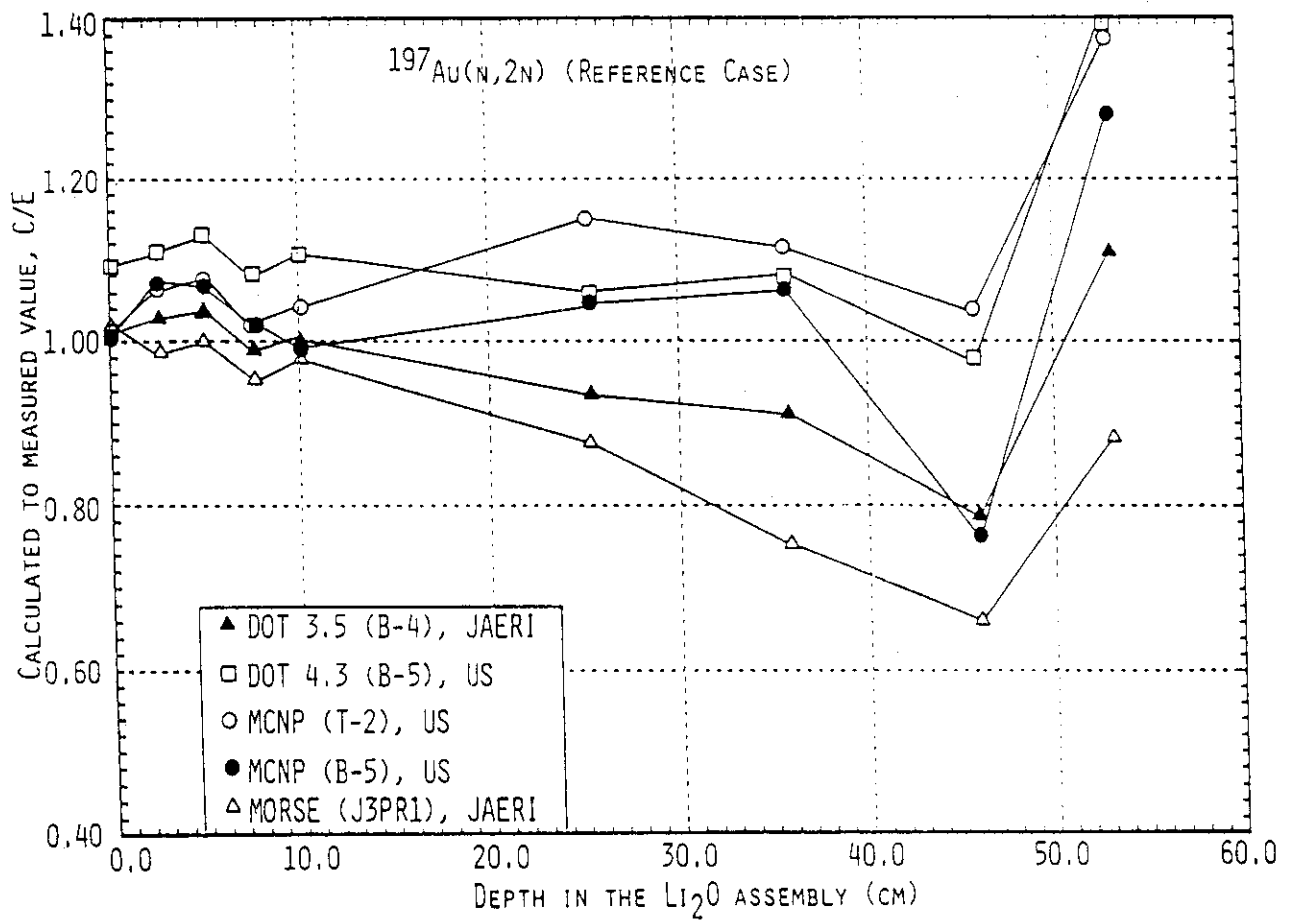
Figure V.1 Cross-sections for activation foils used in reaction rates measurements

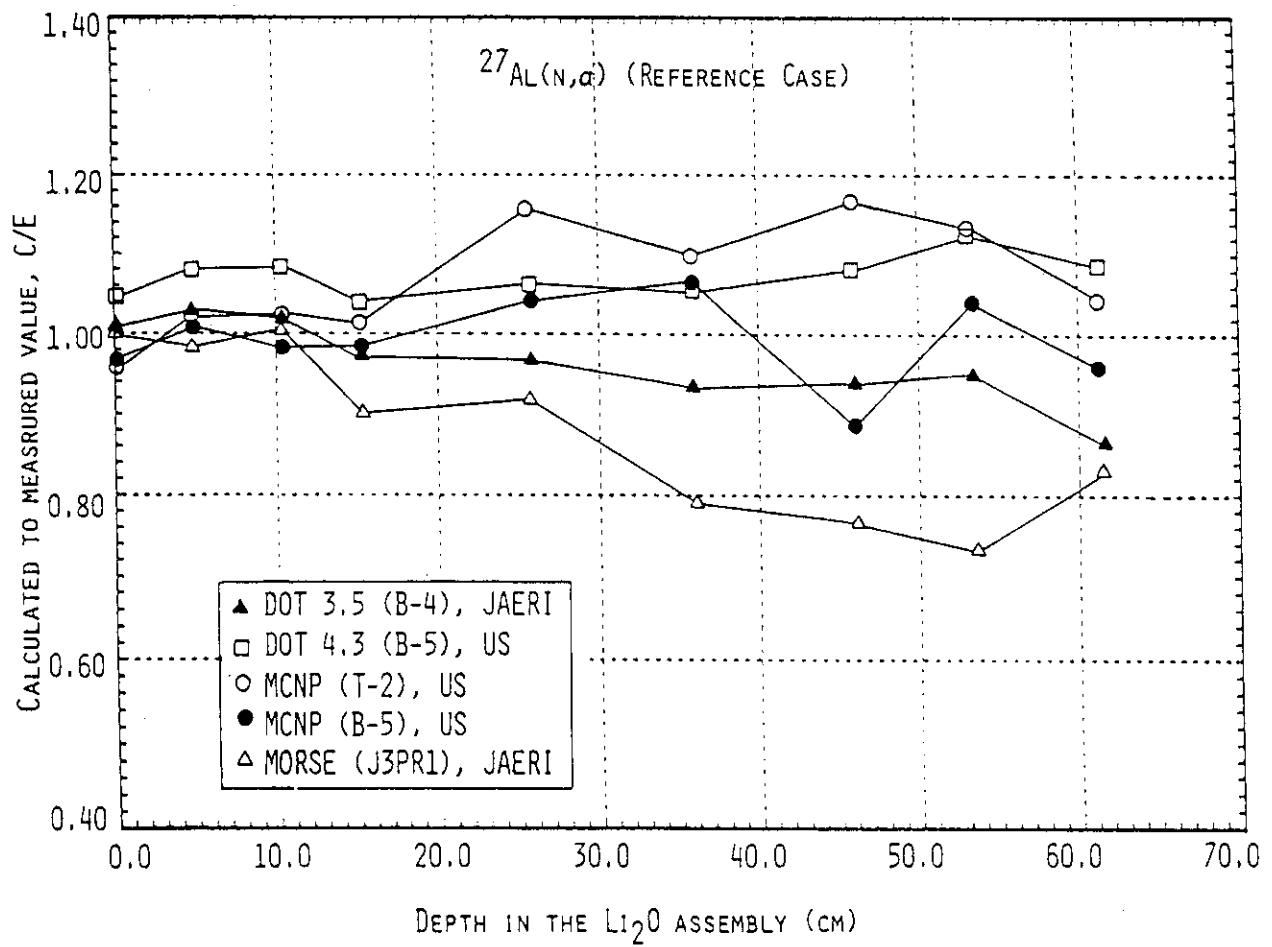
Figure V.2 $^{58}\text{Ni}(n,2n)$ in the reference case

there is a large experimental error at that location. Another dip at $Z = 46$ cm can also be seen on the MCNP(B5) calculated C/E distribution but not explicit on that of the MCNP(T-2). However, as shown in Fig. V.2, the DOT3.5(B4) and DOT4.3(B5) calculated C/E distributions show a similar drop at this location. Note also from the figure that the DOT4.3 calculations tend to show larger C/E values at the back locations in comparison to all other codes and libraries. In these particular calculations, the MATXS6 library was utilized where the latest evaluation of the T-2 group for ${}^7\text{Li}$ was used.

The result for the reaction rate ${}^{197}\text{Au}(n,2n){}^{196}\text{Au}$ is presented in Fig. V.3. In JAERI's calculations using the DOT and MORSE-DD codes, all the C/E values are around unity at $Z = 0$ cm and decrease as the distance from the surface increases. At the back locations beyond $Z = 40$ cm, the variation in the C/E values becomes large. This could be attributed to the statistics involved in the measured values. The trend of the spatial dependence of this reaction is quite similar to the case of the ${}^{58}\text{Ni}(n,2n){}^{57}\text{Ni}$ reaction though the agreement is better. The difference between ENDF/B-IV and JENDL3/PR1 is also similar to that found in the nickel case. In the U.S. calculations performed by the MCNP code, the C/E values are very close to unity near the front surface, as was shown in JAERI's calculations. However, in general, the predictions by the U.S. for the ${}^{197}\text{Au}(n,2n)$ reaction, is larger than those obtained by JAERI. This could be caused by the fact that the direct neutron component is larger than those predicted by JAERI (See Table II.2). Also notice from Fig. V.3 that the MCNP calculations performed by the T-2 evaluation for ${}^7\text{Li}$ are also larger than those obtained by the B-5 evaluation, Version 1. The MCNP(T-2) calculated C/E values change from 1.01 to 1.37, but they vary from 0.76 to 1.06 as predicted by MCNP(B5). As seen in Fig. V.3, in the front region, all the computations show C/E values greater than unity at $Z = 2.4$ and 5.0 cm followed by a drop at $Z = 7.5$ cm. Both MCNP(T-2) and MCNP(B5) calculated C/E distributions have similar trends from $Z = 10$ cm to the rear end. However, the former distribution has consistently higher values than the latter in this region. The dip at $Z = 46$ cm is also shown in all the calculations. The C/E drop is more explicit in the present reaction, and the rise in value at $Z = 53$ cm is also steeper.

In Fig. V.4 the C/E values for the ${}^{27}\text{Al}(n,\alpha){}^{24}\text{Na}$ reaction are shown. The values are about unity at the front surface except in DOT4.3 calculations which are ~ 1.08 at this location. In JAERI's calculations, the C/E values gradually decrease to about 0.85 with the ENDF/B-IV in the DOT3.5 calculation, but if JENDL3/PR1 data is used in the MORSE-DD calculations, these values become less. The gradient of decrease in the C/E curves is not as large as for the ${}^{58}\text{Ni}(n,2n)$ and ${}^{197}\text{Au}(n,2n)$ reactions. This is due to the difference in the threshold energies. In the U.S. calculations shown in Fig. V.4, the Monte Carlo results are still larger than those obtained by the MORSE-DD code used by JAERI. Also, notice again that the MCNP calculations with the T-2 evaluation for ${}^7\text{Li}$ are still larger than those obtained with the B-5 evaluation, Version 1. This is noticed particularly at the rear locations. The DOT4.3 results show that the C/E values are steady and flat throughout the assembly and they range from 1.05 to 1.1. The MCNP(T-2) calculated C/E values change from 0.95 to 1.15, and they change from 0.88 to 1.06 in the MCNP(B5) calculations. At distance $Z < 15$ cm from the mouth of the experimental port, both calculations give C/E

Figure V.3 $^{197}\text{Au}(n,2n)$ in the reference case

Figure V.4 $^{27}\text{Al}(n,\alpha)$ in the reference case

values close to unity and are consistent with JAERI's calculations. At locations greater than 15 cm, the MCNP(T-2) calculated C/E values increase to 1.10. The MCNP(B5) calculated C/E distribution increases slightly ($< 6\%$) and is still within the error bounds. However, a dip with $C/E = 0.88$ is found at $Z = 46$ cm on the MCNP(B5) C/E distribution. The relative standard deviation in the computation at this location is no more than 6%, and the experimental error is about 3%. The discrepancy cannot be covered by the error bounds. Comparing with all other C/E distributions of the $^{27}\text{Al}(n,\alpha)$ reaction, the dip at $Z = 46$ cm is unique in the MCNP(B5) calculations. Therefore it is not likely to be caused by the measured value. The reason for this dip is not clear.

As was mentioned earlier, the threshold energy for $^{27}\text{Al}(n,\alpha)$ reaction is about 6 MeV. This is a lower energy threshold than for $^{58}\text{Ni}(n,2n)$ and $^{197}\text{Au}(n,2n)$ reactions. Therefore, one notices from Fig. V.4 that the decrease in the gradient of the C/E curves is smoother for this reaction in comparison to the $^{58}\text{Ni}(n,2n)$ and $^{197}\text{Au}(n,2n)$ reactions. This is also true for the $^{58}\text{Ni}(n,p)$ reaction, as shown in Fig. V.5. However, as one notices from that figure, the C/E values at the surface are larger than 1 as predicted by both JAERI and the U.S., except for the MCNP(T-2) calculations which have values close to unity at the front surface. The discrepancy at the surface of the system may not be caused by the value or discrepancies in the reaction cross-section itself because this cross-section is often used as a reactor standard activation cross-section as is the case with $^{27}\text{Al}(n,\alpha)$. Hence these cross-sections are believed to be well-known. In addition, this discrepancy may not be true at 14 MeV or higher energy. The overestimation at the entrance of $^{58}\text{Ni}(n,p)$ reaction rate is not simple to interpret but two possibilities could be considered. First, this overestimation could be due to the overestimation of incident neutrons. As was shown in Section III, there is overestimation of integral flux by the NE213 detector. Second, this discrepancy could be caused by the backscattering component due to an improper angular distribution of elastic scattering by ^7Li . From a simple estimation, the contribution of the backscattered neutrons to Ni(n,p) reaction is about 24%, which is much higher than those with high energy threshold reactions such as $\text{Al}(n,\alpha)$, $\text{Ni}(n,2n)$ or $\text{Au}(n,2n)$. Note from Fig. V.5 that the C/E values obtained by JAERI tend to decrease as one proceeds toward back locations where the values fall below unity. This descending trend could be seen in all the threshold reactions. As for the $^{58}\text{Ni}(n,2n)$ cross-section, the new evaluation by Ikeda⁽³³⁾ for $^{58}\text{Ni}(n,p)$ gives better agreement with measurements. In the MCNP calculations performed by the U.S., the $^{58}\text{Ni}(n,p)$ activity cross-section data in the ENDL-73 library seems to be adequate. The C/E values are within 0.99 to 1.11 by MCNP(T-2) calculations, and 0.83 to 1.05 by MCNP(B5). The dip at $Z = 46$ cm still exists in MCNP(B5), DOT3.5(B4), and DOT4.3(B5) calculated C/E distributions. Another common dip at $Z = 25$ cm is observed in all but the MCNP(T-2) distribution. The MCNP(T-2) calculated reaction rates agree very well with the experimental results at locations $Z < 15$ cm. At deeper locations, the C/E values increase monotonically. The DOT4.3(B5) calculations, which actually used T-2 evaluation for ^7Li , and ENDF/B-V activity cross-section for $^{58}\text{Ni}(n,p)$ reaction, show a C/E distribution that is very consistent with that of MCNP(B5) instead of MCNP(T-2) at $Z > 15$ cm. Since both MCNP(T-2) and DOT(B5) used T-2 evaluation for ^7Li , their C/E curves are similar.

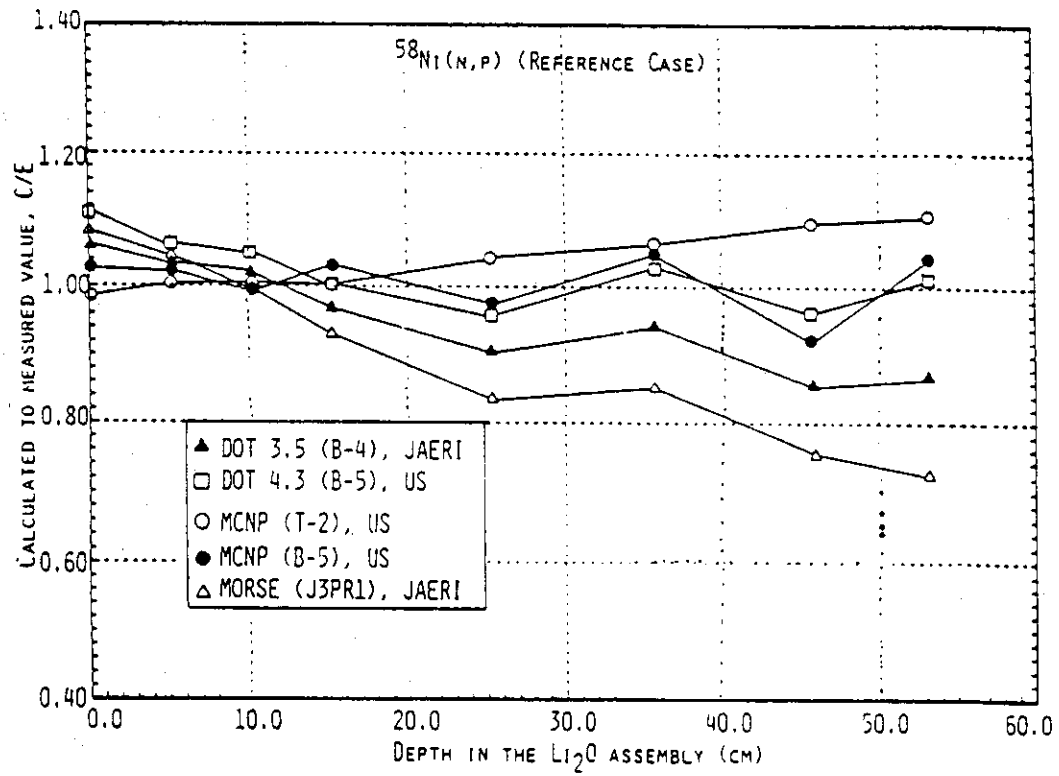
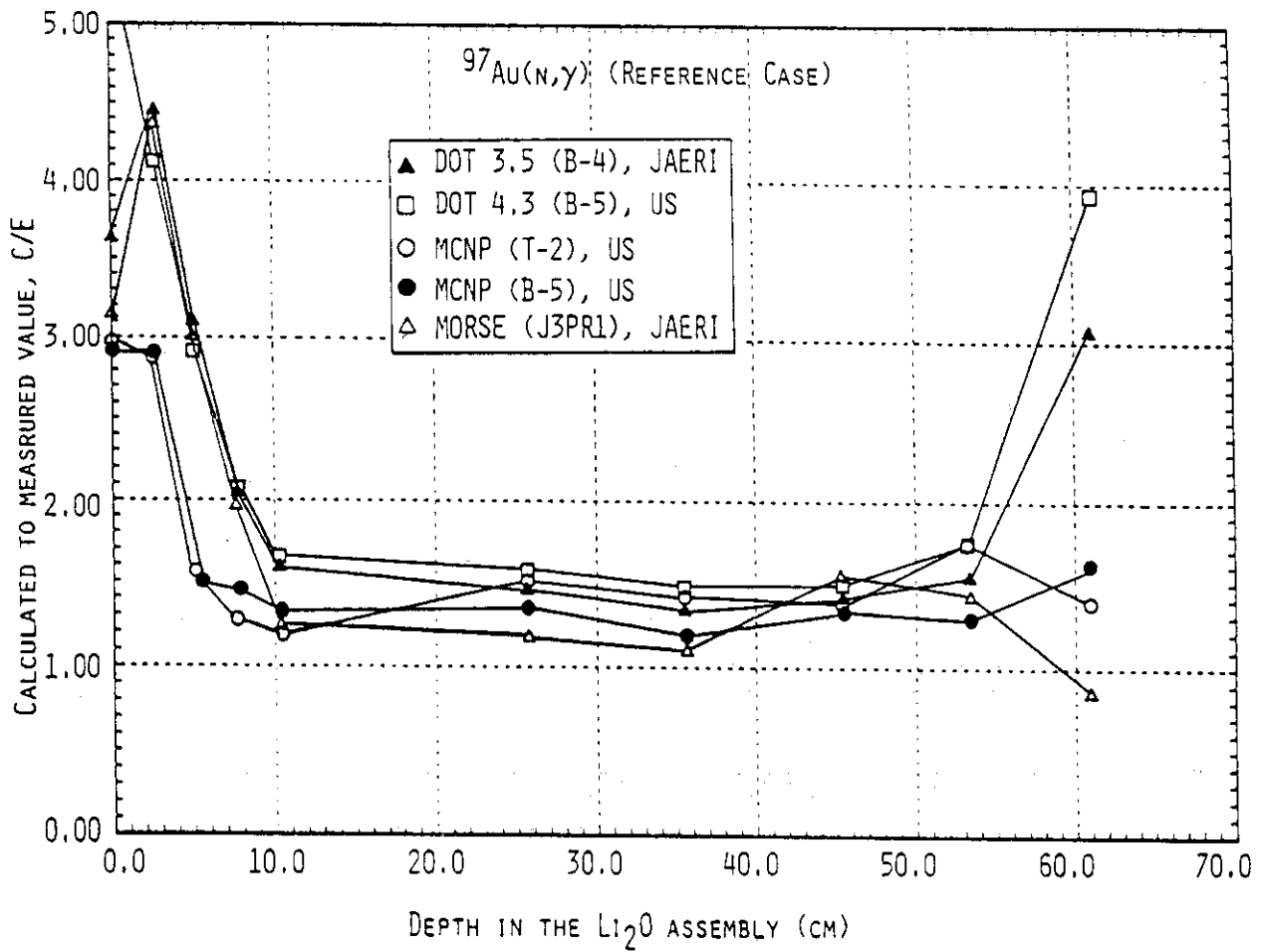


Figure V.5 C/E values for $^{58}\text{Ni}(n,p)$ reaction rate in the reference system

To investigate the distribution profile of a nonthreshold reaction, the $^{197}\text{Au}(n,\gamma)^{198}\text{Au}$ has also been measured using gold foils. As is well known, this reaction is very sensitive to the low-energy neutrons, e.g., in the eV region, because of the existence of strong capture resonances. Accordingly, the correction for self-shielding effect is very important if the foil used is not sufficiently thin. In the present experiment, very thick foils were used in the reference system. The impact is obvious in Fig. V.6, which presents the C/E values along the Z axis. Since all the measurements have not been corrected for self-shielding effect, the measured reaction rates were underestimated compared with the calculations which correspond to an infinitely diluted density. The figure shows that in the front region ($Z = 0 \sim 10$ cm), the C/E values are very large. In the range, $Z = 10 \sim 50$ cm, the C/E values are almost flat, although the influence of the self-shielding effect is still apparent. The tendency that the C/E values decrease from unity with increasing distance is not seen for the nonthreshold reaction, as was observed in the threshold reactions. For the nonthreshold reaction, and in the Monte Carlo calculations, reducing the variance to a reasonable level with limited computing time is very difficult. As shown in Fig. V.6, the MCNP(T-2) calculated C/E values are in the range of 1.16 to 2.88, and are 1.20 to 2.87, in the MCNP(B5) calculations. The lowest relative standard deviation in both computations is about 10%. The trend of the C/E curves in the front region is similar to the T_6 comparison discussed in Section IV due to the room-return source component.

JAERI has also performed other code and library intercomparisons, and the C/E values for the various reaction rates discussed above are shown in Figures V.7 to V.11. These figures show results based on DOT3.5 with the JACKAS library and on MORSE-DD with the DDL/B-4 library. The trends observed in these figures are similar to those discussed for Figures V.2 to V.6. In all these figures, it appears that the MORSE-DD calculations with ENDF/B-IV data give closer C/E values to unity in comparison to the results obtained with the DDL/J3P1 library, particularly at the back locations. However, in the DOT3.5 calculations with the JACKAS library, slight improvement in the C/E values is observed, as compared to the results obtained with the ENDF/B-IV data. Note also that the U.S. predictions for these reaction rates are still larger than JAERI's predictions. Also note that the C/E curves for the threshold reactions, as obtained by JAERI, tend to decrease as one moves to the back end of the Li_2O assembly. We can guess some reasons for such discrepancies:

1. The total cross-sections of Li_2O is overestimated. This could primarily be from overestimation in elastic scattering by ^7Li . The fact that the DOT3.5-JACKAS calculations always give the largest C/E values in the back locations supports the above reasoning because JACKAS uses the JENDL3/PR2 data base, in which the elastic scattering cross-section of ^7Li is smaller than that of JENDL3/PR1.
2. The inelastic scattering cross-sections of Li_2O may cause an overmoderation of neutron energy.
3. Improper modeling of the experimental system, such as density, streaming effect, homogenization, etc.

Figure V.6 $^{97}\text{Au}(n,\gamma)$ in the reference case

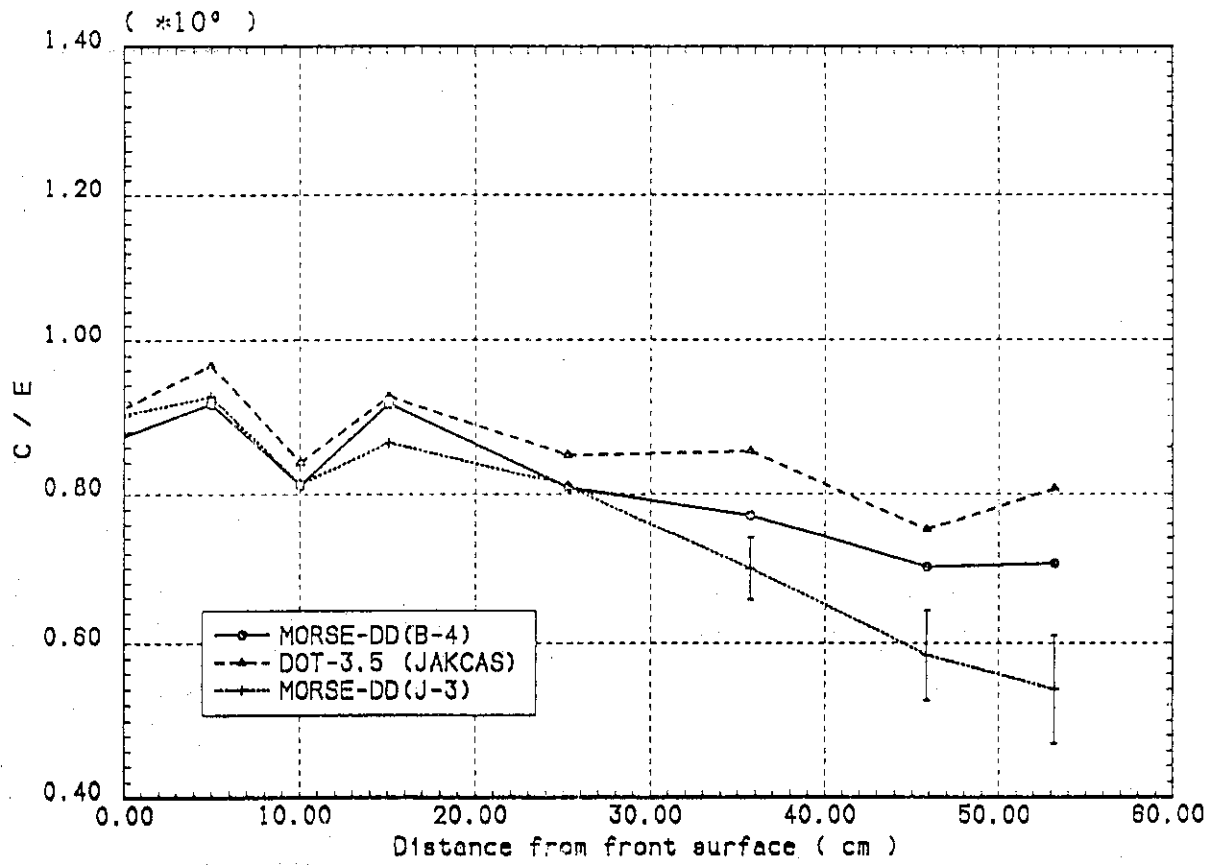


Figure V.7 C/E values for $^{58}\text{Ni}(n,2n)^{57}\text{Ni}$ reaction rate in the reference system (JAERI)

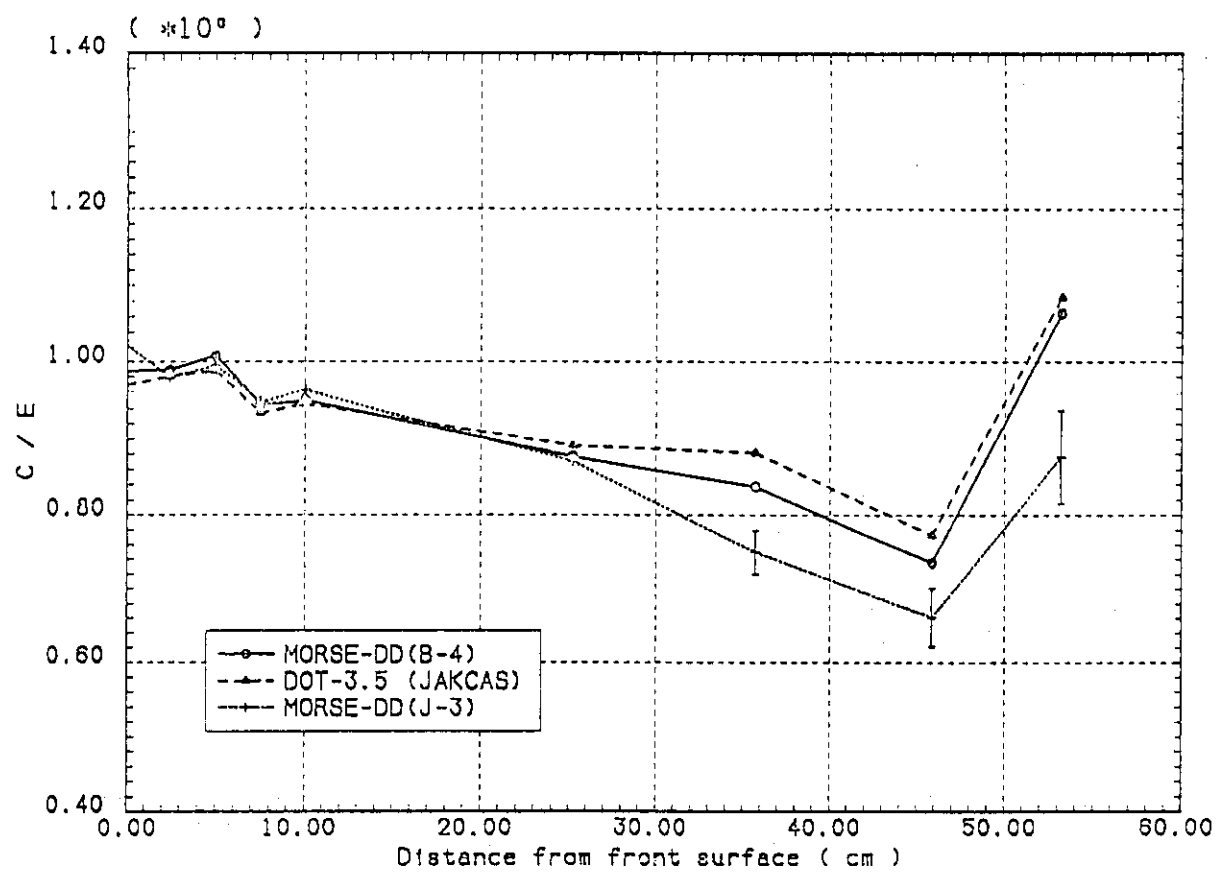


Figure V.8 C/E values for $^{197}\text{Au}(n,2n)^{196}\text{Au}$ reaction rates in the reference system (JAERI)

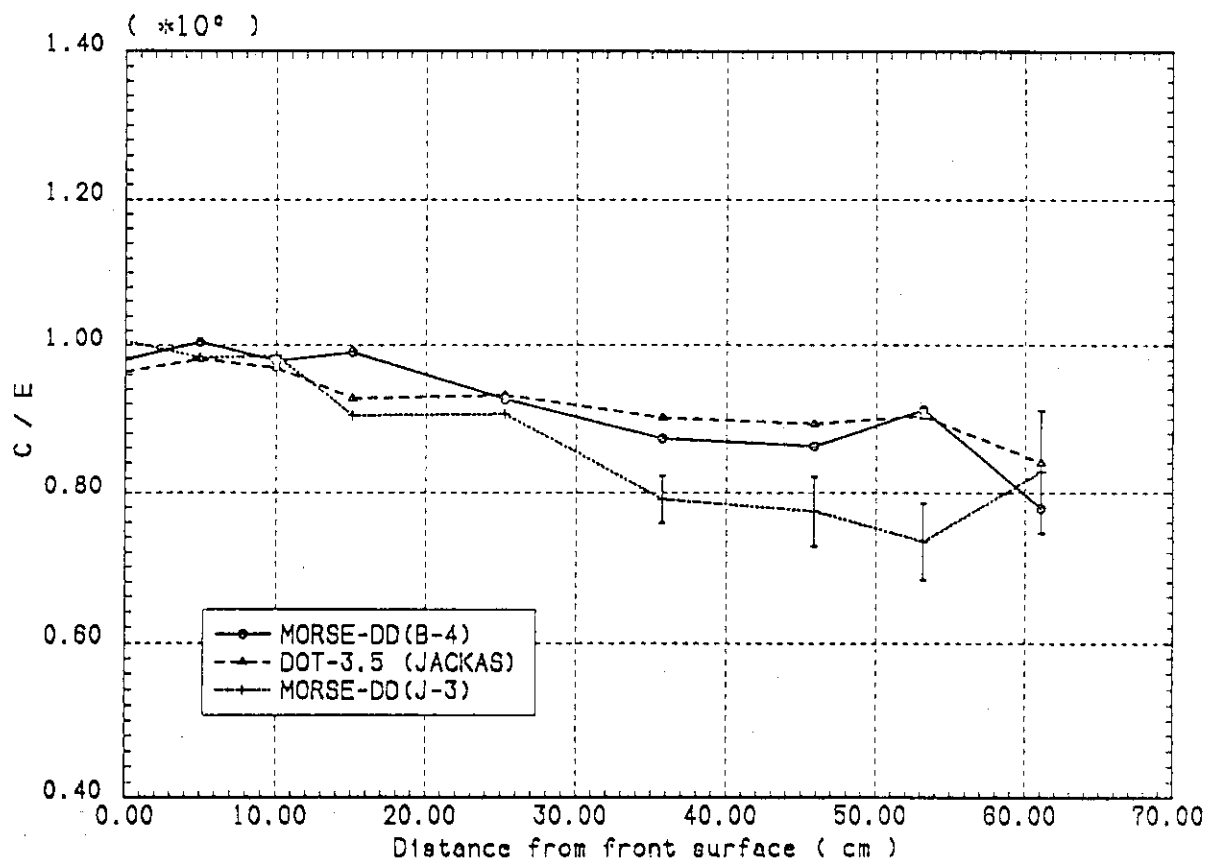


Figure V.9 C/E values for $^{27}\text{Al}(n,\alpha)^{24}\text{Na}$ reaction rate in the reference system (JAERI)

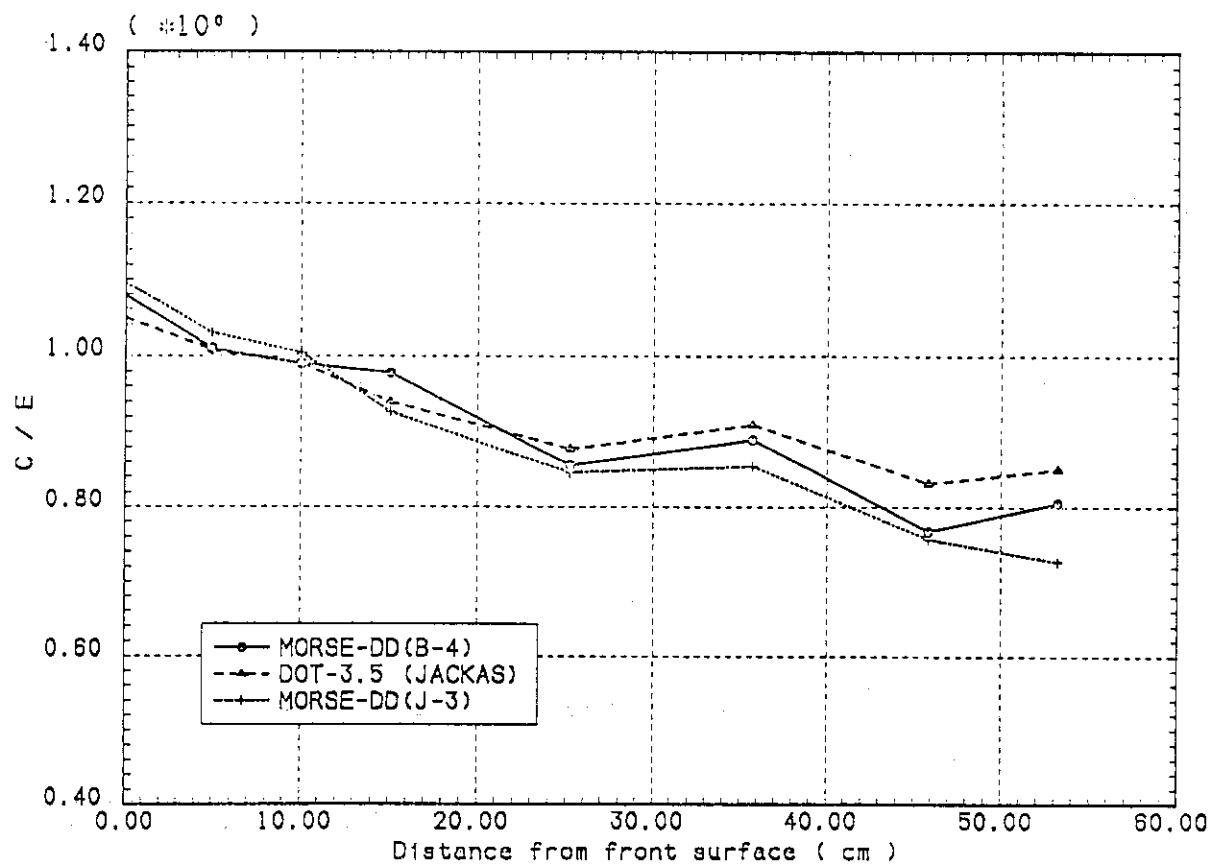


Figure V.10 C/E values for $^{58}\text{Ni}(n,p)^{58}\text{Co}$ reaction rate in the reference system (JAERI)

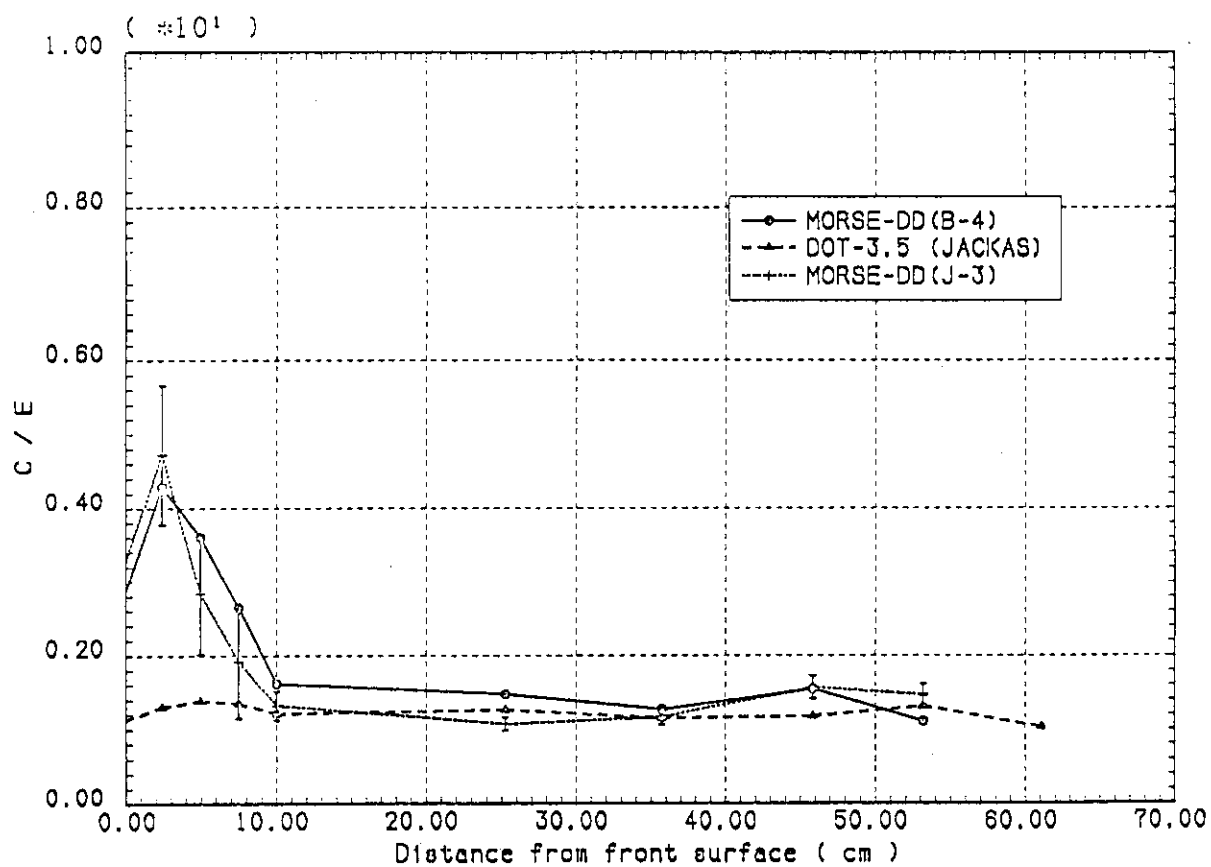


Figure V.11 C/E values for $^{197}\text{Au}(n,\gamma)^{198}\text{Au}$ reaction rate in the reference system

But it is difficult to suspect all the reaction cross-sections. Among the reasons mentioned above, the first is the most likely. This was confirmed by direct intercomparison between the various cross-sections used by JAERI and the U.S. This intercomparison and the reasoning for the trends of the C/E curves shown in Figs V.2 to V.11 are discussed further in subsection V.3.

V.2 Beryllium-Sandwiched System

Foil activation rate measurements were also performed in the beryllium-sandwiched system. These include $^{27}\text{Al}(n,\alpha)^{24}\text{Na}$, $^{58}\text{Ni}(n,2n)^{57}\text{Ni}$, $^{115}\text{In}(n,n')^{115}\text{In}$ and $^{80}\text{Zr}(n,2n)^{79}\text{Zr}$. The C/E values for the $\text{Al}(n,\alpha)$ reaction are shown in Fig. V.12. In JAERI's calculations, the C/E values of about 0.9 at $Z < 20$ was predicted by both DOT3.5/JACKAS and the MORSE-DD(J3PR1). The very low value given by MORSE-DD at $Z = 30$ cm is due to a statistical problem. The low values at the entrance $Z = -10$ cm (shown also in the U.S. calculation but to a lesser extent) are probably due to an inadequacy in the cross-section of beryllium. The underestimation at the front surface is also apparent in Figures V.13 and V.14. On the other hand, the U.S. calculations show better agreement with the measurements throughout the Li_2O test assembly, as shown in Fig. V.12, particularly in the calculations performed by DOT4.3/MATXS6, where the C/E values are 0.95 to 1.02. The MCNP results shown in Fig. V.12 (and Fig. V.15) are based on the RMCCS library that utilizes Young's evaluation for ^7Li (T-2 group) and the latest evaluation for beryllium⁽¹⁸⁾ which is also used in the DOT4.3 calculations. Note that the C/E values in the U.S. calculations are still less than unity at the front surface for the $^{27}\text{Al}(n,\alpha)$ reaction, as was observed in JAERI's calculations. This could be caused by underestimation in the Be (n, elastic) cross-section, and/or inadequacy in the neutron emission cross-sections of Be which tend to underestimate backscattered neutrons.

Concerning the reactions $^{93}\text{Zr}(n,2n)$ and $^{115}\text{In}(n,n')$, the MORSE-DD and DOT3.5 results give similar C/E values but the results for the former reaction rate show, on the average, better agreement with the measurements where there is no peak in the beryllium or at the interface region.

The C/E values for the $\text{Au}(n,\gamma)$ reaction show dips and peaks over the region from the surface to the front part of the Li_2O system (see Fig. V.15). The thickness of gold foils used in this case is so thin that the self-shielding correction factors are very small. The agreement between measurements and calculations is generally good in the range $Z = 15$ cm \sim 40 cm. Large differences are observed in the results obtained by the MORSE-DD and MCNP codes, but the differences could be caused by the large fractional standard deviation (FSD) observed in the calculations. Note that $\text{Au}(n,\gamma)$ is strongly sensitive to the very low energy neutrons and a large computation time is required to obtain high accuracy in the calculations.

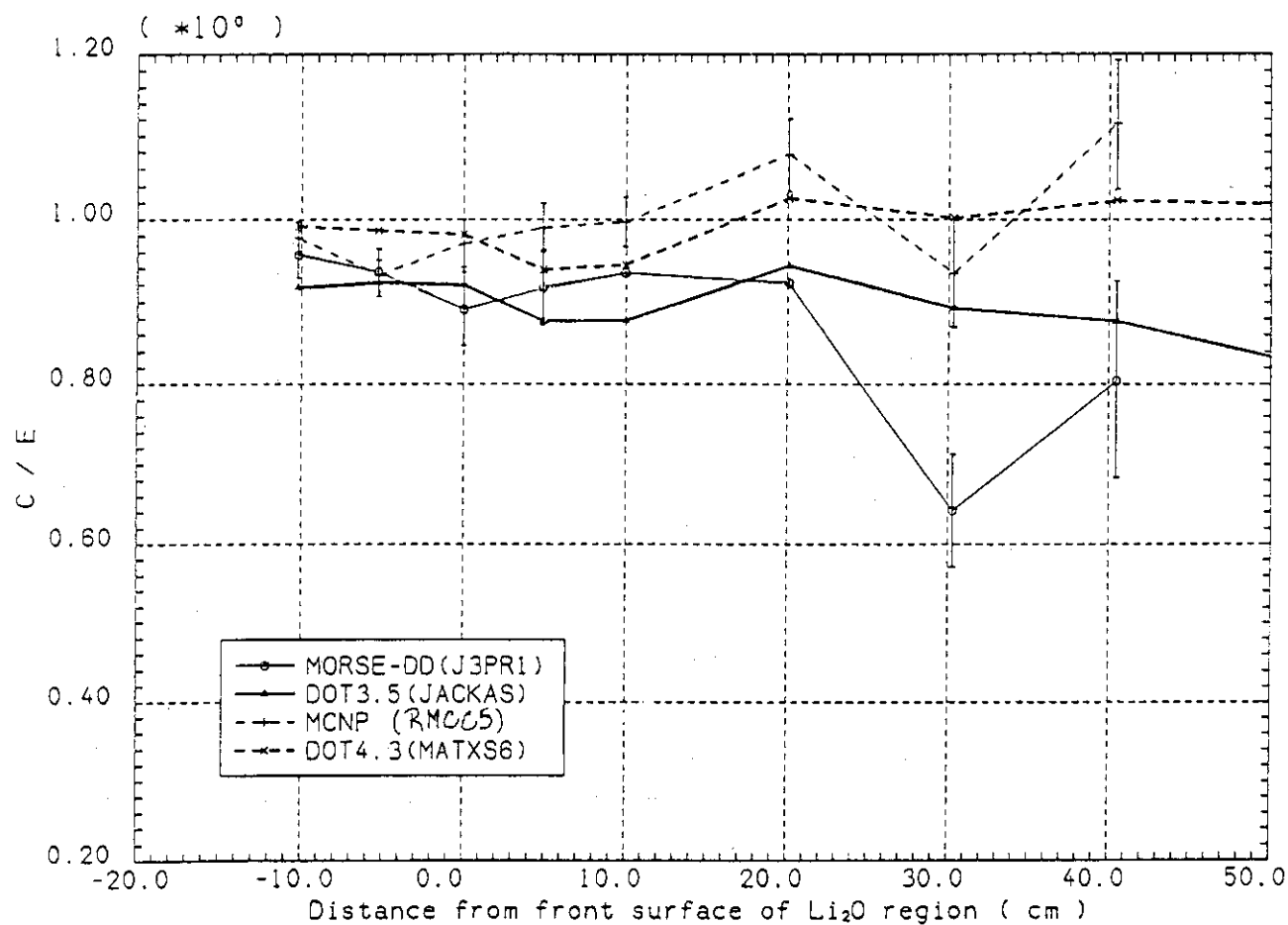


Figure V.12 C/E values for $^{27}\text{Al}(n,\alpha)^{24}\text{Al}$ reaction rate in the Be-sandwiched system

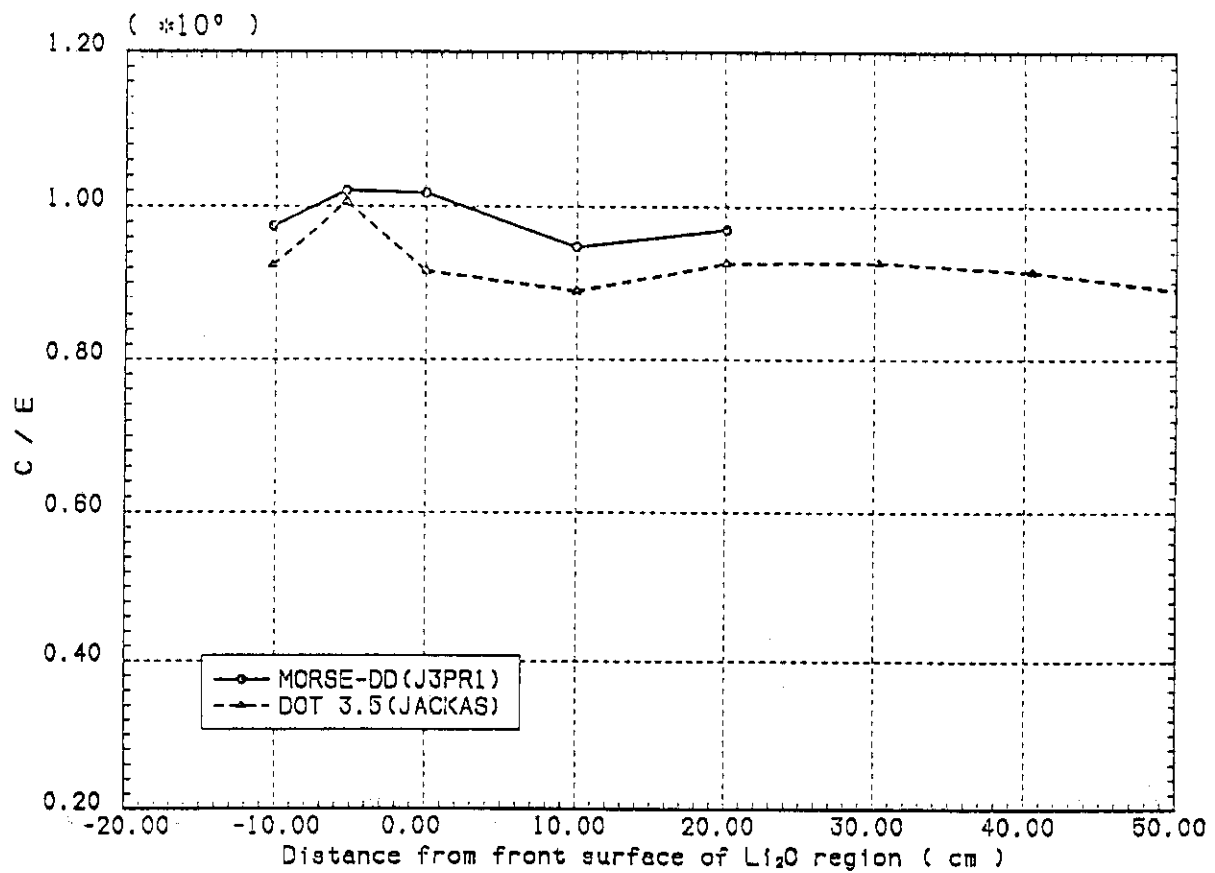


Figure V.13 C/E values for $^{90}\text{Zr}(n,2n)^{89}\text{Zr}$ reaction rate in the Be-sandwiched system

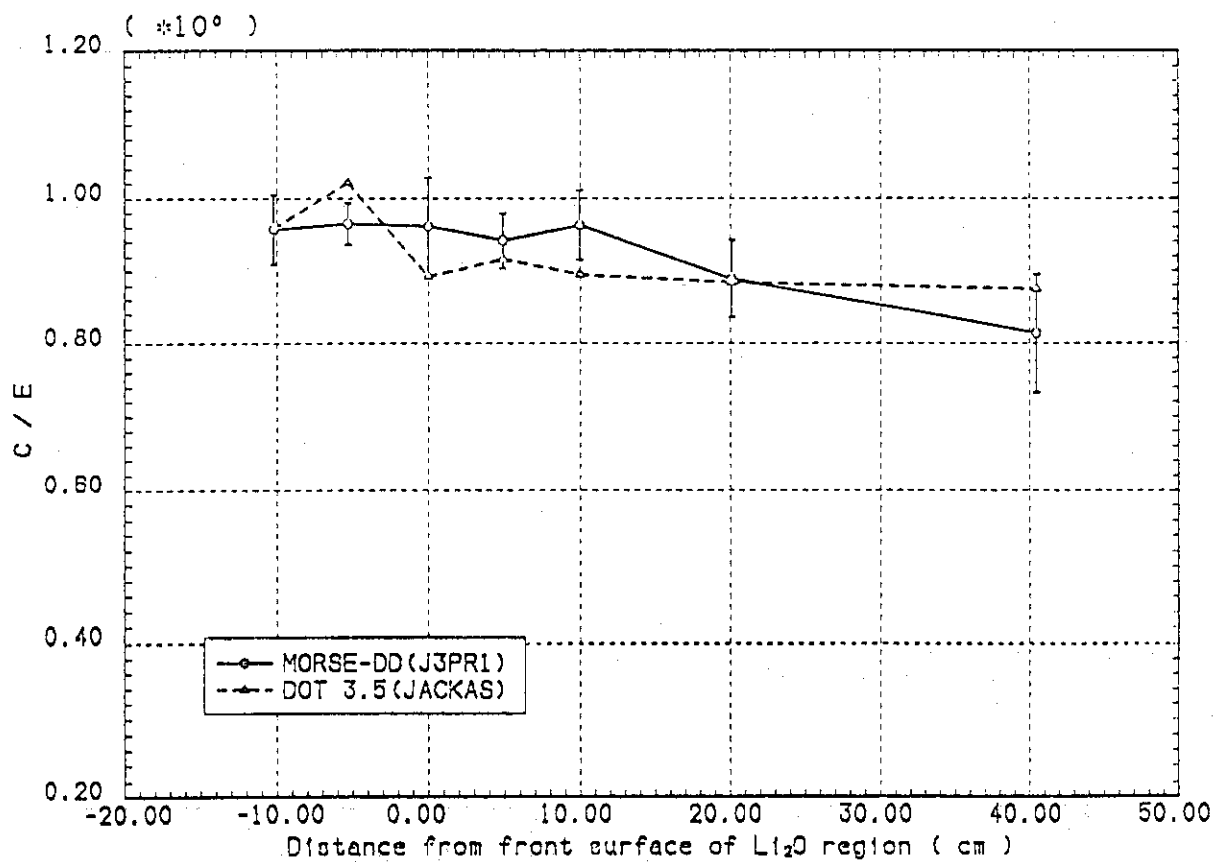


Figure V.14 C/E values for $^{115}\text{In}(n,n')^{115\text{m}}\text{In}$ reaction rate in the Be-sandwiched system

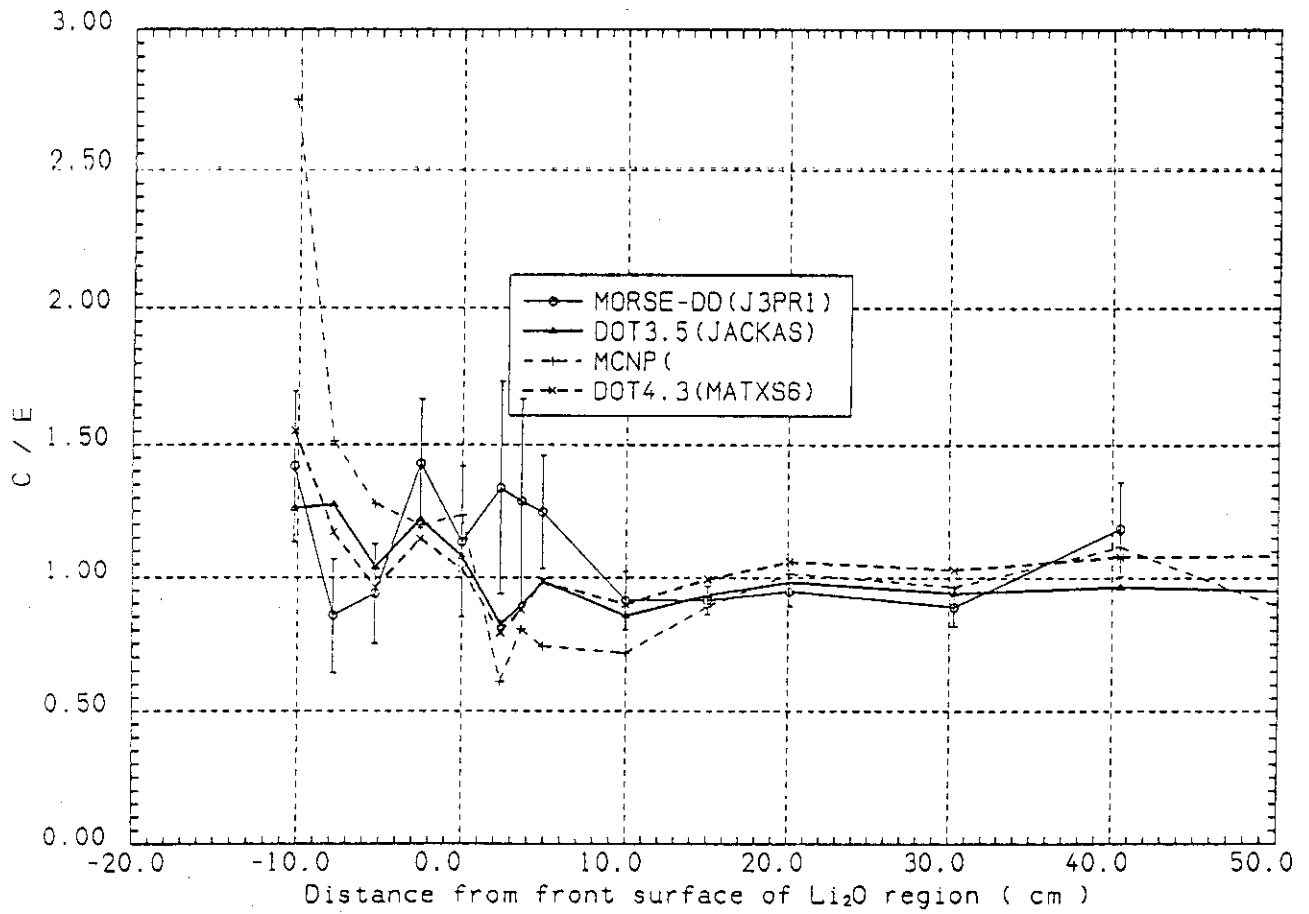


Figure V.15 C/E values for $^{197}\text{Au}(n,\gamma)^{198}\text{Au}$ reaction rate in the Be-sandwiched system

V.3 Possible Causes for the Observed Trends in the C/E Curves of Various Activation Reaction Rates

As discussed above, there are several persistent features and trends in the C/E curves of the various reaction rates shown in Figs V.2 to V.15. These trends are summarized below:

1. The C/E curves for $^{58}\text{Ni}(n,2n)$ reaction shown in Fig. V.2 is always lower than unity as predicted by all codes and libraries and the underprediction is ~10 - 30% at various locations inside the Li_2O assembly. The exception is for the C/E curves based on DOT4.3/MATXS6 calculations. It seems, therefore, that the cross-section for the $^{58}\text{Ni}(n,2n)$ reaction in the ENDF/B-IV, and ENDL-73 (in MCNP calculations) files is underestimated. Recent measurements by Ikeda et al.⁽³³⁾ for that cross-section showed indeed that the measured values are larger than those currently implemented in these data files. The calculations based on the MATXS6 library showed a different trend as shown in Fig. V.2, where the C/E values are larger than unity at $Z > 12$ cm. The cross-section for the $^{58}\text{Ni}(n,2n)$ reaction in this library is based on ENDF/B-V. Further intercomparison for that reaction between various libraries is required.
2. In the MCNP calculations based on Young's evaluation for ^7Li cross-sections, the C/E values are larger than those based on ENDF/B-V, version 1, at back locations and the divergence increases as one proceeds toward the back end of the Li_2O assembly. This trend was noticed for all the threshold reactions considered but no difference was noticed between the two calculations at the front surface [except for $^{58}\text{Ni}(n,2n)$ reactions].
3. In JAERI's calculations based on both the deterministic and the Monte Carlo methods, the C/E curves tend to decrease (fall below unity) at deeper locations inside the Li_2O assembly. This descending trend is more pronounced in the high-threshold reactions [e.g., $^{58}\text{Ni}(n,p)$]. On the other hand, the C/E curves for these reactions as calculated by the U.S. do not have the steepness observed in JAERI's curves and they are, in general, larger in value.
4. It appears that MORSE-DD (JAERI) calculations based on ENDF/B-IV gives closer C/E values to unity in comparison to the results based on the JENDL3-PR1 file, particularly at back locations. Also, the DOT3.5 calculations based on the JACKAS library are slightly improved in comparison to results based on ENDF/B-IV data.

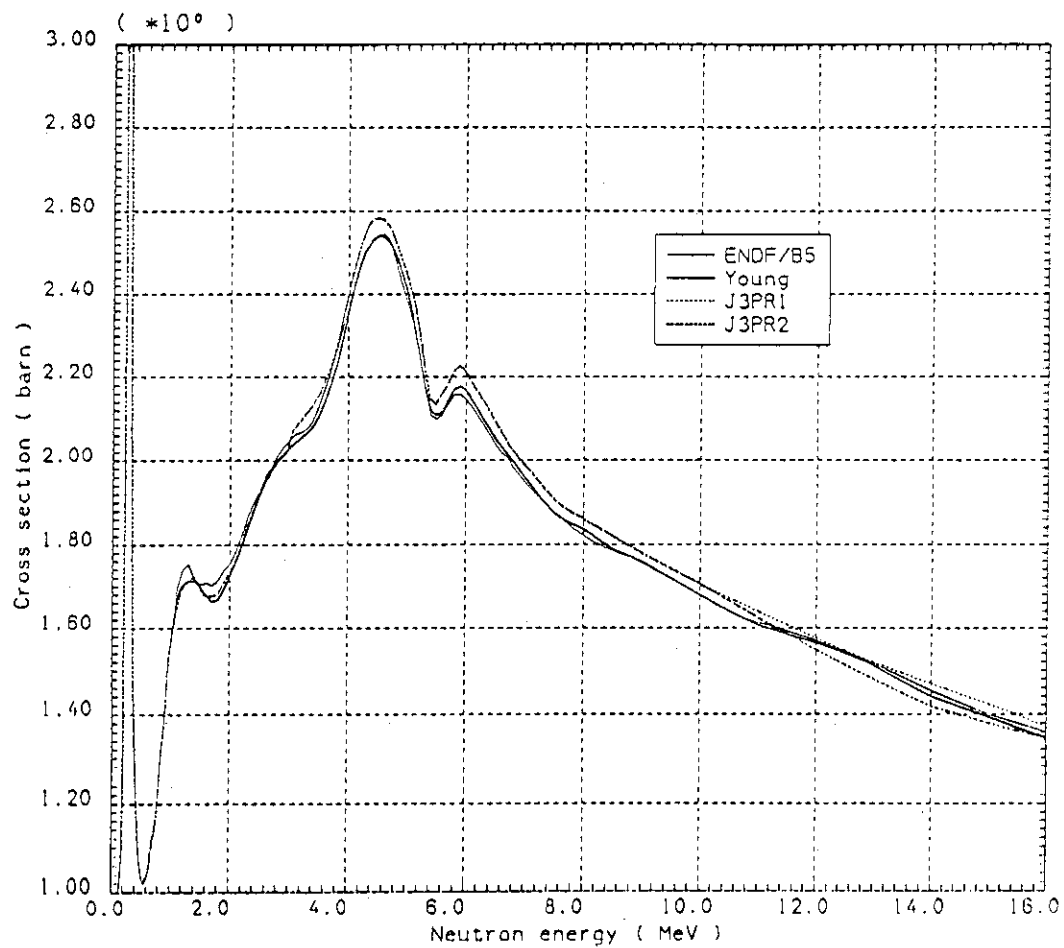
The trends in the C/E curves for various reactions that are discussed above can be explained based on results from cross-section sensitivity analysis as well as on direct intercomparison between various cross-sections of the materials that constitute the Li_2O assembly. First, the trend in the U.S. calculations discussed in (2) above where the values of the C/E curves as predicted by the MCNP code are larger at back locations when Young's evaluation for ^7Li cross-sections is used in comparison to the results based on the ENDF/B-V, Version 1 (B5) can be explained as follows. [Note that in both calculations, all the data for other elements present in the Li_2O assembly are from the RMCCS library which is based on ENDF/B-V and the only difference is the data for ^7Li .] From the cross-section sensitivity analysis presented in Section VII, it was shown that T_7 is most sensitive to variations in ^7Li cross-sections (see Table VII.4 and Fig. VII.21). The integrated sensitivity coefficients for ^7Li (n,inelastic) cross sections [basically $^7\text{Li}(n,n'\alpha)t$ cross-section] is negative in this case and its absolute values tends to increase at back locations. This means that a decrease in the $^7\text{Li}(n,n'\alpha)t$ cross-section leads to an increase in T_7 , or in other words, to an increase in the high energy component of the neutron spectrum. Consequently, threshold reactions such as $^{58}\text{Ni}(n,2n)$, $^{197}\text{Au}(n,2n)$, $^{27}\text{Al}(n,\alpha)$, and $^{58}\text{Ni}(n,p)$ will increase in the MCNP(T-2) calculation since Young's evaluation for $^7\text{Li}(n,n'\alpha)t$ cross-section is about 10-20% less than the corresponding cross-section in ENDF/B-V, version 1. (See Fig. IV.11).

In Table V.1 we introduce approximate values (for the purpose of this discussion) for $^7\text{Li}(n,n'\alpha)t$, $^7\text{Li}(n,\text{inelastic})$, $^7\text{Li}(n,\text{total})$, and $^7\text{Li}(n,\text{elastic})$ cross-sections at 10 MeV based on the values displayed in Figs IV.11, V.16 and V.17, as currently implemented in Young's evaluation (T-2), JENDL/3-PR1 (and PR2) and ENDF/B-5, version 1 (B5) data. As shown at this energy point, Young's evaluation for $^7\text{Li}(n,n'\alpha)t$ is less by ~18% as compared to B5. However, the $^7\text{Li}(n,\text{elastic})$ is larger by ~7% in Young's evaluation. From the sensitivity analysis discussed in Section VII, an increase in $^7\text{Li}(n,\text{elastic})$ cross-section leads to a decrease in T_7 , i.e., a decrease in the high energy component of the neutron spectrum due to the moderating effect of the elastic scattering processes and a consequent decrease in the threshold reactions. This is a compensating effect to the increase in the threshold reaction rates upon using the lower values for $^7\text{Li}(n,n'\alpha)t$ cross-section evaluated by Young. However, the sensitivity coefficient for the $^7\text{Li}(n,\text{elastic})$ cross-section is a factor 2.3 - 2.5 lower than the corresponding value for the $^7\text{Li}(n,\text{inelastic})$ cross-section as can be seen from Table VII.4. In addition, the increase in the $^7\text{Li}(n,\text{elastic})$ cross-section in Young's evaluation is less than the decrease in the $^7\text{Li}(n,n'\alpha)t$ cross-section by about a factor of 2.6 at 10 MeV. Thus, the increase in the high-energy component resulting from the lower value of the $^7\text{Li}(n,n'\alpha)$ cross-section of Young's evaluation dominates the compensating effect resulting from the increase in $^7\text{Li}(n,\text{elastic})$ cross-section. Note that the summation of both cross-sections is the same and there are no differences in the cross-sections of other reactions such as $^7\text{Li}(n,\gamma)$, $^7\text{Li}(n,d)$ and $^7\text{Li}(n,3n)\alpha$ between the two evaluations, as shown in Table V.1 and Fig. V.16 where the $^7\text{Li}(n,\text{total})$ cross-section is the same.

Table V.1 Cross-sections for ^7Li at 10 MeV

File	(n,elastic) barns	(n,n' α)t barns	(n,elastic) + (n,inelastic)	(n,total)
Young's	1.20(1.07) ^a	0.36(0.82)	1.56(1.00)	1.68 (1.00)
J3PR1	1.24 (1.11)	0.35 (0.80)	1.59 (1.02)	1.70 (1.02)
ENDF/B-V (version 1)	1.12 (1.00)	0.44 (1.00)	1.56 (1.00)	1.68 (1.00)

a Ratio of cross-section to the cross-section of ENDF/B-V, version 1

Figure V.16 Comparison of total cross-sections for ^7Li

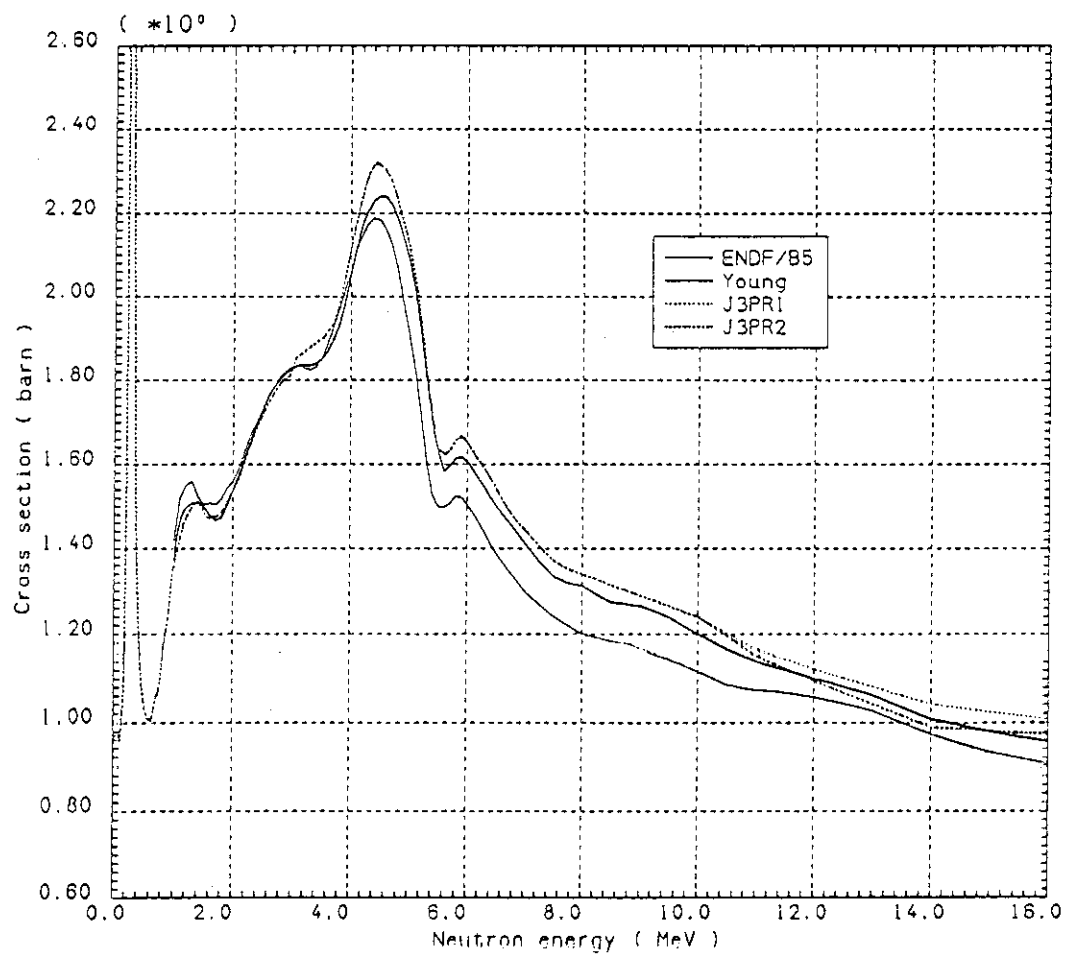


Figure V.17 Comparison of elastic scattering cross-sections for ^7Li

The differences between the C/E curves as evaluated by MCNP (T-2) and MCNP (B5) are not observed at locations near the front surface as the Li₂O assembly, particularly for ⁵⁸Ni(n,2n) and ¹⁹⁷Au(n,2n) reaction rates. Since neutrons at front locations have not encountered as many collisions as those neutrons reaching the back locations, the perturbation (or change) in neutron flux resulting from differences in the ⁷Li (n,elastic) and ⁷Li(n,n'α)t cross-sections is small and thus high threshold reactions rates will change slightly between the MCNP (T-2) and MCNP (B-5) calculations. As shown in Fig. VII.21, the indirect contribution to T₇ sensitivity coefficient that is attributed to flux perturbation is very small in comparison to the direct contribution from a change in ⁷Li cross-sections. This is further understood by examining the C/E curves for T₇ shown in Fig. IV.12 where the decrease in the ⁷Li(n,n'α)t cross-section of Young resulted in a direct decrease in T₇ at front locations but that decrease leads to indirect flux increase in the high energy component of the spectrum at back locations and hence a rise in the C/E curve obtained by the MCNP(T-2) calculations.

The descending trend discussed in item (3) above in the C/E curves obtained by JAERI could be explained by noticing that the ⁷Li (n, elastic) cross-section as implemented in JENDL/3PR1 (and PR2) file is larger than the corresponding cross-section of Young (and B5) below 10 MeV and that the JENDL/3PR1 evaluation is always larger above 10 MeV. This overestimation leads to overmoderation in neutron energies through elastic collisions and that effect is more pronounced at deeper locations where neutrons have already suffered more of such collisions. Consequently, the high energy component of neutron spectrum as predicted by JAERI gets smaller at these locations and this leads to the descending trend in the C/E curves of the threshold-reactions. In addition, the total cross-section in JENDL3-PR1 (and PR2) is generally larger than the values found in Young's and B5 evaluations below 10 MeV, as shown in Fig. V.16, and the difference could also be attributed to the overestimation in other reactions such as ⁷Li(n,d) and ⁷Li(n,γ). These reactions lead to neutron disappearance and hence to a further decrease in the threshold reactions, and as a consequence, the C/E curves for these reactions fall below unity in JAERI's calculations.

To confirm this observation, we compare the total cross-sections for ⁷Li in Fig. V.16. Note from Fig. V.16 that around 14 MeV, JENDL3/PR1 data shows the largest total cross-section, followed by the JENDF/B-V, Version 1 evaluation. The smallest cross-section is that of JENDL3/PR2, which will give the flattest Z dependence of C/E. However, the JENDL3/PR2 evaluation has not yet resolved all the problems since it still gives C/E values of about 0.9 in the region beyond Z = 30 cm. One resolution for the observed discrepancies in JAERI's calculations is to increase the ⁷Li(n,n'α)t cross-section and to decrease the elastic scattering cross-section. The change in the total cross-section will be small. The former modification will improve the C/E values for T₇ as discussed in Section IV, and will not necessarily decrease the neutron population by this reaction, although neutron energy may decrease. The latter modification will improve the discrepancy in the activation rates in JAERI's calculation. Since Young's

evaluations for ^7Li cross-sections already have these two modifications, the C/E values obtained by the U.S. for the threshold reactions are closer to unity than those obtained by JAERI using the JENDL/3PR1 (or 2) library. It is very informative to carry out such a cross-section comparison for other materials, such as oxygen, iron, nickel, and beryllium.

VI. IN-SYSTEM SPECTRA

VI.1 Reference System

In-system neutron spectra above 1 MeV have been measured by using an NE213 counter along the central channel as described in Volume I. Calculated spectra predicted by MORSE-DD with the DDL/J3P1 library were smeared using Gaussian function whose half width was derived from the detector resolution, while its energy dependence was determined by fitting the experimental values with a straight line on a log-linear scale.

The calculated spectra thus obtained were compared with the measured values along the center axis at $Z = 0, 2.5, 10, 20, 30$, and 40 cm, respectively. Figures VI.1 - VI.6 compare the spectra at each position. Since the detector positions (center of detector which is sensitive to neutrons) were usually not at the same locations where calculations were performed, two calculated spectra are shown in each figure and the predicted spectrum that corresponds to the measuring position is between them.

At the location $Z = 0$ cm, the structure of the spectrum is fairly different between the calculated and measured values in the energy range 4-10 MeV. The cause for this discrepancy is attributed to the inadequate evaluation of the backward component of inelastic scattering for ${}^7\text{Li}$ and ${}^{16}\text{O}$. Figures VI.2 - VI.5 show a fairly good agreement with measurements though the height of the peak value decreases by an order of magnitude within a depth of ~ 30 cm. The calculations generally overestimate the measured values below 10 MeV and at locations near the front surface, a discrepancy appears around 6 MeV. At the location $Z = 40$ cm, the calculated values at $Z = 41.5$ cm agree well with measurements though a discrepancy around 3 MeV is apparent. This discrepancy may be due to the larger functional standard deviation (FSD) than actually seen in the figure.

The integrated flux is also compared in Figs. VI.7 and VI.8. The high and low experimental values show the most probably values $\pm 1 \sigma$ width which were determined based on an unfolding method. Prediction of the integrated flux above 10 MeV is in good agreement with measurements over the whole region. On the other hand, the calculated integrated flux between 10 MeV and 1 MeV is overestimated in the region $Z = 0 - 20$ cm as seen in Fig. VI.8.

VI.2 Beryllium Sandwiched System

Similar measurements and calculations have been carried out for the beryllium sandwiched system. Measurements were taken at $Z = -10, -5, 0, 2.5, 5, 10, 20, 40$ cm, respectively. A comparison with calculations is made in Figs. VI.9 - VI.16. In Fig. VI.9, an agreement between the calculated and measured values is not necessarily good, that is, we can see an underestimation around 10 MeV, overestimation above 3 MeV and again underestimation around 2 MeV. Fig. VI.10 compares the spectra at the interface of the front Li_2O and beryllium regions. In Figs. VI.10 to VI.15, the comparison with measurements has a similar trend that is the calculated values are larger than the measured values by a few

tens percent in the energy range 8 MeV - 2 or 3 MeV. The measured spectrum at $Z = 40$ cm lies almost within the range of two calculated spectra at $Z = 38.5$ and 41.5 cm.

Around 14 MeV and on the higher energy side of peak, there is one measured value that is apparently shifted to the lower energy side as can be seen in most of the figures discussed above. It is not easy to identify the reason for such a discrepancy because the measured point is the only one taken around this energy range. If this discrepancy resulted from calculations, the resolution adopted in these calculations will be improper since the same resolution used in the reference system was also used in the Be-sandwiched system. Nevertheless, the resolution is system-dependent and it is narrower in the Be-sandwiched system by about 10% as compared with that of the reference system. On the other hand, the measured values may have problems in using the unfolding method.

Typical discrepancies that appeared in Fig. VI.11 and others are due to the inaccuracy of the beryllium cross-sections. Such discrepancies were also observed in the benchmark calculation for the beryllium sphere discussed in Ref. 3 for which measurements were carried out at LLNL⁽³⁵⁾. Based on this calculational benchmark performed by JAERI and the U.S., it was found that a large difference in this energy range exists between JENDL3/PR1 and ENDF/B-V⁽³⁶⁾, that is, JENDL3/PR1 gives smaller flux in the energy range 9 - 3 MeV than ENDF/B-V. It was also found that a fairly large difference exists below 2 MeV when ENDF/B-IV data was used. Accordingly, this benchmark suggests that ENDF/B-V will give a better agreement in the energy range 9 - 3 MeV. Such an expectation was proven recently by the experiment measuring angular spectra from a beryllium plate⁽³⁷⁾.

The integrated fluxes above 10 MeV are compared in Fig. VI.17 and those from 1 to 10 MeV are compared in Fig. VI.18. The calculated values are larger than measurements over the whole region in the Li_2O system, contrary to the reference case.

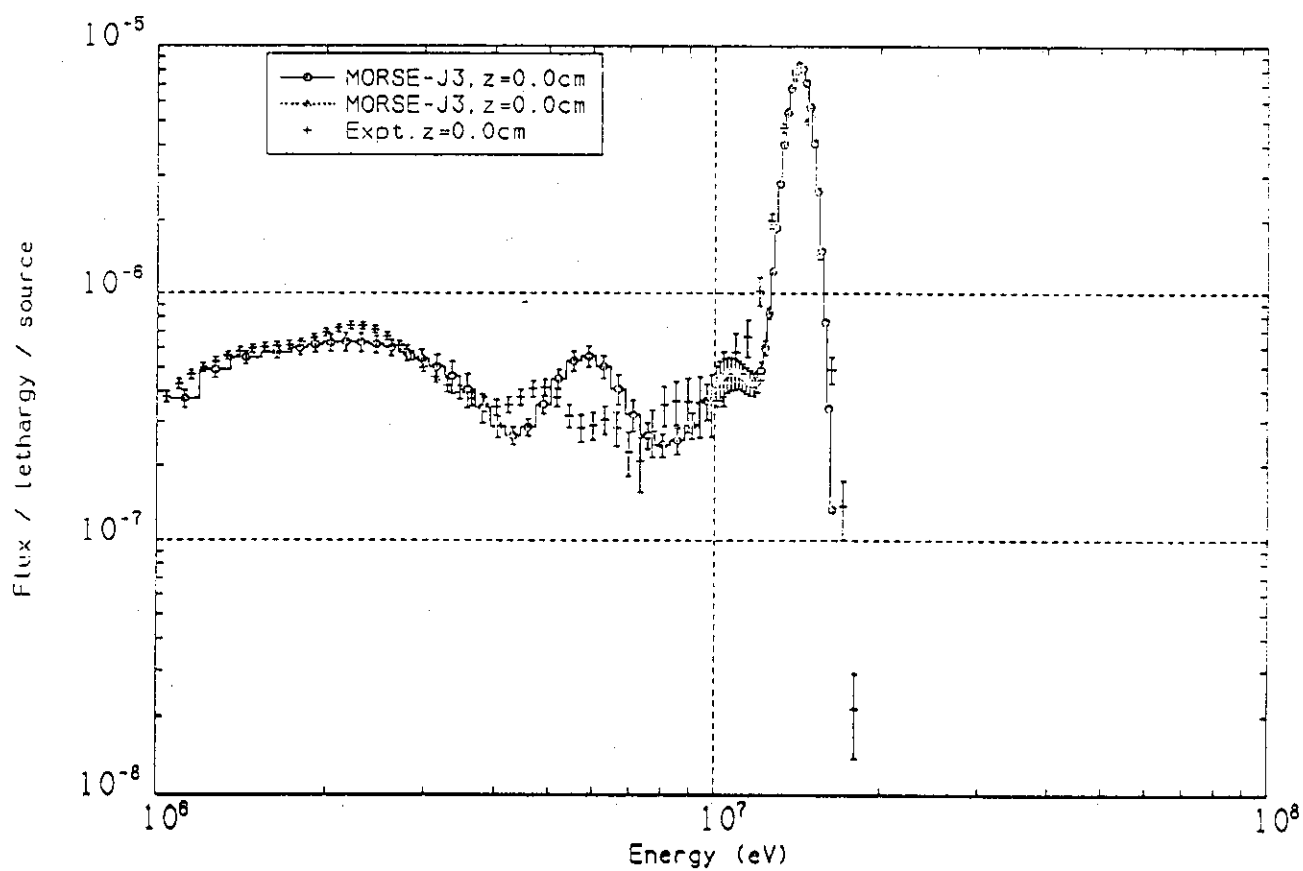
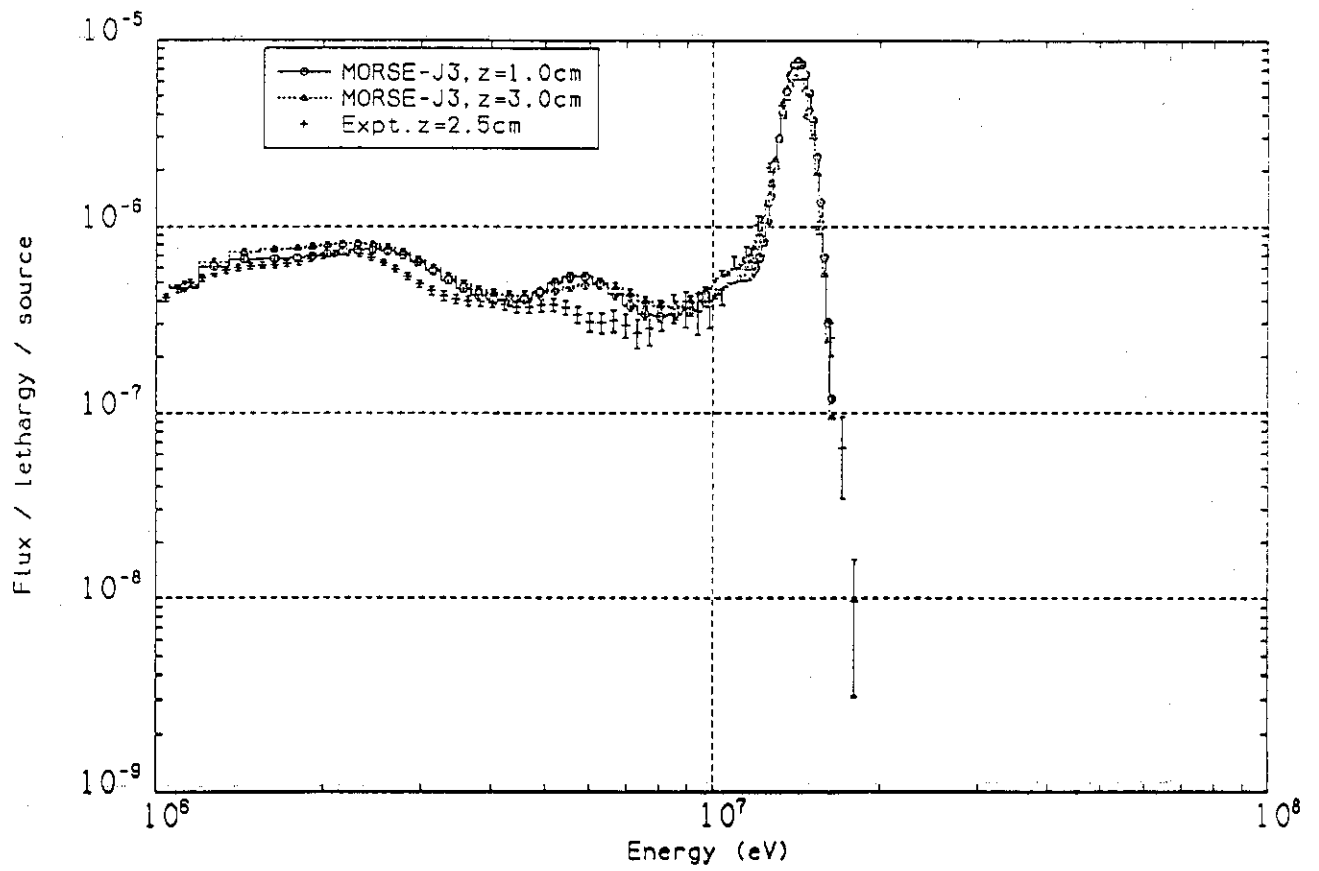
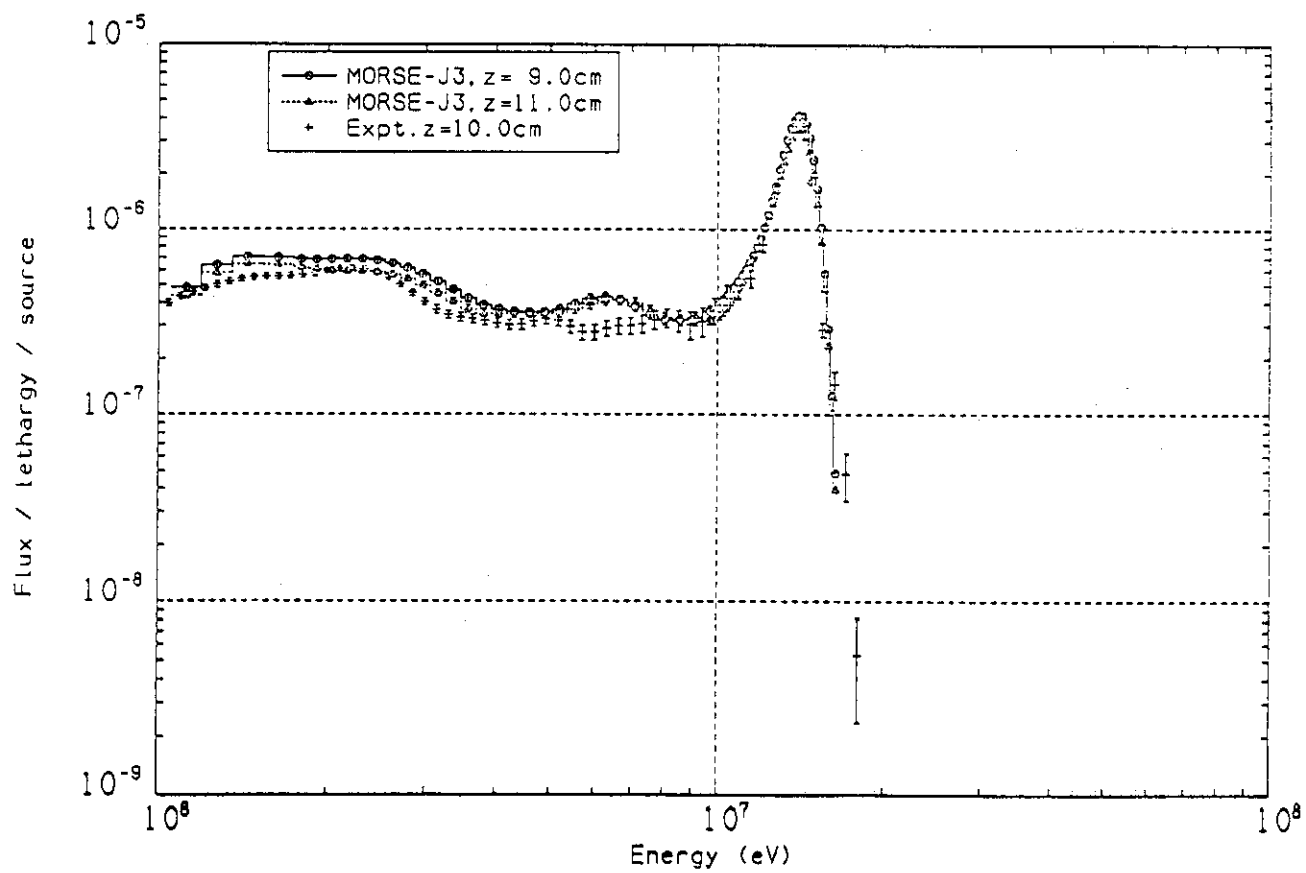
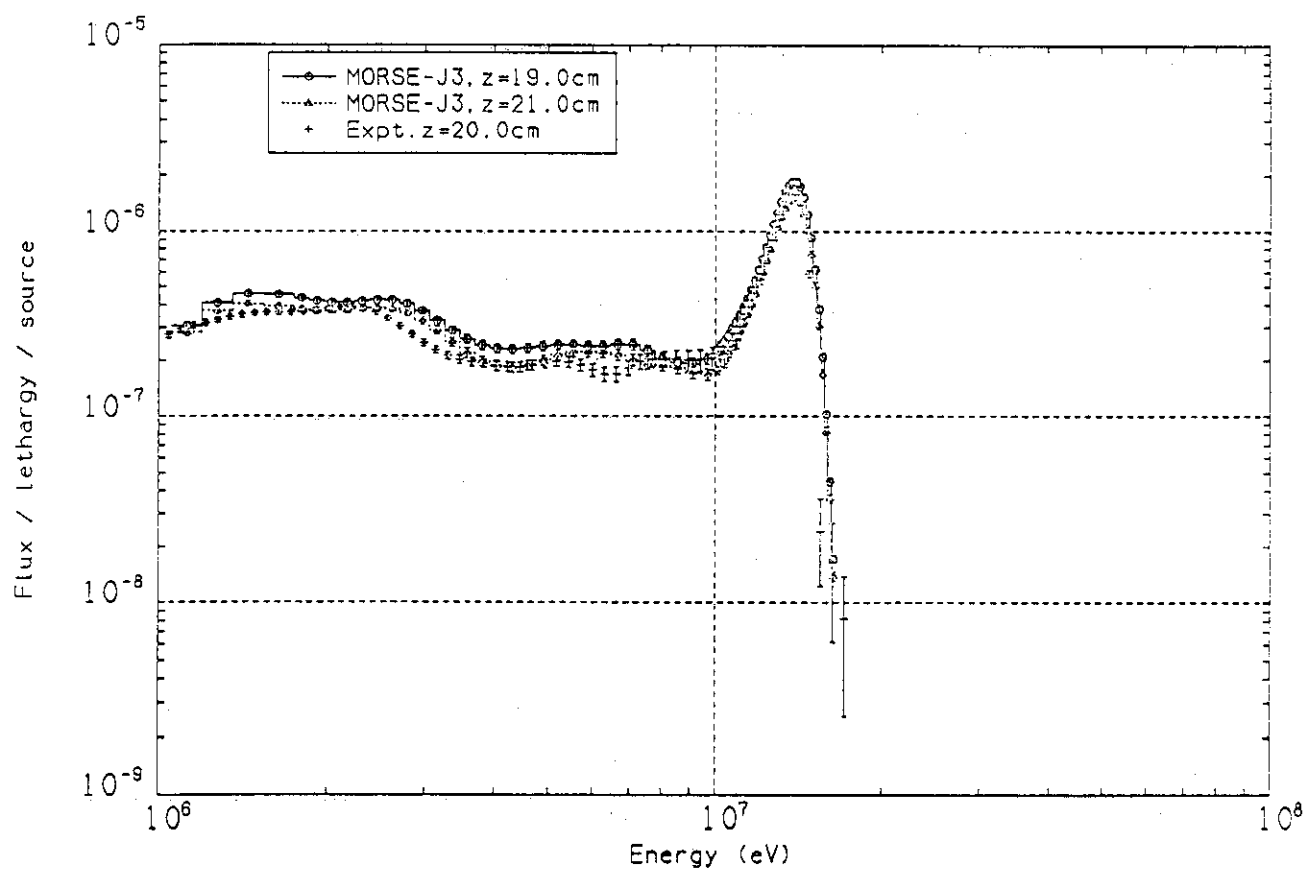
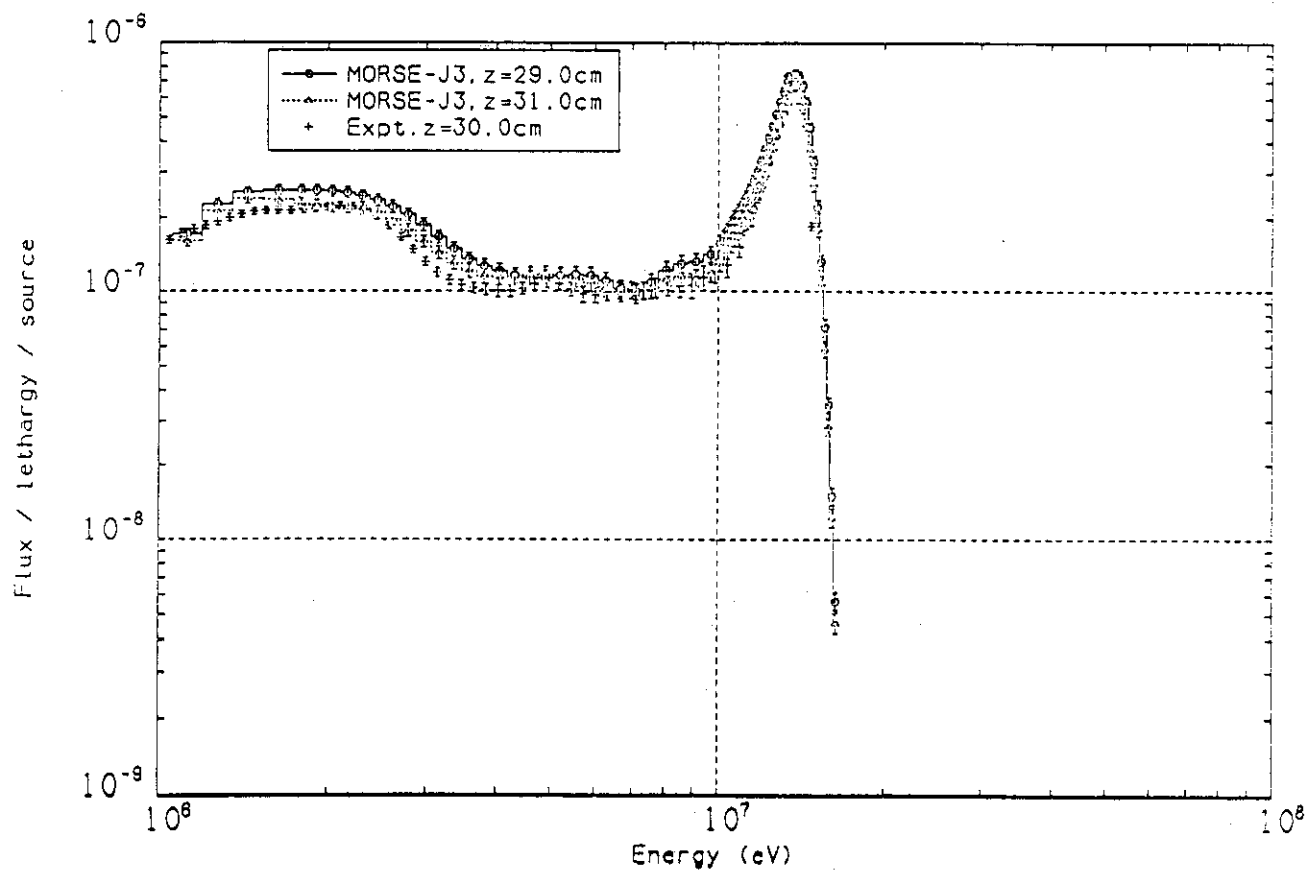


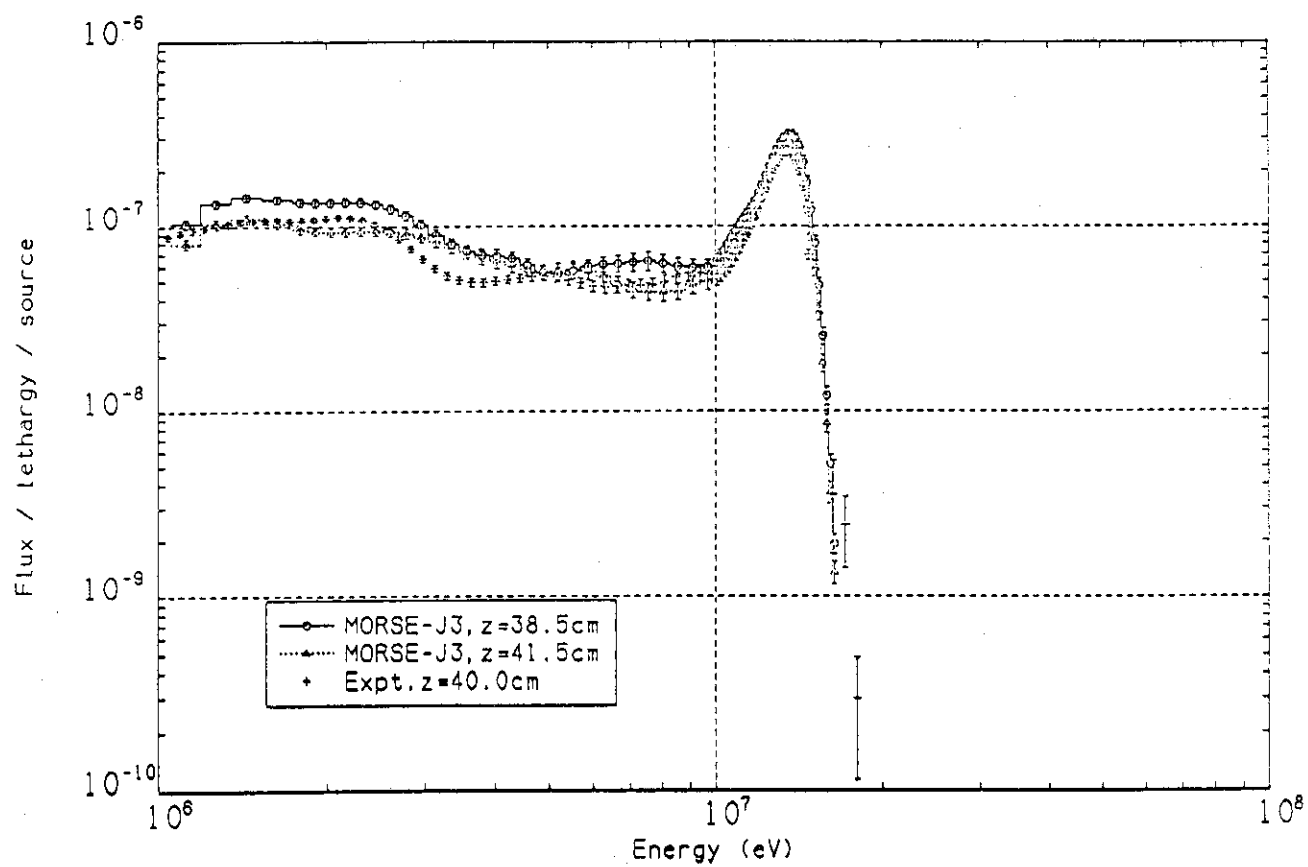
Figure IV.1 Neutron spectrum at $z = 0$ cm in the reference system

Figure VI.2 Neutron spectrum at $Z = 2.5$ cm in the reference system

Figure VI.3 : Neutron spectrum at $z = 10\text{ cm}$ in the reference system

Figure VI.4 Neutron spectrum at $z = 20\text{ cm}$ in the reference system

Figure VI.5 Neutron spectrum at $z = 30$ cm in the reference system

Figure VI.6 Neutron spectrum at $z = 40$ cm in the reference system

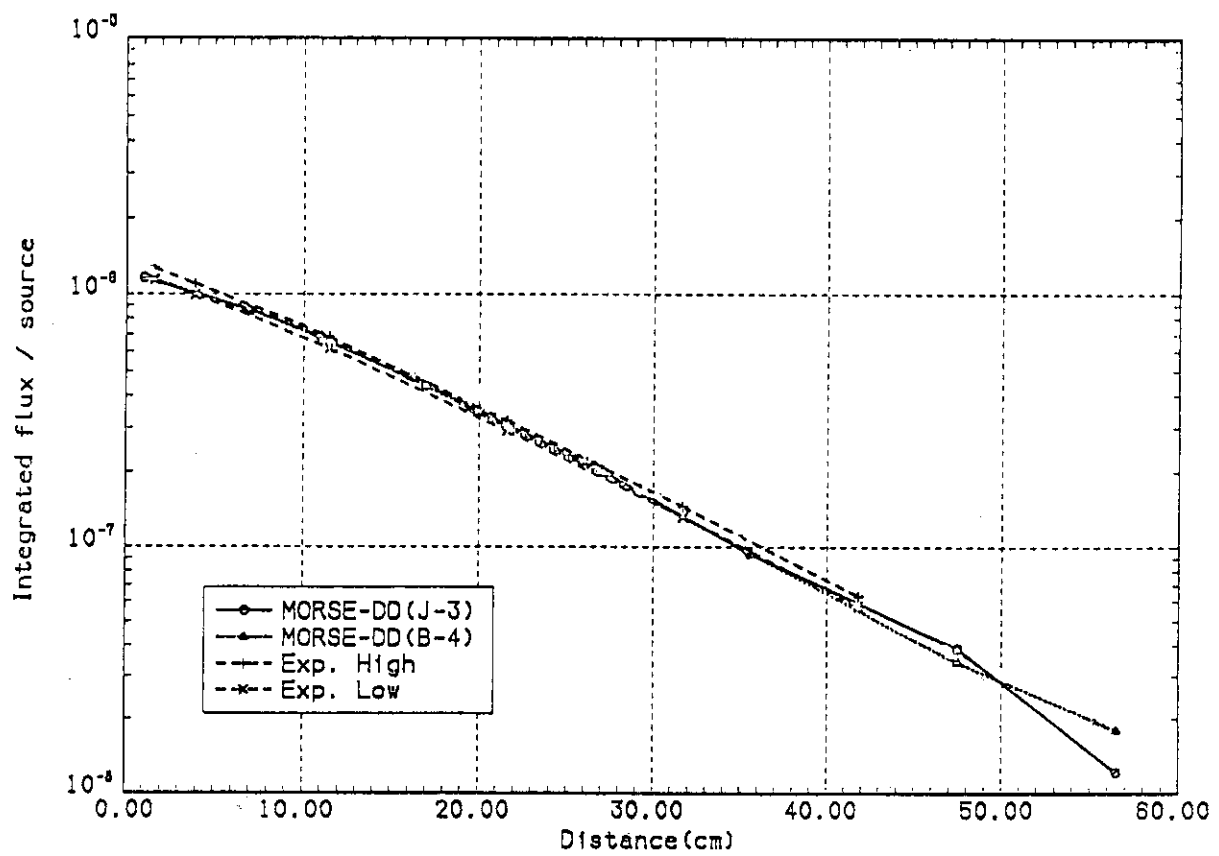


Figure VI.7 Integrated flux above 10 MeV in the reference system

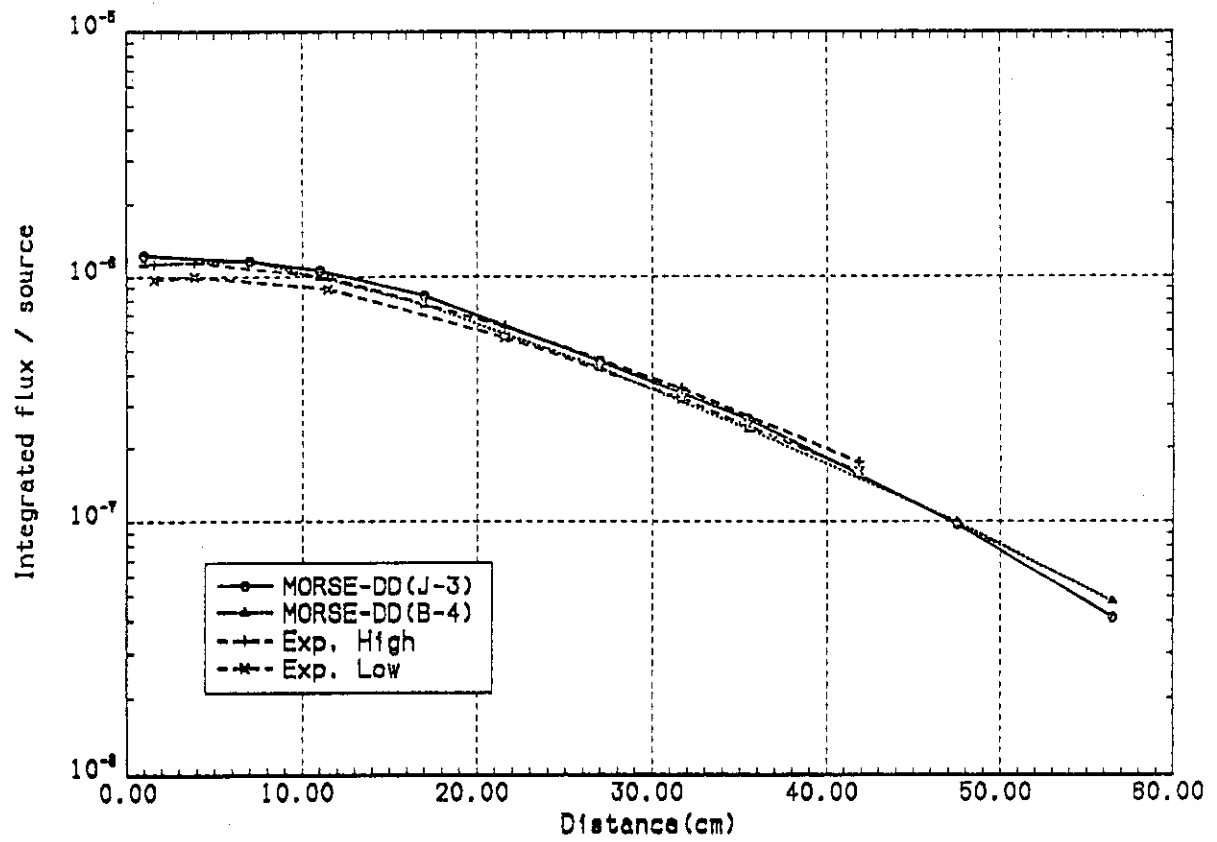


Figure VI.8 Integrated flux from 1 MeV to 10 MeV in the reference system

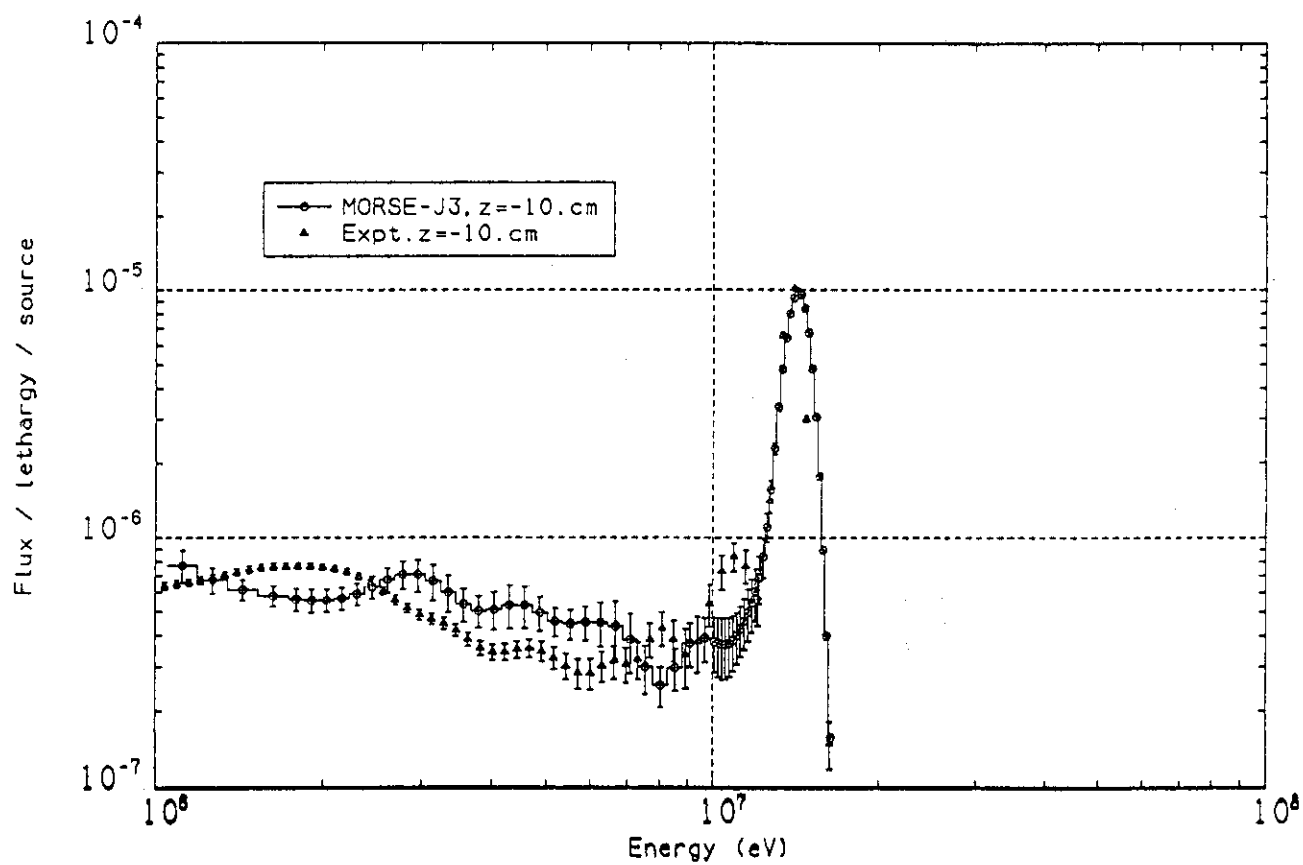
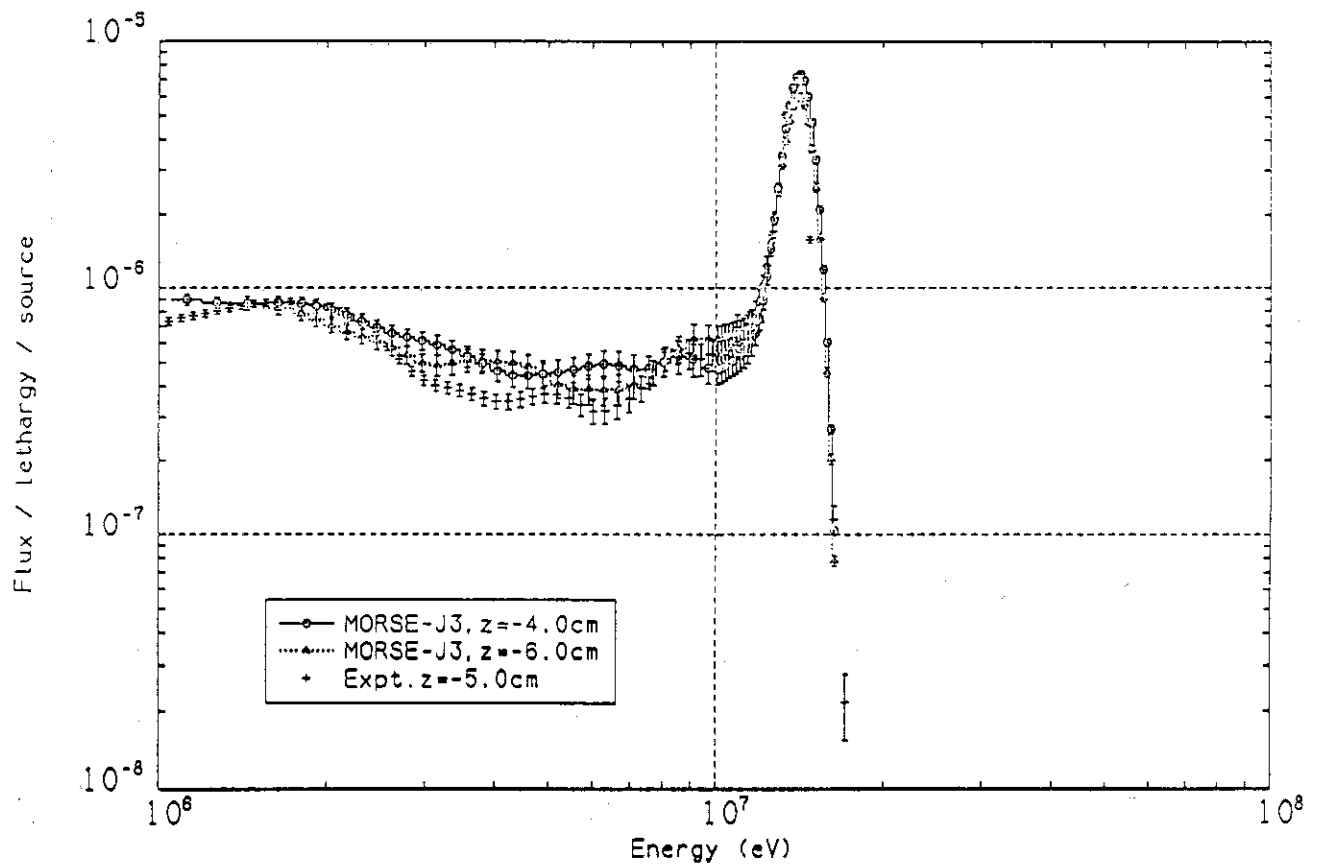


Figure VI.9 Neutron spectrum at $z = -10$ cm in the Be-sandwiched system

Figure VI.10 Neutron spectrum at $z = -5$ cm in the Be-sandwiched system

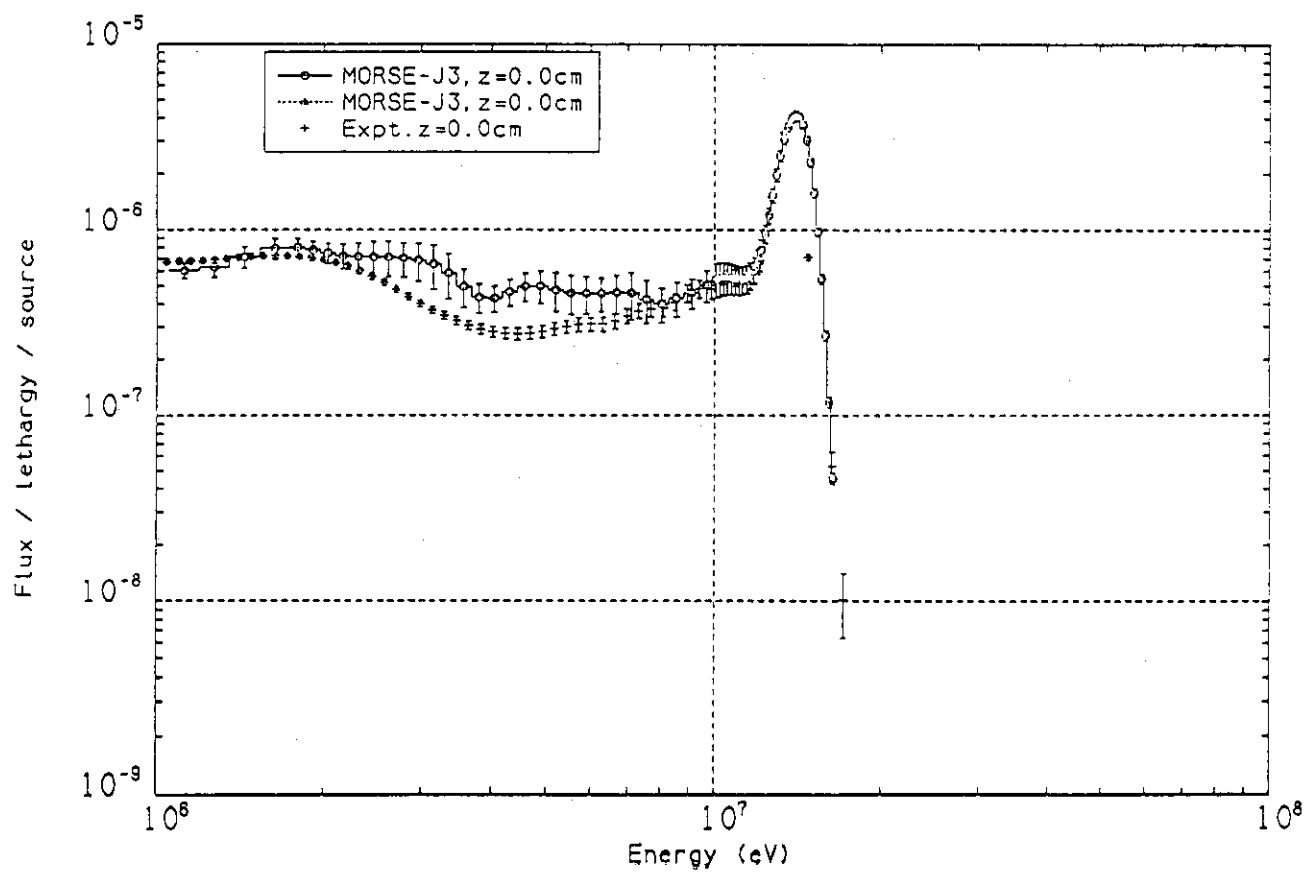
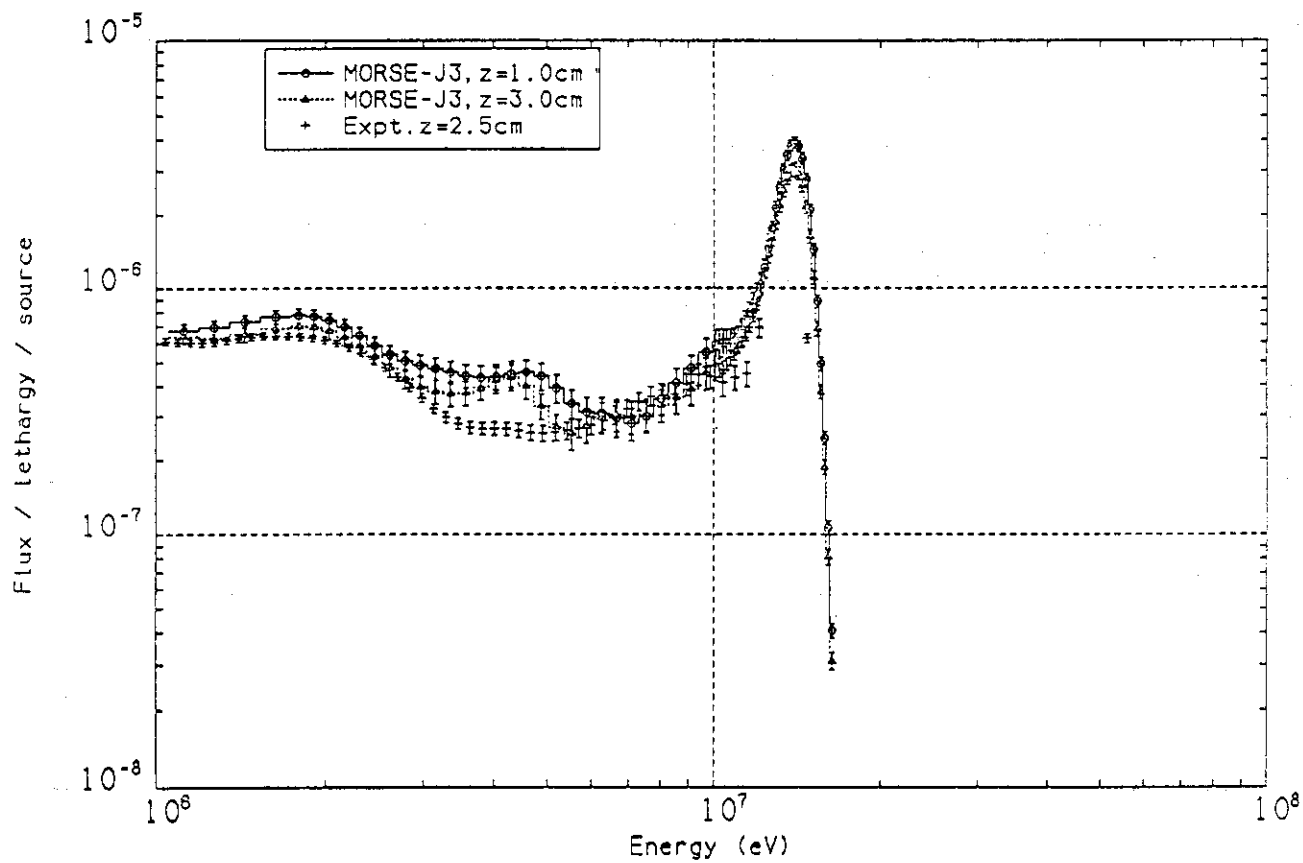


Figure VI.11 Neutron spectrum at $z = 0$ cm in the Be-sandwiched system

Figure VI.12 Neutron spectrum at $z = 2.5$ cm in the Be-sandwiched system

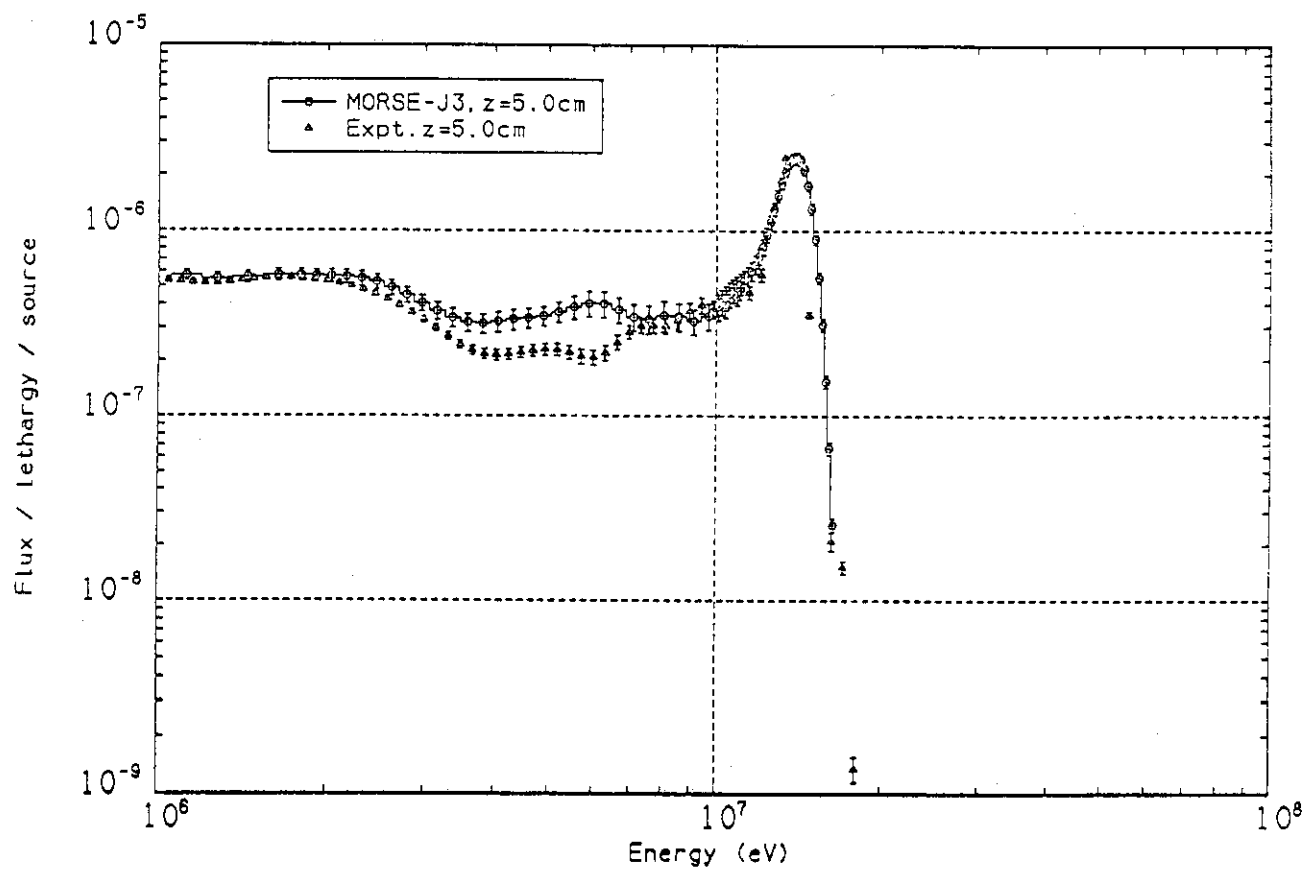


Figure VI.13 Neutron spectrum at $z = 5 \text{ cm}$ in the Be-sandwiched system

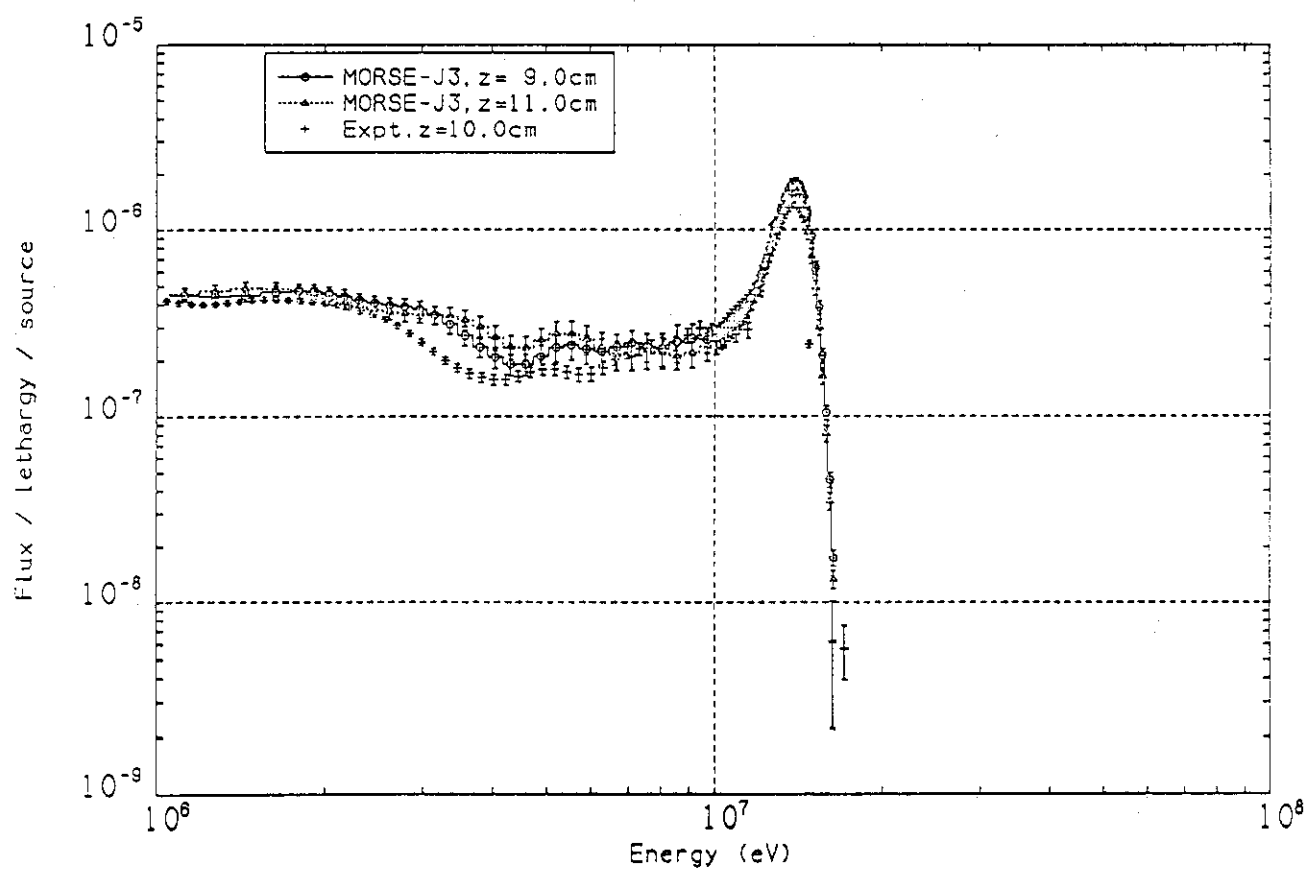


Figure VI.14 Neutron spectrum at $z = 10$ cm in the Be-sandwiched system

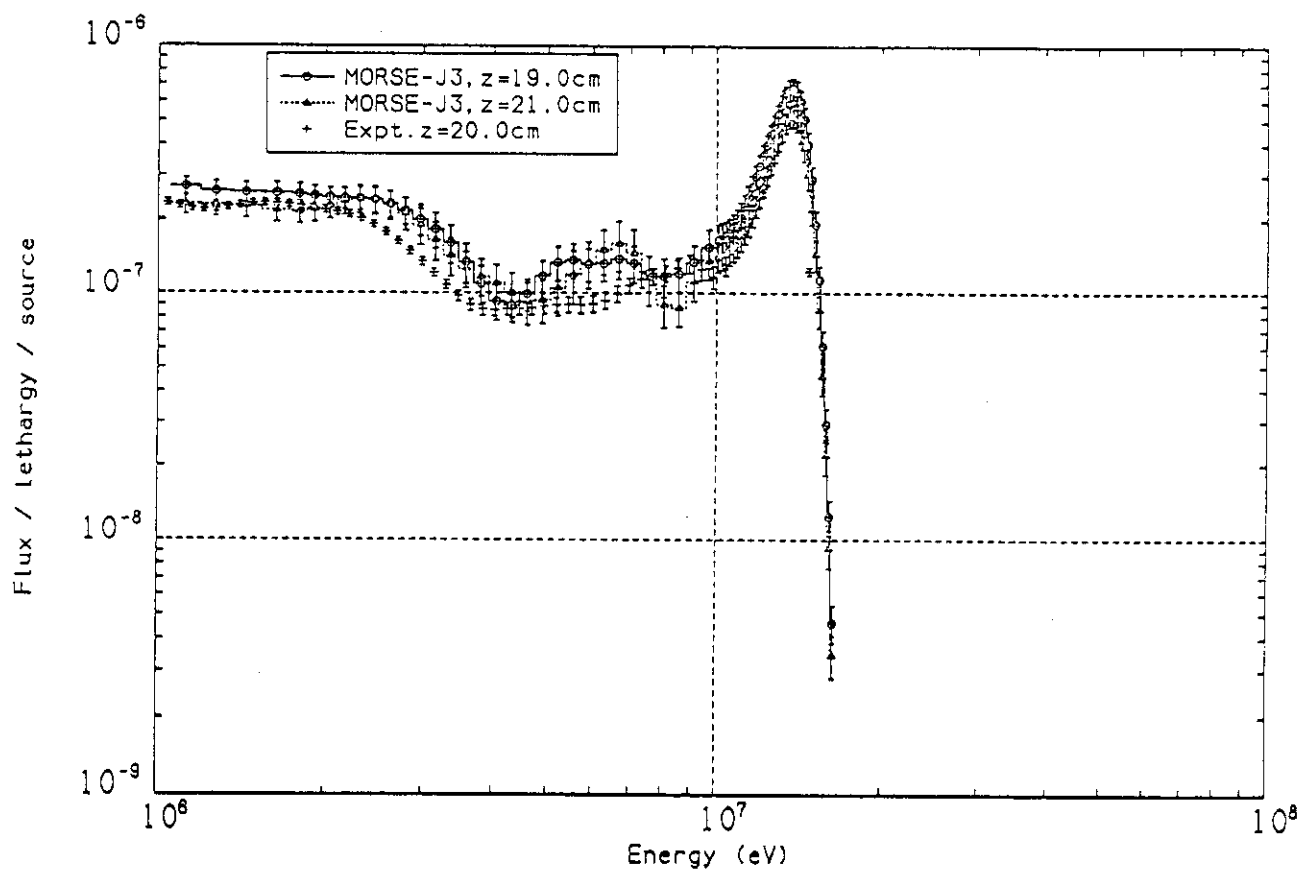
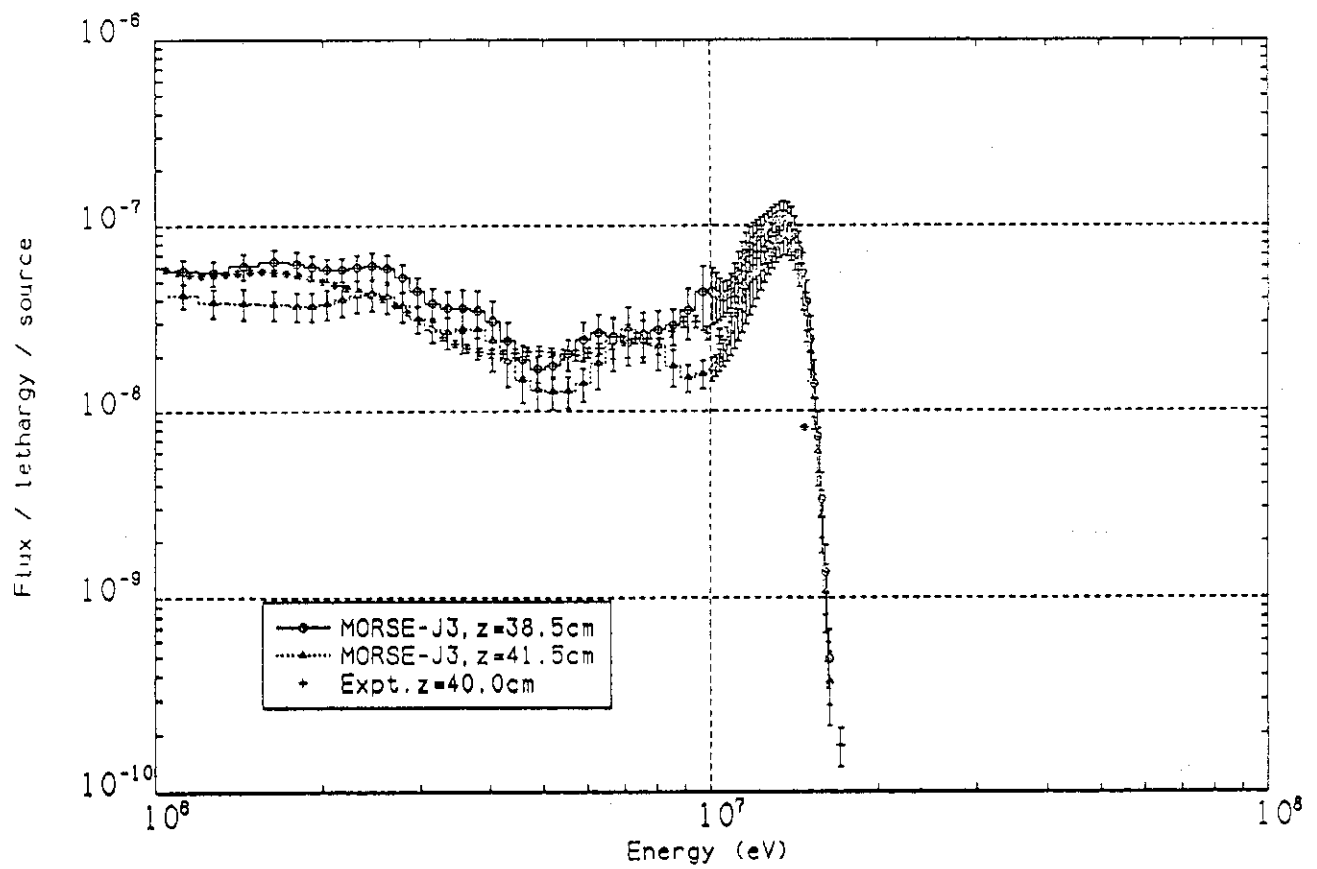


Figure VI.15 Neutron spectrum at $z = 20$ cm in the Be-sandwiched system

Figure VI.16 Neutron spectrum at $z = 40$ cm in the Be-sandwiched system

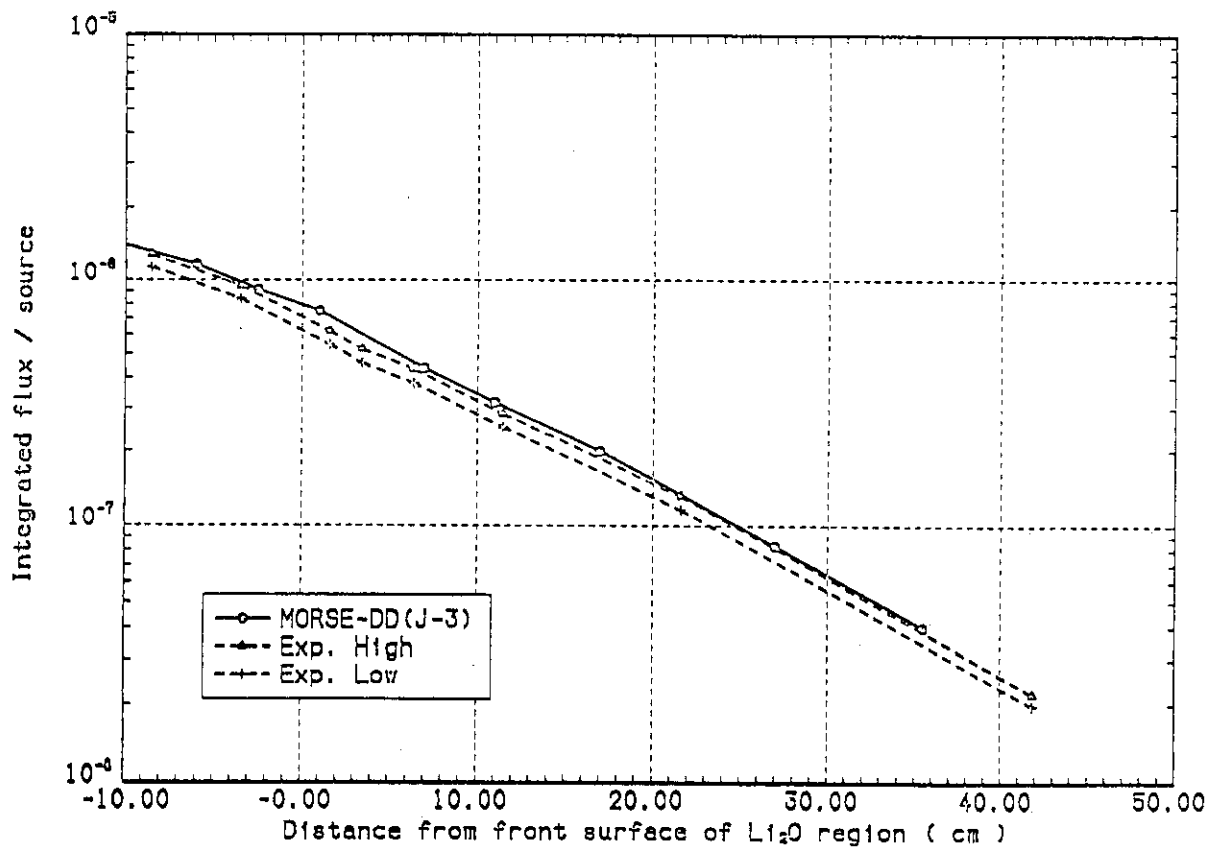


Figure VI.17 Integrated flux above 10 MeV in the Be-sandwiched system

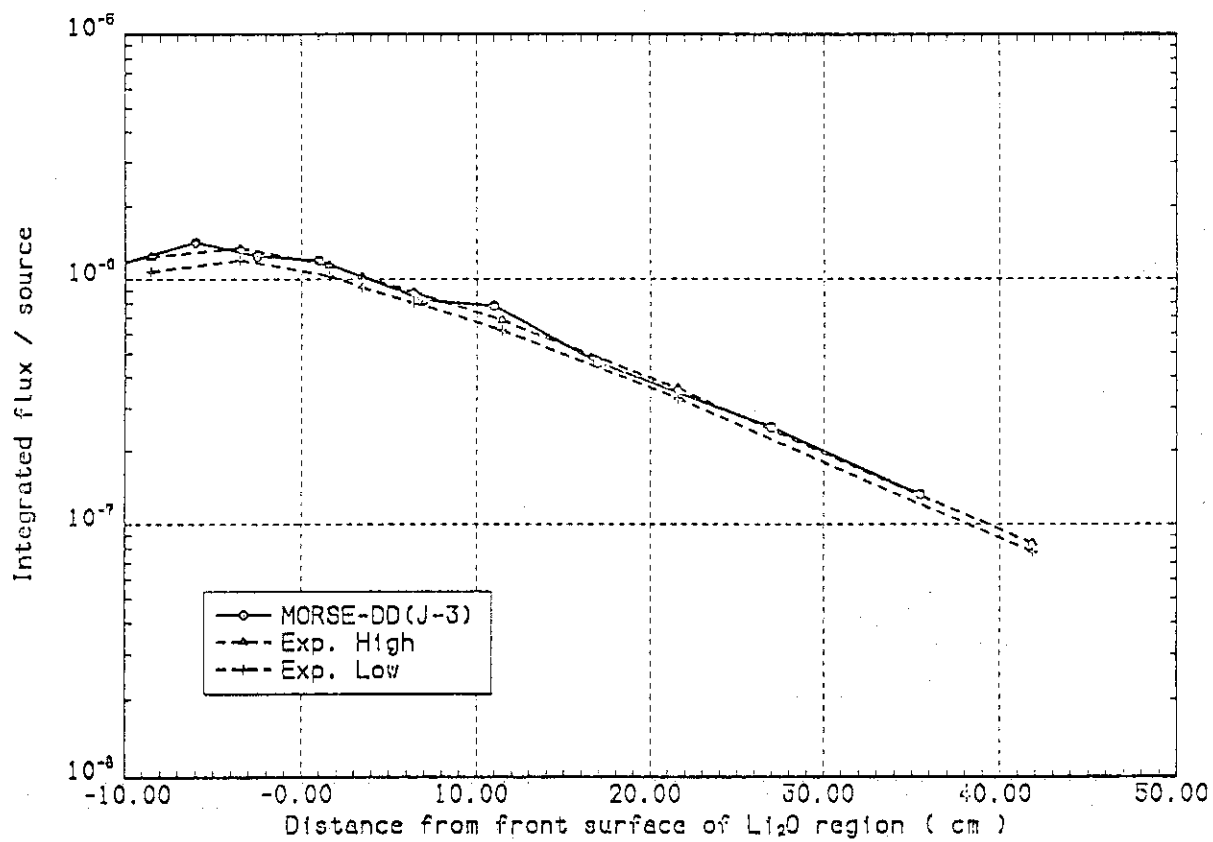


Figure VI.18 Integrated flux from 1 MeV to 10 MeV in the Be-sandwiched system

VII. CROSS-SECTION SENSITIVITY AND UNCERTAINTY ANALYSIS

VII.1 Introduction

As was shown in Section IV, discrepancies were found between predictions and measurements for both T_6 and T_7 . In particular, the C/E values for T_6 deviate appreciably from unity near the front surface of the Li_2O assembly in the reference experiment, and near zone boundaries in the first wall and beryllium experiments. Fig. VII.1 shows the C/E values for T_6 in the reference experiments where predictions were obtained by the 2-D calculational model (see also Fig. IV.3) and measurements were carried out by the Li-glass detectors. The C/E values for T_7 in the reference experiment are also shown in Fig. VII.2, using the NE213 indirect method (see Fig. IV.12). As shown, the C/E values for T_6 at the middle locations are ~ 1.2 (U.S.) and 1.1 (JAERI) as predicted by the deterministic methods. The corresponding C/E values for T_7 are ~ 1.18 (U.S.) and 1.05 (JAERI).

The subject of this section is to evaluate the contribution to the uncertainty in predicting both T_6 and T_7 that results from the current uncertainties in the neutron cross-section data base. An extensive two-dimensional cross-section sensitivity and uncertainty analysis has been performed to arrive at an estimate for such uncertainties. In this regard, the first order perturbation theory has been applied to estimate the cross-section sensitivity profiles for the responses T_6 and T_7 , individually, at various locations within the Li_2O test assembly used in two experiments, namely, the "clean benchmark" experiment (see below), and the reference experiment (the benchmark experiment is not part of the JAERI/U.S. collaborative program on Fusion Neutronics and it was performed independently by JAERI). These profiles will identify the materials, energy ranges, and cross-section types whose variations result in appreciable change in the response R_k ($R_k = T_6$ or T_7).

These profiles are then coupled with the cross-sections' uncertainty information and their correlations that are currently implemented in the ENDF/B-V (file 33) to arrive at an estimate for the variance in T_6 and T_7 at various locations. Pointwise and zonalwise TPR were considered in the analyses. In addition, the dependency of the uncertainty in T_6 and T_7 on the incident neutron spectrum was studied thoroughly. It should be emphasized that the choice for performing the sensitivity and uncertainty analysis in two-dimensional configurations was essential in order to account for the geometrical arrangement of the experiments considered. That can be realized by noting that the sensitivity profiles are strictly system-dependent.

The theoretical background for the methodology used in the present sensitivity/uncertainty analysis is briefly outlined in Subsection VII.2. The methodology discussed was recently reviewed thoroughly in Ref. (38). The experiments simulated in the analysis and the calculational model used are described in Subsection VII.3. The calculational procedure followed to carry out the sensitivity and uncertainty analyses is discussed in Subsection VII.4. Comparison between the TPR profiles in the benchmark system and the reference system is discussed in Subsection VII.5. The results of the sensitivity analysis are discussed in Subsection VII.6 for all the responses considered, while the results of the uncertainty analysis are given in Subsection VII.7. Subsection VII.8 contains the summary and conclusions drawn from the analysis.

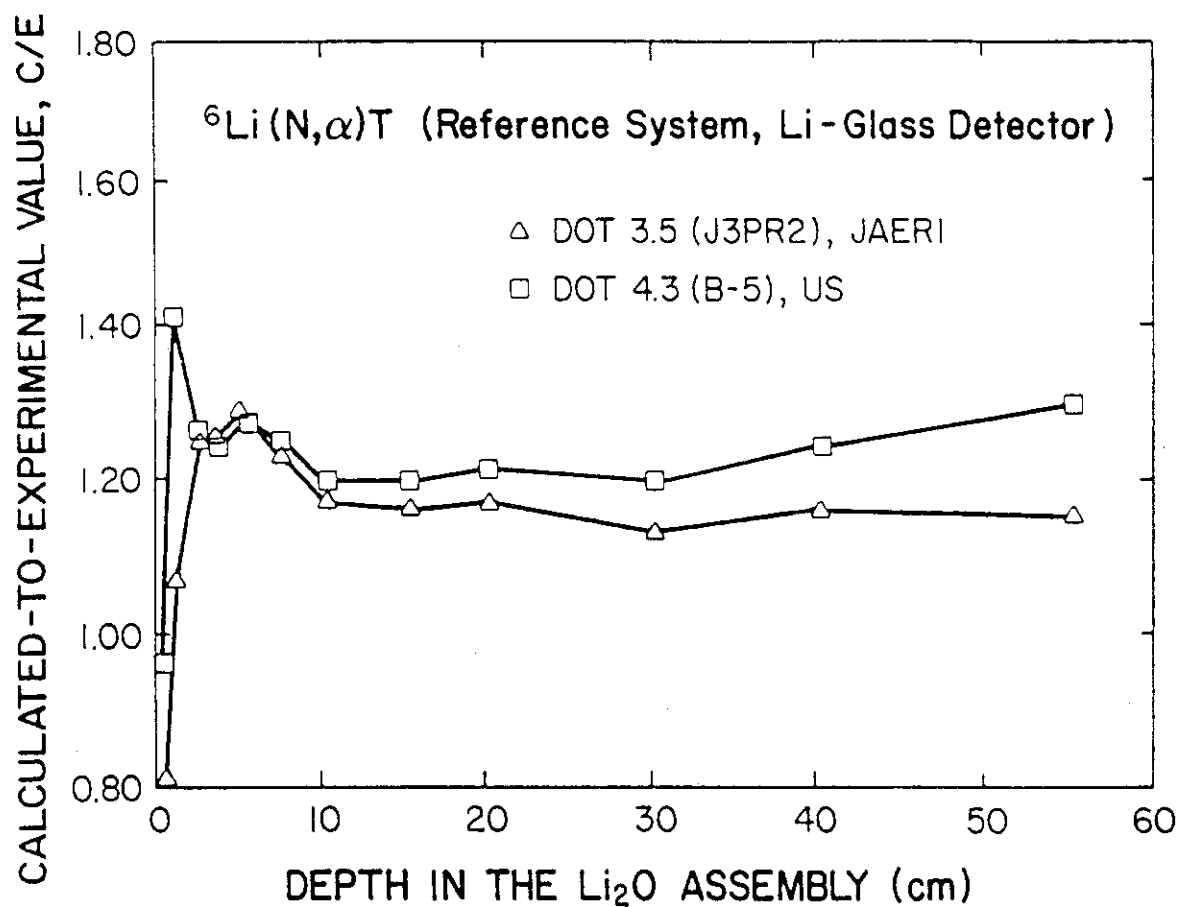


Figure VII.1 Calculated-to-experimental values of tritium production rate rate from ${}^6\text{Li}$, T_6 in the reference experiment (experimental values are corrected for self-shielding effect)

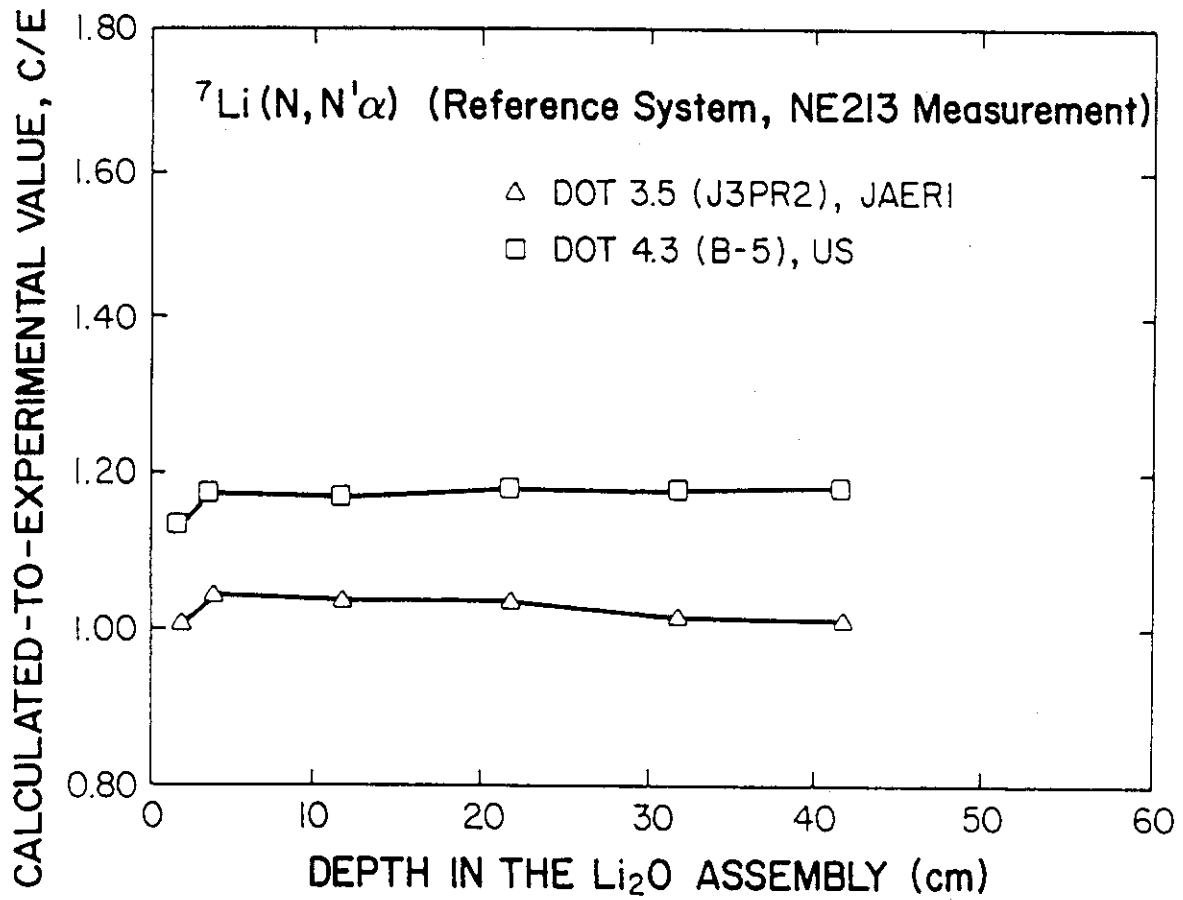


Figure VII.2 Calculated-to-experimental values of tritium production rate from ${}^7\text{Li}$, T_7 , in the reference experiment

VII.2 Definitions and Theoretical Background

The statistical variance in the integrated TPR, R_k (T_6 or T_7) is given by

$$\left(\frac{\Delta R_k}{R_k}\right)^2 = \sum_{g, g'} P_{\Sigma_x}^{g, k} P_{\Sigma_y}^{g', k} \text{corr}(\Sigma_x^g, \Sigma_y^{g'}) \text{RSD}(\Sigma_x^g) \text{RSD}(\Sigma_y^{g'}) \quad (\text{VII.1})$$

where

Σ_x^g = neutron interaction cross-section type x in energy group g

$\text{corr}(\Sigma_x^g, \Sigma_y^{g'})$ = correlation matrix for the multi-group cross-sections Σ_x^g and $\Sigma_y^{g'}$

$P_{\Sigma_x}^{g, k}$ = Relative cross-section sensitivity profile of the response R_k due to variation in the cross-section type Σ_x^g at energy group g , and is defined as the fractional change (in percent) in the response R_k due to a 1% increase in cross-section Σ_x^g at neutron group g

The coefficient $P_{\Sigma_x}^{g, k}$ is system dependent and its evaluation is straightforward using first-order perturbation theory (38) and is given by

$$P_{\Sigma_x}^{g, k} = \frac{\delta R_k / R_k}{\delta \Sigma_x^g / \Sigma_x^g} = - \frac{1}{R_k} \langle \phi_k^*, L_{\Sigma_x} \phi \rangle_g, \quad (\text{VII.2})$$

where

ϕ, ϕ_k^* = forward and adjoint angular flux, respectively

L_{Σ_x} = portion of the Boltzmann transport operator L , which contains the perturbed cross-section Σ_x .

It should be noted that the integration appearing in Eq. VII.2 is performed over the angular direction, $\bar{\Omega}$ and at all spatial locations, \bar{r} where the perturbation in the cross-section Σ_x is assumed. Using the dualism identity (39), the response R_k is evaluated as:

$$R_k = \langle \Sigma_r, \phi \rangle, \quad (\text{VII.3(a)})$$

or as:

$$R_k = \langle \Sigma, \phi_k^* \rangle, \quad (\text{VII.3(b)})$$

where the forward flux, ϕ , and the adjoint flux that corresponds to the response R_k , ϕ_k^* , are evaluated from the equations $L\phi = S$ and $L^* \phi_k^* = \Sigma_r$ respectively, and Σ_r is the response function. The integration appearing in Eq. VII.3(a) is performed over the energy E , the angle $\bar{\Omega}$ and the spatial locations of interest which can be either a given spatial point in space or at a predefined spatial zone. Commonly these locations are called "detector" locations. One should also notice that Eq. VII.2 accounts for only the indirect effect of the perturbed cross-section. If the response is also evaluated directly from Σ_x (i.e., $\Sigma_r = \Sigma_x$), a direct contribution to $P_{\Sigma_x}^{g,k}$ should be added.

The integrated relative sensitivity coefficient, $S_{\Sigma_x}^k$ is defined as

$$S_{\Sigma_x}^k = \sum_g P_{\Sigma_x}^{g,k} \quad (\text{VII.4})$$

and is defined as the percentage change in the integrated parameter, $\delta R_k/R_k$, due to a simultaneous 1% increase in the group cross-section, Σ_x^g , in all energy groups.

The relative sensitivity profile given by Eq. VII.2 is derived from the relative sensitivity function, $F_{\Sigma_x}^k(E)$, as follows:

$$P_{\Sigma_x}^{g,k} = \frac{1}{\Delta u_g} \int_{E_{g-1}}^{E_g} F_{\Sigma_x}^k(E) dE \quad (\text{VII.5})$$

where Δu_g is the lethargy width of neutron group g . Written explicitly, the sensitivity function $F_{\Sigma_x}^k(E)$ is given by(38):

$$\begin{aligned} F_{\Sigma_x}^k(E) = & -\frac{1}{R_k} \int d\bar{r} \int d\bar{\Omega} \phi(\bar{r}, E, \bar{\Omega}) \Sigma_T(\bar{r}, E) \phi_k^*(\bar{r}, E, \bar{\Omega}) \\ & + \frac{1}{R_k} \int d\bar{r} \int d\bar{\Omega} \int d\bar{\Omega}' \int dE' \phi(\bar{r}, E, \bar{\Omega}) \Sigma_s(\bar{r}, E \rightarrow E', \bar{\Omega} \rightarrow \bar{\Omega}') \phi_k^*(\bar{r}, E', \bar{\Omega}') \end{aligned}$$

$$+ \frac{1}{R_k} \int d\vec{r} \int d\vec{\Omega} \Sigma_T \phi(\vec{r}, E) \phi(\vec{r}, E, \vec{\Omega}) \quad (\text{VII.6})$$

The first, second and third terms correspond to the collisional loss, scattering gain, and direct effect terms, respectively. The last term should only be included if the cross-section perturbed Σ_x is equal to the response Σ_T .

The correlation matrix $\text{corr}(\Sigma_x^g \Sigma_y^{g'})$ represents the correlation between the multi-group cross-sections Σ_x^g and $\Sigma_y^{g'}$ and its elements are independent of the specific system (i.e. experiment) under consideration. The RSD (Σ_x^g) in Eq. VII.1 is the relative standard deviation (RSD) of cross-section Σ_x^g and the information required to construct the correlation matrices and the RSD's for various cross-section types is implemented in file 33 of the ENDF/B-V basic data file ⁽⁴⁰⁾.

The relative variance in the response R_k given by Eq. VII.1 is made up of contributions from each material present in a particular system. In the uncertainty analysis results given in Subsection VII.7, we assume that the uncertainty associated with cross-sections of a particular material is uncorrelated to the uncertainties in the cross-sections of other materials. Thus, $(\Delta R_k/R_k)^2$ given by Eq. VII.1, is the algebraic sum of the contributions from each material. For a particular material, however, the correlations between errors in the cross-sections of that material are considered according to Eq. VII.1.

VII.3 Experiments Considered and Calculational Models

Two experiments were considered in the present analysis. These are the clean benchmark experiment and the reference experiment discussed in Section I. In the former experiment, the cylindrical test assembly was placed in the large room No. 1, and a water-cooled stationary target was located at a distance of 20 cm from the front circular surface. The neutron room-return component is negligibly small in this experiment due to the large dimensions of the room (~15 m x 15 m x 12 m). This clean benchmark experiment was independently performed by JAERI, but it was considered in the present analysis for the purpose of comparing its results to those of the reference system.

The R-Z two-dimensional geometrical models used for the benchmark and the reference systems are shown in Figures VII.3(a) and VII.3(b), respectively. The Li₂O test assembly is the same in both systems. Since in the reference system the assembly is embedded in the concrete wall in target room #2, the mortar layer and part of the concrete wall were accounted for in the calculational model shown in Fig. VII.3(b). The thickness of the concrete layer is truncated to ~30 cm which was judged to be adequate in the present analysis. The atomic densities of materials considered in both systems are shown in Table VII.1. Note that the inner Li₂O zone has different atomic densities than the outer zone, as was discussed in Section II.

The external D-T neutron source for the benchmark system is located at 20 cm from the front surface of the Li₂O assembly. The D-T neutron spectrum from the stationary target used in the benchmark experiment was calculated previously by Seki ⁽⁴¹⁾ using the Monte Carlo method. This

spectrum was used and assumed to be isotropic in the present 2-D calculation. For the reference experiment, the external neutron source from the rotating target that is located at the center of target room #2, a distance of 248 cm from the Li_2O assembly, was modeled by using two source components, namely, the direct component that results from those neutrons emitted at the D-T reaction spot and scattered into the direction of the Li_2O assembly, and the indirect room-return component that includes those neutrons scattered by the room walls into the direction of the assembly. The values for these two components were obtained from the MCNP calculations discussed in Sections III and IV.

In the forward flux 2-D calculation for the reference system, the two components were treated separately and the resultant flux is the sum of the flux evaluated for each component. In this regard, the room-return component was modeled as an isotropic planner source located at ~ 0.5 cm from the test assembly, as shown in Fig. VII.3(b). All the transport calculations were performed using the DOT4.3 code with $S_{16}P_5$ approximation. The 30-g library derived by the AMPX⁽⁴²⁾ module (see Subsection VII.4) was used for that purpose. Since the external source in the benchmark system and the neutron direct component in the reference system are modeled as point sources, the first collision sources were first obtained by the GRTUNCL⁽⁴³⁾ code and were used as input for the transport calculations performed by the DOT4.3 code. This was necessary in order to mitigate the ray-effect resulting from using a point source.

For each of the responses R_k considered (see below), an adjoint transport calculation was performed to derive the flux ϕ_k^* required for the sensitivity analysis. Most of the responses are TPR's at various spatial points in the test assembly. Since the response function Σ_r appears in these cases as point source to the adjoint equation, the first collision source was obtained by the GRTUNT⁽⁴⁴⁾ code in a similar fashion to the forward calculations.

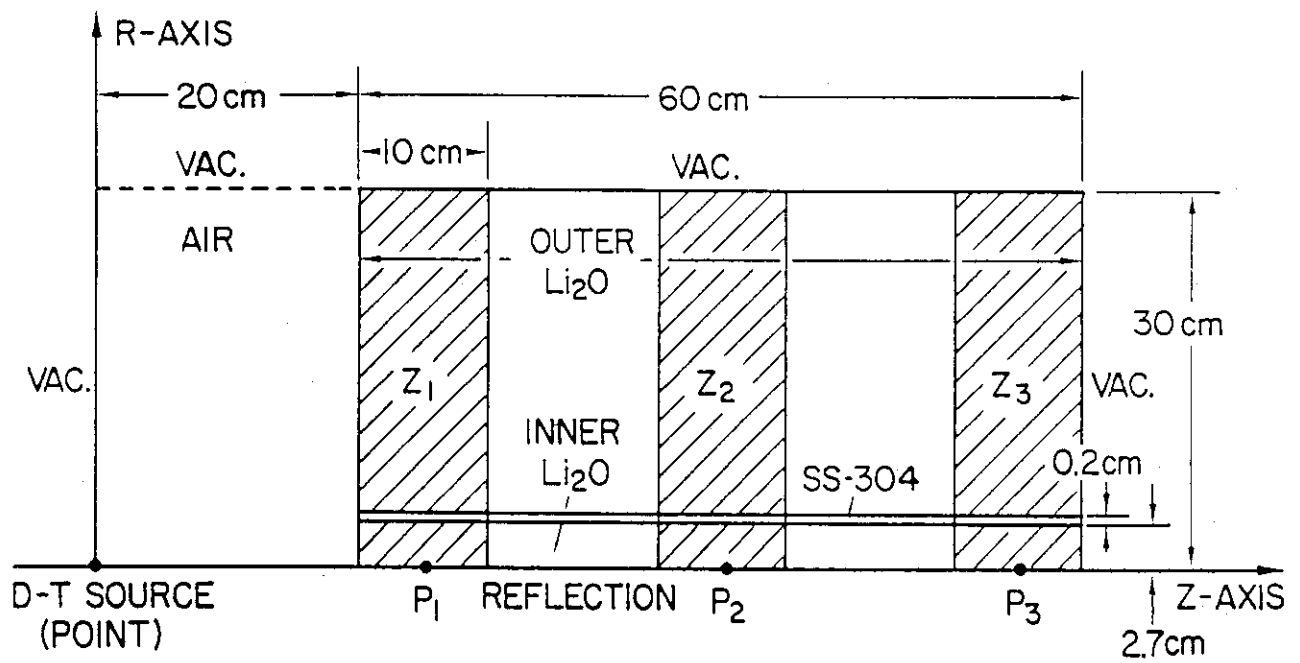


Figure VII.3(a) The R-Z two-dimensional geometrical model for the benchmark system. The detector locations P_i and Z_i are shown

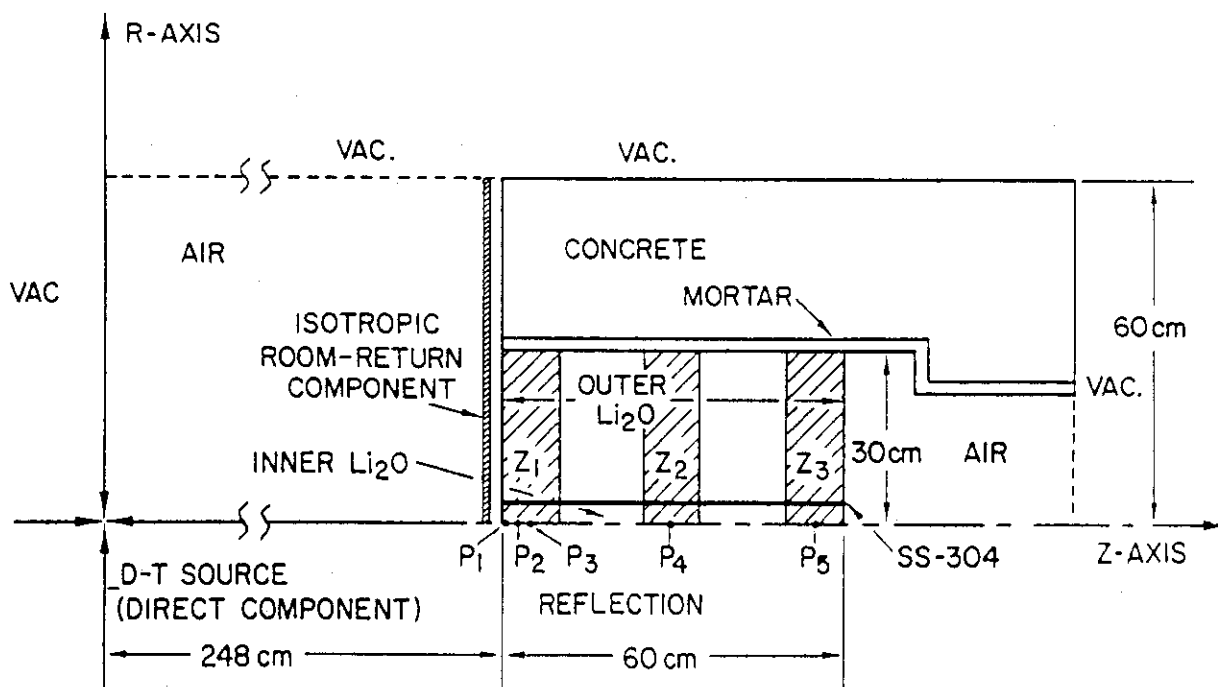


Figure VII.3(b) The R-Z two-dimensional geometrical model for the reference system. The detector locations P_i and Z_i are shown.

Table VII.1 The Atomic Densities of Materials Considered in the Analysis (Atoms/cm³ 10⁻²⁴)

Element	Air	Inner Li ₂ O	SS-304	Outer Li ₂ O	Mortar	Concrete
⁶ Li	---	4.2211-3	----	4.1915-3	----	----
⁷ Li	---	5.2774-2	----	5.2404-2	----	----
¹⁶ O	1.1300-5*	2.8498-2	----	2.8798-2	3.7680-2	4.3150-2
Fe	---	5.2049-4	2.3245-2	1.1119-3	6.8100-4	5.8590-4
Cr	---	1.4333-4	6.3975-3	3.0675-4	----	----
Ni	---	6.2963-5	2.8121-3	1.3516-4	----	----
Mn	---	7.2449-6	3.2948-1	1.8801-5	----	----
H	---	----	----	----	9.4246-3	7.9740-3
Al	---	----	----	----	1.9408-3	2.6370-3
Na	---	----	----	----	5.0802-4	7.8590-3
Ca	---	----	----	----	3.7143-3	2.5640-3
Si	---	----	----	----	1.1347-2	1.4810-2
K	---	----	----	----	3.3427-4	5.2880-4
C	---	----	----	----	7.4297-4	5.4090-4
¹⁴ N	4.1845-4	----	----	----	----	----

*Reads as 1.1300 x 10⁻⁵

VII.4 Calculational Procedures

Although the transport calculations based on the deterministic methods shown in Figures VII.1 and VII.2 were performed with fine-group cross-section libraries (U.S.: MATXS6 library, 80-g, ENDF/B-V; JAERI: JACKAS library, 125-g, JENDL3-PR2), the sensitivity and uncertainty analyses were performed with the thirty-group structure of the MATXS5 library.⁽⁴⁵⁾ This group structure covers neutron energy ranges from 1.4×10^{-4} eV to 17 MeV which is adequate to describe the spectra emitted from the D-T source for both experiments. The transport cross-sections required for the forward and adjoint calculations were generated from the DLC-113/VITAMIN-E master interface fine-group library⁽⁴⁶⁾ (174-g), using the CHOX and MALOCS codes of the AMPX processing system.⁽⁴²⁾ The 30-g forward and adjoint libraries with P_5 Legendre components were then converted to group-organized cross-section sets by using the GIP⁽⁴⁷⁾ code and were used in the DOT4.3 transport calculations.

The total and partial cross-sections required for the sensitivity and uncertainty analyses were also generated from the VITAMIN-E master library in 30-g structure by using the NITWAL⁽⁴²⁾ module of the AMPX system. This module represents a relatively large portion of the AMPX system and has many options for formatting the libraries that can be generated. The ANISN-formatted transfer matrices of the total and partial cross-section library was then converted to the MATXS format⁽⁴⁵⁾ required for the sensitivity analysis by using the ANTMX code of the FORSS system⁽⁴⁸⁾ (see below).

The response function ${}^6\text{Li}(n,\alpha)t$ cross-section is thus generated from the VITAMIN-E library. As for the response function ${}^7\text{Li}(n,n'\alpha)t$ cross-section, it was generated by subtracting the first inelastic cross-section from the total inelastic cross-section, as implemented in the VITAMIN-E library.

Emphasis was placed on studying the impact of current cross-section uncertainties on the TPR from ${}^6\text{Li}$ and ${}^7\text{Li}$ at various point locations in the test assembly. Three locations were selected for each T_6 and T_7 in the benchmark system at distances 5, 30, and 55 cm from the front surface of the Li_2O assembly. These locations are denoted P_1 , P_2 , and P_3 , respectively, in Fig. VII.3(a). The point detectors selected for T_6 in the reference system are at the positions P_1 , P_2 , P_3 , P_4 , and P_5 located at distances of 0.5, 1.5, 5.0, 30 and 55 cm from the front surface, respectively. The choice for the P_1 and P_2 locations was necessary since the T_6 profile is very steep near the surface of the Li_2O assembly, as discussed in Section IV. However, the detector locations selected for T_7 in the reference system are P_1 , P_2 , and P_3 located at depths of 5, 30, and 55 cm.

Zonal TPR from ${}^6\text{Li}$ was also considered in both systems. The zone detectors are denoted Z_1 , Z_2 , and Z_3 , as shown in Figures VII.3(a) and (b), and are placed at positions 0-10; 25-35, and 50-60 cm, respectively. Each of these detectors has a thickness of 10 cm. In addition, the TPR from ${}^6\text{Li}$ in the entire assembly (Z_4) was also considered in the benchmark system. The detector locations for T_6 and T_7 in both systems are summarized in Table VII.2. As shown, a total of 21 adjoint calculations were performed for the responses R_k . A GRTUNT run, followed by a DOT4.3 run, was required for the 14 cases where point detectors are considered. However, only two forward calculations were needed, one for

each system (not counting the source superposition in the reference system and the necessary GRTUNCL runs).

The FORSS module developed at Oak Ridge National Laboratory (ORNL) was applied extensively in the analysis. The Volume Integrated Product (VIP) code developed specifically for the two-dimensional sensitivity analysis by Child⁽⁴⁹⁻⁵⁰⁾ was used. In this regard, and for each response considered, the forward and adjoint fluxes are used as input for the VIP code and the so-called $\langle \phi_k^* \phi \rangle$ file is generated. The partial cross-section file generated by the NITWAL code is converted to the MATXS format using the ANTMX code and is used, along with the $\langle \phi_k^* \phi \rangle$ file, as input for the JULIET code of the FORSS module to arrive at the sensitivity profiles defined in Eq. VII.2. The JULIET code is a substantial part of the FORSS system and has many options (paths) that can be performed. The standard deviation in various cross-section types, and the relative covariance and correlation matrices required for the uncertainty analysis are derived from the ENDF/B-V error file (file 33) by using the PUFF-2 code.⁽⁵¹⁾ The generated "COVREX" uncertainty file obtained by the PUFF-2 code and the "SENPRO" sensitivity file generated by the JULIET code are used as input to the CAVALIER code of the FORSS system to arrive at an estimate for the variance in the response, R_k , according to Eq. VII.1. The above sensitivity/uncertainty analysis procedures are outlined in Fig. VII.4.

FORSS SENSITIVITY / UNCERTAINTY PROCEDURE

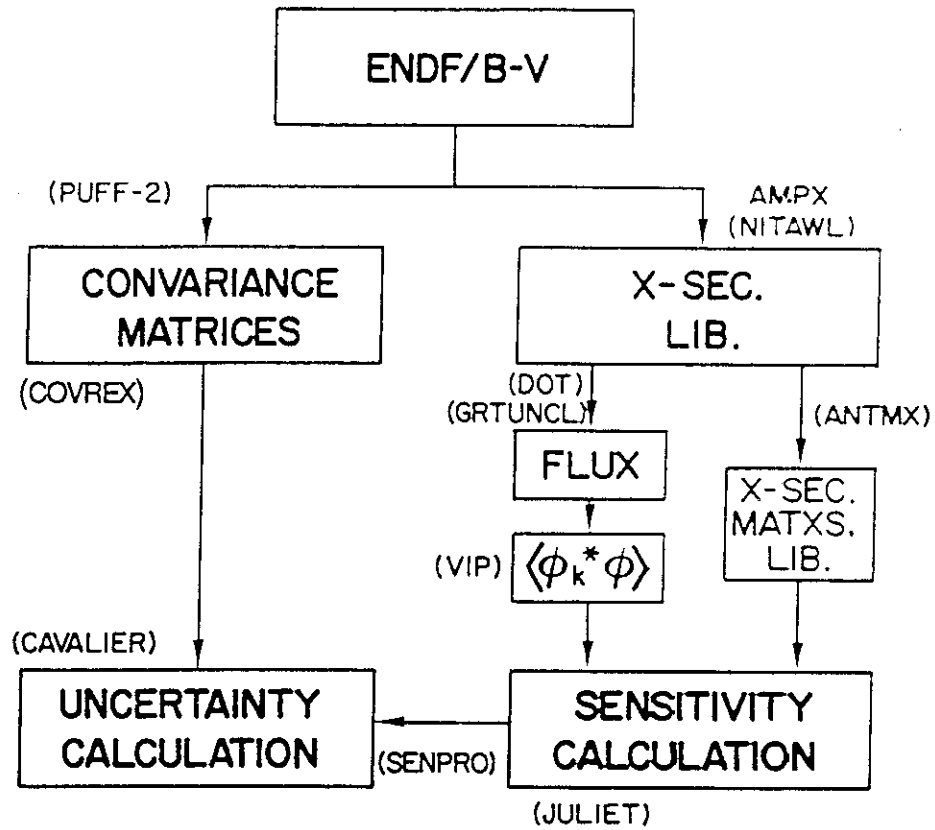


Figure VII.4 Outlines of the FORSS sensitivity and uncertainty procedures. Computer codes used are shown.

Table VII.2 Locations of the Point Detectors, P_i and Zone Detectors, Z_i , in the Benchmark and the Reference Systems^(a)

Detector Notation	T_6		T_7	
	Benchmark	Reference	Benchmark	Reference
P_1	5.0	0.5	5.0	5.0
P_2	30.0	1.5	30.0	30.0
P_3	55.0	5.0	55.0	55.0
P_4	----	30.0	----	----
P_5	----	55.0	----	----
Z_1	0-10	0-10	----	----
Z_2	25-35	25-35	----	----
Z_3	50-60	50-60	----	----
Z_t	Entire Assembly	----	----	----

(a) Units in cm

VII.5 Tritium Production Rate Profiles

The profiles for TPR from ${}^6\text{Li}$ and ${}^7\text{Li}$ along the central axis of the Li_2O assembly are shown in Fig. VII.5 for the benchmark and reference systems. The external source spectrum incident on the Li_2O front face is shown in Figs. VII.6 and VII.7 for the two systems, respectively. Note that the incident spectrum above 10 MeV in the benchmark system is about two orders of magnitude higher than the corresponding spectrum in the reference system. The spectrum around 100 eV is the same in both systems. However, below 100 eV, the source spectrum in the reference system is much larger than in the benchmark system, and the difference is basically attributed to the room-return component of the incident D-T source.

In the benchmark system, the TPR from ${}^6\text{Li}$, T_6 , peaks at a depth of about 5 cm in the Li_2O assembly, then gradually decreases. The peak is due to the increase in low-energy neutrons resulting from elastic, inelastic, and $(n,2n)$ reactions with the assembly materials up to that depth which leads to large T_6 . The decrease in T_6 throughout the rest of the assembly is due to the decrease in the low-energy component of the flux resulting from absorption as neutrons travel through the assembly. The profile for T_6 in the reference system is quite different, as was shown in Section IV. Near the front surface, the values for T_6 are very large with a rapid decrease within the first few centimeters in the Li_2O assembly. At middle locations, the profile is rather flat. However, near the rear surface (~ 60 cm), the T_6 profile shows a steep increase. As was discussed in Section IV, the high value for T_6 near the front surface, and its sharp decrease within a short distance, is due mainly to the low-energy room return component of the incident neutrons which have large ${}^6\text{Li}(n,\alpha)t$ cross-sections. The steep increase in T_6 near the back end of the assembly is caused by the large increase in the low-energy neutrons reflected directly to the back locations by the concrete walls of the experimental cavity (see Fig. VII.3[b]).

The profile of T_7 decreases steadily as one proceeds towards the back locations. Because the high-energy component of the incident neutrons is about two orders of magnitude higher in the benchmark system, the T_7 values in that system are also 1-2 orders of magnitude higher in comparison to the reference system. Note, however, that the T_7 profile has a larger slope (i.e., faster rate of decrease) due to the fact that the distance of the point source in the benchmark system, d_s , is 20 cm, while $d_s = 248$ cm in the reference system.

VII.6 Sensitivity Analysis Results

In the following, the relative cross-section sensitivity profile of T_6 when the response considered is the TPR from ${}^6\text{Li}$ in the zone detector Z_1 defined in Table VII.2, and for a 1% increase in a particular cross-section type of a given material, Σ_x , over the whole assembly in the benchmark system is denoted as $P(T_6, Z_1, \Sigma_x)_B$. Likewise, the notation $P(T_7, P_1, \Sigma_x)_R$ refers to the sensitivity profile for the TPR from ${}^7\text{Li}$ at the point detector P_1 , defined in Table VII.2, resulting from a 1% increase in cross-section type Σ_x , over the entire assembly in the reference system.

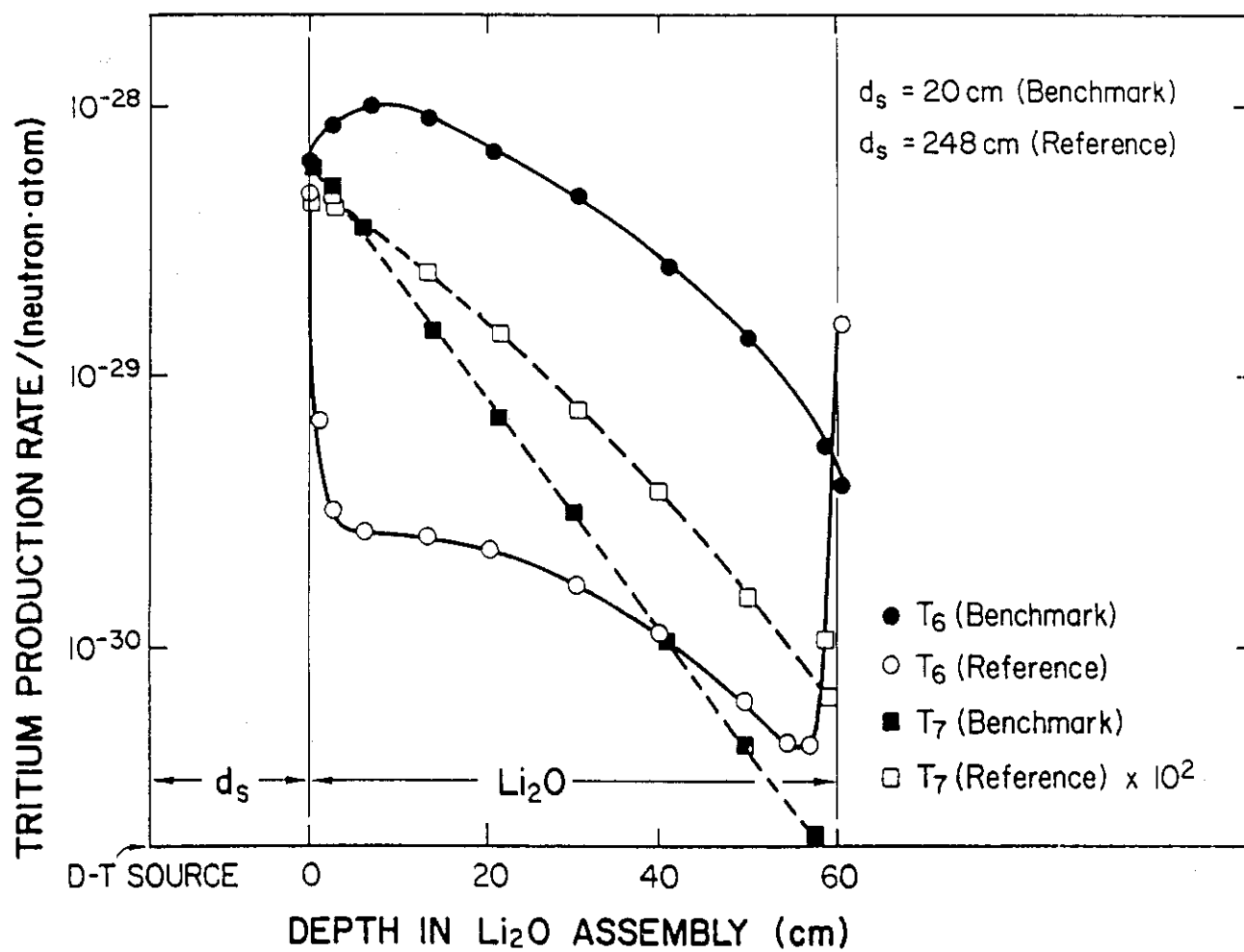


Figure VII.5 Profiles for the TPR from ^6Li and ^7Li along the central axis of the Li_2O assembly

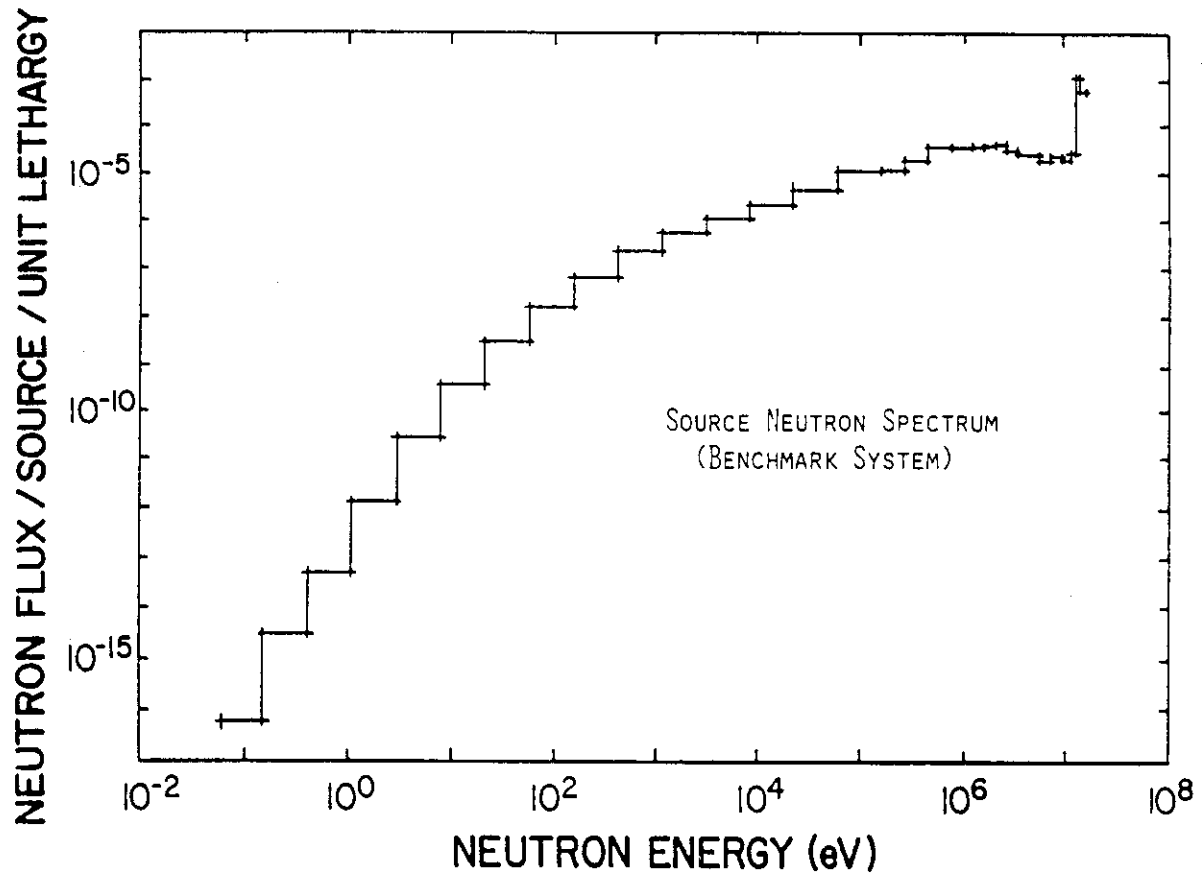


Figure VII.6 The incident D-T neutron spectrum in the benchmark system

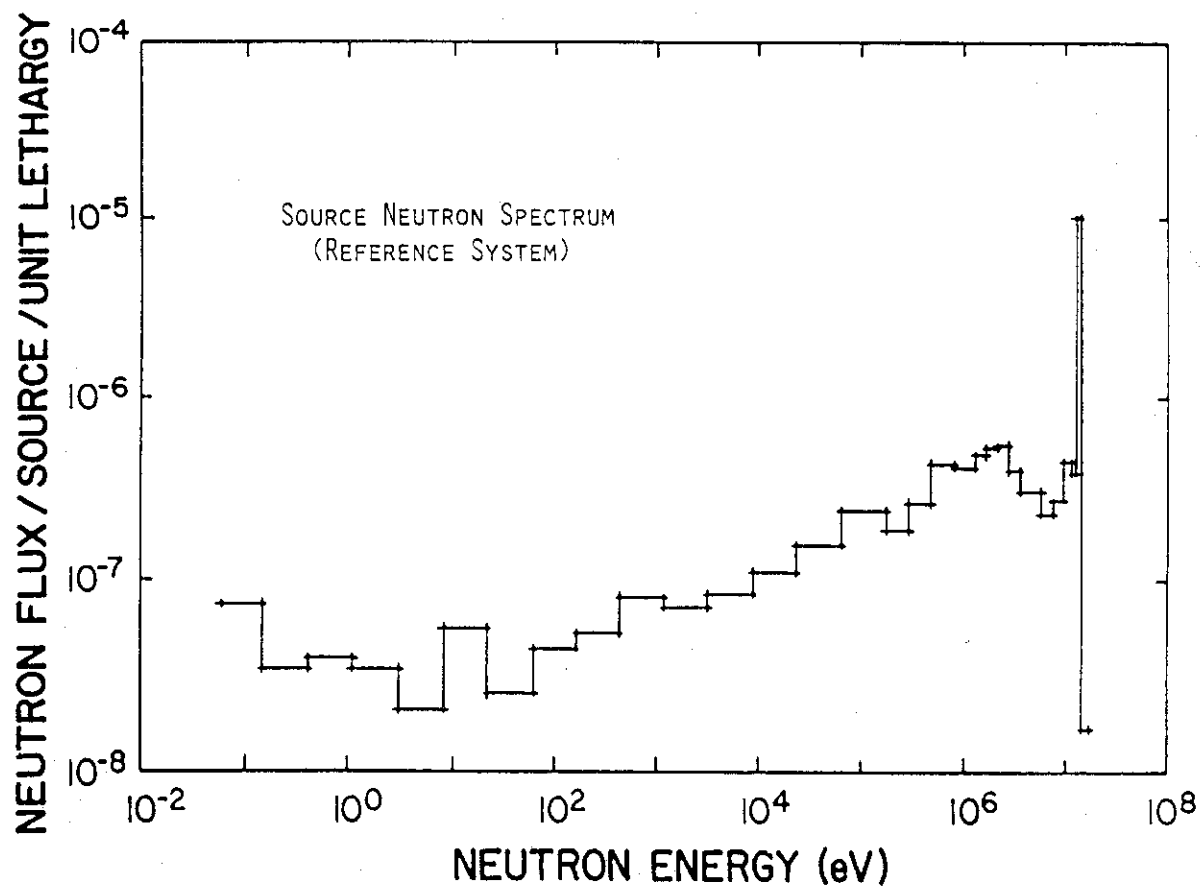


Figure VII.7 The incident D-T neutron spectrum in the reference system

The sensitivity profiles as defined by Eqs. VII.2 and VII.5 were evaluated in both systems for T_6 and T_7 for the responses (detectors) defined in Table VII.2. The profiles were obtained for variations in the total cross-section of each material present in the Li_2O assembly as well as for each partial cross-section. The integrated relative sensitivity coefficient, $S_{\Sigma_X}^k$, defined by Eq. VII.4, was also evaluated for each response R_k . This coefficient was evaluated for perturbation in both the total and partial cross-sections. As expected, it was found that both T_6 and T_7 are most sensitive to variation in the total cross-section of ${}^6\text{Li}$, ${}^7\text{Li}$, ${}^{16}\text{O}$, and Fe for all the responses considered with small impact from the presence of other elements (e.g., Ni, Mn, etc.). The analysis is discussed below, with emphasis on these profiles and a comparison between the results obtained for the point detectors and zone detectors.

VII.6.1 Sensitivity Profiles of T_6

VII.6.1.1 Variation in Σ_t of ${}^6\text{Li}$

In the benchmark system, the profiles $P(T_6, P_i, \Sigma_t)_B$ for $i=1-3$ due to variation in the total cross-section of ${}^6\text{Li}$ are shown in Fig. VII.8. Each profile is positive at all energies. This was found to be the case for all the point and zone detectors considered, except the detector P_2 , where negative values were found in the energy range 0.4 eV-100 eV. In Fig. VII.8 and all subsequent figures, solid lines represent positive values while dashed lines represent negative values. The profiles shown in Fig. VII.8 are obtained by adding the direct effect to the indirect effect parts of the profile according to Eq. VII.6. The direct effect part is always positive since an increase of 1% in Σ_t is also an increase by 1% in the cross-section $\Sigma(n, \alpha)t$.

For the indirect part, we notice that at low energy, Σ_t is dominated by $\Sigma(n, \alpha)t$ whose profile is negative. Thus, the indirect effect part [collisional loss, scattering gain, see Eq. VII.6] is basically negative at thermal and epithermal energy ranges. However, this part was found to be positive above 1 MeV. This is due to the fact that Σ_t in this range is made up of $\Sigma(n, \text{elastic})$, $\Sigma(n, \text{inelastic})$, and $\Sigma(n, 2n)$, whose profiles are positive above 1 MeV since these reactions slow down neutrons to lower energies where their chance to be absorbed by ${}^6\text{Li}$ is high and hence an increase in T_6 occurs. In general, the direct effect part dominates the indirect part with a positive net profile.

From Fig. VII.8 one notices that the profile shape is similar in trend to the incident source spectrum. There is a prominent peak at 250 KeV, especially for the P_1 point detector at $Z=5$ cm, where the cross-section $\Sigma(n, \alpha)t$ has a resonance, and another peak around 14 MeV. The profile value around this 14 MeV peak tends to get smaller in value as the detector location is moved to P_3 at $Z=55$ cm. Also, the sensitivity profile becomes relatively large in the energy range from 0.1 KeV to several hundred KeV as the detector location changes from P_1 to P_3 . At these deep locations, the neutron spectrum is softer than at P_1 .

The profiles for the zonal detectors are similar in shape to the ones shown in Fig. VII.8 and are positive at all energies and for all zone detectors.

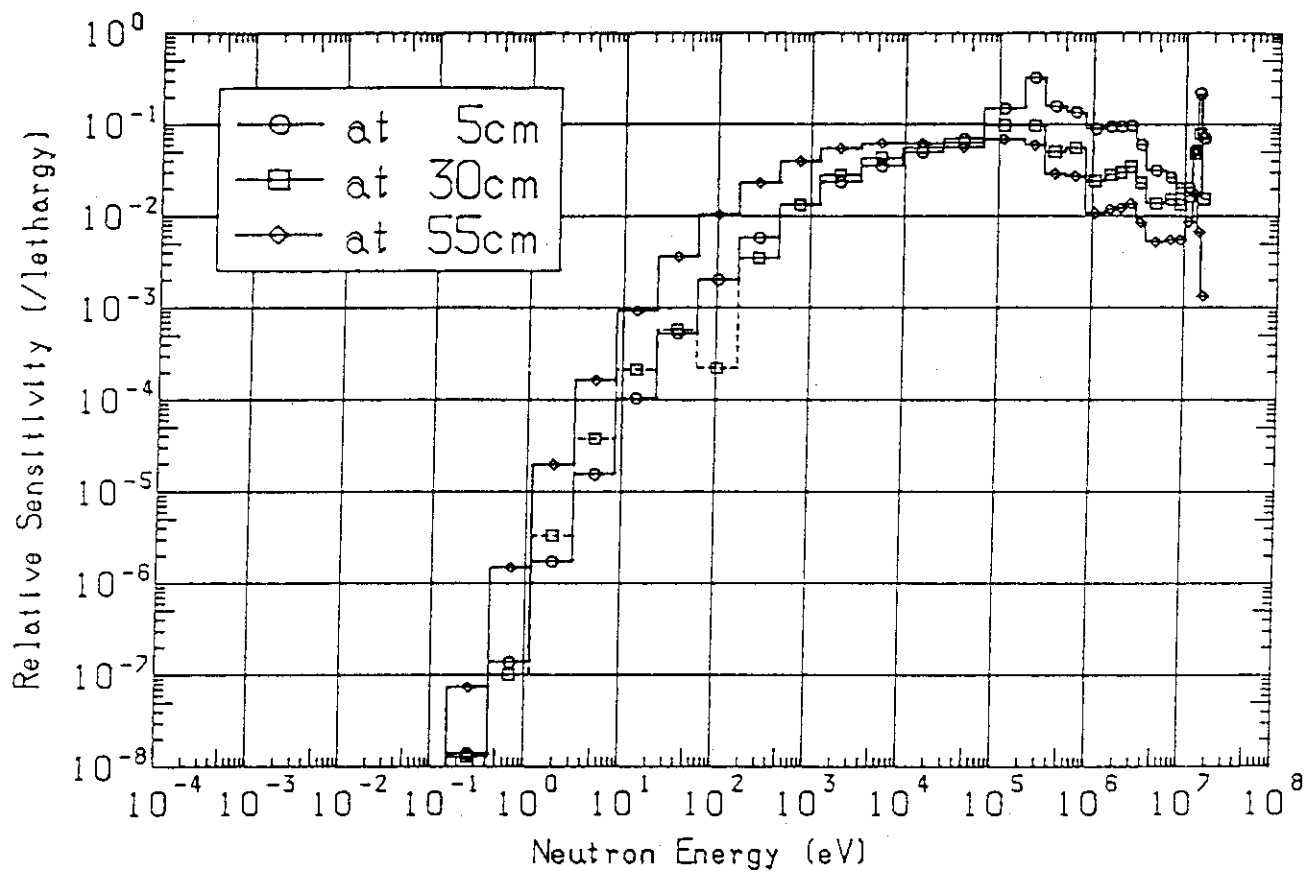


Figure VII.8 The sensitivity profiles $P(T_6, P_i, \Sigma_t)B$ [$i = 1-3$] due to a 1% increase in Σ_t of ${}^6\text{Li}$ in the benchmark system. Point detectors P_1 , P_2 and P_3 at $Z = 5, 30$, and 55 cm are considered

The integrated relative sensitivity coefficients as defined by Eq. VII.4, due to a 1% increase in Σ_t in the whole assembly is shown in Fig. VII.9 as a function of the point detector location. The total values (direct + indirect) are positive and decrease at deeper locations. The integrated coefficient of the indirect part is always negative and increases in its absolute value as one moves toward the back locations. This is expected since the thicker the portion of the assembly that is in front of the detector location, the larger the chance that neutrons get absorbed through the ${}^6\text{Li}(n,\alpha)t$ reactions, while absorption events are less if the detector location is near the front surface. These features are also the same when zonal detectors are considered. The integrated relative sensitivity coefficients are shown in Fig. VII.10 for each reaction type for ${}^6\text{Li}$ as a function of the point detectors shown in Table VII.2. Reaction types that produce low-energy neutrons have positive coefficients since the ${}^6\text{Li}(n,\alpha)t$ cross-section is larger for slow neutrons. These reaction types are (n, elastic), (n,inelastic), and (n,2n) and their coefficients decrease at deeper locations. On the other hand, reactions that lead to neutron disappearance, such as the (n,p) reaction, have negative coefficients that increase in their absolute values at deeper detector locations. Note in particular that the integrated indirect part of the coefficient for ${}^6\text{Li}(n,\alpha)t$ reaction has a negative value that increases at back locations. Also shown in Fig. VII.10 is the net positive coefficient for that reaction which includes the direct part. As shown, this coefficient is the largest in comparison to the coefficient of other reactions at all detector positions.

In the reference system, the incident neutron spectrum and the geometrical arrangement are different from those of the benchmark system. Accordingly, the sensitivity profiles are also different. This can be seen from Fig. VII.11, which shows the profile $P(T_6, P_i, \Sigma_t)_R$ for $i=1, 3, 4, 5$ (see Table VII.2) due to variation in Σ_t of ${}^6\text{Li}$ throughout the assembly. At the point detector P_1 (depth of 0.5 cm), the T_6 sensitivity profile has large values in the low-energy range. As shown, the largest value is in the lowest energy group. At this detector position, the direct effect part of the sensitivity profile dominates the indirect part. This is expected since the T_6 profile (see Fig. VII.5) is very steep within the first few centimeters in the Li_2O assembly, and the large values for T_6 at these locations are due to the room-return component of the incident neutrons whose energy is low. Therefore, increasing Σ_t of ${}^6\text{Li}$ (equivalent to increasing the atomic density of ${}^6\text{Li}$) results in a large increase in T_6 at these locations. However, since the mean free path for these low-energy neutrons is short, they are absorbed in the first few centimeters. At the point detector location of 5 cm-depth (P_3), the sensitivity profile changes its shape noticeably at low-energy range. This can be seen from Fig. VII.11, where the profile exhibits low and negative values in the energy range 1-12 eV, while the values are positive and large at higher energies. The range where the profile values are negative gets wider ($E_n=1-100$ eV) at the detector location P_4 (depth of 30 cm). These negative values indicate that the indirect negative part of the sensitivity profile is larger than the positive direct part at these point locations. In all the sensitivity profiles (P_1 through P_5), the prominent peaks at 14 MeV and 250 KeV are evident.

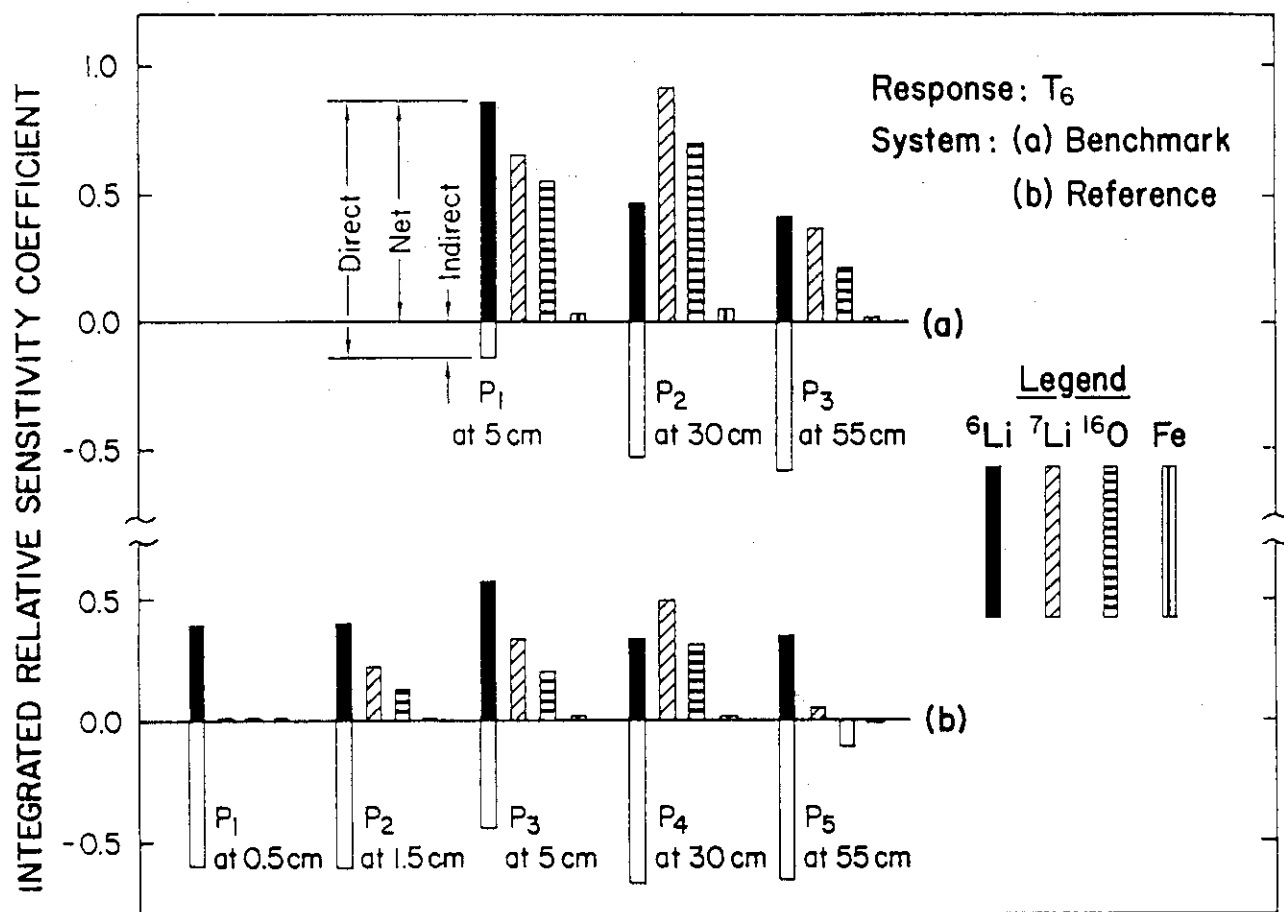


Figure VII.9 The integrated relative sensitivity coefficients for T_6 in the benchmark and reference systems due to variations in the Σ_t of various elements. Point detectors are considered

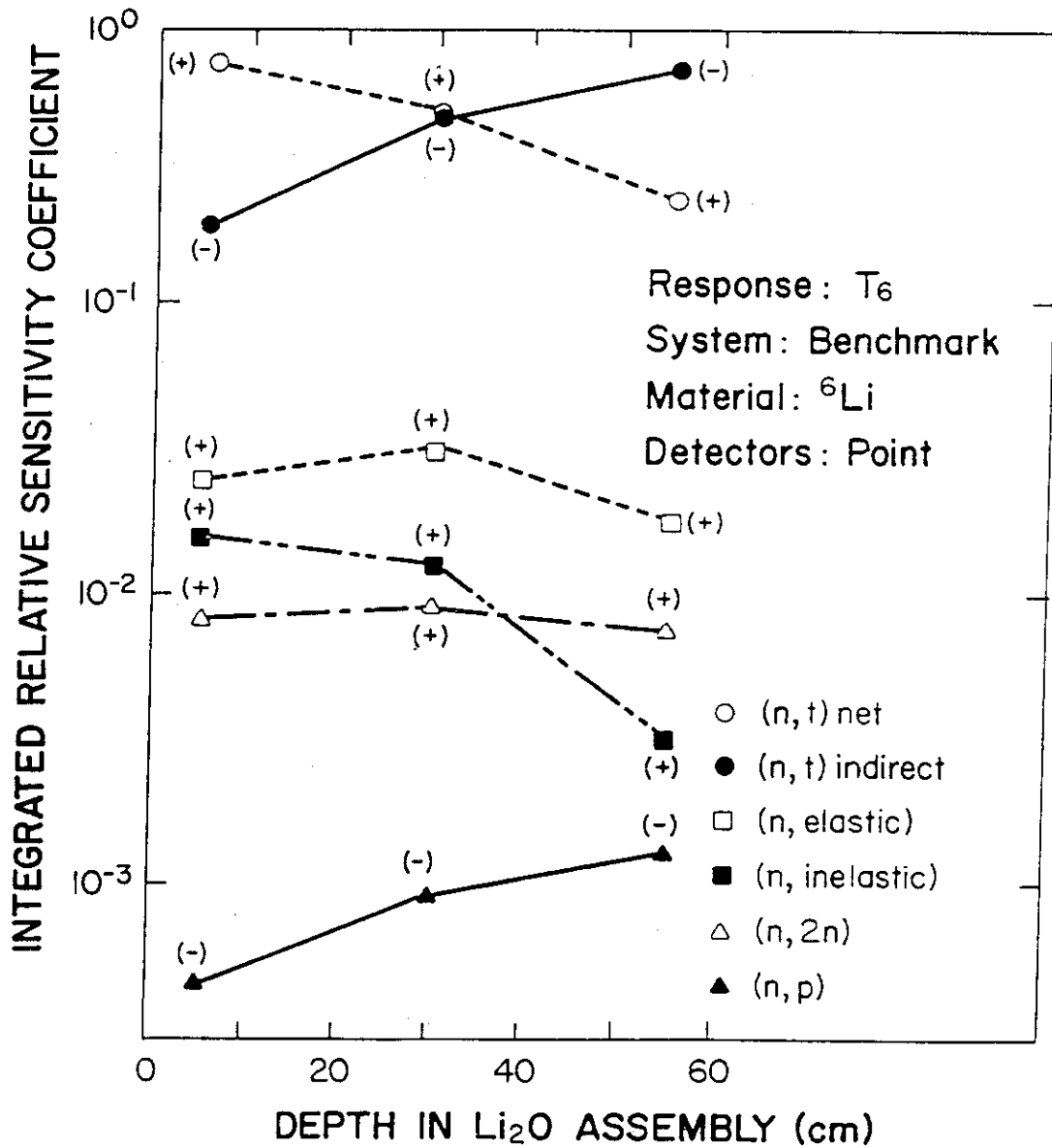


Figure VII.10 The integrated relative sensitivity coefficients for T_6 in the benchmark system due to variations in various partial cross-sections of ${}^6\text{Li}$. Point detectors are considered

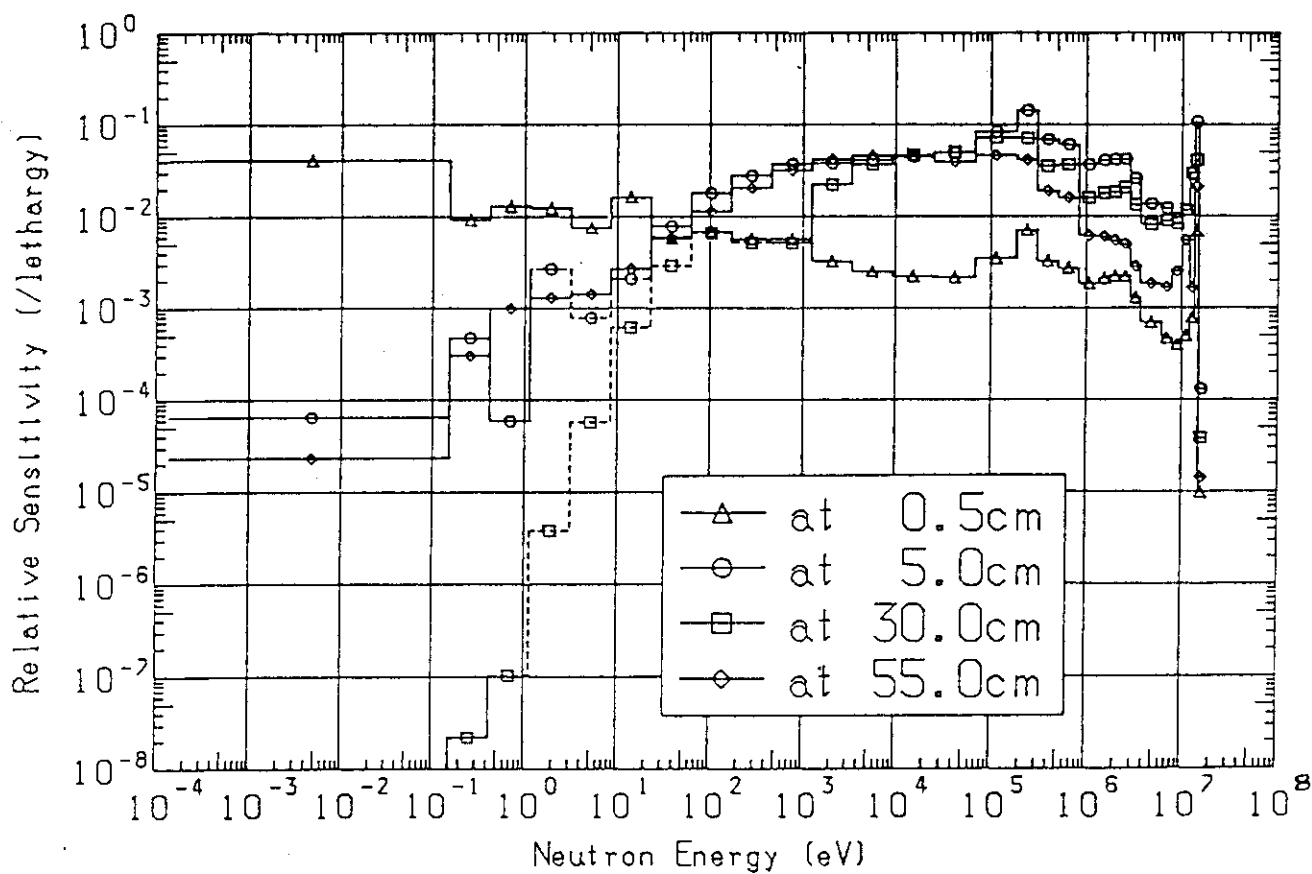


Figure VII.11 The sensitivity profiles $P(T_6, P_i, \Sigma_t)_R$ [$i = 1, 3, 4, 5$] due to a 1% increase in Σ_t of ^6Li in the reference system. Point detectors P_1, P_3, P_4 , and P_5 at $Z = 0.5$, 5, 30, and 55 are considered

The T_6 zone detectors exhibit significantly different profiles from those found for the point detectors. The profile for the detector Z_1 at a depth of 0-10 cm is very similar to the profile at the point detector P_1 , but very different from the profile at P_3 shown in Fig. VII.11. This shows that at this zone detector location, the profile $P(T_6, Z_1, \Sigma_t)_R$ is dominated by the effect resulting from the room-reflected component. Also, while the profile $P(T_6, P_4, \Sigma_t)_R$ has negative values below 100 eV, the profile $P(T_6, Z_2, \Sigma_t)_R$ has positive values at all energies. [Note that point detector P_4 and zone detector Z_2 are at the middle of the Li_2O assembly (see Table VII.2).] This is due to the fact that the slow neutrons reflected by the concrete walls at the Li_2O /concrete boundaries lead to large low-energy flux near these boundaries. Accordingly, any variation in the Σ_t of 6Li leads to a large direct component to the sensitivity profile which is integrated over the detector volume Z_2 , whereas at the point detector P_4 , the indirect component of the sensitivity profile is larger at low energies than the direct component at this inner point.

The profiles $P(T_6, P_5, \Sigma_t)_R$ [at $Z=55$ cm, see Fig. VII.11] and $P(T_6, Z_3, \Sigma_t)_R$ are also different. The profile $P(T_6, P_5, \Sigma_t)_R$ is positive at all energies, except at the 14 MeV peak, while the profile $P(T_6, Z_3, \Sigma_t)_R$ has negative values at the 14 MeV peak and at energies below 10 eV. In comparison to the profile $P(T_6, P_3, \Sigma_t)_B$ in the benchmark system, where it is positive at all energies, the negative peak at the 14 MeV in the reference system at P_5 and Z_3 can be explained by noticing that the 14 MeV peak of the incident neutron spectrum is lower in the reference by two orders of magnitude in comparison to the 14 MeV peak of the incident spectrum of the benchmark system. Accordingly, reaction types such as (n,2n) and (n,inelastic) which lead to positive contribution to the sensitivity profiles of T_6 are lower in the reference system at the back locations, which makes the indirect negative component (collisional loss) dominate the positive components (direct, scattering gain) of the sensitivity profile at these locations.

The integrated relative sensitivity coefficients, as defined by Eq. VII.4, are also shown in Fig. VII.9, for the point detectors considered. One notices that these coefficients are smaller in the reference system than in the benchmark system. In addition, the negative indirect parts of these coefficients are relatively large in the reference system.

VII.6.1.2 Variation in Σ_t of 7Li

In the benchmark system, the sensitivity profiles $P(T_6, P_i, \Sigma_t)_B$ for $i=1-3$ due to variation in the total cross-section of 7Li are shown in Fig. VII.12. The shape of these profiles was found to be very similar to those of the zone detectors. Note also the similarity in shape to the incident spectrum for the benchmark system. The common feature for both the point and zonal profiles is as follows: (a) a dominant positive peak at 14 MeV that decreases in its value at deeper locations, (b) positive values at all energies except below a cutoff energy, E_c , where the profiles are negative. This cutoff energy increases as one proceeds toward the back end of the Li_2O assembly. Also, the value for E_c is lower for the zone detectors in comparison to the point detectors (not shown).

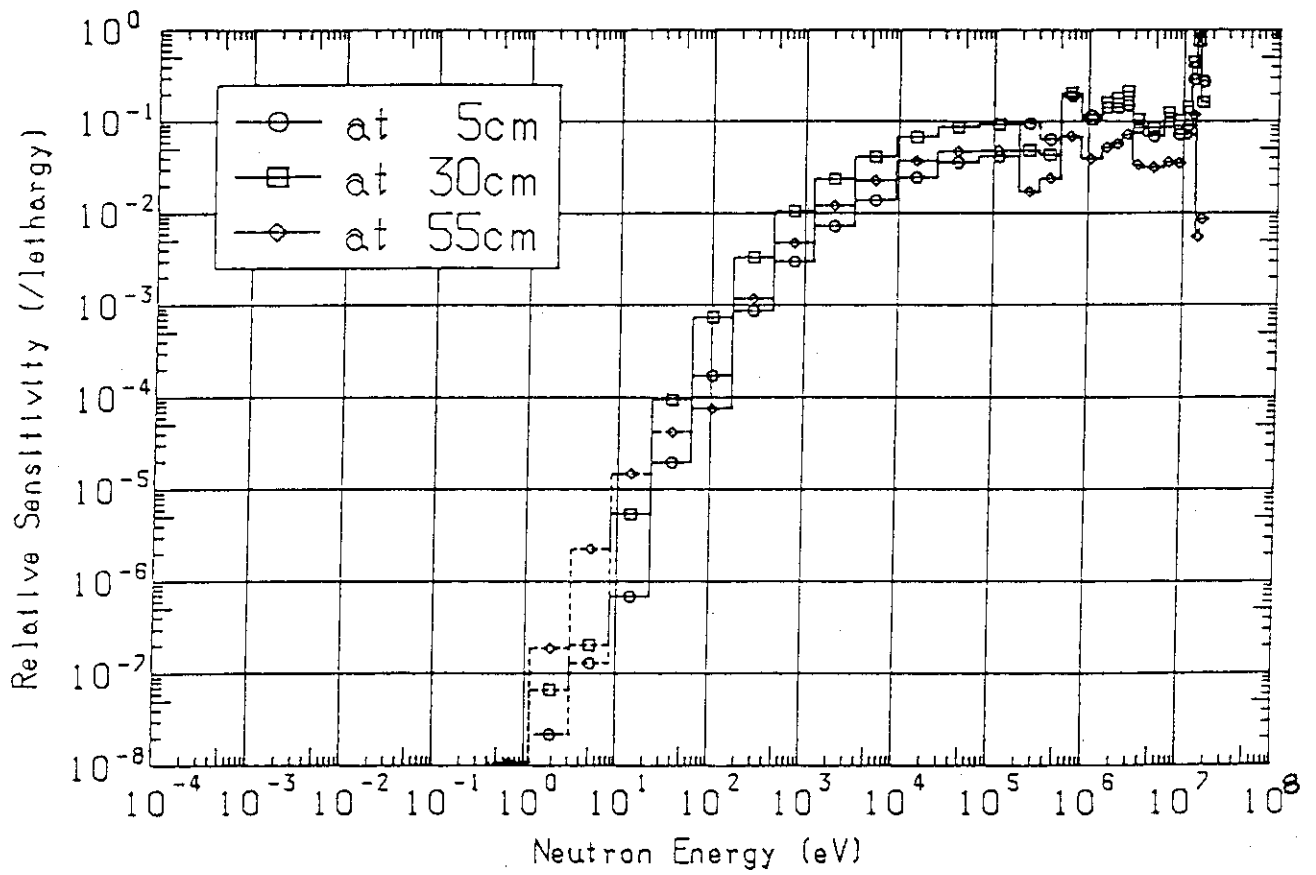


Figure VII.12 The sensitivity profiles $P(T_6, P_i, \Sigma_t)_B$ [$i = 1-3$] due to a 0.1% increase in Σ_t of ^7Li in the benchmark system. Point detectors P_1 , P_2 , and P_3 at $Z = 5, 30$, and 55 cm are considered

The positive values for the sensitivity profiles above the cutoff energy, E_c , is expected since an increase in the Σ_t of ^7Li above E_c means an increase in the cross-sections $(n,2n)$, $(n, \text{inelastic})$, $(n, \text{elastic})$ and $(n, 3n)\alpha$. This increase leads to low-energy neutrons that contribute to an increase in T_6 . The similarity found between the profiles for the zone and point detectors can also be explained by noticing that ^7Li does not have reactions that have large cross-sections in the low-energy range, and the neutron flux is basically affected by the elastic, inelastic, and $(n,2n)$ reactions which have a relatively large cross-section for fast neutrons. Thus, the similarity observed is more pronounced here than in the case of variation in Σ_t of ^6Li discussed earlier.

The negative values observed below the cutoff energy, E_c , are due to the fact that a large negative contribution from the (n,γ) reactions occurs, which dominates the positive contribution to the sensitivity profiles that comes from elastic, inelastic and $(n,2n)$ reactions in this low-energy range. Furthermore, the impact of the negative contribution gets larger as the detector location is moved towards the back of the assembly since a thicker portion of the Li_2O assembly is present in front of the detector location.

The integrated relative sensitivity coefficients for the point detectors of T_6 due to variation in Σ_t of ^7Li is also shown in Fig. VII.9. Significant positive values are observed, particularly at middle locations. Thus, any variation in the cross-sections of ^7Li (and other materials) at these locations leads to large variation in T_6 .

In the reference system, the profiles $P(T_6, P_i, \Sigma_t)R$ for $i=1,3,4,5$ due to variation in the Σ_t of ^7Li are shown in Fig. VII.13. It can be noticed by comparison to Fig. VII.7 that the profile at P_1 point detector ($z=0.5$ cm) location follows the shape of the incident neutron spectrum: namely, a sharp peak at 14 MeV and relatively large values below 100 eV. Except for the difference in the absolute values, the features of the profiles found in the benchmark system still apply in the reference system, i.e., positive values above a cutoff energy and the energy range below the cutoff energy where the profiles are negative is widened as one proceeds toward the back end of the assembly. The reasons discussed for the change in the sign of the profiles are the same as in the benchmark system. One notices, however, that at locations P_1 through P_3 , the profiles are negative around 250 KeV (T_6 resonance). This is due to the collisional loss term of the sensitivity profile whose negative value dominates the gain term caused by elastic, inelastic and $(n,2n)$ reactions at this energy range.

As for the zone detectors, similar profiles are obtained except at the detector location Z_3 . The profile for Z_1 has the same shape as the one for the point detector P_1 . However, some differences were found in the profiles for the point detector P_5 (55-cm depth) shown in Fig. VII.14 and the zone detector Z_3 shown in Fig. VII.15. Negative values are obtained around 14 MeV. The negative peak corresponds to the D-T neutron direct component for which the negative profile for the (n,d) reactions at this back location dominates the positive contribution to the sensitivity profile caused by the inelastic reactions, which are depressed by the thick materials in front of the detector location. Note also that the profile for the zone detector Z_3 has negative values at almost all neutron energies.

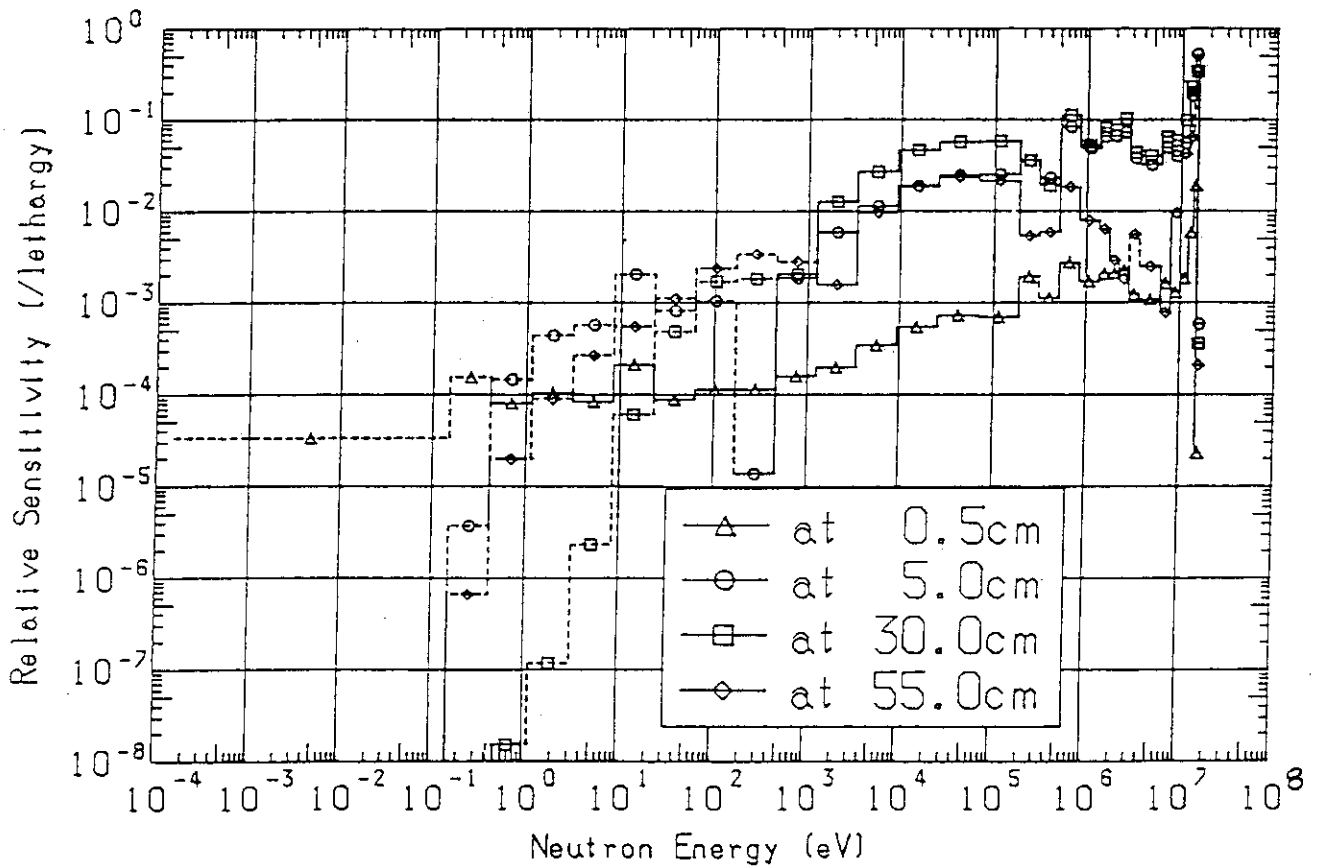


Figure VII.13 The sensitivity profiles $P(T_6, P_i, \Sigma_t)_R$ [$i = 1, 3, 4, 5$] due to a 1% increase in Σ_t of ^7Li in the reference system. Point detectors P_1, P_3, P_4 , and P_5 at $Z = 0.5, 5, 30$, and 55 are considered

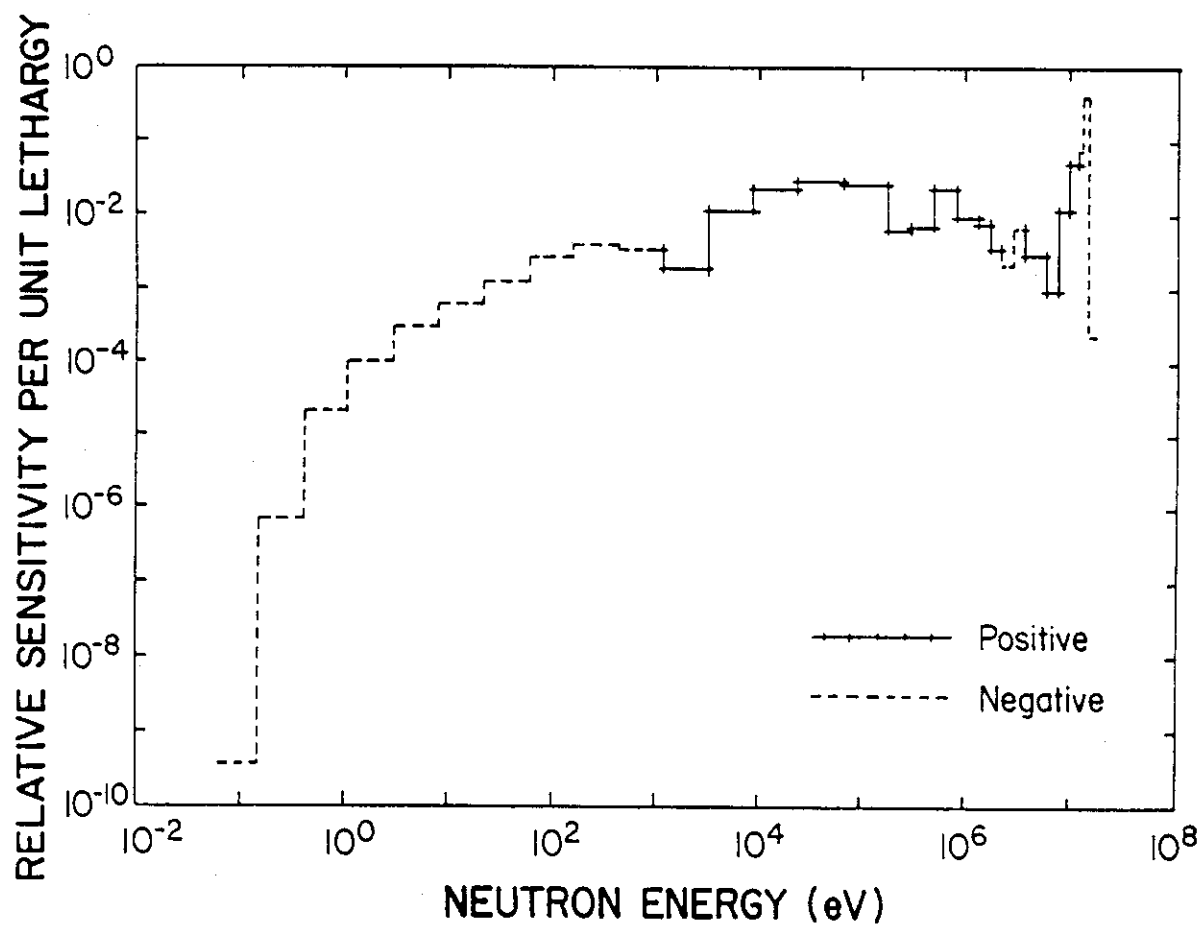


Figure VII.14 The sensitivity profile $P(T_6, P_5, \Sigma_t)_R$ due to a 1% increase in Σ_t of ${}^7\text{Li}$ in the reference system. Point detector P_5 is considered

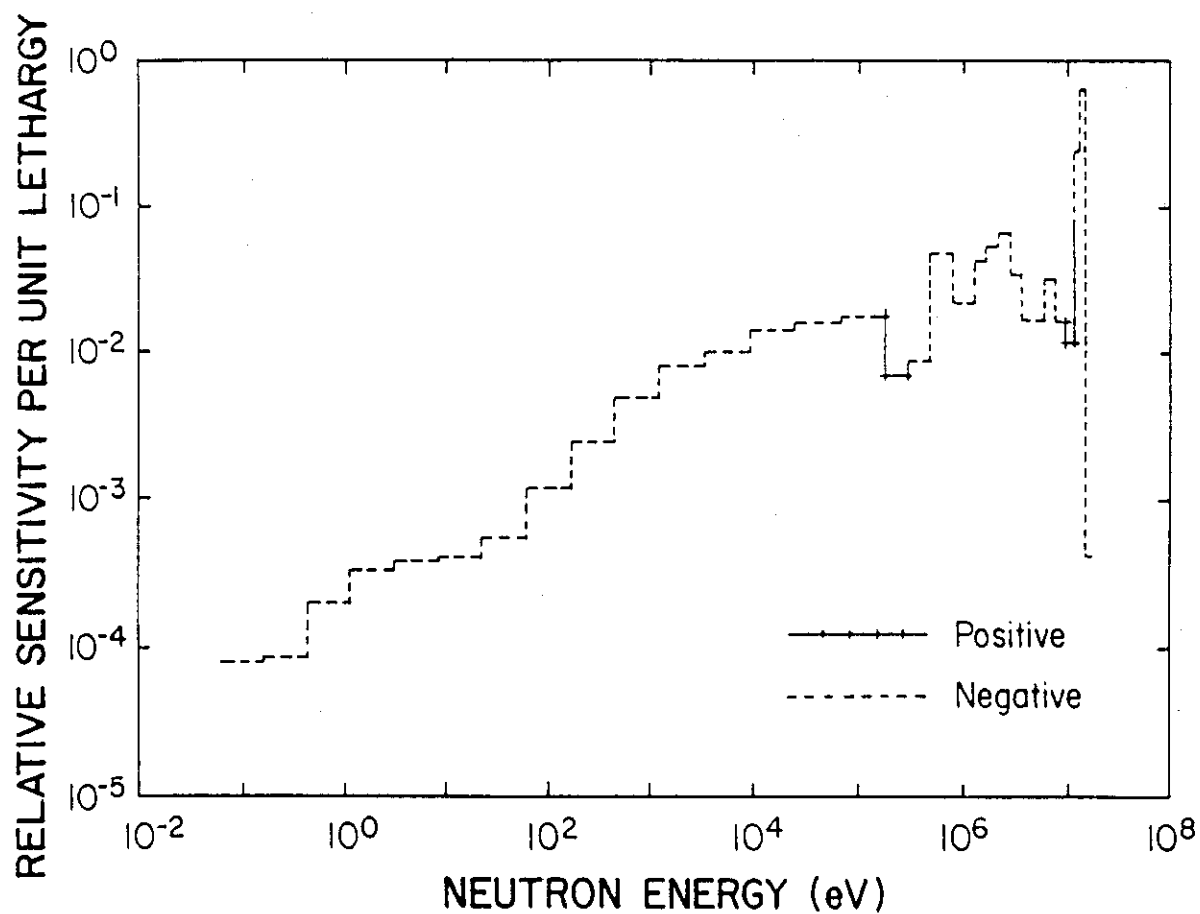


Figure VII.15 The sensitivity profile $P(T_6, Z_5, \Sigma_t)_R$ due to a 1% increase in Σ_t of ^7Li in the reference system. Zone detector Z_3 is considered

The integrated sensitivity coefficients are also shown in Fig. VII.9 for the point detectors considered. The figure shows a steady increase in the value of these coefficients when the detector position moves deeper in the assembly. As in the benchmark system, the largest coefficient found is when the detector location is at the middle of the assembly. Notice, however, that the magnitude for these coefficients is smaller in the reference system than in the benchmark system.

VII.6.1.3 Variation in Σ_t of Oxygen

The atomic density of oxygen in the Li_2O assembly is relatively high, as shown in Table VII.1. Accordingly, one would expect large cross-section sensitivity coefficients, as turned out to be the case. In the benchmark system, the profiles for the point detectors considered due to variations in Σ_t of ^{16}O are very similar in shape and magnitude to the ones found in the ^7Li case, as shown in Fig. VII.16. That is, the profiles are positive at all energies above a cutoff energy, E_c , and negative below that energy, with a dominant peak around 14 MeV, and a shape that resembles the incident source neutron spectrum. However, the profiles are negative around the 14 MeV peak for the point detectors P_2 and P_3 and around the ^6Li resonance (~ 250 KeV) for the point detectors P_1 and P_2 . The reasons for having a positive profile above E_c and negative values below E_c are the same as for the ^7Li case, i.e., the inelastic and elastic reactions at higher energies tend to slow down neutrons to the energy range where T_6 is large. However, around 14 MeV for the detector locations P_2 and P_3 , the positive contribution resulting from these reactions is less than the negative contribution resulting from those reactions such as (n,p) , (n,α) , and (n,d) that lead to neutron disappearance and thus have negative values. However, the integrated sensitivity coefficients, defined by Eq. VII.4, are all positive at the point detector locations considered. This is shown in Fig. VII.9, where again the largest coefficient is found at the middle detector location.

The breakdown of the contribution to the total integrated sensitivity coefficient at various detector locations is shown in Fig. VII.17. As shown, the negative contribution from neutron disappearance reactions tends to increase for those detectors located at back locations, while positive contributions from elastic and inelastic reactions have a reversed trend. This is expected since more absorption by ^{16}O occurs as the thickness of the Li_2O layer in front of the detector location increases.

The profiles for the zone detectors have shapes similar to those for the point detectors except that they are positive at all energies (except at the 14 MeV peak). The positive contribution from the elastic and inelastic reactions occurring in a spreaded zone (10 cm thick) dominates the negative contribution from absorption reactions, a trend that is reversed at low energies for the inner detector locations for which the profiles are negative below the cutoff energy E_c . Thus, the integrated sensitivity coefficients for the zonal detectors are slightly larger than those for point detectors.

As was observed in the ^6Li and ^7Li cases, the sensitivity profile in the reference system for the P_1 detector is large at low energies due to the soft component of the incident neutrons, as shown in Fig. VII.18, where the profile is positive at all energies (except at the resonance of ^6Li and below $E_c=0.01$ eV).

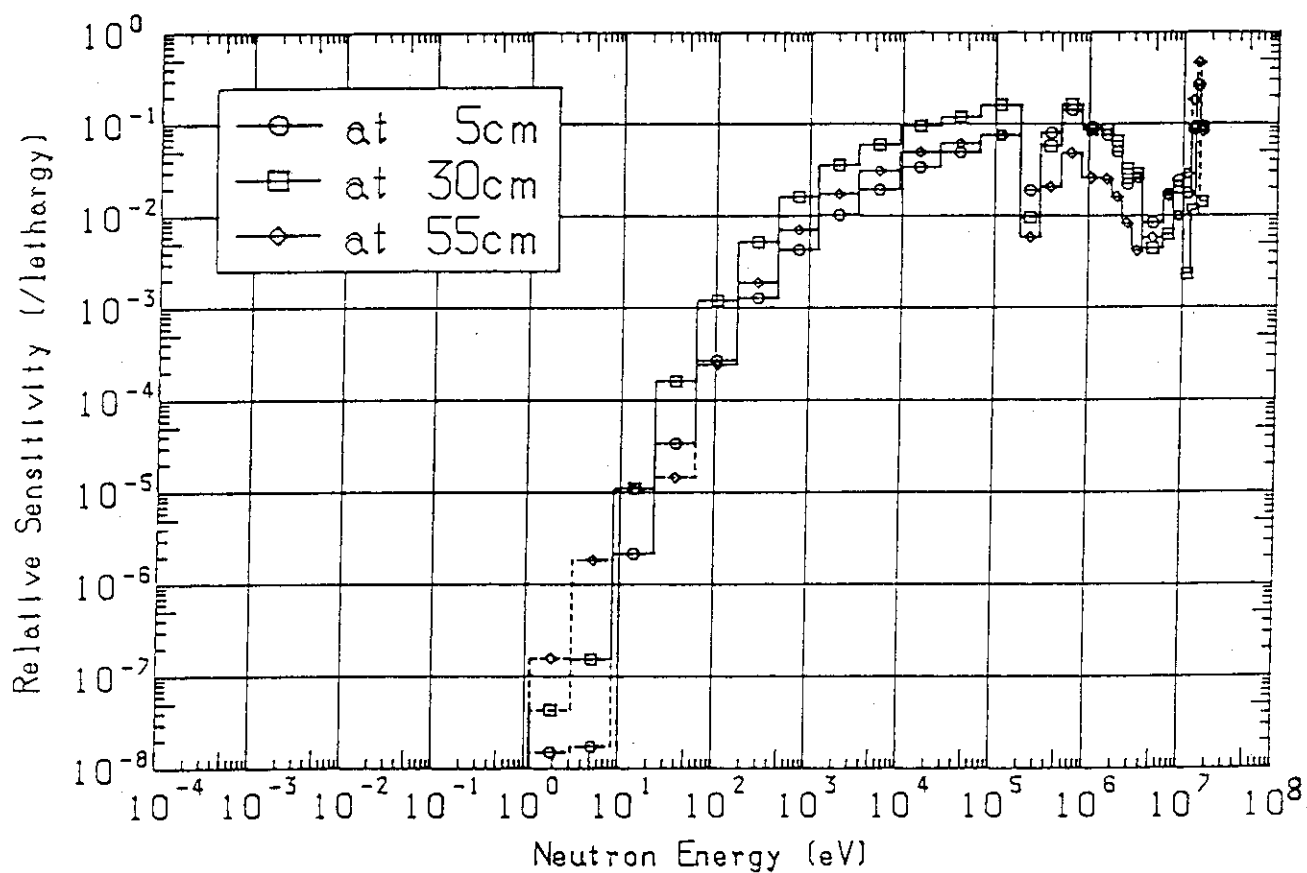


Figure VII.16 The sensitivity profiles $P(T_6, P_i, \Sigma_t)_B$ [$i = 1-3$] due to a 1% increase in Σ_t of ^{16}O in the benchmark system. Point detectors P_1 , P_2 , and P_3 at $Z = 0.5$, 5, 30, and 55 are considered.

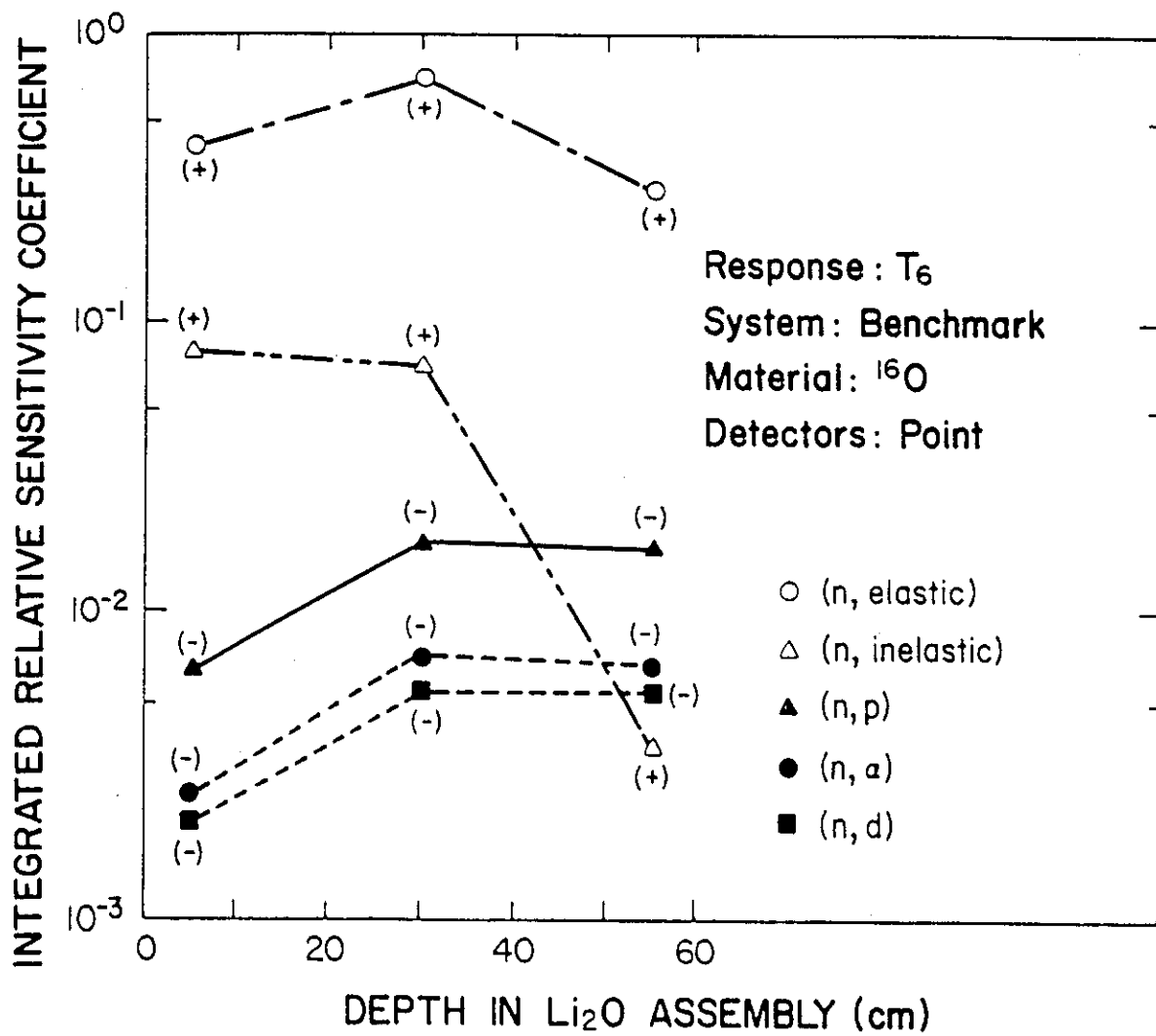


Figure VII.17

The integrated relative sensitivity coefficients for T_6 in the benchmark system due to variations in various partial cross-sections of oxygen. Point detectors are considered

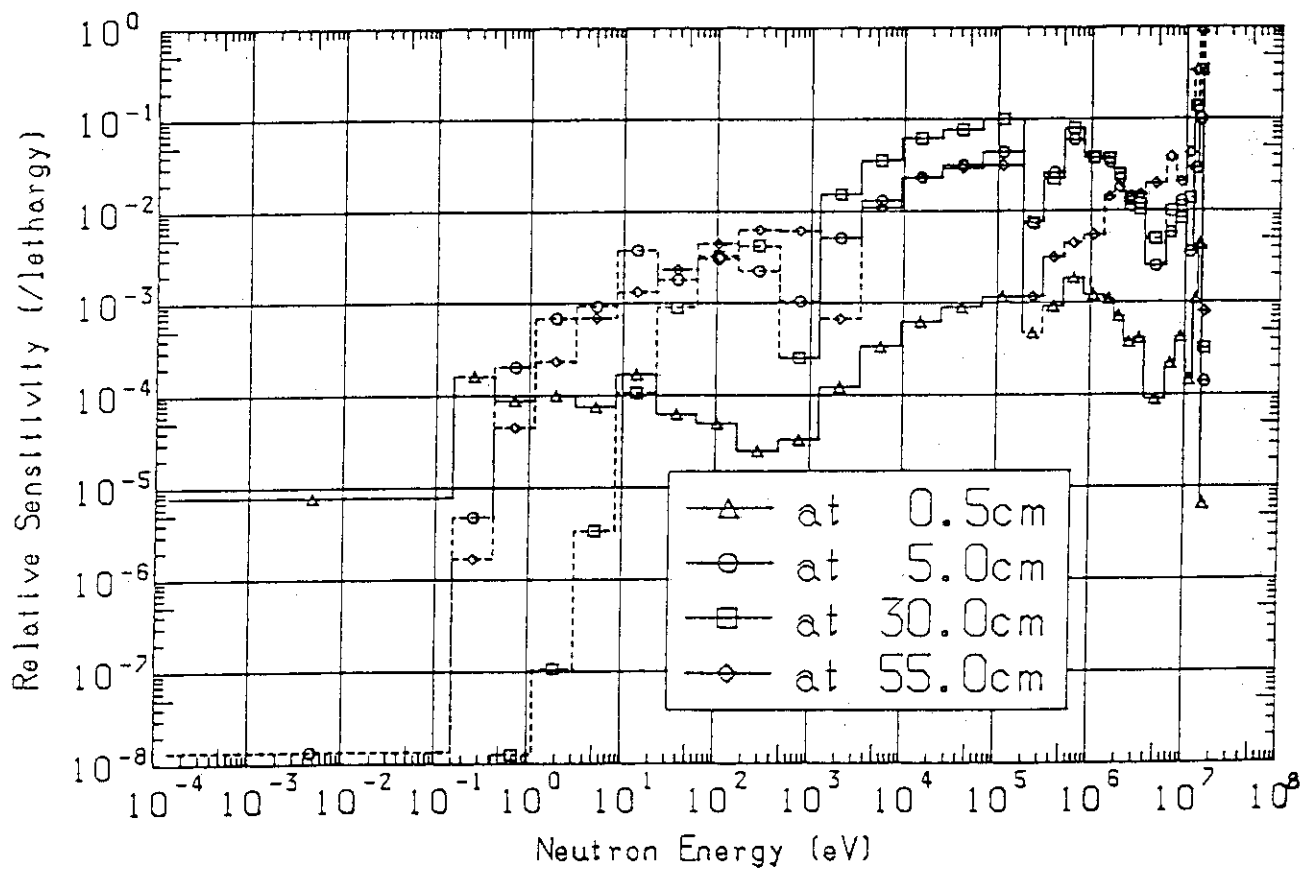


Figure VII.18 The sensitivity profiles $P(T_6, P_i, \Sigma_t)R$ [$i = 1, 3, 4, 5$] due to a 1% increase in Σ_t of oxygen in the reference system. Point detectors P_1, P_3, P_4 , and P_5 at $Z = 0.5, 5, 30$, and 55 are considered

However, below the cutoff energies $E_c = 1$ KeV, 1 KeV, and 3 KeV for P_3 , P_4 , and P_5 detectors, the profiles have negative values, which is due to the increase in the absorption by ^{16}O at low energies from reactions such as (n,γ) , (n,p) , (n,α) , and (n,d) . The profiles for the zone detectors show different trends than for the zone detectors of the benchmark system. Shown in Fig. VII.19 is the profile $P(T_6, Z_3, \Sigma_t)_R$. As shown, the profile for the zone detector Z_3 is negative at all energies, demonstrating that the negative contribution to the sensitivity profile from absorption reactions dominates the contribution from scattering reactions that serve as a gain term to the sensitivity profile. Moreover, the profile shown in Fig. VII.18 for the point detector P_5 ($Z=55$ cm) has a different shape and is positive only in the energy range 2 KeV-300 KeV. It is true that ^{16}O has a large absorption cross-section for (n,α) , (n,p) and (n,d) reactions. For the zone detector Z_3 , these reactions tend to remove those slow neutrons produced by elastic and inelastic collision at higher energies before reaching the detector location, resulting in a negative profile at all energies, as shown in Fig. VII.19.

VII.6.1.4 Variation in Σ_t of Iron

Iron is present in the Li_2O assembly with lower atomic density in comparison to ^6Li , ^7Li and ^{16}O . Consequently, the sensitivity profiles obtained are in general lower than those of other materials. In the benchmark system, the profiles for all the detectors considered have shapes similar to the ones found for ^{16}O , i.e., a dominant peak at 14 MeV, positive at all energies except around 250 KeV (^6Li resonance) and below the cutoff energy E_c , and resemblance in shape to the incident neutron source. The reasoning for these features was discussed above. The profiles for the zone detectors Z_i ($i=1-3$) very closely resemble those found for the point detectors. The integrated relative sensitivity coefficients are positive at all locations, as shown in Fig. VII.9. However, their values are much less (by more than one order of magnitude) than the coefficients calculated for ^7Li (same as for the ratio of atomic densities).

In the reference system, the sensitivity profiles at all detectors considered have features similar to those found for ^7Li and ^{16}O , i.e., larger values at low energies due to the appreciable low-energy component of the incident D-T neutrons in comparison to the benchmark system. The integrated relative sensitivity coefficients are much smaller than in the benchmark system, as shown in Fig. VII.9. In contrast to the benchmark system, the coefficient at P_5 is negative since the sensitivity profile has negative values at almost all energies.

VII.6.1.5 Variation in Σ_t of Other Materials

Although the Li_2O assembly includes other materials such as Mn, Cr, and Ni, the sensitivity coefficients were found to be small because of the low atomic densities for these materials. Therefore, discussions regarding their sensitivity profiles are excluded in the present work.

In Table VII.3, the integrated relative sensitivity coefficients of T_6 at the middle point detector (P_2 in benchmark; P_4 in reference system) are given for the total and partial cross-sections of ^6Li , ^7Li ,

Table VII.3 Integrated Relative Sensitivity Coefficients of T_6 at the Middle Point of the Li_2O Assembly

Cross-Section Perturbed	^6Li		^7Li		^{16}O		^{56}Fe	
	Benchmark	Reference	Benchmark	Reference	Benchmark	Reference	Benchmark	Reference
elastic	4.278-2 ^a	2.241-2	6.479-1	3.321-1	7.159-1	3.738-1	3.050-2	1.399-2
inelastic	1.628-2	8.320-3	1.905-1	9.286-2	7.167-2	4.461-2	1.397-2	7.587-3
(n,2n)	1.105-2	7.212-3	7.325-3 ^b	4.925-3 ^b			1.417-2	8.838-3
(n,3n) α			2.542-2	1.619-2				
(n,n') α							3.584-5	9.886-6
(n,n')P							3.693-4	1.419-4
(n,cont)							6.824-3	4.020-3
(n, γ)	-2.155-5	-2.661-5	-3.104-5	-3.799-5	-6.185-7	-8.257-7	-1.683-3	-1.994-2
(n,P)	-1.136-3	-9.359-4			-1.744-2	-2.063-2	-2.506-3	-1.314-3
(n,d)			-7.451-3	-5.372-3	-5.569-3	-6.622-3	-9.720-5	-7.974-5
(n,t)	-5.931-1	-7.050-1					-2.647-7	-8.735-8
	(4.069-1) ^c	(2.950-1) ^c						
(n, ^3He)							-2.677-8	-9.065-9
(n, α)					-7.001-2	-8.390-2	-7.091-4	-6.411-4
(n, absorption)	-5.942-1	-7.060-1	-7.762-3	-5.752-3	-9.302-2	-1.112-1	-4.996-3	-5.029-3
TOTAL	-5.241-1	-6.676-1	9.192-1	4.811-1	6.962-1	3.103-1	5.504-2	1.578-2
	(4.759-1) ^c	(3.324-1) ^c						

a) Reads as 4.278×10^{-2} b) (n,2n) α

c) Sensitivity including direct effect

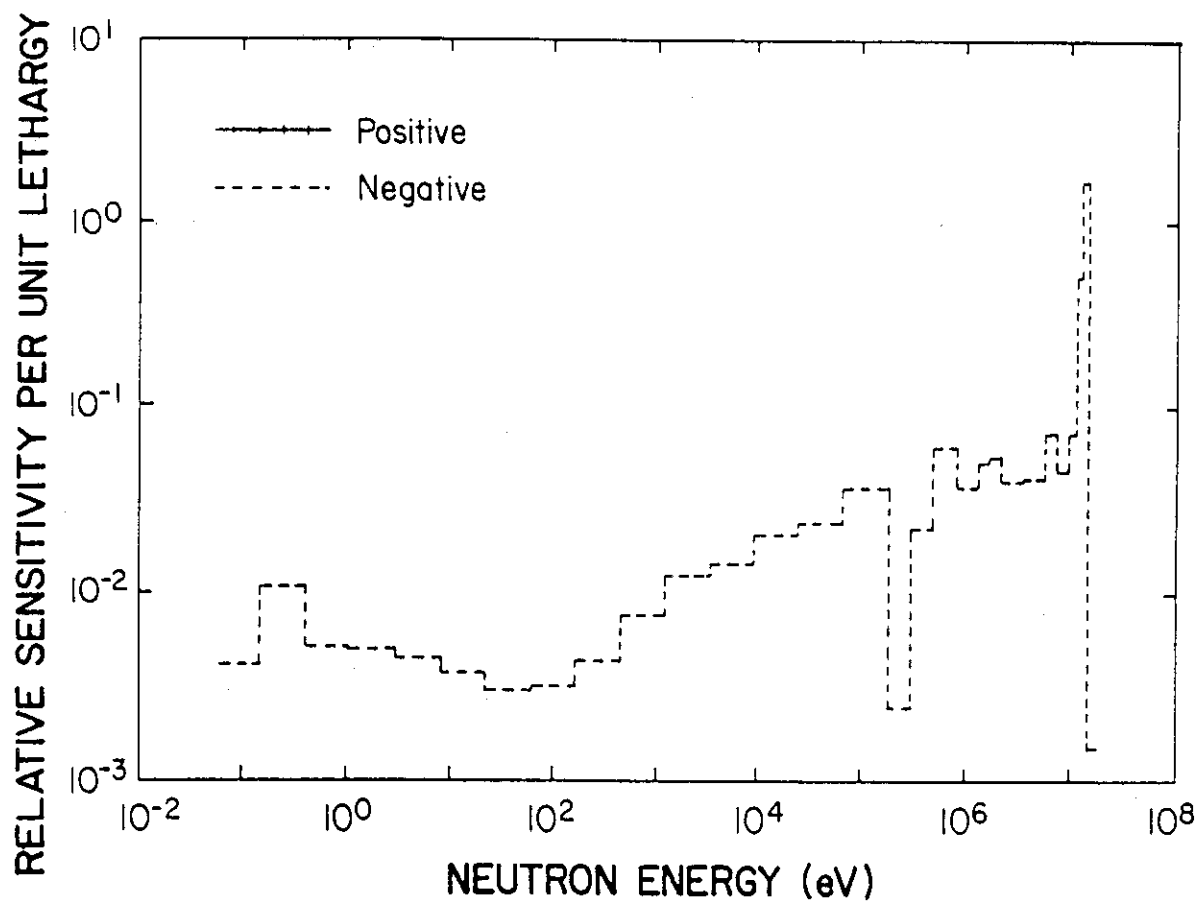


Figure VII.19 The sensitivity profile $P(T_6, Z_3, \Sigma_t)_R$ due to a 1% increase in Σ_t of oxygen in the reference system. Zone detector Z_3 is considered

^{16}O and Fe. As shown, the largest coefficient is for ^7Li in the benchmark system, where a 1% increase in Σ_t of ^7Li in the whole assembly leads to a 0.919% increase in T_6 at this location. Note that the coefficients are larger by a factor of two in the benchmark system than those found for the reference system, except for ^6Li , where it is larger by a factor of ~ 1.5 .

VII.6.2 Sensitivity Profiles of T_7

Tritium production from ^7Li , T_7 , has a threshold energy around 3 MeV. Accordingly, all the sensitivity profiles $P(T_7, P_i, \Sigma_x)_B$ and $P(T_7, P_i, \Sigma_x)_R$ in the benchmark and reference systems have zero values below this threshold energy, for all the point detector locations shown in Table VII.2. Furthermore, variation in a cross-section type, Σ_x , having a value above this threshold energy leads to negative sensitivity profiles for all the elements considered (except for ^7Li , see below). Neutron interactions with these materials, such as elastic and inelastic scattering, $(n,2n)$, $(n,3n)$, lead to neutrons with energies below the $^7\text{Li}(n,n'\alpha)t$ threshold energy and thus reduce the chance for the $^7\text{Li}(n,n'\alpha)t$ reactions.

Examples of the T_7 profiles are shown in Fig. VII.20 for the benchmark system for variation in the Σ_t of ^{16}O , at the point detector P_2 . The profile for ^{16}O in the reference system is very similar. This is due to the fact that, in contrast to T_6 , the T_7 is sensitive to the high-energy component of the incident neutron source above the threshold energy for $^7\text{Li}(n,n'\alpha)t$ reactions (~ 3 MeV), and this component, in a relative sense, is similar for the two incident spectra, shown in Fig. VII.6 and VII.7. Thus, the difference in the low energy component of the two incident spectra has practically no impact on T_7 (except for the difference arising from the $1/r$ effect discussed in Subsection VII.5). Moreover, the shape shown in Fig. VII.20 closely resembles the $^7\text{Li}(n,n'\alpha)t$ cross-section curve in shape. The profiles obtained for all materials considered and at all detectors in both systems are more or less similar in shape to the profile shown in Fig. VII.20. Note, in particular, the peak around 14 MeV that is dominant in all the profiles considered.

Figure VII.21 shows the integrated relative sensitivity coefficients as a function of the point detector locations in the benchmark system due to variation in Σ_t of various materials. Aside from the ^7Li case discussed below, the coefficients are all negative at all the detector locations. The coefficients get larger as one proceeds toward the back end of the Li_2O assembly for every material shown. In addition, the contribution from variation in the Σ_t of ^{16}O leads to the largest negative coefficient among the other materials. As discussed earlier, the deeper the location of the detector, the greater the chance that neutrons are absorbed and do not contribute to T_7 at the detector location. This is also shown in Fig. VII.22, where the integrated sensitivity coefficient for each partial cross-section of ^{16}O is shown as a function of detector location. All the reaction types shown have negative coefficients which become larger at deeper locations.

As for the variation in Σ_t of ^7Li , the sensitivity profiles are positive at all energies at the detector locations P_1 and P_2 for both systems and have a shape similar to that shown in Fig. VII.20. The direct

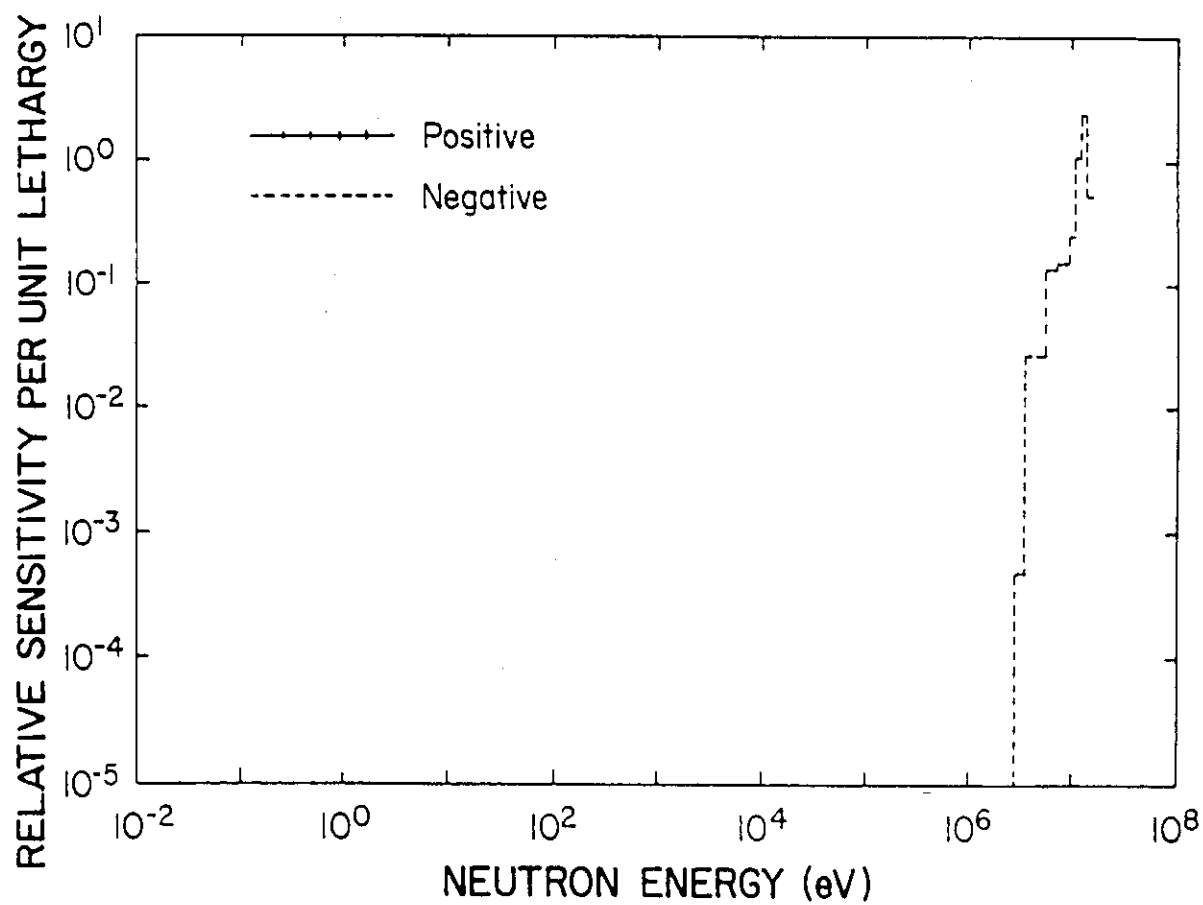


Figure VII.20 The sensitivity profile $P(T_7, P_2, \Sigma_t)_B$ due to a 1% increase in Σ_t of oxygen in the benchmark system. Point detector P_2 is considered

INTEGRATED RELATIVE SENSITIVITY COEFFICIENT

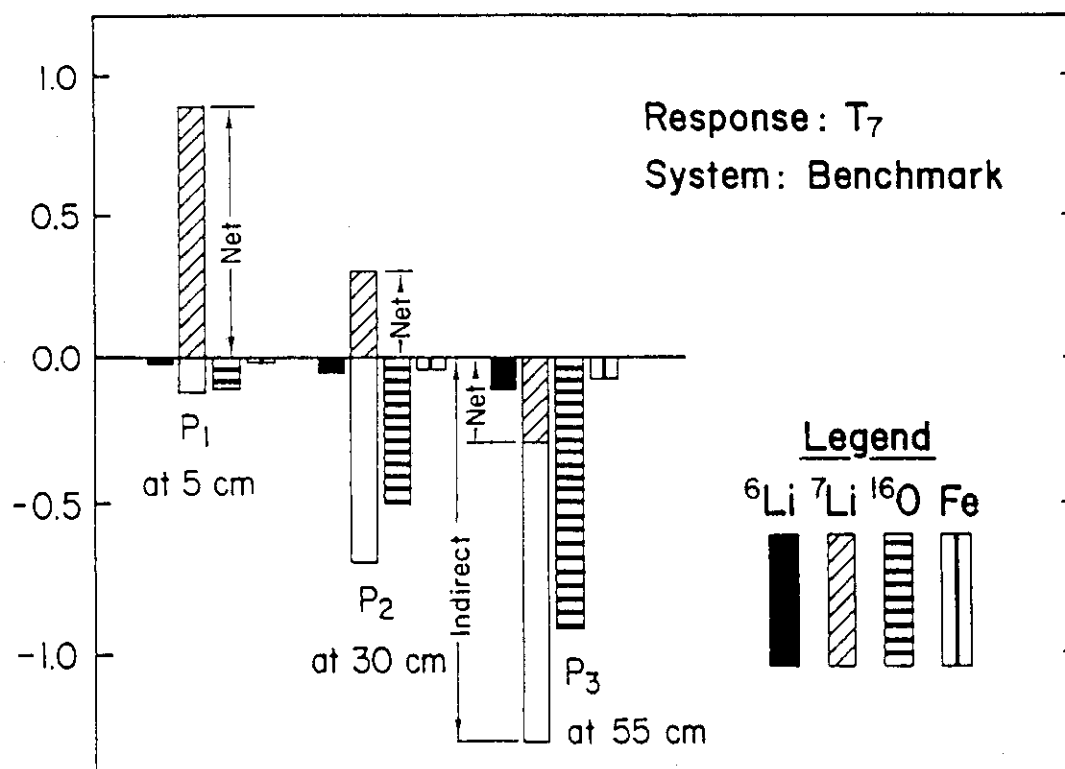


Figure VII.21 The integrated relative sensitivity coefficients for T_7 in the benchmark system due to variations in the Σ_t of various elements. Point detectors are considered

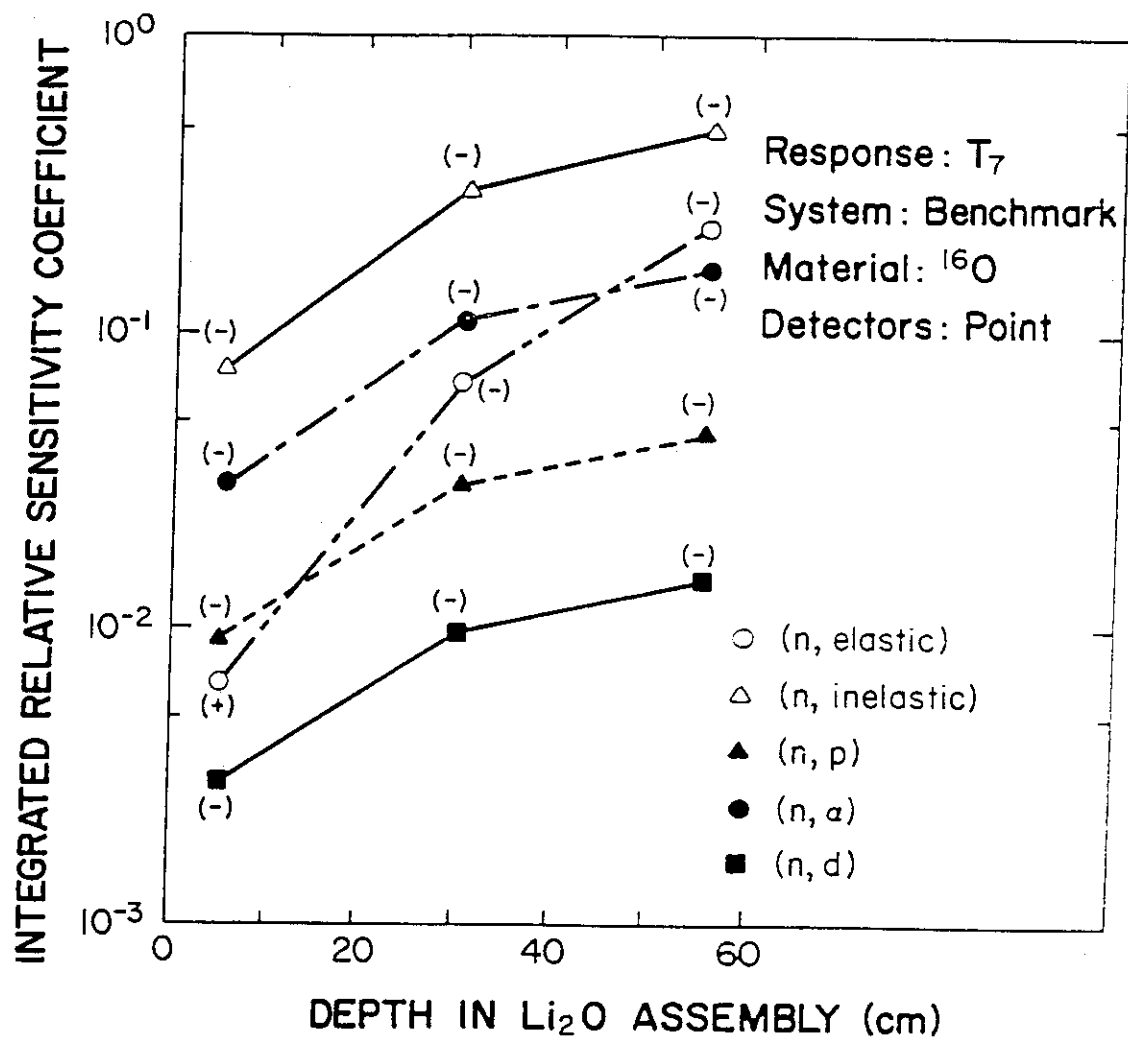


Figure VII.22 The integrated relative sensitivity coefficients for T_7 in the benchmark system due to variations in various partial cross-sections of oxygen. Point detectors are considered

part of the sensitivity profile, which is always positive, dominates the negative contribution from the other indirect effect. However, for P₃ detectors in both systems, the profile around 14 MeV has negative values, where the negative indirect part [e.g., from (n, elastic), and (n,d) reactions] has a larger contribution than the positive direct part. Accordingly, the net integrated relative sensitivity coefficient is negative at this detector location, as shown in Fig. VII.21. Note from the figure that variation in Σ_t of ⁷Li on T₇ has a greater impact as one moves toward the back end of the assembly and that T₇ is most sensitive to variations in ⁷Li cross-sections. The relative values of the integrated coefficients shown in Fig. 22 are almost the same in both the benchmark and reference systems for the reasons discussed earlier.

The integrated relative sensitivity coefficients of T₇ at the middle of the Li₂O assembly are given in Table VII.4 for variations in the cross-section of various elements. As shown, the coefficients are negative for all reaction types and for all elements. However, the net coefficients for variation in the Σ_t or (n, inelastic) cross-sections of ⁷Li are positive. Note also that the coefficients shown are comparable in both the benchmark and reference systems. This is in contrast to the coefficients shown in Table VII.3 for T₆.

VII.7 Uncertainty Analysis Results

The uncertainty in the TPR, both from ⁶Li and ⁷Li, is best quantified by evaluating the relative standard deviation (RSD) in T₆ and T₇ at the detector locations under consideration as:

$$\text{RSD in } R_k = \left[\sum_m (\Delta R_k / R_k)_m^2 \right]^{1/2}$$

where m denotes each material present in the assembly and the variance $(\Delta R_k / R_k)^2$ is derived by coupling the sensitivity profiles with the uncertainty correlation matrices and the standard deviations of the cross-sections in the manner given by Eq. VII.1. In the following, estimates for the uncertainty in T₆ and T₇ are given for both the benchmark and reference systems at various point detector locations.

VII.7.1 Uncertainty in T₆

The contribution to the RSD in T₆ from each material present in the benchmark and reference systems is shown in Fig. VII.23 as a function of point detector location. In the benchmark system, the RSD attributed to the uncertainties in ⁶Li cross-sections at 5-cm depth (P1) is about 2.87%, twice the values attributed to ⁷Li and ¹⁶O. As shown in Fig. VII.8, the sensitivity profile at this location due to variation in Σ_t of ⁶Li has large values, particularly at the high energy range where the uncertainty in the ⁶Li(n,α)t cross-section has a relatively large RSD. The combined effect of having large sensitivity profiles and large RSD in a cross-section yields the somewhat large contribution to the RSD in T₆ from

Table VII.4 Integrated Relative Sensitivity Coefficients of T_7 at the Middle Point of the Li_2O Assembly

Cross-Section Perturbed	^6Li		^7Li		^{16}O		Fe	
	Benchmark	Reference	Benchmark	Reference	Benchmark	Reference	Benchmark	Reference
Elastic	-1.064-2 ^a	-1.279-2	-1.760-1	-2.140-1	-6.706-2	-9.240-2	-1.465-3	-1.703-3
Inelastic	-4.079-2	-4.309-2	-4.602-1	-4.916-1	-3.024-1	-3.347-1	-2.784-2	-2.962-2
(n,2n)	-8.262-3	-8.433-3	(5.398-1) ^b	(5.084-1) ^b			-1.073-2	-9.937-3
(n,3n) α			-5.772-3 ^c	-6.163-3 ^c				
(n,n') α			-1.848-2	-1.906-2				
(n,n')p							-8.974-5	-5.128-5
(n,cont)							-9.977-4	-7.736-4
(n, γ)	-1.356-6	-1.378-6	-1.652-6	-1.678-6	-7.321-9	-8.125-9	-2.376-2	-2.527-2
(n,p)	-1.106-3	-1.141-3			-3.020-2	-3.424-2	-2.820-5	-2.777-5
(n,d)			-1.262-2	-1.219-2	-9.645-3	-1.103-2	-4.128-3	-4.201-3
(n,t)	-4.272-3	-4.399-3					-1.683-4	-1.551-4
(n, ^3He)							-4.011-7	-1.614-7
(n, α)							-4.071-8	-1.687-8
(n, absorption)	-5.380-3	-5.542-3	-1.264-2	-1.221-2	-1.090-1	-1.233-1	-1.247-3	-1.255-3
					-1.488-1	-1.686-1	-5.572-3	-5.639-3
TOTAL	-6.420-2	-6.869-2	-6.984-1	-7.616-1	-5.141-1	-5.906-1	-4.662-2	-4.756-2
			(3.016-1) ^b	(2.384-1) ^b				

a) Reads as 1.064×10^{-2}

b) Sensitivity including direct effect

c) Includes (n,2n) α

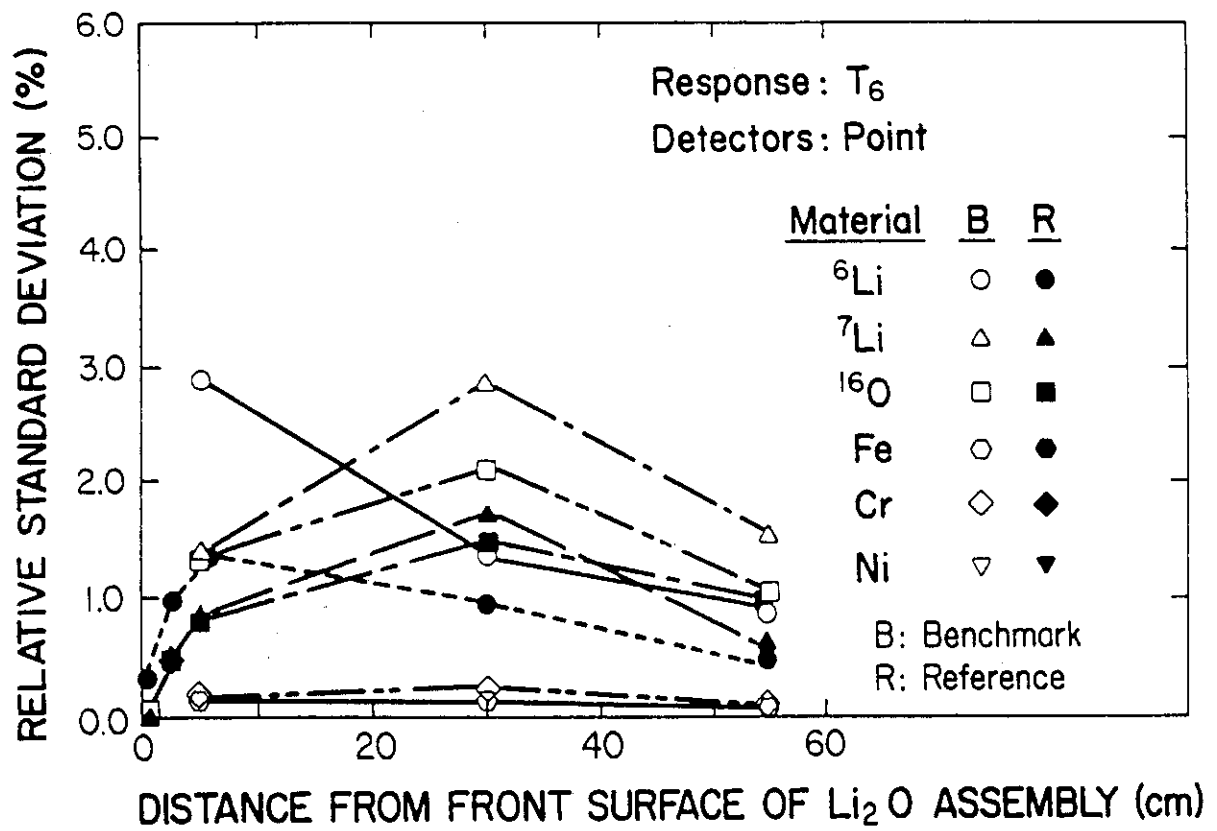


Figure VII.23 The relative standard deviation in T_6 in the benchmark and reference systems due to uncertainties in the cross-sections of various materials. Point detectors are considered

^6Li cross-section uncertainties. Also, although the sensitivity analysis showed that the sensitivity coefficient for variation in Σ_t of ^7Li is larger than that for ^{16}O by a factor of 1.5, the uncertainty analysis showed that the contribution from the uncertainties in ^7Li and ^{16}O cross-sections is almost the same at this detector location. This is due to the fact that the uncertainties in the (n,inelastic), (n,p) and (n, α) cross-sections of ^{16}O are large. Also, as shown in Fig. VII.23, the RSD's in T_6 from the uncertainties in other material cross-sections are small compared to the principal elements (^7Li , ^6Li , and ^{16}O) at all the detector locations considered.

At the middle detector location (P_2), the RSD in T_6 due to the uncertainties in ^7Li data is $\sim 2.85\%$, which is the largest value. This is also the case for the detector location P_3 . The uncertainties in ^{16}O cross-sections give larger RSD's in T_6 ($\sim 2.12\%$) than those for ^6Li , which yields a RSD in T_6 of 1.4%. The low value obtained in the ^6Li case is due to the rapid decrease in the value of the high-energy part of the sensitivity profile as one moves toward the back locations. Also, the ratio of the RSD in T_6 due to the uncertainties in ^7Li and ^{16}O cross-sections is almost the same as the ratio of their relative sensitivity coefficients (see Table VII.3). At the deeper detector location (P_3 at 55-cm depth), all the RSD's in T_6 show smaller values than those at the detector location P_2 . The decrease in the RSD's of T_6 is proportional to the decrease in the corresponding sensitivity coefficients.

In the reference system, a similar trend for the RSD's of T_6 is found, also shown in Fig. VII.23, except that the uncertainties in the ^{16}O cross-sections give the largest RSD's in T_6 at the detector located at 55-cm depth. This is due to the large uncertainties in the (n,p), (n,d) and (n, α) cross-sections, whose sensitivity profiles are large at deep locations. As for the detector locations at 0.5 cm and 1.5 cm depth, the RSD's in T_6 due to the uncertainties in the ^6Li , ^7Li , and ^{16}O cross-sections show a fast increase near the front locations. The low value obtained at 0.5-cm depth ($\sim 0.31\%$) due to the uncertainties in ^6Li cross-sections, although the sensitivity coefficient is rather large, can be explained by the fact that the sensitivity profile shown in Fig. VII.11 has large values in the low-energy range, particularly at the thermal energy, due to the large fraction of room-return neutrons. However, the RSD in the ^6Li cross-sections at this energy range is less than 0.5%, which leads to a low RSD in T_6 . The steep increase in the RSD of T_6 at the P_2 and P_3 detector locations is due to the shift in sensitivity region, where the values are large, toward the higher energy side (see Fig. VII.11), where the RSD's in the ^6Li cross-sections gradually increase in addition to the increase in the sensitivity coefficient itself as shown in Fig. VII.9, where the highest value is encountered at the detector location at 5-cm depth. The increase in the RSD of T_6 due to uncertainties in the ^7Li and ^{16}O cross-sections is due simply to the increase in the integrated relative sensitivity coefficients (also shown in Fig. VII.9), where the largest coefficients are found at the detector location at 30-cm depth. In general, the RSD's in T_6 for the reference system are lower than those for the benchmark system.

The total RSD's in T_6 that result from the summation of contributions from each material are shown in Fig. VII.24 as a function of the detector location. The values of these RSD's are 3.5, 3.8, and

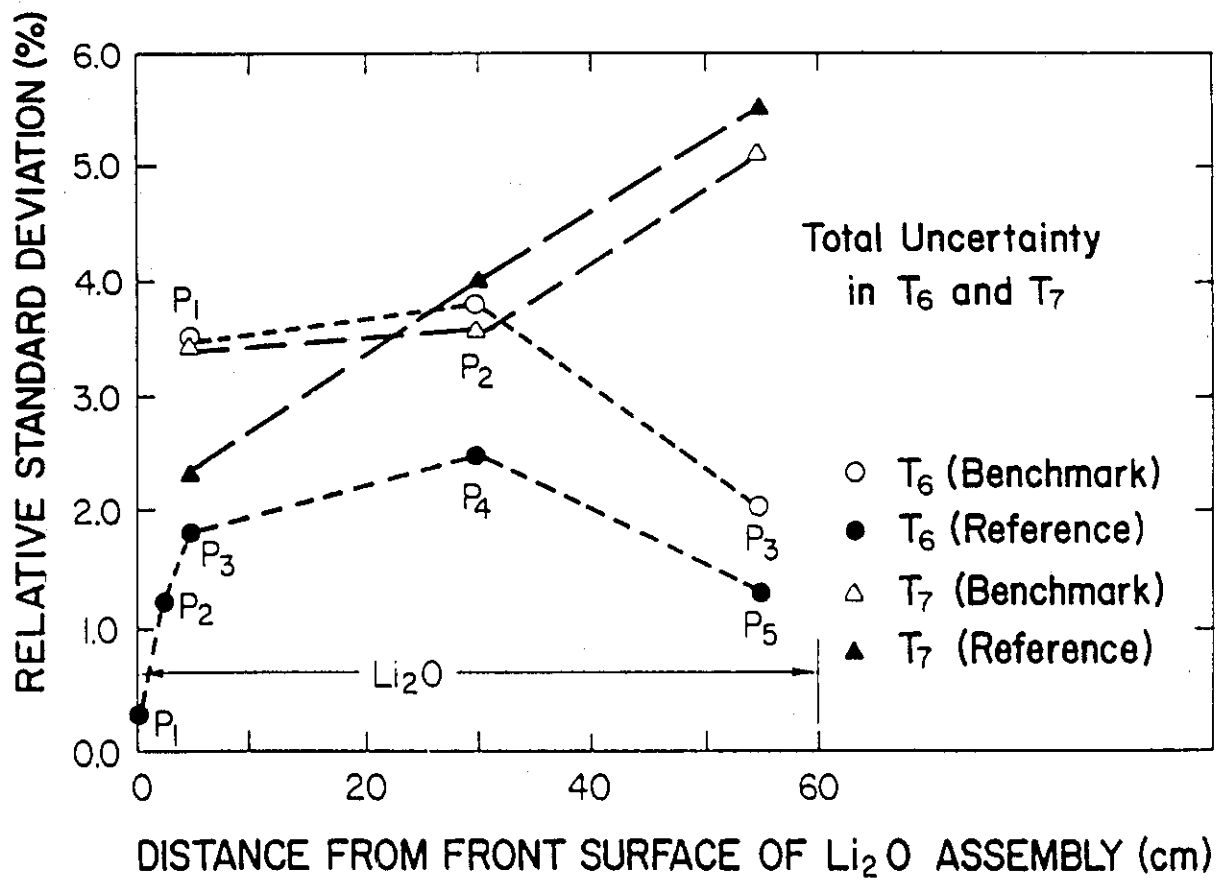


Figure VII.24 The total uncertainty in T_6 and T_7 in the benchmark and reference systems.
Point detectors are considered

2.0% for detectors P_1 , P_2 , and P_3 , respectively, in the benchmark system, while they are 0.31, 1.23, 1.79, 2.47, and 1.28% for the detectors P_1 through P_5 , respectively in the reference system. It is worthwhile to note that more than 99% of the RSD in T_6 is attributed to the uncertainties in the ${}^6\text{Li}$, ${}^7\text{Li}$ and ${}^{16}\text{O}$ cross-sections at the detector locations considered in both systems. Moreover, the uncertainties in T_6 are more pronounced in the benchmark system than in the reference system. This observation was found to be true in the study cited in Ref. (3) where it was shown that the uncertainties in the nuclear data base have more impact on T_6 values in open geometries (such as the benchmark system) with hard incident neutron spectra than in closed geometries (such as the reference system) having a large portion of low-energy neutrons in the incident spectra.

VII.7.2 Uncertainties in T_7

The RSD's in T_7 arising from the uncertainties in the cross-sections of the various materials as a function of the point detector positions are shown in Fig. VII.25. Uncertainties in ${}^7\text{Li}$ cross-sections give the largest RSD's in T_7 at the front detector location (P_1) in both the benchmark and reference systems (3.3% and 2.0%, respectively). The larger value encountered in the benchmark system (by a factor of 1.65) is due to a larger sensitivity profile at the first neutron group in which the inelastic cross-section (basically ${}^7\text{Li}(n,n'\alpha)t$ cross-section) dominates other partial cross-sections. At this energy group, the sensitivity profile has a 20% contribution to the total integrated sensitivity coefficient in the benchmark system, while the corresponding contribution in the reference system is 0.1%. This is related to the incident spectra shown in Figs. VII.6 and VII.7, where the first group spectrum is much lower in the reference system. In addition, from the uncertainty information processed by the PUFF-2 code, it was found that the RSD in the inelastic cross-section for ${}^7\text{Li}$ is ~15% in this first group (above 15 MeV), while the RSD's at lower energies are ~4%. At deeper detector locations, however, the RSD's in T_7 due to uncertainties in the ${}^7\text{Li}$ cross-sections are lower (~1.5%) and have the same magnitude in both systems. The decrease in the RSD of T_7 itself is due to the decrease in the sensitivity coefficient as shown in Fig. VII.21 (note that, regardless of the sign, the absolute value for the coefficient is the same for the 30-cm and the 55-cm depth detectors).

As for other materials, the RSD in T_7 increases as the detector location moves toward the back of the assembly. This is due to the increase in the absolute values in the integrated coefficients as shown in Fig. VII.21. In particular, the RSD in T_7 due to the uncertainties in the ${}^{16}\text{O}$ cross-sections shows a noticeable increase, and it has the largest values as compared to contributions from other elements. For that element and at 30-cm and 55-cm depths, the RSD in T_7 is 3.24% and 4.79%, respectively, in the benchmark system. In the reference system, the values are comparable (3.72% and 5.31%, respectively). These relatively larger values are attributed to the increase with depth in the sensitivity coefficients of the (n,p) and (n, α) reactions (see Fig. VII.22) whose cross-sections have a rather large RSD at high energies. The impact of the uncertainties in the cross-sections of other materials is rather small due to their small sensitivity coefficients.

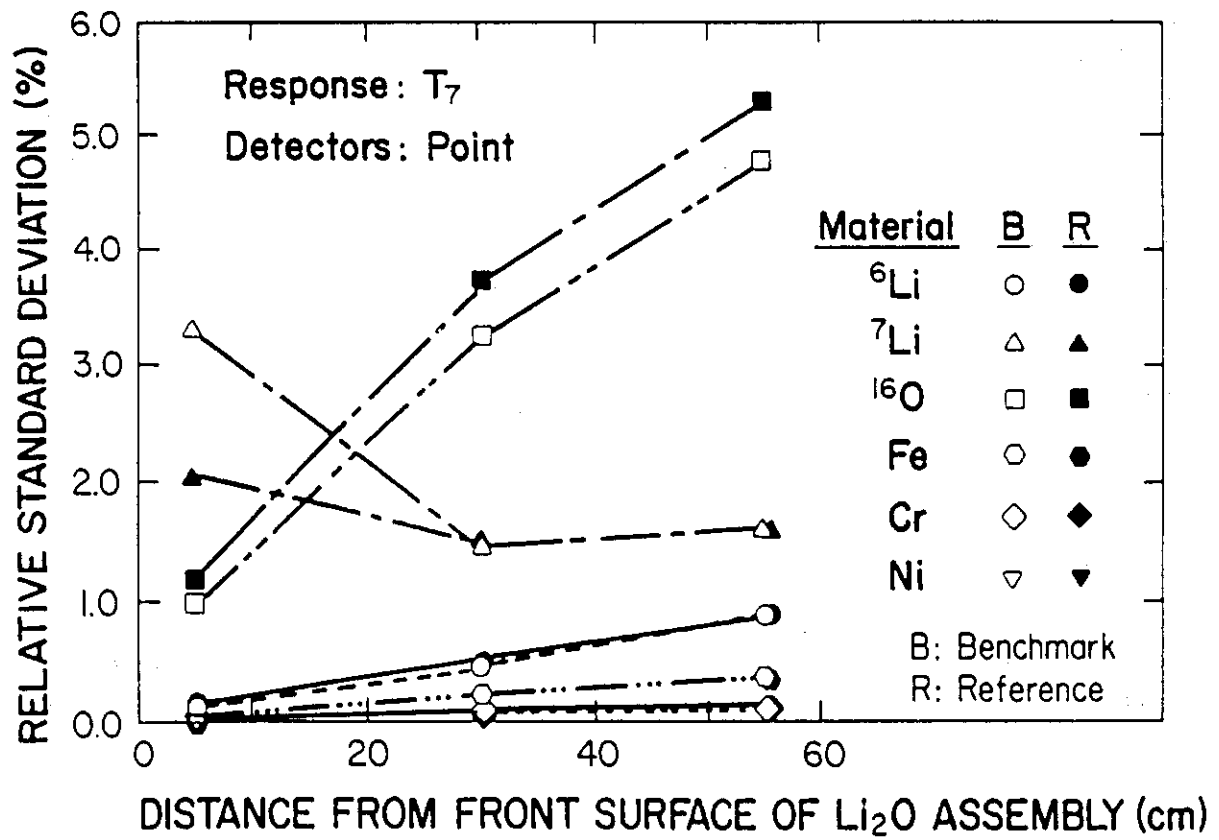


Figure VII.25 The relative standard deviation in T_7 in the benchmark and the reference systems due to uncertainties in the cross-sections of various materials. Point detectors are considered

The total RSD in T_7 at various detector locations varies from 3.5% to 5.5% as shown in Fig. VII.24. The contribution from the uncertainties in the cross-sections of ^7Li and ^{16}O amounts to ~96% of the total RSD in T_7 at all detector locations. In particular, at the back location, the contribution from the uncertainties in the ^{16}O cross-sections is about 86% in both systems. Two major observations can be made from Fig. VII.24. First, in contrast to the divergence in the RSD in T_6 found in the benchmark and reference systems, this divergence is less pronounced for T_7 . This is because T_7 has a threshold energy and, thus, less sensitivity to the difference in the low-energy component of the incident neutron spectrum of the two systems, while the T_6 is sensitive to that component and to the neutrons reflected by the surrounding structure (e.g., concrete wall). Secondly, the RSD in T_7 increases with depth in the assembly, while the RSD in T_6 has its largest values at middle locations. This is due to the increase in the integrated sensitivity coefficients of T_7 with depth since more neutron absorption events take place, while for T_6 , the change in the in-system spectrum and the neutrons reflected by the surrounding structure have a dominant role at the middle locations.

VII.8 Summary and Conclusions

The comprehensive two-dimensional cross-section sensitivity and uncertainty analysis carried out aimed at estimating the range of uncertainty in predicting both tritium production from $^6\text{Li}(T_6)$ and $^7\text{Li}(T_7)$ due to the current uncertainties in cross-section data as presently implemented in ENDF/B-V, file 33. The analysis was performed for two systems, namely, the benchmark system (open geometry and hard incident neutron spectrum) and the reference system. Several point detectors (responses) were considered at various locations along the central axis of the Li_2O assembly for both T_6 and T_7 . These positions simulate those chosen for the tritium production measurements in the two systems. An analysis for zonal detectors was also carried out for comparison.

The uncertainties estimated for T_6 were found to be 2.0-3.6% and 0.3-2.5% in the benchmark and reference systems, respectively, with the largest uncertainties occurring at the middle locations of the assembly. The uncertainty in T_6 was mainly attributed to the current uncertainties in ^6Li data at those locations near the front surface, while the uncertainties in the ^7Li and oxygen cross-sections are the main contributors to the uncertainty in T_6 at the middle and back locations.

At locations very close to the front surface in the reference system, the uncertainty analysis showed very small uncertainties in T_6 (0.3%), despite the fact that the cross-section sensitivity is large at these locations. The large discrepancies found between the calculated and experimental values at these locations, shown in Fig. VII.1, (C/E 0.8-1.4) are not, therefore, attributed to the uncertainties in the data base. Rather, these discrepancies are attributed to inaccuracies in characterizing the source neutron spectrum (particularly the room-reflected component) and in the self-shielding factor applied, as pointed out in Section IV. At middle locations, the C/E values are 1.1-1.2, as shown in Fig. VII.1, as predicted by the 2-D model applied. Since the experimental errors are on the order of 3-4%, the analysis showed that

the contribution to the uncertainty in predicting T_6 at these locations is 2.5% in the reference system and it is clear that there are other sources contributing to the rather large values of C/E shown in Fig. VII.1. As discussed in Section IV, these sources could be the neutron group structure effect, the weighting spectrum used to generate the data libraries applied, and the methods used to calculate the neutron fluxes (Monte Carlo vs. discrete ordinates). It seems that these sources have a larger impact on the uncertainty in the prediction of T_6 than those arising from the current uncertainties in data, at least for tritium production from ${}^6\text{Li}$.

As for the uncertainties in T_7 , there is no significant difference between the benchmark and reference systems in the trend of the uncertainty with the depth of the detector location. These uncertainties were found to be 3.5-5.5%, larger than those found for T_6 , with the largest values occurring at the back locations in the assembly. The current uncertainties in the ${}^7\text{Li}(n,n'\alpha)t$, ${}^{16}\text{O}(n,\alpha)$, ${}^{16}\text{O}(n,p)$, and ${}^{16}\text{O}(n,\text{inelastic})$ cross-sections are the main contributors to the uncertainties in T_7 . The present analysis revealed that the uncertainties in the oxygen cross-sections have a large impact on the uncertainty in T_7 , especially at deeper locations in the test assembly, where their contribution amounts to ~90%. Improving the ${}^7\text{Li}(n,n'\alpha)t$ above 15 MeV, and the (n, inelastic), (n,p), and (n, α) cross-sections of ${}^{16}\text{O}$ above several MeV will improve the uncertainty in T_7 .

The C/E values for T_7 for the reference system shown in Fig. VII.2 are 1.05 and 1.18. As was shown in Fig. IV.11, the ${}^7\text{Li}(n,n'\alpha)t$ cross-section of JENDL3-PR1 is underestimated by ~7%. Thus, the C/E value range is 1.12-1.18. With the current estimation of the uncertainty in predicting T_7 of ~6% due to data uncertainties, still other sources exist that contribute to the discrepancy between calculation and measurement. It seems that the flat C/E curves shown in Fig. VII.2 suggests that this discrepancy is systematic and is due mainly to the basic values for the ${}^7\text{Li}(n,n'\alpha)t$ cross-section which needs re-evaluation. This was pointed out in Section V.

VIII. SUMMARY AND CONCLUDING REMARKS

The analyses of Phase I experiments of the JAERI/U.S. Collaborative Program on Fusion Blanket Neutronics have been performed independently by both parties. The predictions of key neutronics parameters were compared to measurements to derive information on the accuracy involved in the calculations of these parameters. First, measurements were performed to characterize the neutron field by the foil activations method and spectrum measurements using both TOF technique as well as NE213 and proton recoil counters. The measurements inside the Li_2O assembly included tritium production rate (TPR), foil activation and neutron spectrum measurements above 1 MeV. Analyses for these measured parameters were performed by using two-dimensional discrete ordinates codes, DOT3.5 (JAERI) and DOT4.3 (U.S.) and Monte Carlo codes, MORSE-DD (JAERI) and MCNP (U.S.). The nuclear data used by JAERI were based on JENDL3/PR1 and PR2 while the U.S. calculations were based on ENDF/B-V and data evaluated at LANL for ^7Li and Be.

The configurations considered for the test assembly were: (a) a reference Li_2O assembly, (b) first wall preceded the Li_2O assembly with and without a coolant channel simulated by polyethylene, and (c) beryllium zone in front of the Li_2O assembly as well as sandwiched between a front Li_2O zone and the main assembly. The summary of the comparisons between measurements and calculations for the neutronics items mentioned above is given below.

Source Characterization

The calculational results for the source characteristics agree satisfactorily with the measurements for both the spectrum and integral quantities. As for the neutron spectrum at the entrance of the experimental hole, good agreement between calculations and measurements was obtained in the energy range 15 MeV - several keV for the cases with and without a shadow shield placed between the D-T neutron source and the experimental hole. However, if the Li_2O assembly exists, the agreement worsens in the energy range, 8 MeV ~ several hundred keV. The magnitude of source neutrons reflected by the room walls was confirmed to be very large below several MeV as expected before starting the experiments.

With respect to the integral quantities, reaction rate distributions for several reactions were compared in horizontal and in vertical directions on the surface of the Li_2O system. The calculation predicts most measurements fairly well, with the exceptions of $^{58}\text{Ni}(n,2n)^{57}\text{Ni}$ and $^{197}\text{Au}(n,\gamma)^{198}\text{Au}$ reactions. The discrepancy in the $\text{Ni}(n,2n)$ reaction is attributed to the improper reaction cross-sections as currently implemented in both ENDF/B-IV and ENDF/B-V data files and the discrepancy in the $\text{Au}(n,\gamma)$ reactions is due to the self-shielding effect introduced by the use of thick foils.

Tritium Production Rate

TPRs have been measured along the central test channel of the Li_2O assembly. We make the following observations based on the comparison between calculations and measurements:

(A) Reference System

1. Both JAERI and U.S. results overestimated T_6 by 5 - 25% in the bulk of the Li_2O assembly and the U.S. predictions is larger by 10-15% than JAERI's calculations. Large discrepancies were found at the front zone for T_6 (by a factor of 0.8-3) due to the uncertainty in predicting and interpolating the low-energy component of the incident neutron.
2. The Monte Carlo results used by both countries give a better agreement in general with the measurements, although the overprediction in the bulk zone still persists.
3. Concerning T_7 , the C/E values depend on the measuring methods adopted. If the Li-metal method is used (which gives higher values by about 10% than the NE213 method), the JAERI results underestimate T_7 by 7-10%. On the other hand, the U.S. results overestimate T_7 by 1 - 8%. When the NE213 method is used, the C/E values are ~1.1-1.2 (U.S.) and ~1-1.05 (JAERI). Thus the divergence in T_7 predictions is ~1-20%.
4. With respect to JENDL-3/PR1 or PR2, the cross-section of ^7Li should be reevaluated to reduce the discrepancy as discussed in chapter V. The $^7\text{Li}(n,n'\alpha)t$ cross-section should be increased while the $^7\text{Li}(n,\text{elastic})$ cross-section should be decreased in JENDL-3 evaluations. The over-estimation in $^7\text{Li}(n,\text{elastic})$ cross-section in comparison to Young's values (U.S.) tends to overmoderate neutrons in JAERI's calculation and this leads to a decrease in C/E curves for threshold reactions.
5. The sensitivity/uncertainty analysis indicated that the uncertainty in T_7 due to current uncertainties in cross-sections of all materials present in the ENDF/B-V data is ~6% and is mainly due to uncertainties in the $^7\text{Li}(n, n'\alpha)t$ and $^{16}\text{O}(n,n')$ cross-sections. Direct comparison between ENDF/B-V and JENDL3/PR1 data for oxygen showed that the $^{16}\text{O}(n,n')$ cross-section is overestimated in JENDL3/PR1 by a value as large as 90% at 12.5 MeV in comparison to ENDF/B-V data. The combination of lower values of $^7\text{Li}(n,n'\alpha)$ cross-section and larger values for $^7\text{Li}(n, \text{elastic})$ and $^{16}\text{O}(n, \text{inelastic})$ in JENDL3/PR1 lead to lower T_7 in JAERI's calculations.

(B) First Wall System

1. JAERI's predictions overestimate T_6 by 15% in all cases, while the overestimation in the U.S. calculations is ~20%.
2. JAERI's predictions overestimate T_7 by 2 - 4% in the range $4\text{ cm} < Z < 20\text{ cm}$ inside the Li_2O assembly when the NE213 method is used. The U. S. calculations show an overprediction of ~16% with this measuring method. The observations regarding T_7 in the reference system are also applicable in the FW system.

3. The inclusion of a FW/PE layer in front of the Li_2O assembly tends to improve the C/E curves for T_6 and T_7 (closer values to unity).
4. The relative change in the TPRs due to varying the FW thickness is well reproduced by the calculations.

(C) Beryllium-Sandwiched System

1. The multiplication effect in the Li_2O system in comparison to the reference system is underestimated in JAERI's calculations by a few percent by DOT3.5 and about 10% by MORSE-DD.
2. On the C/E values of TPRs for T_6 , a similar overestimation as in the reference case was observed by both JAERI and the U.S., although the C/E values vary by about 5 - 10%, depending on the measuring methods used. The C/E values for T_6 are almost the same as in the reference system in the bulk of the Li_2O assembly.
3. The trend at the interface between the beryllium and the Li_2O assembly is fairly different between calculations and the measured values. This suggests examining the secondary energy and angular distribution for the emitted neutrons from the $^9\text{Be}(n,2n)$ reactions.
4. The peak of C/E values appears in the middle of the beryllium region.
5. The self-shielding factors were compared among the values obtained by calculations and by experiment. With the exception of one calculation, the calculated values agree fairly well with each other, but differ by 10% or more compared with the experimentally derived values in the front region of the Li_2O system.
6. The multiplication effect on T_7 upon including the Be layer is less than unity as expected and is well predicted over the whole system. The C/E values for T_7 show two different tendencies depending on the measuring techniques used as pointed out earlier. The differences in C/E values between JAERI and the U.S. are similar to the case of the reference system.
7. As for tritium production rate from natural lithium (T_N), the C/E values are almost unity in the range $0 < Z < 35$ cm, but a peak value was also seen in the beryllium region.

Activation Foil Measurements

1. The C/E values for most reaction rates, as calculated by JAERI, have a descending trend with increasing distance from the front surface. This is particularly apparent for threshold reactions such as $^{58}\text{Ni}(n,2n)$ and $^{197}\text{Au}(n,2n)$. This feature is due to the overestimation of neutron moderation by $^7\text{Li}(n,\text{elastic})$ and $^{16}\text{O}(n,\text{inelastic})$ reactions as predicted by JENDL3/PR1 and PR2 data. This trend is not apparent in the U.S. calculations.
2. The $^{58}\text{Ni}(n,2n)^{57}\text{Ni}$ reaction cross-section is underestimated in ENDF/B-IV and V data and the C/E curves for this reaction are below unity. The newly evaluated cross-sections at FNS should give better agreement.

3. JENDL3/PR1 data gives lower C/E values more than JENDL3/PR2 data does in the back locations of the Li_2O assembly. This is due to the improved (and lower values) for the ${}^7\text{Li}(n,\text{elastic})$ cross-section of JENDL3/PR2 above 10 MeV in comparison to JENDL3/PR1 data. However, further improvement is needed in both evaluations of this cross-section below 10 MeV.
4. In the beryllium sandwiched system, trends 1 and 3 mentioned above are less pronounced, compared with the reference case.
5. The non-threshold reaction ${}^{197}\text{Au}(n,\gamma){}^{198}\text{Au}$ is well predicted in the range $5\text{ cm} < Z < 40\text{ cm}$ if sufficiently thin foils were used in measurements. The activation foil measurements provided good integral data to examine the calculation in addition to TPR. However, reaction types whose cross-sections are known to have a high accuracy should be carefully selected.

In-System Spectrum Measurement

Only the in-system spectrum measurements offered the differential data inside the test assembly. The following is a summary of the observations drawn from comparing calculational results to the measured values.

1. In the reference system, the calculated values are slightly lower than the measured values in the energy range, 7 MeV - 3 MeV, except for the spectrum at $Z = 0\text{ cm}$.
2. The prediction for the integrated flux above 10 MeV is in good agreement with measurement. However, the predictions for the integrated flux in the energy range 1 MeV to 10 MeV are lower than measurements in the front half of the Li_2O system.
3. In the beryllium sandwiched system, this underestimation becomes notable in the range 7 MeV - 3 MeV, which could be attributed to the inadequacy in the beryllium cross-sections.
4. In this system, the measured values are larger than the calculated values both above 10 MeV and in the energy range 1 MeV - 10 MeV, hence such a trend is inconsistent with that mentioned above in connection with the reaction rates distributions. One reason for such inconsistency could be introduced by the unfolding method used in determining the spectrum.

From the Phase I experiment and analysis, we can obtain much useful information, as mentioned above. Nevertheless, some discrepancies are left to be resolved in Phase II and in future experiments. As an overall concluding remark, it could be stated that for an important integrated quantity such as the TPR, the prediction accuracy is not satisfactory because the discrepancy in T_6 is $+25\% - 5\%$ and is $\pm 20\%$ in T_7 in the bulk of the Li_2O zone, including experimental uncertainties. In addition, the discrepancies in T_6 at front locations were found to be very large ($C/E = 0.8-5$) in all the experiments performed. These discrepancies are attributed to the large uncertainty involved in estimating and predicting the transport of the low-energy component of the input neutron source that is mainly due to neutrons scattered by the room walls. Possible causes are:

Modeling:

- (1) Modeling the geometrically complicated target and room walls
- (2) Source separation model used in the Monte Carlo calculation

- (3) Isotropic source assumption and cylindrical modeling used in the 2-D calculation which impacted the prediction accuracy of the room-return neutron source
- (4) Sensitivity of the results to the spatial mesh size, especially at front locations.

Data processing:

- (1) Interpolation scheme used to interpolate calculated values to measuring locations near the front surface (e.g., Lagrangian, log-linear) where the T_6 profiles are very steep
- (2) Approximations used to derive the self-shielding correction factors
- (3) Determinations of exact locations of detectors, particularly at zone boundaries (e.g., Be and Li_2O zones) where T_6 profiles are steep
- (4) Determination of accurate atomic densities of the concrete wall constituents.

The analysis also revealed the need to re-evaluate several cross-sections and nuclear data to reduce the observed discrepancies, particularly ${}^7\text{Li}(n,n'\alpha)t$ and ${}^7\text{Li}(n,\text{elastic})$ cross-sections. Also, the current evaluations for the secondary energy and angular distributions of neutrons emitted from the ${}^9\text{Be}(n,2n)$ reactions need improvement since large discrepancies in low-energy reactions such as T_6 , were found inside the beryllium zone and at Be/ Li_2O boundaries. The direct comparison for ${}^7\text{Li}$ neutron cross-sections between ENDF/B-V and JENDL3/PR1 and 2 data was shown to be useful in explaining the differences in the C/E curves obtained by JAERI and the U.S. The differences observed in the present study are mostly consistent with those obtained in the calculational benchmarks performed by both parties and discussed in Ref. 3. Such intercomparison should be carried out for other elements such as oxygen, iron, nickel, etc.

With a prediction accuracy in local tritium production rate from ${}^6\text{Li}$ of 5-25% (excluding front zone) and from ${}^7\text{Li}$ of ~20%, it seems from the experiments performed in Phase I that it is still difficult to predict tritium breeding ratio for demonstration and commercial fusion reactors utilizing Li_2O as the breeding material with a target accuracy of 5%. It is thus required from the experiments planned for Phase II of the program to resolve and reduce the discrepancies found in the prediction of tritium production rate. It will also be most useful to be able to measure tritium production rate in large zones such as the whole central zone of the Li_2O assembly and make comparison to the calculated integral value. Such intercomparison will be more indicative of the uncertainty involved in tritium breeding ratio as opposed to the uncertainties in local values which are normally large. It is planned in Phase II experiments to carry out these measurements and intercomparison in a better simulation of the incident neutron spectrum to the one found in fusion reactors.

References

1. T. Nakamura and M. A. Abdou, "Summary of Recent Results from the JAERI/U.S. Fusion Neutronics Phase I Experiments," Fusion Technol. **10**, 541 (1986).
2. H. Maekawa, et al., "Measured Neutron Parameters for Phase I Experiments at the FNS Facility," Fusion Technol. **10**, 564 (1986).
3. M. Youssef, M. Nakagawa, et al., "U.S./JAERI Computational Benchmarks for Nuclear Data and Codes Intercomparison," Fusion Technol. **10**, 1466 (1986). See also PPG-900, UCLA-ENG-85-37, University of California, Los Angeles, (Dec. 1985).
4. ENDF/B Summary Documentation, BNL-NCS-17541 (ENDF-201), 2nd edition compiled by D. Garber, available from the National Nuclear Data Center, BNL, Upton, NY (1975).
5. K. Shibata, et al., JAERI-M84-198, JAERI, M84-204, and JAERI-M83-221, Japan Atomic Energy Research Institute (1984).
6. S. Chiba, "Proc. Specialist Meeting on Nuclear Data for Fusion Neutronics," JAERI-M 86-029, 32-40 (1986).
7. A. Hasegawa, Private communication.
8. T. Mori, M. Nakagawa and Y. Ishiguro, "PROF-DD, A Code System for Generation of Multi-Group Double-Differential Form Cross-Section Library," JAERI-M 86-124 (1986).
9. W. A. Rhoades and F. R. Mynatt, "The DOT III Two-Dimensional Discrete Ordinates Transport Codes," ORNL-TM-4280 (1973), see also "DOT3.5: Two-Dimensional Discrete Ordinates Radiation Transport Codes," CCC-276, Radiation Shielding Information Center, RSIC.
10. M. Nakagawa and T. Mori, "MORSE-DD, A Monte Carlo Code Using Multigroup Double Differential Form Cross-Sections," JAERI-M84-126, Japan Atomic Energy Research Institute (July 1984).
11. M. B. Emmett, "The MORSE Monte Carlo Radiation Transport Code System," ORNL-4972 (1975).
12. M. Nakagawa, T. Mori and Y. Ishiguro, "Benchmark Test of MORSE-DD Code Using Double Differential Form Cross-Sections," JAERI-M 85-009 (1985).
13. Los Alamos Monte Carlo Group, "MCNP--A General Monte Carlo Code for Neutron and Photon Transport," Version 2B, LA-7396, Los Alamos National Laboratory (1980).
14. R. MacFarlane, et al., "The NJOY Data Processing System," Vol. I and II (ENDF-9203-M), Vol. I, LA-9303-M, Vol II (ENDF-324), Los Alamos National Laboratory (May 1982).
15. C. R. Weisbin, R. W. Roussin, J. J. Wagschal, J. E. White, and R. Q. Wright, "VITAMIN-E: An ENDF/B-V Multigroup Cross-Section Library to LMFBR Core and Shield, LWR Shield, Dosimetry, and Fusion Blanket Technology," ORNL-5505, Oak Ridge National Laboratory (1979).
16. W. W. Engle, Jr., "A User's Manual for ANISN, A One-Dimensional Discrete Ordinates Transport Code with Anisotropic Scattering," K-1693, Oak Ridge National Laboratory, (1967).
17. R. MacFarlane, "TRANSX-CTR: A Code for Interfacing MATXS Cross-Section Libraries to Nuclear Transport Codes for Fusion System Analysis," LA-9363-MS, Los Alamos National Laboratory (Feb. 1984).
18. P. G. Young, and L. Stewart, "Evaluated Data for $n + {}^9\text{Be}$ Reactions," LA-7932-MS (ENDF-283), Los Alamos National Laboratory (July 1979).

19. P. G. Young, "Evaluation of $n + {}^7\text{Li}$ Reactions Using Variance-Covariance Techniques." Trans. Am. Nucl. Soc., **39**, 272 (1980). See also "ENDF-201 Supplement I. ENDF/B-V.2 Summary Documentation," BNL-NCS-17541 (ENDF-201). Brookhaven National Laboratory (Jan. 1985).
20. J. Kimlinger and E. Plechaty, "TARTNP User's Manual," Lawrence Livermore National Laboratory, UCID-17026 (1976).
21. R. E. Prael and L. J. Milton, "A Users Manual for the Monte Carlo Code VIM," Argonne National Laboratory, FRA-TM-84 (1976).
22. W. Gruber, et al., "Geometric Description Technique Suitable for Computer Analysis of Both the Nuclear and Conventional Vulnerability of Armored Military Vehicles," MAGI-6701 (1967).
23. K. D. Lathrop, "DTF-IV, A FORTRAN-IV Program for Solving the Multigroup Transport Equation with Anisotropic Scattering," Los Alamos National Laboratory, LA-3373 (1965).
24. W. A. Rhoades and R. L. Childs, "An Updated Version of the DOT 4 (version 4.3) One- and Two-Dimensional Neutron/Photon Transport Code," CCC-429, Radiation Shielding Information Center, RSIC (1982).
25. R. T. Santoro, J. M. Barnes, J. D. Drischler, and R. G. Alsmiller, Jr., "Multigroup Energy-Angle Distributions for Neutrons from the $T(d,n) {}^4\text{He}$ Reaction ($E_d = 100 - 400$ keV)," Oak Ridge National Laboratory, ORNL/TM-9251.
26. J. Benveniste, et al., and J. Zenger, "Information on the Neutrons Produced in the ${}^3\text{H}(d,n) {}^4\text{He}$ Reaction," UCRL-4266 (1954)
27. J. Benveniste, et al., Nucl. Instrum. Methods, **7**, 306 (1960)
28. Y. Seki, et al., J. Nucl. Sci. Technol., **20**, (8) 686 (1983)
29. Y. Seki, et al., "Monte Carlo Calculation of the Characteristics of Source Neutrons and Irradiation Field of the FNS Rotating Target," JAERI-M-84-193, Japan Atomic Energy Research Institute (October 1984).
30. Y. Ikeda, et al., "Measurement of High Threshold Activation Cross-Sections for 13.5 to 15 MeV Neutron," Proc. International Conference on Nuclear Data for Basic and Applied Science, May 13-17, 1984, Vol. 1, 175, Santa Fe, NM (1985).
31. S. C. Mo and K. O. Oh, Nucl. Sci. and Eng. **95**, 214 (1987).
32. H. Sekimoto, M. Ohtsuka, and N. Yamanuro, Nucl. Sci. and Eng., **80**, 407 (1982).
33. B. Underwood, Nucl. Inst. and Methods, **164**, 247 (1979).
34. G. C. Hanna, "The Neutron Flux Perturbation Due to an Absorbing Foil: A Comparison of Theories and Experiments," Nucl. Sci. Eng., **16**, 325 (1963).
35. C. Wong, et al., UCRL-51144 (Rev. 1) (1971).
36. D. Garber, Ed., "ENDF/B-V," BNL-17541 (ENDF-201) National Nuclear Data Center, Brookhaven National Laboratory (1975).
37. Y. Oyama, et al., Private communication.
38. M. Z. Youssef, "Status of Methods, Codes and Applications for Sensitivity and Uncertainty Analysis," Fusion Technol., **8**, 1552 (1985).

39. D. E. Bartine, E. M. Oblow and F.R. Mynatt, "Radiation-Transport Cross-Section Sensitivity Analysis--A General Approach Illustrated for a Thermonuclear Source in Air," Nucl. Sci. and Eng., **55**, 147 (1974).
40. "ENDF-102: Data Format and Procedure for the Evaluated Nuclear Data File, ENDF," National Nuclear Data Center, Brookhaven National Laboratory, BNL-NCS-50496, ENDF-102 (1979).
41. Y. Seki, et al., "Monte Carlo Calculation of Source Characteristics of FNS Water-Cooled Type Tritium Target," J. Nucl. Sci. and Technol., **20**, 686 (1983).
42. N. M. Green, et al., "AMPX: Modular Code System for Generation Coupled Multigroup Neutron-Gamma-Ray Cross-Section Library from Data in ENDF Format," Radiation Shielding Information Center, Oak Ridge National Laboratory, PSR-063/AMPXII, ORNL/TM-3706 (1980).
43. "DOT 3.5: Two-Dimensional Discrete Ordinates Radiation Transport Code," Radiation Shielding Information Center, Oak Ridge National Laboratory, RSIC/CCC-276 (1973).
44. R. Santoro, Oak Ridge National Laboratory, private communication. (1979).
45. R. MacFarlane, "TRANSX-CTR: A Code for Interfacing MATXS Cross-Section Libraries to Nuclear Transport Codes for Fusion System Analysis," LA-9363-MS, Los Alamos National Laboratory (Feb. 1984).
46. "DLC-113/VITAMIN-E: A Coupled 174 Neutron, 38 Gamma Ray Multigroup Cross-Section Library for Deriving Application-Dependent Working Libraries for Radiation Transport Calculation," Radiation Shielding Information Center, Oak Ridge National Laboratory, RSIC/DLC-113 (1984).
47. W. A. Rhoades and R. L. Childs, "DOT IV Version 4.3: One- and Two-Dimensional Transport Code System," Radiation Shielding Information Center, Oak Ridge National Laboratory, RSIC/CCC-429 (1982).
48. C.R. Weisbin, et al., "Application of FORSS Sensitivity and Uncertainty Methodology to Fast Reactor Benchmark Analysis," Oak Ridge National Laboratory, ORNL/TM-5563 (1976). See also "FORSS: A Sensitivity and Uncertainty Analysis Code System, Radiation Shielding Information Center, Oak Ridge National Laboratory RSIC/CCC-334 (1983).
49. R. L. Childs, D. E. Bartine and W.W. Engel, Jr., "Perturbation Theory and Sensitivity Analysis for Two-Dimensional Shielding Calculations," Trans. Am. Nucl. Soc., **21**, 543 (1975).
50. R. L. Childs, "Generalized Perturbation Theory Using Two-Dimensional Discrete Ordinate Transport Theory," Oak Ridge National Laboratory, ORNL/CSD/TM-127 (1980).
51. "PUFF-2: Determination of Multigroup Covariance Matrices from ENDF/B-V Uncertainty File," Radiation Shielding Information Center, Oak Ridge National Laboratory, RSIC/PSR-257 (1981).